THE UNIVERSITY *of* EDINBURGH

Thermoplastic Resin Transfer Moulding of Tough Recyclable Composites for High Volume Manufacturing

James J. Murray

Thesis submitted to The University of Edinburgh in partial fulfilment of the requirements for the degree of Doctor of Philosophy

March 2020

THE UNIVERSITY *of* EDINBURGH

Declaration

I declare that this thesis is an original report of my research, has been written by me and has not been submitted for any previous degree. The experimental work is almost entirely my own work; the collaborative contributions have been indicated clearly and acknowledged. Due references have been provided on all supporting literatures and resources.

James J. Murray

April 2020

Abstract

The aim of this project was to develop tough thermoplastic composite materials and moulding processes aimed at high rate production applications. The use of anionically polymerised polyamide 6 (APA-6) as a matrix in continuous fibre reinforced composites, manufactured using thermoplastic resin transfer moulding (TP-RTM) was investigated.

The requirements for high speed manufacturing of composite parts and the importance of the polymer matrix choice in terms of temperature and pressure were outlined. In order to manufacture laminates, a TP-RTM setup had to be designed and built. The system designed consisted of a mixing/injection unit with a set of tanks and pumps heated above the melt temperature of the raw materials. During infusion of a composite part, the materials would be melted in the tanks, pumped through a mixing head for homogenising and delivered to the mould which contained a textile. Together, the system is capable of producing 340 mm x 390 mm panels with varying thicknesses, depending on that desired.

Decisions for the choice of raw materials, their mixing ratios and processing temperatures were outlined. These decisions were based on literature and experiments carried out in order to produce a tough matrix material suitable for its purpose. 4 mm thick polymer plates were manufactured using the TP-RTM system and were characterised in terms of their chemical, thermo-morphological and mechanical properties. The distribution of thickness and density across plates was studied to better understand the effects of the mould geometry, molten flow and heat transfer on the degree of shrinkage in the material. It was found from this work that the APA-6 had a melt temperature of ~219 °C, glass transition temperature of ~70-85 °C and degree of crystallinity of ~42%. The tensile strength and modulus of the APA-6 were found to be ~83 MPa and 2.8 GPa respectively.

Following analysis and testing of pure APA-6, unidirectional composite laminates were manufactured using the TP-RTM system. A non-crimp stitched glass fabric was used such that fibre volume fractions of approximately 51-52% would be achieved. As for the pure polymer, the distribution of thickness and density was determined across laminates. Likewise, the thermo-morphological properties were determined and compared with those of the pure polymer to determine the role of the fibres and the degree to which they effect the matrix properties. Finally, extensive mechanical testing was carried out to determine the transverse and longitudinal properties of the composite. In order to observe the effects of flow during manufacture on the final internal geometry of the composite, X-ray CT and micro section studies were carried out. The studies confirmed the presence of asmall percentage of voids in

the materials as a result of the stitching and determined the degree to which this effected the properties. The mechanical properties of the composite compared extremely well with similar products which are commercially available. The strength and modulus of the composite were ~1109 MPa and ~41 GPa in tension respectively and ~691 MPa and ~42 GPa in compression respectively.

The effects of different fibre sizings on fibre-matrix interface was investigated. Two different sizing types were looked at, one of which consisted of a reactive coating which would theoretically result in greater bonding. Firstly, scanning electron microscopy and atomic force microscopy of the fibres was carried out to observe distribution of the sizings on fibres at the microscale and nanoscale respectively. Thermogravimetric analysis was carried out to determine the temperature at which oxidation occurred in each sizing. Pyrolysis was carried out on larger quantities of fibres to determine the amount of sizing by mass on each fibre type. Unidirectional composite laminates using both fibre types were manufactured and tested to determine the effects on transverse, interlaminar shear and fracture toughness properties. The results indicated that the composite with the reactive sizing performed around 16% better in terms of strength on average but showed little difference in modulus. Results from testing indicated that it might also perform better in terms of Mode I fracture toughness; however, high scatter in results meant that this was inconclusive.

Finally, quasi-isotropic laminates were manufactured using both of the aforementioned fibre sizing types and the effects of out-of-plane impact were investigated. Tests were firstly carried out on the pure APA-6 material and were compared to those for a standard epoxy in terms of energy absorption and force induced due to impact. The epoxy only absorbed around 44% the amount of energy before fracture compared to the APA-6. Laminates made using both fibre types were compared by testing at different energy levels and carrying out post-impact mechanical tests. The fibre type wasn't shown to significantly influence the energy absorbed by the materials before break; although, differences in the nature of failure were observed. Carbon fibre laminates made from both APA-6 and epoxy matrices were manufactured and tested to measure energy absorption and force induced in each. The epoxy composite absorbed around 84% the amount of energy before fracture compared to the APA-6 composite.

Overall, it is shown that thermoplastic composites with excellent strength, toughness and impact performance were manufactured using a production process with potential for high production rates. Unidirectional laminates were produced using injection pressures of around 10% of those required to achieve the same fibre volume fraction and degree of wet-out using a typical thermoset RTM resin, negating the need for expensive equipment.

Lay Summary

Fibre reinforced polymer composite materials are generally used for applications where a high stiffness/strength-to-weight ratio is required. Due to the expense of the raw materials and high manufacturing costs, the use of composites has mainly been limited to higher end applications. The materials used generally consist of a polymeric resin and a high performance reinforcement material such as carbon fibre. The manufacturing processes used to produce aerospace standard composite materials from the raw materials are time consuming and sufficient quality can only be achieved using expensive autoclaves. In comparison, a liquid composite moulding process known as resin transfer moulding (RTM) can produce parts in significantly shorter cycle times; and for large scale production, can be cost-effective. This process involves placing a textile into a mould and injection a polymeric resin which cures. These polymers can be split into two groups known as thermosets and thermoplastics. The key difference is that the latter can be remelted and recycled whereas the former cannot. Many thermoplastics are very tough compared to thermosets, meaning that they can absorb a lot of energy before fracture. This means that they have good resistance to crack growth and are suitable for high impact applications. While the properties of the thermoplastics are desirable in in many composite applications, they are generally too viscous to flow into the fabric, unlike thermosets which are more fluid like. For this reason, thermosets have been the choice in most applications. The aim of this project is to produce thermoplastic composites using a process called thermoplastic RTM or TP-RTM. Rather than injecting the melted thermoplastic polymer into the textile, the reactant precursor materials are injected into the textile and react in-situ. These precursor materials unlike their polymer offspring, have water-like properties when melted, allowing them to flow easily into a textile.

This thesis investigates the characteristics of composite materials produced using TP-RTM in in terms of its suitability as a tough material for high rate manufacturing. A system was designed and built to process the materials which had to be controlled under very specific conditions during processing. For manufacturing, the precursor materials were heated above their melt temperature and injected into a glass-fibre textile contained within the mould. By application of pressure, defects in the product due to small percentages of pockets of air (or voids) were reduced to enhance properties. The fabric type used was what is known as a unidirectional stitched fabric. Such fabrics consist of bundles of fibres in each, held together in parallel by stitches. Along the fibre length, the stitches were located in 5mm increments. Due to the tightening of the stitch on each bundle, the fibres were tightly packed at each stitch. Studies were carried out under a microscope to determine the effects this had on voids within the material and their distribution was studied using X-ray CT scans. The material was

characterised in terms of its mechanical properties and it was shown that some secondary effects due to the stitching caused reduced properties.

Quite often fibres contain a type of coating called a *sizing*. The sizing is used to protect the fibres and can be used also as a method of increasing the bond strength with the polymer. Two different sizing types were tested, one with a standard coating and another which contained one of the reactants which partakes in the chemical reaction. The fibres were observed at various magnifications using different microscopic techniques to look at the distribution and structure of the sizings, while the amount of sizing on fibres for each type was determined by weight. Composite laminates manufactured from both types were tested and compared in terms of strength and stiffness. A type of test known as a double cantilever beam (DCB) test was carried out on both types of laminates to measure the material's resistance to crack growth. The sample roughness of the surfaces were then determined to explain the results of each. In all test types, the sizing which contained the reactants performed better.

Having tested the samples in terms of crack resistance, out-of-plane impact tests were also carried out. This involved supporting samples, dropping weights from different heights and recording load values and the energy absorbed. These tests were firstly carried out on the pure APA-6 polymer and epoxy to compare the thermoplastic and thermoset cases. Glass fibre laminates made from both of the aforementioned sizing types were tested. In addition, composite samples from carbon fibre with both APA-6 and epoxy were tested and compared.

There are many potential benefits from this work to both the academic community and industry. This research broadens the depth of knowledge in liquid composite moulding with the aim of making it a more developed technology. TP-RTM offers a pathway to produce parts that are tough, recyclable and weldable which are potentially faster and cheaper to produce when compared with standard RTM processes used. This research builds on the pathway for industry to use this technology by solving technical problems which reduces the risk, and hence, makes the technology more economical and feasible.

Acknowledgements

Firstly, I'd like to thank my PhD supervisor, Prof. Conchúr Ó Brádaigh who gave me this opportunity to do my PhD in composites at The University of Edinburgh and supported me through the journey. As with all his PhD students, I have been given amazing opportunities to visit and work in locations around the globe as a result of connections made through his vast network. I was privileged to be able to work on the MARINCOMP project as a result of Conchúr's connections (Come on the Rossies!). I would like to thank Dr. Eddie McCarthy who became my adopted second supervisor and supported my work through the journey. Eddie helped me brush up on my chemistry knowledge for which I have been very grateful.

I'd like to thank Johns Manville, ÉireComposites Teo., CIMComp and the College of Science and Engineering for funding my PhD. A big thanks to my industrial supervisor, Klaus Gleich from Johns Manville who was very supportive and kind throughout the project and the staff members in the School of Engineering (I will miss the chats in the hallway). I'd like to thank all the friends I made and the staff members at The University of Auckland, particularly Prof. Simon Bickerton who supervised my work and his colleague, Dr. Tom Allen, who offered much support.

I'd like to give a huge thank you to all the undergraduate/masters students who I worked with over the years on their final year projects (Winson Ho, James Quinn, Jessica Chan, Nevil Patel and Eda Ozkan – It was a pleasure to work with you all). A massive thanks to Eddie Monteith who machined and fabricated almost everything for the project and became a good friend over the years. I want to thank Colin, Dimitrios, Dipa, Wini and Christophe whose company and knowledge was much appreciated. Eva, you were the best thing to come out of this PhD. I want to thank you for your love and support and for being such a great friend - Ευχαριστώ πολύ! Martin, Eli, Maguire and Maria, thanks for putting up with me in the flat, I'll look back on these times with fond memories. Davidson and Quinn, we need to find another James to get the number back to 4. I want to thank you both for your company in the office, friendship and support. Jake, the fun chats and embarrassing moments both inside and outside the office will be remembered with both happiness and laughter

Finally, I want to thank my family who were so supportive throughout this journey and indeed my friends from home (The Shlugs) for supplying craic 24/7 when I returned for visits.

This thesis was written in lockdown due to the COVID-19 pandemic which has affected the lives of us all. Here's hoping that we discover a vaccine and can return to normalality soon!

Go raibh míle maith agaibh go léir agus tabhairigí aire daoibh féin!

List of Publications

Journal Articles

1. Murray, J. J., Robert, C., Gleich, K., McCarthy, E. D., Ó Brádaigh, C. M., 'Manufacturing of unidirectional stitched glass fabric reinforced polyamide 6 by thermoplastic resin transfer moulding', *Materials and Design*, 189, 2020, DOI: https://doi.org/10.1016/j.matdes.2020.108512.

2. Murray, J. J., Robert, C., Gleich, K., McCarthy, E. D., Ó Brádaigh, C. M., 'Interfacial properties and novel fibre sizings for PA-6 composites produced by TP-RTM', In preparation.

3. Murray, J. J., Gleich, K., Allen, T., Bickerton, S., McCarthy, E. D., Ó Brádaigh, C. M., 'Impact properties of PA-6 composites produced by TP-RTM', In preparation.

Conferences

1. Murray, J. J., Robert, C., Gleich, K., McCarthy, E. D., Ó Brádaigh, C. M., 'Properties of polyamide-6 composites using a low-viscosity thermoplastic resin transfer moulding system', *22nd International Conference on Composite Materials*, Melbourne, Australia, 2019.

2. Murray, J. J., Gleich, K., Allen, T., Bickerton, S., McCarthy, E. D., Ó Brádaigh, C. M., 'Impact Performance of Thermoplastic Resin Transfer Moulded Carbon Fibre Composites', *SAMPE Europe Conference,* Amsterdam (online), Netherlands, 2020.

3. Murray, J. J., Robert, C., Gleich, K., McCarthy, E. D., Ó Brádaigh, C. M., 'TP-RTM: Interfacial properties of anionically polymerised PA-6/glass-fibre composites', *23rd International Conference on Composite Materials*, Belfast, United Kingdom, 2021, abstract submitted.

Table of Contents

List of figures

List of Tables

Nomenclature

a	Crack length
$A_{1,2}$	Arrhenius constants
A_{cs}	Cross-sectional area
A_b	Surface area of bottom panel
A_o	Surface area of all outer panels combined
A_t	Surface area of top panel
A_v	Surface area of vertical panel
b	Width
C_p	Heat capacity
$C_{p\,air}$	Heat capacity of air
$C_{p\,al}$	Heat capacity of aluminium
$C_{p\,mat}$	Heat capacity of precursor materials in tank
$C_{p\,st}$	Heat capacity of steel
c	Concentration of polymer solution
c_0	Initial concentration of reactive groups
DC	Degree of conversion
d	Pipe diameter
$E_{1,2}$	Activation energies
E'	Storage modulus
E''	Loss modulus
e	Exponent
F	Correction factor for DCB
F_c	Preform compaction force
F_m	Force at mould inlet due to fluid pressure
F_p	Clamping force
F_s	Elastic reaction exerted by mould seal
G_1	Mode I fracture toughness
$G_{1c\,Max}$	Mode I initiation fractire toughness determined by max. load
$G_{1c\,NL}$	Mode I initiation fracture toughness from linearity deviation
$G_{1c\,VIS}$	Mode I initiation fracture toughness determined visually
$G_{1p\,Avg}$	Average mode I propoagation fracture toughness
g	Distance of bore hole from bottom of DCB block
ΔH	Heat energy from reaction
ΔH_c	Enthalpy of fusion of purely crystalline polymer
ΔH_m	Enthalpy of fusion of polymer
ΔH_{vap}	Molar heat of vapourisation
h	Thickness
h_i	Heat transfer coefficient for inner walls
h_{ib}	Heat transfer coefficient of bottom inner panel
h_{it}	Heat transfer coefficient of top inner panel
h_{iv}	Heat transfer coefficient of vertical inner panels
h_{ob}	Heat transfer coefficient of bottom outer panel
h_{ot}	Heat transfer coefficient of top outer panel
h_{ov}	Heat transfer coefficient of vertical outer panels
h_o	Heat transfer coefficient for outer walls

Δh_p	Specific enthalpy of polymerisation
Δh_c	Specific enthalpy of crystallisation
K'	Mark-Houwink constant
K_v	Flow coefficient
$k_{1,2}$	Reaction rate constants
k	Constant (Flory-Fox)
k_{al}	Thermal conductivity of aluminium
k_c	Thermal conductivity of caprolactam
k_{gw}	Thermal conductivity of glass wool
k_m	Thermal conductivity of bulk material
k_n	Thermal conductivity of nitrogen
L'	Distance of bore hole from side of DCB block
l	Length
l_{mat}	Latent heat of fusion of precursor materials
n	Rotational speed
p	Mark-Houwink constant
P	Load
M_n	Number average molecular weight
M_v	Viscosity average molecular weight
m_{al}	Mass of aluminium parts
m_m	Mass loss from extraction
m_{mat}	Mass of precursor materials in tanks
m_{st}	Mass of steel parts
m_t	Total mass of sample before extraction
N	Correction factor for DCB
P_{CV1}	Check valve cracking pressure
P_{CV2}	Check valve pressure due to obstruction
P_{comb}	Combined tube pressure (post-mixing)
P_{ind}	Individual tube pressure (pre-mixing)
$P_{p\,min}$	Minimum pump pressure required
P_{MH}	Mixing head pressure drop
P_{vap}	Vapourisation pressure
Q	Flow rate
Q_{ch}	Heating flow from ceramic heater
Q_{hm}	Heating flow from heating mat
Q_{loss}	Heating flow lost to surroundings
Q_m	Flow rate through the mould
Q_{mat}	Heat flow required to heat materials
Q_o	Heating flow from outer walls
Q_p	Flow rate through the pipe
Q_{parts}	Heat flow required to heat parts
R	Gas constant
$R_{1,2}$	Electrical resistance of resistors 1 and 2 respectively
R_{al}	Thermal resistance of aluminium
R_{enc}	Thermal resistance of entire enclosure
R_{gw}	Thermal resistance of glass wool
R_{ib}	Thermal resistance due to convection on bottom inner panel
R_{it}	Thermal resistance due to convection on top inner panel
R_{iv}	Thermal resistance due to cvtn. on vertical inner panels
R_{ob}	Thermal resistance due to convection on bottom outer panel
R_{ot}	Thermal resistance due to convection on top outer panel

R_{ov}	Thermal resistance due to cvtn. on vertical outer panels
Re	Reynold's number
SG	Specific density
t	Time
t_0	Time taken for pure solvent to pass through viscometer
t_{al}	Thickness of aluminium wall panel
t_{gw}	Thickness of glass wool insulation
T	Temperature
T_0	Initial temperature
T_{amb}	Ambient temperature
T_b	Boiling temperature
T_c	Crystallisation temperature
T_{enc}	Enclosure temperature
T_g	Glass transition temperature
$T_{g,\infty}$	Glass transition temperature at highest molecular weight
T_m	Melt temperature
T_{max}	Maximum temperature
T_o	Outer wall temperature
T_p	Torque required to drive pumps
V	Volume
V_f	Fibre volume fraction
V_g	Rotational volumetric displacement
V_{in}	Voltage input prior to voltage divison
V_{out}	Voltage out after voltage divison
V_v	Void volume fraction
v_c	Composite volume
v_f	Fibre volume
X	Degree of conversion
X_c	Degree of crystallinity
X_{c1}	Degree of crystallinity on first cooling
X_{c2}	Degree of crystallinity on second cooling
w_c	Composite weight
w_f	Fibre weight
x	Kinetic exponent
z	Kinetic exponent
Δ	DCB compliance coefficient
δ	Opening displacement
κ	Permeability
μ	Dynamic viscosity
η_{inh}	Inherent viscosity
η_{int}	Intrinsic viscosity
η_m	Mechanical efficiency
η_v	Volumetric efficiency
π	Pi
ρ	Density
ρ_c	Composite density
ρ_f	Fibre density
ρ_m	Matrix density

Chapter 1: Introduction

1.1 Project Motivation

There is a major impetus towards the use of composite materials within various global industries, many of which they have not traditionally been associated with. In the past, continuous fibre composites have been used in aerospace and high-end applications where high specific strength and stiffness are desirable. Due to the decreasing cost of the raw materials and manufacturing processes over time, composites are becoming more popular, constantly finding new applications. In the automotive industry, composites are becoming more frequently used in passenger vehicles due to the aforementioned reasons.

Light-weighting of vehicles is one of the solutions to reduce CO2 emissions. A significant global shift is currently underway towards the use of electric vehicles (EVs), incentivised by regulation and consumer demand [1]. Light-weighting EVs is more of a priority than in vehicles powered by internal combustion engines. The large weight of the batteries used in these vehicles (~ 200-550 kg [2]) needs to be countered by reducing weight elsewhere in the car body. In order to handle the same stresses experienced by steel/aluminium structural (or semi-structural) members while also reducing the weight, the use of possibly more expensive composites can be justified.

For the automotive industry and many others, there is also a demand for tough materials where components may be subject to impact loading. This may include a pillar structure in a car, the housing of a pump or an application subject to large vibrations or fatigue cycles. It is important in vehicles that these parts can sufficiently absorb impact in a manner which reduces injury or prevents fatalities due to high speed collisions.

Short cycle times are essential in the production of high volumes of parts such as those for the automotive industry [1][3]. One of the key factors when producing over 200,000 parts per year is the cycle time, which should be under 2 minutes per part [3][4].

One of the main problems associated with composites is the challenges faced at integrating them into a circular economy. If composites are to continue to grow in a world that is becoming increasingly conscious of the environmental impact of materials end-of-life use and their processing footprint, composites must at least evolve towards using reusable materials and perhaps eventually bio-sourced/bio-degradable alternatives.

In summary, the primary motivation behind this thesis is to contribute towards the development of affordable high rate manufacturing processes for tough reusable thermoplastic composite materials.

1.2 Composite manufacturing methods for high rate production

In the aerospace industry, composite parts are generally produced using relatively expensive manufacturing processes which require autoclaves to provide the pressure to achieve the necessary quality. Liquid composite moulding (LCM) processes are those which use low viscosity resins to infuse a textile. One such process is vacuum infusion, where a textile is placed on an open mould surface, a vacuum bag is placed over it with an inlet connected to a resin supply and an outlet connected to a vacuum pump. The vacuum pressure pulls the resin through the textile, infusing the part, which then cures. Resin transfer moulding (RTM) is a popular LCM process used to produce composite parts for high volume manufacturing where the cost of the equipment required can be justified [5]. The process involves injecting a resin under pressure into a reinforcement textile contained within a closed mould [6]. A press is often required to generate reaction forces to keep the mould closed during injection and to prevent the cavity walls from deflecting. By mounting the mould halves to the platens of a press with quick displacement action, part removal speeds and cycle times can be reduced. RTM can produce reasonably high quality, complex parts in series economically, which make it suitable for the automotive industry [7][8][5] .

Two-part thermoset resins are often used in these systems due to their low viscosities. For low volume production of relatively small parts, low pressure resin transfer moulding (LP-RTM) is often used. LP-RTM is generally used for pressures under 20 bar and can often be delivered using a twin cylinder system driven by an overpressure of air. The components in these systems are often mixed using disposable static mixing heads and tubing made from plastic. Alternatively, the resin and hardener can be mixed in advance and placed in a pressure pot. In this case, an overpressure of air can be used to drive the mixture into the mould cavity. The cycle times for LP-RTM are typically between 30 and 60 minutes but depends mainly on the resin system used and the amount of heat applied, if any [9].

For large parts, with reasonably high fibre volume fractions, high pressure resin transfer moulding (HP-RTM) is often required to infuse parts within short times. HP-RTM typically requires pressures of between 30 and 150 bar with cycle times of less than 10 minutes [10]. In order to deliver the resin into the textile at such high pressures, expensive injection machines are usually required. The machines often mix the components and drive the mixture at high flow rates using mechanically driven pumps. The mould halves in these systems tend to be fixed to large presses with heated platens and where high temperatures are used, they often contain in-built circuitry for cooling using flowing water or oil.

Compression resin transfer moulding (C-RTM) involves the introduction of a compression stroke between mould filling and curing. High quality parts can be achieved using C-RTM using injection pressures of only 5-10 bars at a much faster rate than LP-RTM [11]. This can be achieved using well designed seals and a press with good displacement control. A slight gap is introduced between the mould halves such that the textile inside is not compressed. This means that relatively low pressures are required to fill the mould initially but due to the flexibility of the seal material, it can adjust to the gap thickness without leaking. Following filling, pressure is applied from the press to close the mould fully, such that the fibres are fully wetted out. This saves on the costs of expensive injection machines but still requires a heavy duty press. The three different types of basic RTM systems are shown in Fig. 1.1.

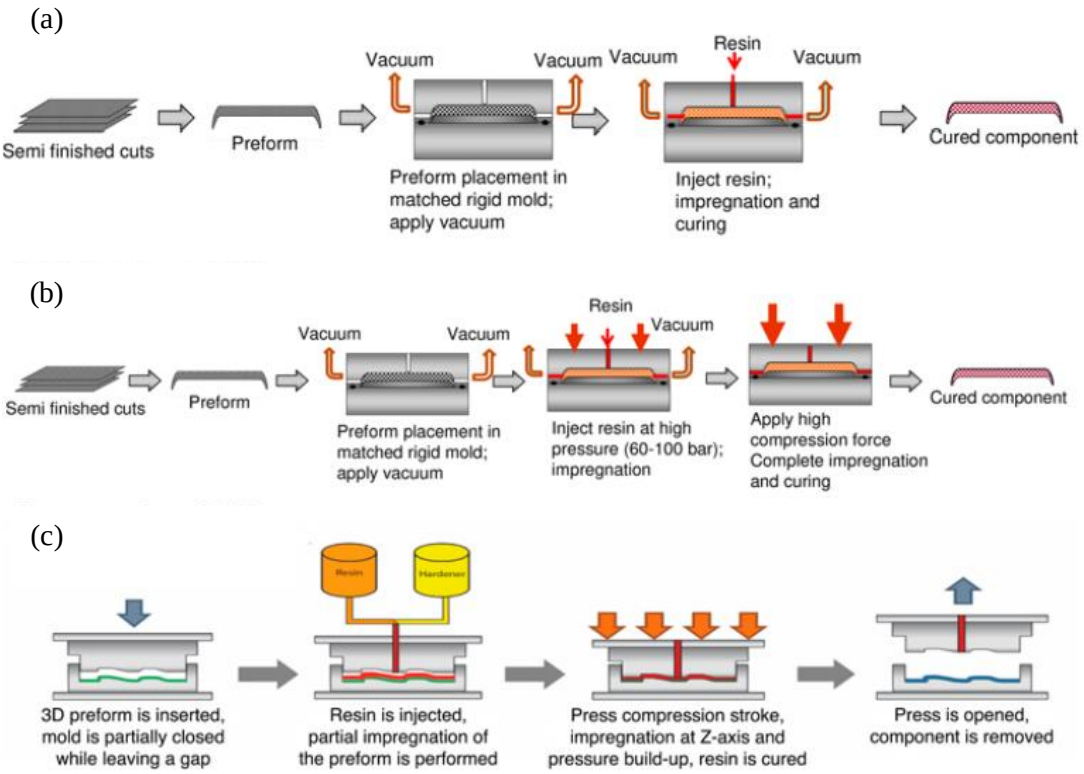

Fig. 1.1: Visual process steps for (a) LP-RTM, (b) HP-RTM and (c) C-RTM [12].

1.3 Thermoplastic composites

Traditionally, LCM processes such as RTM have been exclusively used with thermoset resins. This is due their low viscosities (10 - 1000 mPa.s) compared to thermoplastic melts whose viscosities are significantly higher (> 100,000 mPa.s) [13].

Some thermoplastics have unique properties that render them desirable as matrices for many composite applications where thermoset resins are unsuitable. Joining processes such as welding, manufacturing processes such as thermoforming and end of life material recyclability are some of the many benefits to be realised from their use. Due to their high molecular weight, they are generally tougher than thermoset resins, and because they can be melted, their unique properties can be exploited and tailored for their application in composites. Their high molecular weights, however, also result in higher melt temperatures (> 200 °C) and higher melt viscosities (> 100,000 mPa.s), making them difficult to process. This makes liquid composite moulding (LCM) of thermoplastic melts with high fractions of continuous fibre reinforcement practically impossible, as extremely high pressures would be required to infiltrate fibres and to achieve good fibre/matrix uniformity to ensure sufficient load transfer between fibre and matrix [14]. As a result, their use in composites has been limited to expensive intermediate materials such as commingled fabrics and pre-impregnated tapes which still require the application of additional pressure and temperature to manufacture parts [15], [16].

In summary, while thermoplastics have many desirable properties, their use is limited in composites due to their high viscosities.

1.4 Reactive processing of thermoplastic

The development of what is known as *reactive* processing in recent years has provided a means of enabling LCM of thermoplastics. Rather than injecting the high viscosity thermoplastic melt, the precursor materials from which the polymer is made from can be injected. The precursors, which consist of the monomer and reactants, generally have a much lower melt viscosity and melt temperature than the polymer which they produce. Reactive processing allows for a much better infiltration of fibres and requires less energy (work and heat) to process. In addition, this process negates the need for expensive intermediates used in melt processing such as pre-pregs and films. After infiltration of fibres, the pre-mixed reactants polymerise *in-situ*, resulting in a thermoplastic composite part. There are a range of

thermoplastic precursor systems on the market, which exploit this such as Elium®, an acrylic based system developed by Arkema which polymerises at room temperature [17]. Its drawbacks are the expense of the precursor and the large amount of heat generated by the reaction exotherm, particularly for thicker sections [18]. Work has been carried out in the past on composites with a polybutylene terephthalate matrix produced from cyclic oligomers (pCBT) that can be polymerised isothermally at ~180 °C, demonstrating reasonable mechanical properties. Due to its morphology after polymerisation at this temperature, the material is brittle, yields poor impact properties and often requires additives for toughening [19]–[21]. Wind turbine blades have successfully been manufactured from both Elium and pCBT using exothermic control additives for the former and specialised high temperature tooling for the latter [18], [22]. Much work has been carried out on anionic ring opening polymerisation of lactams to produce polyamides [23]–[29]. Work on polyamide 12 (PA-12) composites produced from laurolactam has been carried out in the past but has largely been surpassed by research on polyamide 6 (PA-6) produced from caprolactam, mainly because PA-6 requires lower processing temperatures and its strength and modulus are superior [30]–[33]. The caprolactam monomer has a viscosity of less than 10 mPa.s at melt, which is lower than some of the lowest viscosity thermoset resins used for RTM and can be polymerised in a fraction of the cure time [34]. Zingraff et al. [32] carried out an in-depth study to observe and reduce the amount of voids produced in anionically polymerised PA-12 composites. Lactams are prone to void formation in RTM style processes due to the use of nitrogen gas which is soluble in the molten lactam. The research achieved a void content reduction from 15% to 1% by limiting the diffusion of nitrogen during preparation of the materials.

1.5 Vacuum infusion of reactive polyamide 6

Much of the literature published on anionically polymerised PA-6 (APA-6) composites derived from a renewed interest in the area after extensive research was carried out by Bersee et al [35]–[38]. This work was aimed at developing a vacuum infusion process to manufacture thermoplastic composite wind turbine blades, but dealt with a broad range of more fundamental research on LCM of APA-6. These studies focused mainly on the effects of processing temperature and different types and quantities of activators/catalysts on the degree of polymerisation, crystallinity and mechanical properties. Work was carried out comparing the interfacial properties of composites using different fibre sizings; however, due to the large void content (up to 10% by volume) and the low repeatability of the vacuum infusion process, there are possibly large deviations in the results for interlaminar shear strength which have not been shown [39]. The resin flow rates can be difficult to control using vacuum as the driving

force, due to the almost water-like viscosity of the precursors, which is extremely sensitive to pressure changes. This means that it is difficult to obtain adequate flow control, even using fine control valves. If the vacuum pressure is too high, the flow rate is rapid and inter-bundle infiltration of fibres is poor. If the vacuum pressure is too low, polymerisation onset may occur before the liquid mixture reaches the outlet of the mould. Moreover, if the monomer is not heated to temperatures above 69 °C, the monomer in the feed lines will freeze, preventing further infusion. The vacuum infusion process requires expensive bagging film and is extremely time consuming. For the aforementioned reasons, vacuum infusion of APA-6 is not suitable for high volume manufacturing; however, many of the results and ideas from work carried out in this area can be applied to other manufacturing processes.

1.6 Thermoplastic resin transfer moulding

A more controlled method of processing APA-6 in terms of flow rate is thermoplastic resin transfer moulding (TP-RTM). The process is like a standard resin transfer process but rather than using a thermoset resin, the mixed thermoplastic precursor materials are injected. Most academic work published on TP-RTM to date, has used an overpressure of gas to drive the liquid precursors [32], [33], [40]–[44]. Due to the viscosities of the monomer (< 10 mPa.s) being even lower than most infusion thermoset resins, similar wet-out can be achieved at lower pressures. Industrial partnerships between automotive companies, raw material suppliers and RTM injection system manufacturers have resulted in the successful serial manufacture of TP-RTM parts using highly sophisticated manufacturing processes [45]–[48]. Such systems are generally expensive because they require the heating and pumping of two components above melt temperature at all times while almost completely eliminating moisture in the system, making the system more complex than standard RTM equipment. This complication, combined with the fact that there is a limited amount of experience in the general composites community in reactive processing of thermoplastic matrices, means that attempts at manufacturing APA-6 composites using quick, controlled processes have been avoided due to the risk involved. Despite the fact the technology exists to produce thermoplastic composites, and although engineers recognise their many advantages, there remain barriers to their deployment such as lack of design data and process experience in the composites community.

A major German collaboration between Volkswagen AG, BASF (with SGL) and Krauss Maffei technologies has resulted in a large scale project to produce B-pillar vehicle reinforcements from a reactively processed PA-6 composite using TP-RTM [47]. Combining chemical expertise from BASF and state of the art metering technology designed by Krauss

Maffei, the collaboration appears to be leading the largest and most anticipated work to date in reactive thermoplastics composites.

Johns Manville (CO, USA) have developed glass fibres with reactive sizing that results in superior interfacial strength between the fibre and matrix. The surface of the glass fibre is coated with a sizing containing the activating group. This causes PA-6 chain growth from the fibre surface, creating a strong interfacial bond. The reactive sizing technology combined with the low viscosity precursor should theoretically result in enhanced mechanical properties and early stage results indicated that this may be the case [49].

1.7 Objectives

The aim of this project is to investigate the development of tough, recyclable thermoplastic composites suitable for high volume manufacturing of parts. This project focuses specifically on TP-RTM of composites using APA-6. In order to achieve this aim, the objectives of the project are outlined as follows:

- Design and build a TP-RTM system for manufacturing composites.
- Manufacture pure APA-6 materials and characterise them in terms of physical, mechanical and thermo-morphological behaviour.
- Manufacture composite laminates using TP-RTM with optimised pressure and flow such that defects are minimised.
- Characterise the composites in terms of their physical, mechanical and thermo-morphological performance.
- Study the effects of different fibre sizings on the composite properties in terms of strength, stiffness and fracture toughness.
- Investigate the energy absorption of TP-RTM produced composites from impact and their post-impact properties.

1.8 Thesis outline

Chapter 2 is a review of literature relevant to this thesis. It begins by looking at the state-of-the-art in automotive manufacturing in terms of material systems, processes, cycle times, economics and quality. Thermoplastics and thermoplastic composites are then reviewed in detail with a particular focus on polyamides. Liquid composites moulding processes are reviewed, particularly RTM style processes.

Chapter 3 outlines the steps carried out in developing the TP-RTM equipment for processing. The requirements are clearly defined initially. The analytical approach in relation to flow and heating are discussed in depth and the choice of design variables outlined. The fabrication of each part in the system and their assembly is then described.

Chapter 4 describes manufacturing procedures for the pure APA-6 polymer and experimental techniques used to characterise the material. Reasons for the choices of various process parameters are initially outlined. Material properties were determined from testing and analysis, and links between the properties and processes parameters identified.

Chapter 5 describes the methods used to manufacture APA-6 composites and the experimental techniques used to characterise them. Microscopy and X-ray CT mehtods are used to study the nature of void defects in the material. The materials are then tested and analysed, and properties linked to process parameters.

Chapter 6 looks at how two different fibre sizings affect the interfacial bonding in the composite between the fibres and polymer matrix. A special reactive sizing developed by project partner Johns Manville is used to enhance performance. The performance of interfacial bonding is compared in terms of transverse mechanical properties and fracture toughness.

Chapter 7 investigates the impact performance of pure APA-6 polymer and composite. Laminates manufactured using the two different aforementioned fibre sizings are compared in terms of energy absorption during impact and post-impact mechanical performance. APA-6, a standard resin infusion epoxy and their composites are compared.

Chapter 8 summarises the key findings and outlines future work which is recommended to further the advancement of TP-RTM.

Chapter 2: Literature review

Summary

This chapter investigates the state-of-the-art in reactive thermoplastic processing of PA-6. This includes the different types of synthesis that can be used to produce PA-6, the process models to determine the degree of conversion, degree of crystallinity and viscosity at any time throughout the polymerisation process, the factors which affect PA-6 properties and the most up to date review of manufacturing processes used.

2.1 Polyamide 6 overview

Polyamide 6 (PA-6), nylon 6 or polycaprolactam is an engineering thermoplastic polymer that was first produced by Paul Schlack in 1938 from ε-caprolactam and has since become one of the most widely used polymers in the world [50]. Polyamides are commonly known by their trade name Nylon. All polyamides are polymers that contain the amide group – CONH – in the recurring unit (or monomer) of the chain [30]. PA-6 is a semi-crystalline polymer and has high specific strength and good resistance to abrasion. One of the main downfalls of PA6 is its high moisture uptake which will be discussed in further detail in section 2.6.2.

2.2 PA-6 synthesis

2.2.1 Hydrolytic polymerisation

Polyamide 6 can be synthesised from the ε-caprolactam monomer using several types of polymerisations; however, the most common synthesis is by hydrolytic polymerisation [30]. Hydrolytic polymerisation consists of three key reactions which are all acid-catalysed. The steps involved are as follows:

(a) Hydrolytic ring opening of ε-caprolactam to produce ε-aminocaproic acid. This reaction is the slowest of the three and is endothermic (see Fig. 2.1 (a)).

(b) Condensation of the linear polymer molecules. This reaction is highly exothermic (see Fig. 2.1 (b)).

(c) The ε-caprolactam addition to the amine end of the growing chain. This exothermic reaction consumes most of the monomer and is the fastest of the three (see Fig. 2.1 (c)).

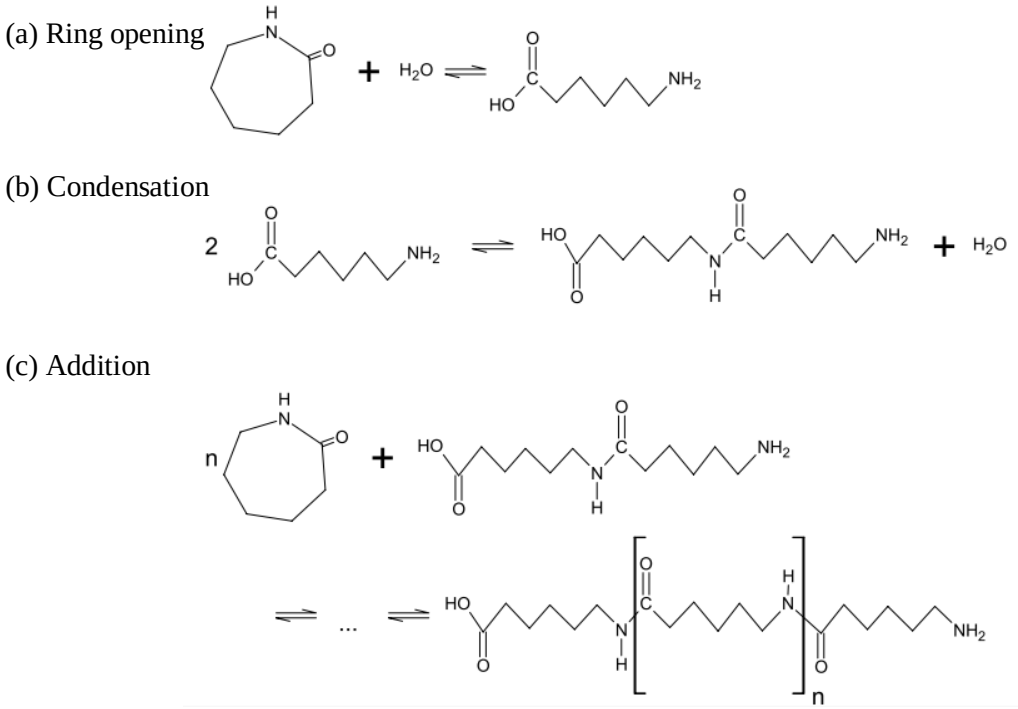

Fig. 2.1: Steps in hydrolytic polymerisation of PA-6.

All three reactions are influenced by water and temperature. More water is required initially for ring opening of the ε-caprolactam to occur and less is favoured for polycondensation. This method of polymerisation is autocatalytic however the time taken is heavily dependent on the production rate of carboxyl end groups due to the ROP step [51]. At equilibrium, the product post polymerisation consists of 10-12 wt% monomer/oligomer, depending on the water content, pressure, end groups, etc. in the melt [30]. These are known as *extractables* and are removed from the product in most applications. The monomer content of the extractables can then be returned to the polymerisation process. For batch production of hydrolytic PA-6 (HPA-6), molten caprolactam and water are fed to a reactor at approximately 80 °C and the temperature is raised to about 260 °C over the course of 3-5 hours. A pressure cycle induces ROP and addition. Pressure can be lowered to reduce the boiling point and hence accelerate condensation. This can be carried out using a vacuum pump which accelerates the process, and hence, increases the molecular weight. Upon reaching the desired molecular weight, the batch is discharged through a die at the bottom of the reactor and the resulting solid is chopped into pellet form. A subsequent leaching step is carried out to remove the extractables by immersing pellets in hot water under pressure.

2.2.2 Anionic polymerisation

One of the main advantages of anionic polymerisations is the ability to synthesise high molecular weight polymer, which can be controlled. The anionic ROP of ε-caprolactam consists of the ε-caprolactam monomer, an activator and a catalyst. The steps in the polymerisation process are as follows and are shown in Fig. 2.2:

(a) Dissociation of the catalyst occurs at elevated temperatures to create the anionic lactam. A strong base such as an alkaline metal or metal hydride is used for the catalyst [52]. The example used is sodium caprolactamate which was that used throughout this project.
(b) Initiation: Ring opening of the anion is followed by the formation of an anionic N-acyllactam chain with the initiator. The initiator is usually an acid chloride or some molecule which can create an imide group after reaction with a lactam monomer.
(c) Initiation is followed by a rapid proton exchange between the caprolactam molecule and the N-acyllactam group. Deprotonation of the caprolactam results in regeneration of the anion. Recurrence of these reactions results in subsequent chain growth to produce PA-6.

This polymerisation is generally carried out at temperatures of around 130-230 °C within a time range from seconds up to an hour depending on the catalyst and parameters used [35], [38], [53], [54]. Anionic ROP of ε-caprolactam is advantageous because with a fast reaction rate at reasonably low temperatures, a polymer with good mechanical properties can be achieved.

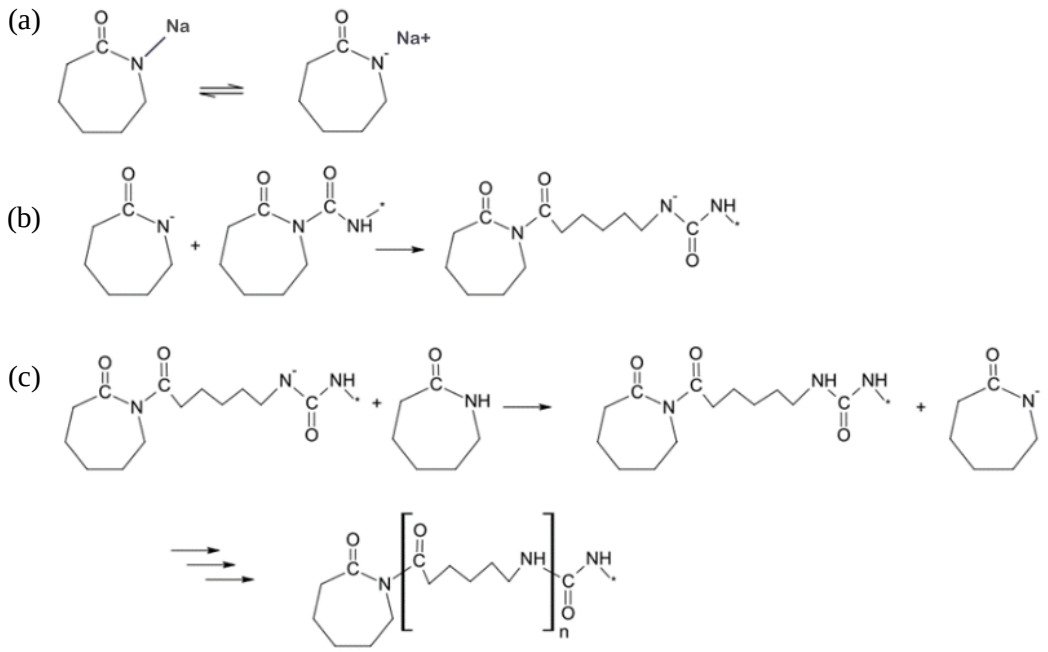

Fig. 2.2: Steps in anionic polymerisation of PA-6 [13].

2.2.3 Effects of moisture and side reactions on anionic polymerisation

One of the downfalls with anionic polymerisation is that it is very sensitive to termination in the presence of moisture. Experiments carried out by Ueda [55] at four different moisture contents showed that by increasing the moisture content, the molecular weight was significantly reduced. By reducing the moisture content from 0.088 mol% to 0.013 mol% when using low concentrations of a mono-functional activator, the molecular weight increased approximately by a factor of 2.5. However, as the activator concentration was increased above 0.15 mol%, the molecular weight was barely affected by the difference in moisture. It is possible that if higher moisture contents were used in the experiment, this would not be the case. The materials can be stored in sealed containers with desiccant and purged with nitrogen prior to sealing. When used in an injection unit, the reactants are often contained in heated tanks under a nitrogen atmosphere to prevent contact with moisture. There is no known literature which outlines the minimum nitrogen purity required for polymerisation to occur. Reaction of the propagating polymer chains with water is the main cause for premature termination of the polymerisation. As such, minimising the moisture content which is in contact with or dissolved within precursor materials is extremely important [55]. It is possible for other side reactions to take place. Claisen condensation can cause branching to occur [25]. Other side reactions include oligomer formation and chain scission [56][57].

2.3 Crystalline and amorphous phases of PA-6

PA-6 is a semi-crystalline polymer, meaning that the material consists of a structured (or crystalline) phase and an un-structured (amorphous) phase. Such polymers undergo two key transitions with respect to temperature; melt at temperature T_m and glass transition at temperature T_g [58]. The former is associated with the crystalline phase of the polymer, above which, the material becomes liquid and can be processed. The latter indicates the temperature above which the amorphous phase transitions from a hard *glassy* state to a soft *rubbery* state. This is caused by frozen polymer chains in the amorphous phase gaining sufficient energy to rotate. The more flexible the chains, the lower the T_g. The degree of crystallinity as well as the size and shape of crystals in semi-crystalline polymers like PA-6 have a great effect on the material's mechanical properties. The degree of crystallinity is affected by the rate at which the melted polymer is cooled as well as the orientation of the melt. During cooling, amide groups form hydrogen bonds with other amide groups in either the same chain or in adjacent chains, causing crystal structures to form [13]. The temperature at which these bonds form during cooling, is called the crystallisation temperature range, T_c. Entanglements of chains in

the polymer prevents the entire material becoming crystalline which cause a partly amorphous phase to remain after cooling below T_c. Initially, nucleation points form at various sites and reel in polymer chains from the surrounding area as the crystals grow in spherulite formation. The chains form lamellae of folding layers in the crystalline phase during crystallisation however when leaving the lamellae, the looping folds can overhang in a random fashion before re-entering the structure. The lamellae crystalline regions combined with the amorphous overhanging folds cause the creation of *switchboards* to occur as shown in Fig. 2.3.

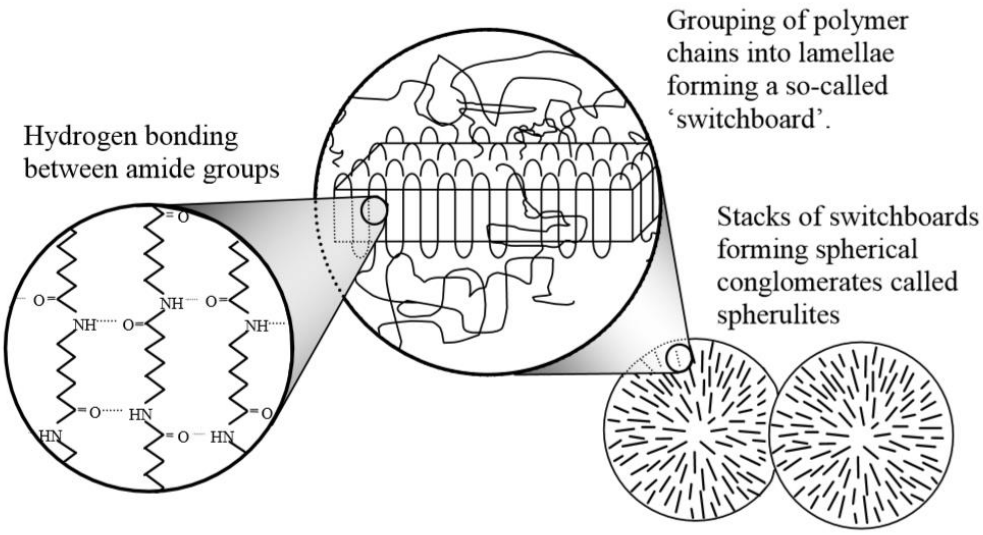

Fig. 2.3: Crystallinity in polyamide 6 [58].

It has been shown that higher crystallinity generally results in higher properties for PA-6 in terms of strength, modulus and resistance to chemical abrasion [13]. Temperatures at the lower end of the crystallisation spectrum result in more nucleation points with smaller crystals. Due to their longer chain lengths, high molecular weight polymers have a greater amount of entanglements in the amorphous phase, causing a reduction in crystallinity. Reducing the cooling rate allows more time for crystals to form, increasing the degree of crystallinity. Generally, if a part geometry is produced, it cannot be remelted to recrystallise the polymer as the part would lose its shape as it turns to a molten state. It is possible however to heat the part to a temperature between T_g and T_m to allow annealing to occur. Annealing removes defects from the crystal structure and can allow the degree of crystallinity to increase [13].

So far, crystallisation has been discussed for melt processed PA-6. However, when using in-situ polymerisation to cast a part, the user doesn't usually intend to reheat the composite unless the parts are being used for post processing (like organo-sheets for thermoforming). For

anionic polymerisations carried out at temperatures below T_c (~185 °C), cold crystallisation occurs simultaneously [27][59]. This means that polymerisation, part formation and crystallisation occur at once, massively reducing the processing times, resulting in a highly crystalline product. Due to the fact that the product does not need to be remelted for moulding, the molecular weight is higher than melt processed PA-6 products [56].

The crystalline phase has mechanical properties which are generally more favourable than those in the amorphous phase, so maximising the degree of crystallinity is often a priority. Due to cold crystallisation, APA-6 by default has a relatively high degree of crystallinity compared to HPA-6. The density of the crystalline phase is 1,240 kg/m^3 and that for the amorphous phase is 1,080 kg/m^3. Van Rijswijk demonstrated that a *parallel model* could be used to determine the modulus of the APA-6 based on modulus values for the pure crystalline material (5.25 GPa) and that for the pure amorphous material (2.2 GPa).

Bessel et al. [60] found that in APA-6, increased molecular weight (achieved at higher polymerisation temperatures), resulted in a tougher material. Where the molecular weight is fixed, the toughness of the material depends almost entirely on the crystallinity. In this study, toughness was defined as the area under tensile stress-strain curves. Samples with a degree of crystallinity of 30 % were shown to possess toughness values that were approximately 4 times the values at 40 %. This demonstrates the importance of crystallinity in APA-6.

2.4 Process modelling

2.4.1 Reaction kinetics

The main reaction scheme for the anionic polymerisation of APA-6 is given in Fig. 2.2. As mentioned in section 2.3, polymerisation and crystallisation occur simultaneously for anionically polymerised PA-6 below 185 °C [27][59]. This can make kinetics models complicated because crystallisation can entrap reactive end-groups and monomer, hindering chain growth [37]. The rates of polymerisation and crystallisation depend on the reactants used and their quantities, initial temperature and whether or not conditions are isothermal or adiabatic [26][61][62].

The processing temperature is controlled by the amount of external heat supplied (by the mould), the heat of the chemical reaction (which causes an exothermic temperature rise) and exotherm due to crystallisation [63]. From literature, the reported value for the exothermic specific enthalpy from polymerization is $\Delta h_p = -144$ J/g [64] and that due to crystallisation is $\Delta h_c = -190$ J/g [65]. Due to both occurring at the same time, quite a large exotherm may

be experienced. It was reported for one particular case in literature, that in quasi-adiabatic conditions, a 52 ℃ temperature rise occurred during polymerisation/crystallisation with a mould temperature of 150℃ [53]. To obtain the required polymer properties, it is important to balance polymerisation and crystallisation which both depend on the mould temperature, resin formulation, part geometry and the fibre reinforcement (if fibres are used) [13].

For fast-reacting thermosetting systems with low thermal conductivity, heat losses can be neglected and adiabatic conditions can be assumed in the bulk [66]. Sources in literature state that the same assumptions can be applied when dealing with APA-6 reactions where fast-reacting catalysts are used [53]. Thus, the heat of reaction (ΔH) can be written as in equation 2.1, where ρ is the density, c_o the initial concentration of the reactive group, C_p the heat capacity, T_o the initial temperature and T_{max} the temperature of the reactants.

$$-\Delta H = \frac{\rho}{c_o}\int_{T_o}^{T_{max}} C_p dT \tag{2.1}$$

The degree of conversion (X) is written as in equation 2.2 where c is the concentration of the reactive group.

$$X = 1 - \frac{c}{c_o} = \left\{\frac{\int_{T_o}^{T} C_p dT}{\int_{T_o}^{T_{max}} C_p dT}\right\} \tag{2.2}$$

Between 120 ℃ and 160 ℃, the specific heat increases from 2,300 J/kg.K to 2,680 J/kg.K [30]; however, due to the small change, it can be assumed to be constant, yielding equation 2.3 [53].

$$X = \frac{T - T_o}{T_{max} - T_o} \tag{2.3}$$

Kinetics models can be used to determine the degree of conversion with respect to time. The approaches used can be either mechanistic, taking all the different reactions into account; or semi-empirical, where curve fitting is done using experimental data. Mechanistic models for this type of polymerisation have been derived in literature [67][68]; however, due to the large number of reactions which are both reversible and irreversible (including side reactions), combined with many oversimplifications required, mechanistic approaches are extremely complex and rarely used [27]. Semi-empirical models can lump together all the different reactions into one equation which describes the entire process. These are typically much simpler compared to the complex mechanistic models for APA-6, and often more accurate.

Such semi-empirical models simplify the polymerisation process into a single step and can take into account complex effects such as auto acceleration [53]. The most popularly used are those of Greenley et al. [69], Malkin et al. [70], Lin et al. [52] and Kamal and Sourour [71][72]. Ruso et al. [26][53], Teuwen [63][73] and Ageyeva [59] summarise these models and discuss their advantages and disadvantages.

Teuwen [63] concludes that Malkin's model is not suitable for slow-reacting polymerisations as it assumes quasi-adiabatic conditions and Lin's model is inaccurate due to oversimplifications. Teuwen was the first to suggest using the Kamal-Sourour method to model anionic ROP of caprolactam, which has traditionally been used to model thermosetting cure cycles. This proved to model both the slow and fast reacting systems with very good accuracy. Russo [53] backed up this evidence by accurately predicting fast-reacting system behaviour using the Kamal-Sourour model.

The Kamal-Sourour autocatalytic reaction rate equation is given in equation 2.4 where t is time, k_1 and k_2 are the apparent rate constants for the non-catalysed and autocatalysed reactions respectively, and z and n are the kinetic exponents where $x + z$ is the order of the reaction.

$$\frac{dX}{dt} = (k_1 + k_2 X^x) \times (1 - X)^z \tag{2.4}$$

The reaction rate is given in equation 2.5 where the rate constants are defined by the Arrhenius equations. A_1 and A_2 are the Arrhenius constants which are related to the collision frequency, E_1 and E_2 are the activation energies and R is the gas constant.

$$\frac{dX}{dt} = \left(A_1 e^{\frac{-E_1}{RT}} + A_2 e^{\frac{-E_2}{RT}} X^x\right) \times (1 - X)^z \tag{2.5}$$

The temperature can be measured, and so, the temperature change with respect to time can be determined. This allows for the determination of the degree of conversion, X using equation 2.3 at any given time. The other value can be determined using curve fitting and/or differential scanning calorimetry.

2.4.2 Crystallisation and viscosity

Several crystallisation models also exist for the APA-6 reaction and are summarised by Ageyeva [59]. These include the Avrami model used by Bolgov et al. for APA-6 [74], The Malkin model [75], [76], Lee and Kim model [77] and Kim model [78]. More recently, Vicard et al. used the Johnson-Mehl-Avrami-Kolmogorov equation [79]. Note that none of these

models consider the effects of pressure on the conversion rate. This is because the pressures used with most APA-6 processes are so low (even for HP-RTM), that their effects are negligible compared to changes due to temperature [59].

The viscosity of caprolactam and the other reactants used to produce APA-6 are almost water like. This is one of the many advantages of this reaction, making it a very suitable system for liquid composite moulding (LCM) processes. The pressure required to inject into a reinforcement is linearly related to the viscosity of the mixture in accordance with Darcy's law, which will be discussed in further detail in section 3.2.3. Initially, as the temperature rises, the viscosity decreases; however, once the reaction onset begins, the viscosity increases rapidly in an exponential manner until a fully polymerised solid is formed. It is therefore important that when processing, the reinforcement is filled prior to onset of the reaction so that the least amount of pressure is required to inject and wet out the fibres. Fig. 2.4 shows viscosity-time curves for polymerisation using 4 different mould temperatures between 140 °C and 170 °C [59][80]. These curves demonstrate the long dwell time relative to the rapid increase in viscosity after polymerisation onset. There are various isothermal models which describe the viscosity behaviour over time during polymerisation. Crystallisation also causes an increase in viscosity and due to polymerisation and crystallisation occurring simultaneously, the accuracy of models to describe the viscosity can change at different stages of the process. Many rheokinetic models exist which have shown to model the APA-6 reaction well [81]–[84]; however, the Sibal model [85] is often chosen due to its simplicity and reasonably good correlation of ~96.4 % with some reported experimental data [28], [73], [86]. The Sibal equation for viscosity η in Pa.s is written in terms of temperature T as follows:

$$\eta = 2.7 \times 10^{-7} . \exp\left(\frac{3525}{T}\right) \tag{2.6}$$

To understand the time dependent nature of viscosity in the APA-6 reaction, a test method was developed by Davé [28] for polymerisation and rheology. In this study, precursors were mixed isothermally in a rheometer and polymerised over a range of temperatures. The viscosity was monitored to determine the rheology of the reaction and correlate it with the kinetics of polymerisation using the Sibal equation. The study showed that when polymerisation temperatures of 130°C and 140°C were used, there was a sharp rise in viscosity beyond 50% conversion, which was attributed to mechanical interlocking of crystallites being formed during polymerisation. This was not observed at a temperatures of 120°C and 160°C due to

the lessened effects of crystallisation at temperatures farther from the 145 °C, i.e. the temperature at which the crystallisation rate is highest.

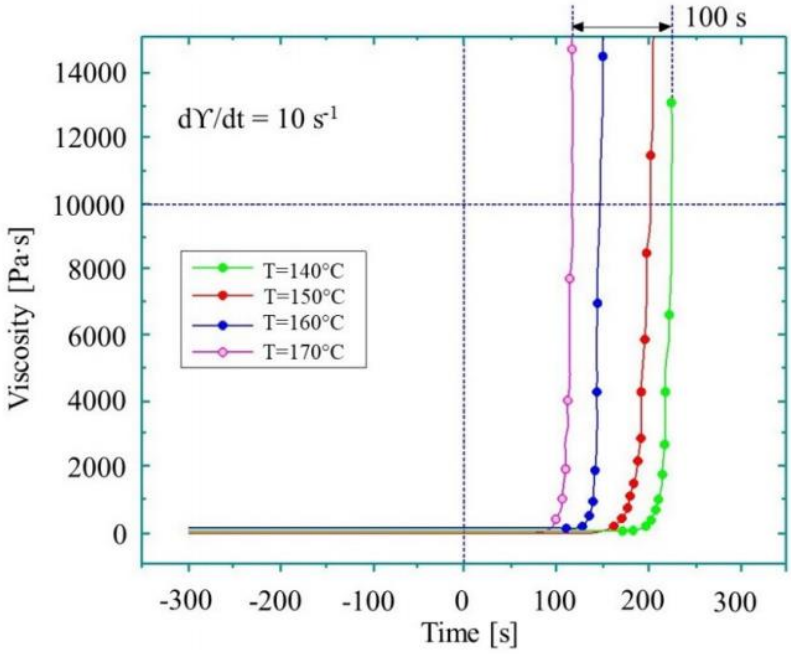

Fig. 2.4: Viscosity-time relationship during APA-6 reaction [59] (based on reference [80]).

2.5 Parameters affecting reaction time

2.5.1 Effects of catalyst-activator on reaction time

For high volume production, it is desirable to minimise the cycle time. One such way of doing this is by reducing the polymerisation time by using a fast acting catalyst-activator combination. Varying the concentration of catalyst will also speed up the process. It was previously mentioned that the reaction rate for APA-6 can vary a lot depending on these parameters. Work carried out by Van Rijswijk et al. [13] used a slow-reacting magnesium bromide caprolactam to allow time for vacuum infusion of a large part prior to polymerisation onset after 20-25 mins. A sodium caprolactamate catalyst combined with the same activator, resulted in polymerisation times of 2-4 mins. Other studies reported similar polymerisation times using the same reactants and similar mould temperatures [53], [87]. It has been reported in literature that reaction speeds can be further increased using newly developed activators from blocked (triethoxysilyl) propylisocyanate which allow polymerisation to occur within tens of seconds [88].

2.5.2 Effects of temperature on reaction time

The reaction time can be reduced further by increasing the mould temperature; however, if the temperature is too high, the autocatalytic effect could cause an even greater exothermic spike. This would hinder the crystallinity, likely yielding less desirable properties. Section 2.4 covered the kinetics of the polymerisation process; however, due to the semi-empirical methods, the reasons for changes in properties was not dealt with individually. The polymerisation temperature affects the conversion, molecular weight and crystallinity; and as a result, affects the mechanical performance of the polymer [23]. Maazouz et al. [54] carried out polymerisations at temperatures below melt (180, 190 and 200 °C) and above melt (230 and 240 °C) using a sodium caprolactamate catalyst and developed an isothermal time-temperature-transformation (TTT) diagram from experimental measurements, as shown in Fig. 2.5. The TTT diagram demonstrates that by increasing the polymerisation temperature, the reaction time can be reduced without significantly affecting the degree of conversion. At temperatures below melt, cold crystallisation can restrict conversion; whereas above melt, cold crystallisation does not occur. In the latter case, the degree of crystallinity is dependent on the cooling rate post-polymerisation. It should be noted, however, that the rate and degree of polymerisation and crystallisation are also heavily dependent on the mixing ratios of materials used. It was also shown by Kim [41] that by adding 0.1 wt% of nanomaterial to the molten mixture, the cycle time could be reduced by more than a factor of 2 and the degree of crystallinity increased. The nanomaterials allowed polymerisations to be carried out at higher temperatures by delaying the induction time. Subsequently, solidification times were reduced significantly and mechanical properties were improved as a result of decreasing the crystallinity at these higher temperatures. Dencheva [99] made single polymer PA-6 composites using an anionically processed matrix and it was shown that by desizing fibres, the strength and modulus of the material could be increased. The transcrystalline region was reduced to a thin layer as a result of desizing, allowing more intimate contact with the reinforcement. It is mentioned in literature that higher processing temperatures results in more branching which reduces the degree of conversion but increases the molecular weight. If the processing temperature is too low, crystallisation growth can occur too fast, hindering polymerisation by trapping reactive materials. Rapid crystallisation can also cause shrinkage induced voids [13]. The best mechanical properties are achieved at some optimum temperature, generally between 150 °C and 170 °C; however, these depend on a large number of parameters for each individual case [38][44]. The mould geometry, formulation and whether or not additives or fibres are used, all affect these properties. Choice of suitable processing temperature also depends on what properties are most desirable and what application the

material is being used in. For example, highly crystalline material may be stronger and stiffer but may be too brittle for some applications where impact resistance is a priority. The trade-off between crystallinity and molecular weight in APA-6 can be seen clearly in studies carried out by van Rijswijk [38], Gong et al. [44] and Yan et al. [87]. In all cases, mechanical testing was carried out on APA-6 processed over a range of temperatures but using different catalyst-activator combinations. The peak average strength in batches from each study was reached at processing temperatures of 150°C, 160°C and 180°C respectively. Although there was a combined influence from the catalyst/activator choice and their ratios, and the processing temperature, the common theme across all studies was that there was an increase in strength up to a certain processing temperature, and in two of these case, it dropped off above this, while simultaneously, an increase in strain-to failure was observed in cases where it was reported.

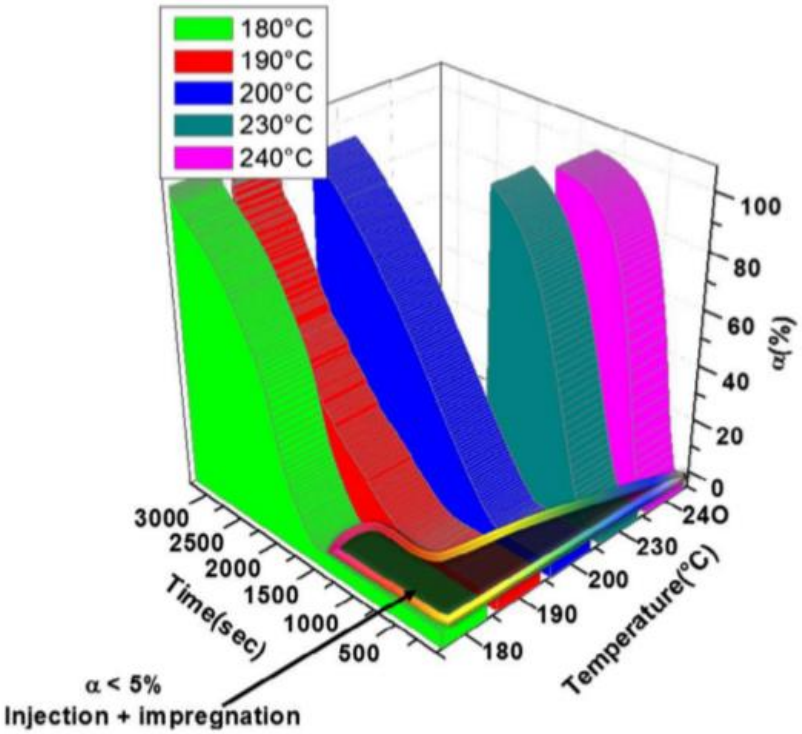

Fig. 2.5: TTT diagram for polymerisations of APA-6 at different temperatures where α represents the degree of conversion measured using FTIR [54].

2.6 Parameters affecting PA-6 properties

2.6.1 Effects of temperature on PA-6 properties

It was discussed in section 2.5.2 how important the processing temperature is in determining the APA-6 reaction. The properties of the product however are also dependent on the temperature of their environment. Increased temperatures result in increased molecular mobility in polymers [89]. Davies carried out a study on the effects of environmental temperature on dry HPA-6 [90] while Van Riswijk [13] did the same for HPA-6 and APA-6. The effects of temperature on the strength, modulus and strain to failure are shown in Fig. 2.6. Note that materials included APA-6 with a degree of crystallinity of 42% (produced using mould temperature of 150 °C), APA-6 with a degree of crystallinity of 37% (produced using mould temperature of 170 °C), HPA-6 with a degree of crystallinity of 37% (Akulon®K222D) and the same grade HPA-6 containing 10 wt% clay platelet nanocomposite.

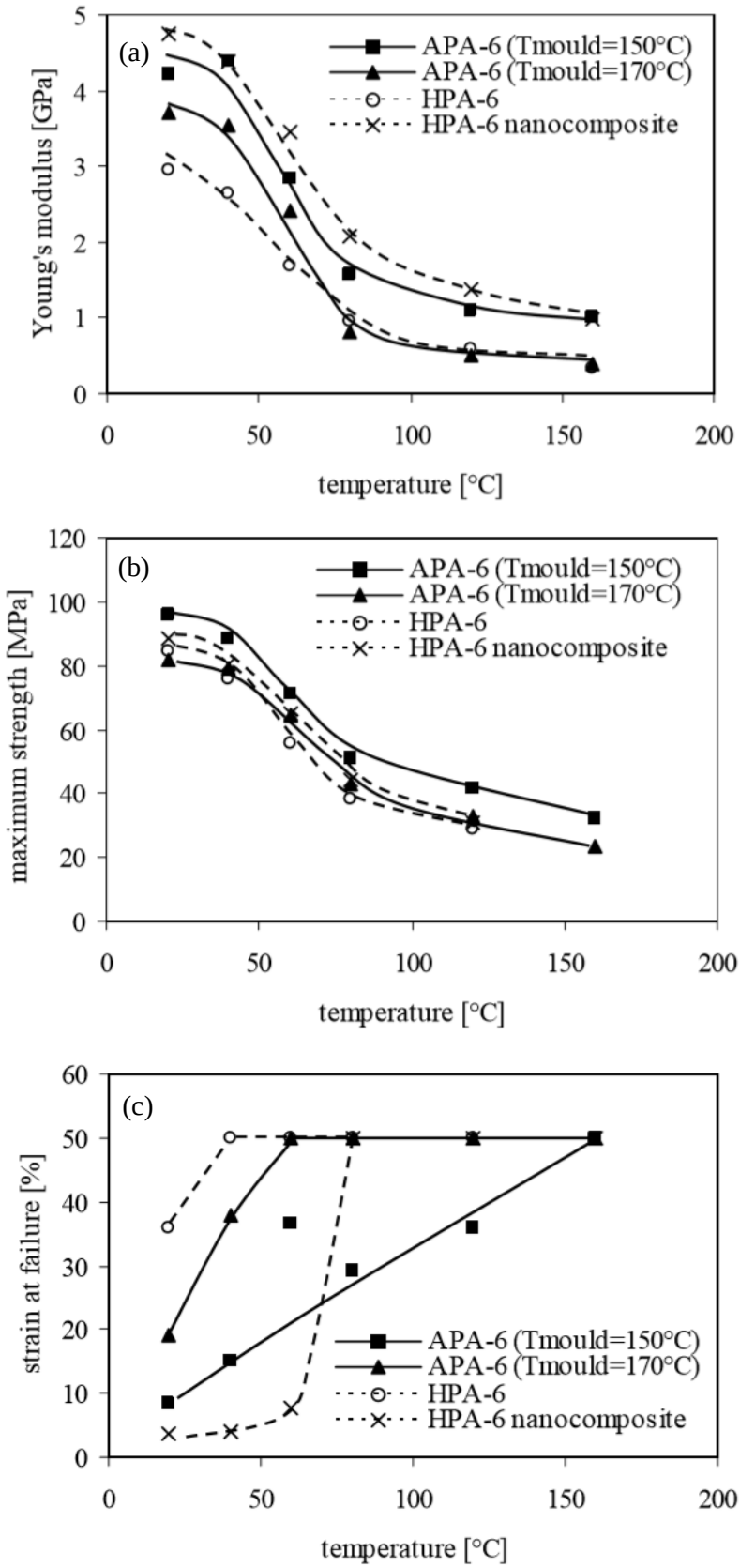

Fig. 2.6: Relationship between temperature and (a) Young's modulus, (b) maximum strength and (c) strain at failure [13].

The relationships shown in Fig. 2.6 demonstrate how dramatically PA-6 properties are affected by temperature. The increased crystallinity in the APA-6 processed at 150 °C means that its behaviour is less susceptible to temperature changes as the temperature only affects the amorphous region below melt.

The yield stress of a polymer is related to the chain mobility, which can be characterised by T_g [91]. As the temperature is increased, chain mobility increases, and so, the yield strength is reduced. Kambour [92] showed that when the difference between the test temperature and that of the T_g for a polymer is plotted against the yield stress, a linear relationship exists. Davies [90] carried out experiments to demonstrate this relationship for PA-6 as shown in Fig. 2.7. Note that this graph also shows experimental data for water content, which also increases chain mobility; however, this is discussed in more detail in section 2.6.2.

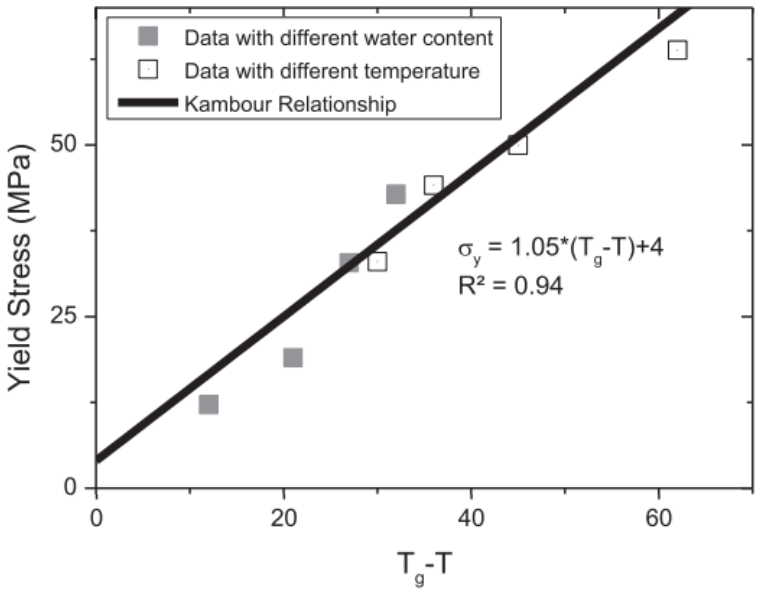

Fig. 2.7: Relationship between the difference in test temperature and T_g versus yield stress for PA-6 [90].

Even though the strength and modulus decrease with temperature, the opposite is true for toughness [30]. Izod impact strength of PA-6 increases significantly at higher temperatures, particularly at those surrounding the glass transition, as demonstrated by Fig 2.8 [93].

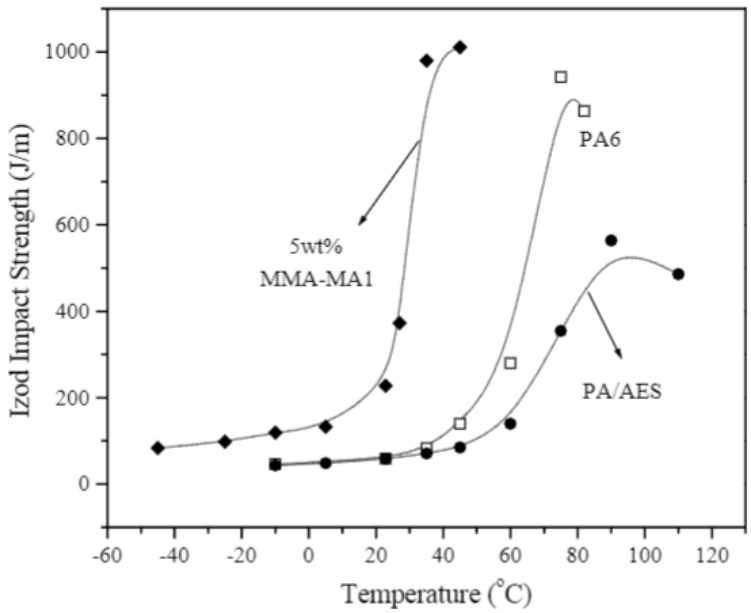

Fig. 2.8: Relationship between the environmental testing temperature and the Izod impact strength of PA-6 [93].

2.6.2 Effects of water absorption on PA-6 properties

Polyamides are well known for their high absorption of water, particularly PA-6, which depends on the relative humidity (RH). PA-6 can absorb up to 9.5 wt% water at 100% RH and up to 2.8 wt% at 50% RH; however; this absorption is reversible [30]. The amount of water absorbed depends on:

- The relative humidity and temperature
- Time exposed
- Crystallinity (and other modifications, if any)

The amide groups form hydrogen bonds with water [13]. The amorphous phase can absorb very large amounts of water but the crystalline phase is too densely packed for water to enter. A higher degree of crystallinity would therefore reduce the amount of water absorption, meaning that APA-6 would be expected to absorb less water than hydrolytically polymerised PA-6. Water absorption has a profound effect on the material properties of PA-6. Absorbed water causes swelling and increased macromolecular chain mobility, which is demonstrated by a significant reduction in glass transition temperature as shown in Fig. 2.9 [90].

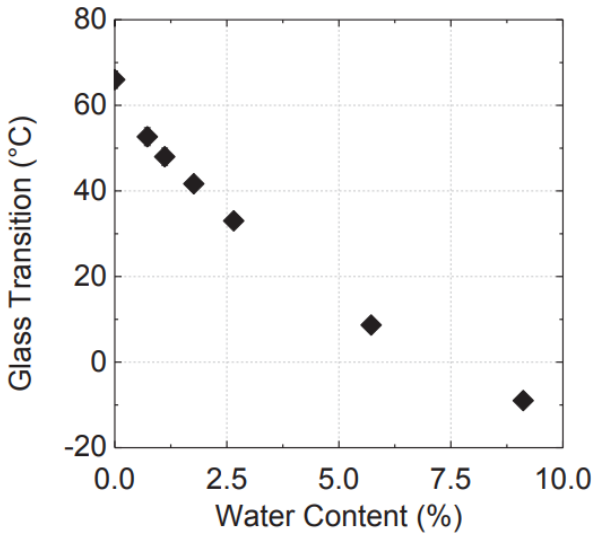

Fig. 2.9: Relationship between water absorbed in PA-6 and T_g [90].

Davies et al. [94][90] carried out extensive modelling and experimental work on water absorption in PA-6 where samples were immersed in seawater. These studies looked at the methods of diffusion and irreversible effects of water ingress on the material. In a humid environment, PA-6 undergoes degradation as a result of the moisture. The two mechanisms by which degradation occurs are plasticisation due to water diffusion and hydrolysis of the backbone. The latter results in chain scission and both cause a significant reduction in properties [95][96]. It was shown that after immersion in seawater for 6 months at 25 °C, there was no reduction in molecular weight. As such, it was deduced that in immersed cases for less than 6 months (at RT) and dry cases for any period of time, hydrolysis can be neglected. Water absorption measurements over time were recorded for batches of samples placed in sea water. The batches were removed after different immersion times and tested. Immersion times ranged from half a day up to 30 days. Saturation (~9.3 wt% water) occurred after ~14 days, after which, no further water could be absorbed over time. Tensile tests were carried out on the batches removed at different times and the results are given in Fig. 2.10.

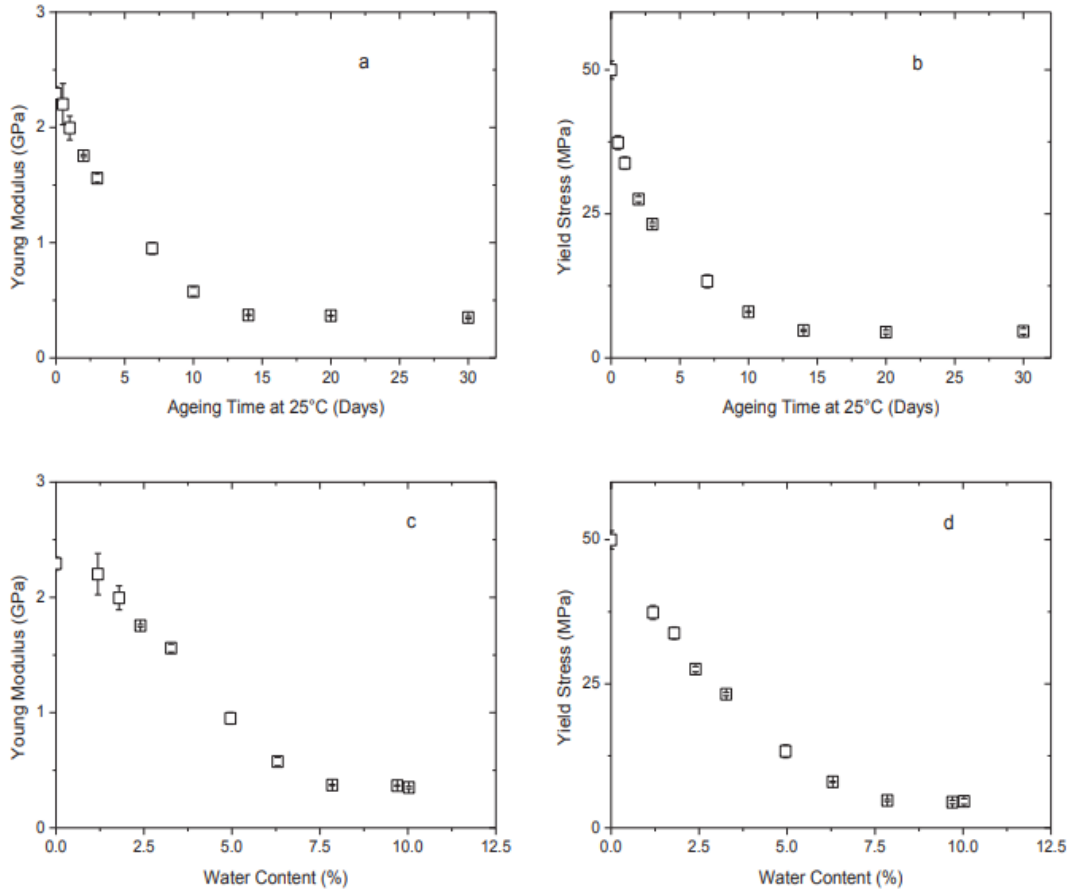

Fig. 2.10: Young's modulus and yield stress during absorption as a function of immersion time in sea water ((a) and (b)) and water content ((c) and (d)).

Van Rijswijk [13] conditioned 2 mm thick PA-6 specimens and measured their properties. These included APA-6 with a degree of crystallinity of 42% (produced using mould temperature of 150 °C), APA-6 with a degree of crystallinity of 37% (produced using mould temperature of 170 °C) and HPA-6 with a degree of crystallinity of 37% (Akulon®K222D).

Water sorption was accelerated by increasing the temperature of the water. When conditioned at 62% RH at 70°C, all samples reached saturation within 140 hrs, absorbing ~2-3 wt% moisture. When conditioned at 100% RH, all samples reached saturation within 80 hrs absorbing ~7-9 wt% moisture. The ultimate strength for all cases was reduced by ~50-60 % and the Young's modulus was reduced by ~68-78 % with less of a drop for the case with a higher degree of crystallinity.

It was shown that overall there was no major difference in mechanical performance between the APA-6 with a crystallinity of 37% and HPA-6 with the same crystallinity. APA-6 with a crystallinity of 42% outperformed these two by a significant margin in terms of both strength

and modulus. Table 2.1 compares the mechanical properties of the two different APA-6 polymers with the HPA-6 in dry-as-moulded form and after conditioning at 50% RH.

Table 2.1: Strength and modulus values for APA-6 w.r.t. HPA-6. Dry-as-moulded (DAM) samples and those after conditioning at 50% RH are presented for two sample types [13].

		APA-6 (T_{mould}=150°C)	**APA-6 (T_{mould}=170°C)**
23°C-DAM	Young's modulus	+ 41%	+ 23%
	Maximum strength	+ 14%	- 2%
23°C-50%RH*	Young's modulus	+ 59%	+ 1%
	Maximum strength	+ 4%	- 10%

Davies et al. [90] also determined the effects of drying on desorption and how this effects properties. The saturated sample were dried at 25 °C over 78 days until there was only 0.3 wt% water left in samples. Test results showed that the mechanical properties can be regained after sufficient drying but it takes extremely long times for desorption to occur (see Fig. 2.11). This demonstrates the reversibility of the plasticisation mechanism.

Even though the strength and modulus decrease with water absorption, the opposite is true for toughness in a similar way to temperature. Izod impact strength of PA-6 increases significantly with increased water absorption. Samples conditioned at 50 % RH had Izod impact strengths that were almost double the impact strengths of the samples tested dry as moulded [30].

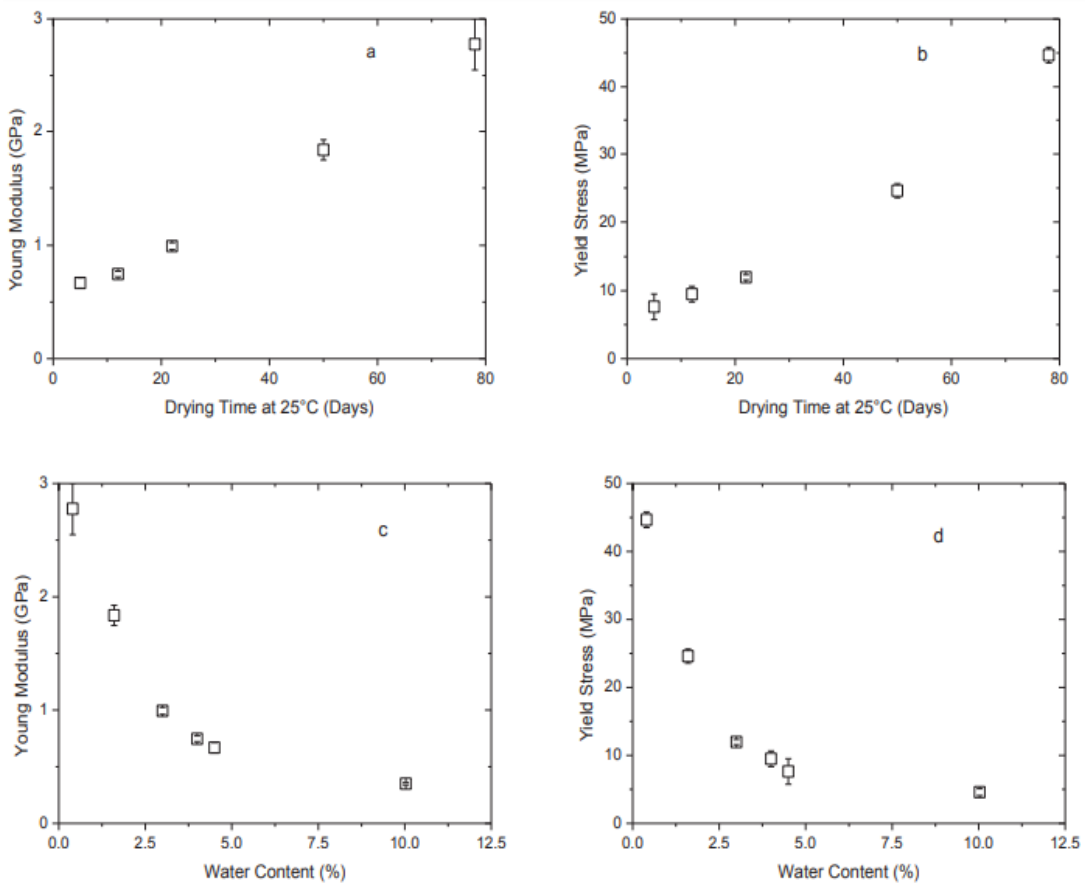

Fig. 2.11: Young's modulus and yield stress during desorption as a function of immersion time in sea water ((a) and (b)) and water content ((c) and (d)) [90].

2.6.3 Effects of fillers on material properties

Filler materials may be added to polymers for a number of reasons: to reduce cost, to add stiffness, to increase strength, to modify processing/thermal conditions (as discussed in 2.5.2 [41]) and many other reasons. Due to the brittle nature of epoxies, fillers have often been added in the past to improve their toughness [97]. Impact resistance, fracture toughness and threshold-to-crack initiation under cyclic loading can be reduced by addition of nanoclay which can effectively deviate the crack propagation path. Studies have shown that by increasing the particle size, the fracture toughness can also increase up to a certain point, before decreasing again, so long as even distribution is maintained [98]. Toughening mechanisms exhibited by fillers include crack front bowing (or pinning), crack-tip blunting, particle-matrix debonding, diffused matrix shear yielding, microcracking, breakage of particles and many others.

2.7 Melt processing of PA-6 composites

Traditionally, the use of PA-6 in composites has been limited to a small number of melt processing techniques. These include commingled fabrics, pre-consolidated laminates and stacks of alternating layers of polymer and fibres [16]. These products require a melting and solidification process [99] but don't require long cycle times like most thermoset processes which have long cure cycles [100]. Disadvantages associated with these technologies include limitations to part thickness and forming [99], poor fibre-matrix interfacial adhesion [101], expensive intermediate materials, expensive processing equipment and the high temperatures they require, which may degrade the thermoplastic matrix [102].

2.8 Reactive processing of APA-6 composites

The main reasons to use engineering thermoplastics like APA-6 as a matrix in composites over thermosets are due to their unique properties such as high toughness and ability to be remelted. The ability of the APA-6 to melt means that the polymer can be recycled, welded and reshaped [103]–[106]. Many of these advantages also apply to composites produced using APA-6 as the matrix. By taking advantage of the low viscosity of the APA-6 precursor materials, reactive processing of thermoplastic composites has been made possible. This has opened the door for their use across a wide range of LCM processes, and hence, new applications where thermosets were used traditionally. This section aims to outline the state-of-the-art in terms of LCM techniques for APA-6.

2.8.1 Casting discontinuous composites

Casting is by far the most simple and low cost LCM process for APA-6 composites. Large parts can be manufactured using very basic equipment. The first published account of casting APA-6 composites was that in a study carried out by Litt and Brinkmann in 1973 using 20-25 % short carbon fibres [107]. They used sodium caprolactamate as the catalyst with 5 different activators and polymerisations were carried out at 220 °C, taking 30-40 mins to process. Horský et al. [108] used short glass fibres (GFs) with various amounts of sizing to see how it affected the kinetics and mechanical properties, and demonstrated the importance of the sizing for fibre-matrix adhesion. Engelmann et al. [109] used 15% short carbon fibres which improved the tensile strength of the unreinforced polymer by 19% and doubled the Young's Modulus. Fig. 2.12 shows two different techniques for casting APA-6 composites using a single pot, and pouring into a mould cavity.

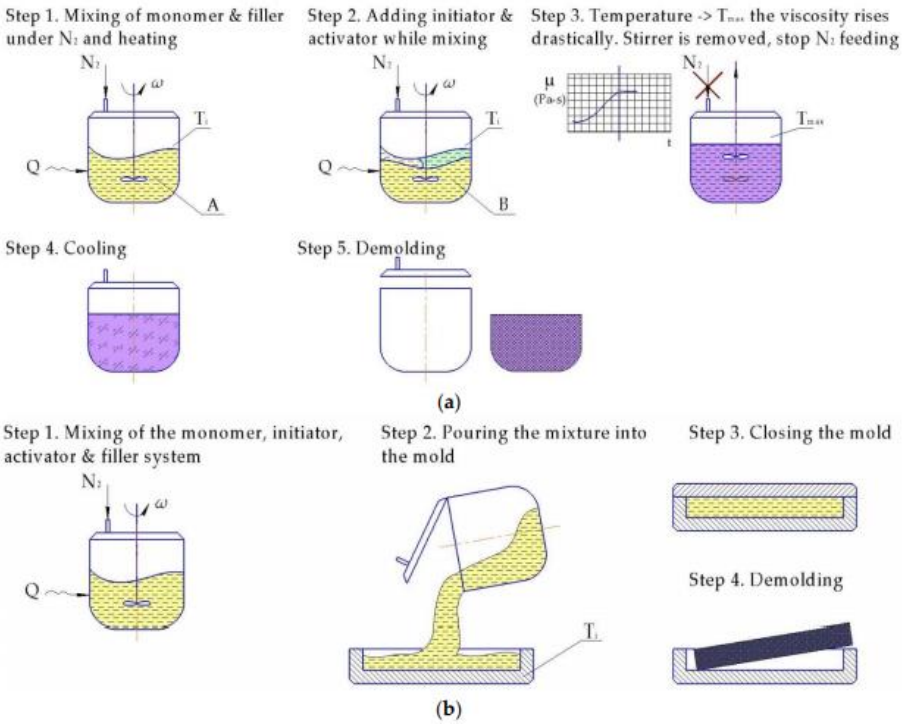

Fig. 2.12: Casting (a) using same mould & (b) by pouring into separate mould [23].

2.8.2 Rotational moulding of discontinuous composites

Rotational moulding or rotomoulding is a process for manufacturing hollow polymeric parts such as tanks [110]. Rusu et al. manufactured both pure APA-6 and APA-6/12 copolymers using centrifugal processing techniques [111]. The results showed that increased amounts of laurolactam (the PA-12 precursor) decreased the degree of crystallinity and melt temperature but increased the impact strength significantly. Harkin-Jones et al. [112] rotationally moulded Nyrim with short GFs to investigate the effects of the initial mould temperature on the crystallinity. Nyrim is a nylon block copolymer based on the polymerisation of caprolactam with a polymeric polyol. The study concluded that above 140 °C, the degree of crystallinity decreased, while the spherulite size increased and that the GF improved flexural properties but negatively affected impact strength. Fig. 2.13 shows the steps involved in rotational moulding of parts.

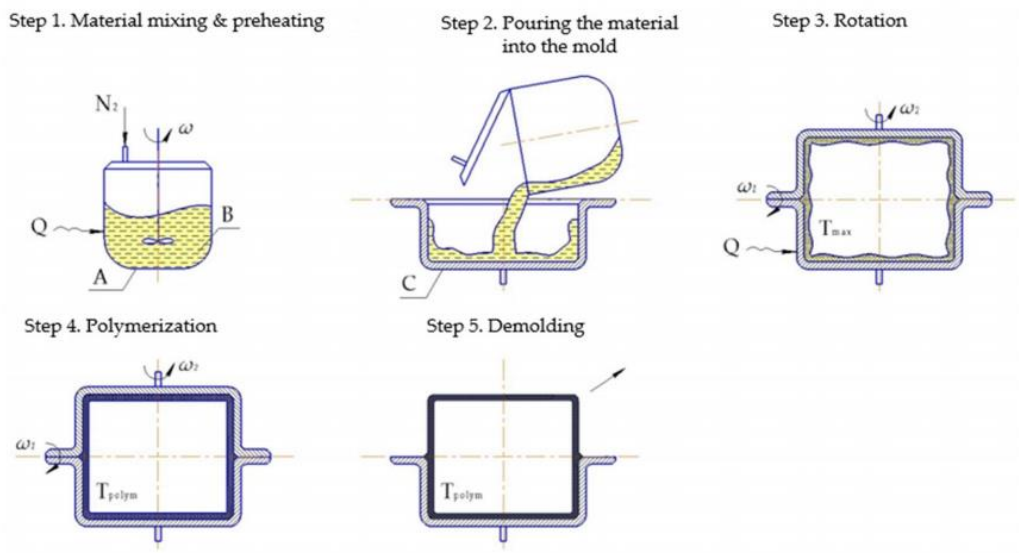

Fig. 2.13: Rotational moulding of APA-6: A is the dosing unit, B is the mixture (monomer + catalyst/activator) and C is the mould [23].

2.8.3 Pultrusion of continuous composites

Pultrusion is a continuous, high-volume manufacturing process used to make parts with a constant cross-section [113]. In the past, pilot pultrusion lines using APA-12 from laurolactam were investigated [114]–[116]. There has been a surge of interest in very recent years to develop reactive thermoplastic pultrusion lines but using APA-6 instead; however, the processes are not yet commercialised [23]. The iPul is a continuous pultrusion system recently developed by a collaboration of industrial and academic partners based in Germany [117]. The pultrusion line allows continuous production at 3 m/min which is extremely competitive with some other high speed pultrusion processes. A collaboration between Hyundai and a number of French partners was also established and they have developed a crash beam containing continuous GF and APA-6 [118]. Fig. 2.14 shows a typical setup for reactive pultrusion of APA-6 composites [23].

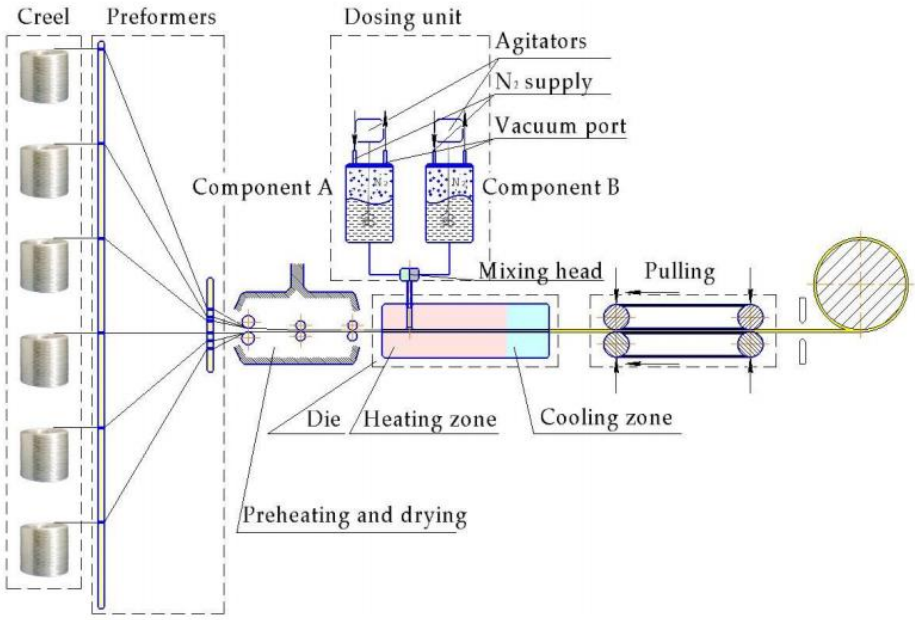

Fig. 2.14: Setup for pultrusion of continuous APA-6 composites [23].

2.8.4 Vacuum infusion of textile composites

The reactive manufacturing process for APA-6 composites with the most amount of information available is that using vacuum infusion. While the cost of the consumables used to manufacture using this method are relatively expensive, they are readily available in most composite manufacturing facilities, and so, have been trialled and tested without the requirement of major investment in presses, sophisticated dosing units and expensive tooling. The vacuum infusion process is suitable for the production of large parts such as wind turbine blades using slower acting catalysts. By far the most extensive work known in this area was carried out by Van Rijswijk [13] at TU Delft using glass fibre as the reinforcement. This work accompanied by that of Yan et al. demonstrated experimentally most of the key relationships between process parameters and the part quality in terms of conversion, molecular weight and mechanical properties [37]–[39], [87], [119]. Van Rijswijk concluded that by far the most important processing parameter was temperature as it has such impact over the degree of conversion and crystallinity of the final polymer as discussed in depth in section 2.5.2 [13][38]. Temperature sweeps were carried out for various different combinations of catalyst and activators in various mixing ratios as discussed in section 2.5.1. This work uncovered many of the unknowns about APA-6 composites and played a significant role in furthering their development. In another study, carbon fibre/APA-6 was manufactured successfully using vacuum infusion [42]. This study showed how preheating the mixture to the same temperature

as the mould (150 °C) resulted in lower crystallinity than that infused at 100 °C. A typical vacuum infusion process is shown in Fig. 2.15. While the figure shows a dosing unit, this is not necessarily required for the vacuum infusion process, as some examples have been reported where standard mixing equipment achieved satisfactory results [87].

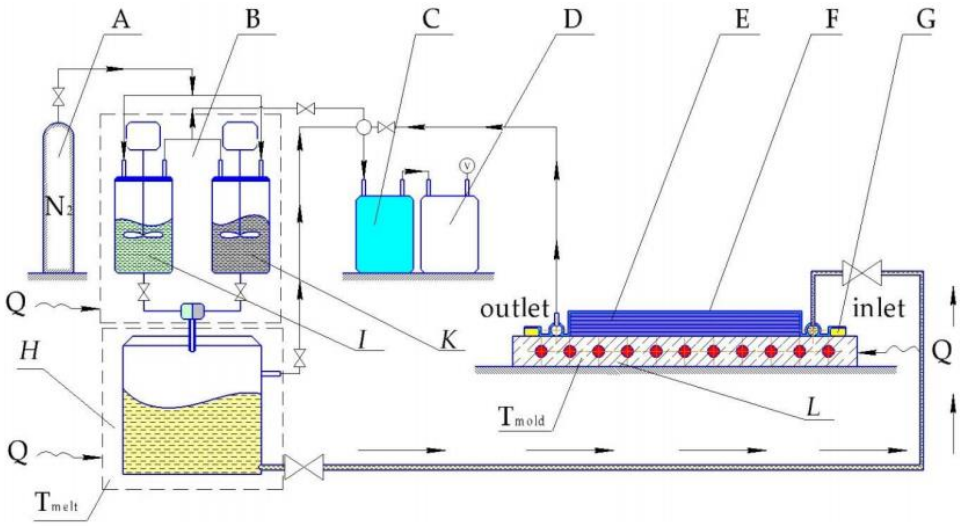

Fig. 2.15: Setup for VaRTM of textile reinforced APA-6 composites. Where A is a nitrogen gas source, B is a dosing unit, C is a cold trap, D is a vacuum pump, E is a textile preform, F is a vacuum bag, G is sealing tape, H is a degassing vessel, I is a tank with caprolactam + catalyst, K is a tank with caprolactam + activator and L is a heated metal plate [23].

2.8.5 TP-RTM of textile composites

Thermoplastic resin transfer moulding (TP-RTM) generally involves expensive equipment and is most suitable for high volume manufacturing where the equipment costs can be justified. While the layout in terms of heating and mixing is similar to vacuum infusion, the equipment used is very different. The system requires a dosing unit able to inject into a textile at pressure and requires heated moulds with high displacement capabilities to reduce cycle times. These requirements are necessary for rapid injection of high fibre volume fraction parts, followed by quick part removal. Industrial collaborations between automotive companies, resin suppliers and injection system manufacturers have been developing TP-RTM processes for the production of parts for high volume manufacturing [45]–[47]. It has been reported that Krauss Maffei recently produced a CF/GF hybrid roadster roof frame with an APA-6 matrix [46]. They achieved a fibre volume fraction of ~70% within a 2 minute cycle time using TP-RTM with a compression step. Such compression steps can reduce the injection time and the injection pressure required by the dosing unit in order to meet the output demand [120]. The largest reported industrial collaboration on TP-RTM is another project by Krauss Maffei, who

in partnership with Volkswagen and BASF produced a B-pillar reinforcement [47]. In order to achieve the desired matrix properties, additives and fillers (other than the activator and catalyst) were added to the mixture. A special type of dosing head was used to manufacture without interruption. It was reported that the process demonstrated potential for economical production of automotive parts. Engel produced a shovel from APA-6/GF to demonstrate the capabilities of their TP-RTM system and the mechanical properties achieved by their product [45]. An example of a typical TP-RTM manufacturing setup is shown in Fig. 2.16.

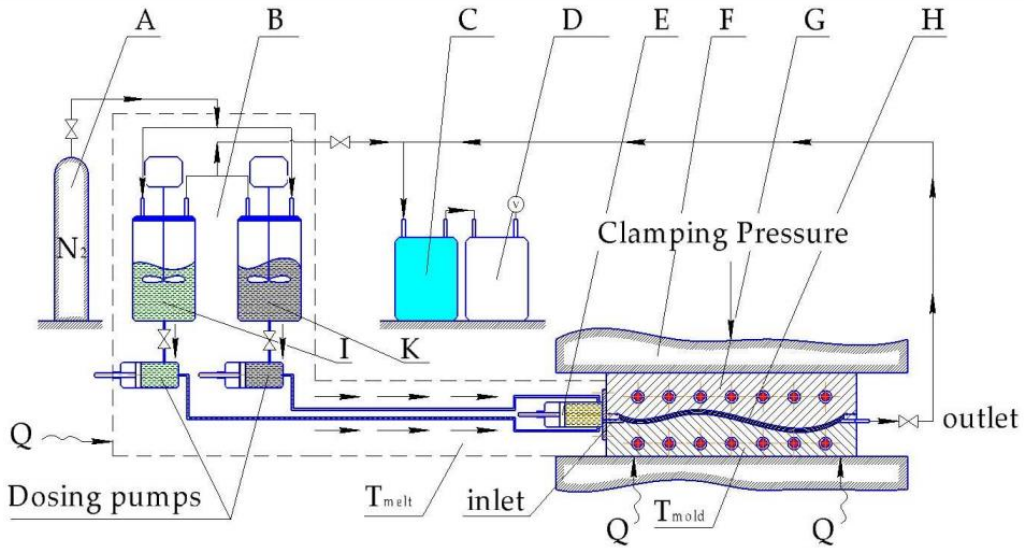

Fig. 2.16: Setup for TP-RTM of textile reinforced APA-6 composites. Where A is a nitrogen gas source, B is a dosing unit, C is a cold trap, D is a vacuum pump, E is a dynamic mixing head, F is a mould carrier, G is the mould, H is the textile preform, I is a tank with caprolactam + catalyst, K is a tank with caprolactam + activator [23].

2.8.6 Process monitoring

It is clear from literature discussed in previous sections how sensitive the anionic polymerisation is to moisture which affects the part quality in terms of polymer conversion. It was also discussed how important the temperature in the mould is to producing a part with the correct crystallinity and how much this affects the mechanical properties. Dielectric sensing technology is being developed for moulds in order to give online measurements of the state of the reaction inside the mould [121]. These live measurements, combined with live temperature measurements can be integrated into a TP-RTM mould to determine the progress of the polymerisation, and hence, part quality. This makes process methodologies like *six sigma* and *Industry 4.0* easier to introduce for effective quality management [122].

2.9 Post-processing

Due to the ability to melt thermoplastics, composites with a thermoplastic matrix have some unique advantages over those with a thermoset matrix, opening a wide range of post-proces techniques.

Thermoforming or sheet-forming is a process which involves taking a flat composite laminate known as a *blank* or *organo-sheet*, heating it above the melt or softening temperature of the matrix and deforming it to produce a specifically shaped part by applying pressure in a mould. A typical thermoforming process and temperature profile are shown in Fig. 2.17. This process is suitable for large scale series production, particularly for thin parts using a matrix with a low melt temperature; however, trimming of the parts is often required [123]. For complex shapes with bends, deformation mechanisms usually limit the quality and consistency of parts. Where multi-ply laminates are used, the dominant mechanisms are interlaminar slip and rotation [124].

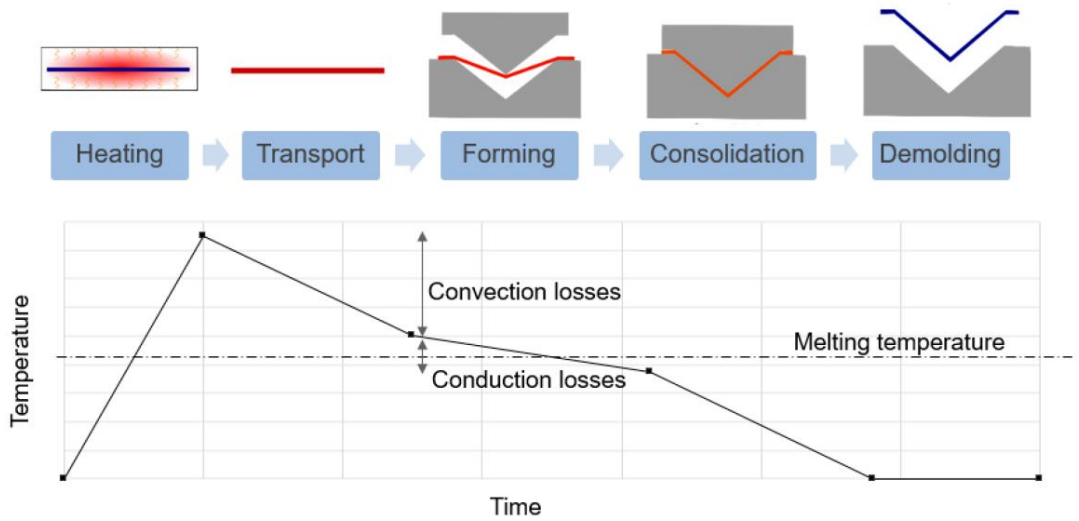

Fig. 2.17: Process steps involved in thermoforming and a typical temperature profile [125].

Fusion bonding by thermal welding for joining parts is another post-process which can be availed of for thermoplastic composites. Local melting of thermoplastic composites means that individual parts can be melted and bonded by interdiffusion of the matrix [126]. This avoids the use of fasteners which require drilling and add weight to parts, introduce stress concentrations and cause a mismatch in thermal expansion properties [127]. Induction welding and resistance welding are two methods of thermoplastic composite welding used industrially in aerospace applications [128][129]. The former process involves inducing eddy currents in the material by electromagnetic induction, causing localised heating, allowing for bonding of

both surfaces. Where non-conductive reinforcements such as glass fibres are used, susceptor materials are usually required between the two bonding surfaces (Fig 2.18 (a)). The susceptor, usually made from a conductive material (like grid metal), absorbs the electromagnetic energy and converts it to heat [130]. Resistance welding involves passing an electrical current through a conductive material placed between two bonding surfaces (Fig 2.18 (b)). The heat generated combined with the addition of pressure, can result in a strong bond. Like the susceptor material used in induction welding, the presence of the conductive material within the bonding zone is not ideal as it acts as a foreign body and stress concentrator. Ultrasonic welding uses high frequency mechanical vibration, which generates heat, to weld parts held under pressure [127]. Ultrasonic welding is suitable for spot welds, whereas the aforementioned welding techniques are suitable for continuous welding [106].

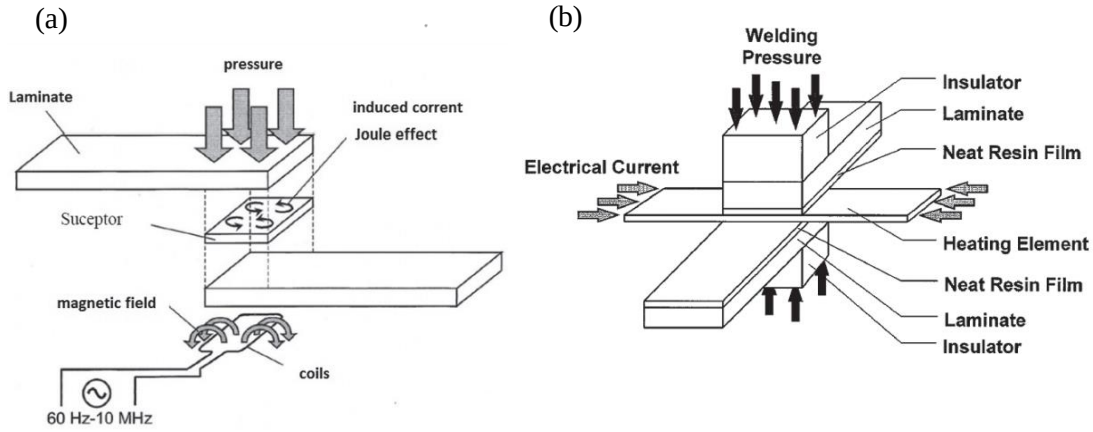

Fig. 2.18: Thermoplastic composite welding techniques using (a) induction welding and (b) resistance welding.

2.10 End-of-life use of APA-6 composites

The market for glass fibre reinforced polymers are predicted to grow by ~ 9 % annually up to the year 2025 [131]. The increased use of materials would result in an increased amount of waste at their end-of-life. This has a negative impact on resource conservation and the environment and there is increasing demand for reuse as part of a circular economy. In order to drive such a circular economy, the methods of recycling cannot be highly energy intensive and must be economically justified for reuse. For glass-fibre and carbon fibre composites, methods can be used to recover the fibres at the product's end-of-life. Incineration can be used to burn off the polymer matrix at temperatures above the degradation temperature of the matrix; however, this has been shown to negatively affect the mechanical properties of the recovered fibres. Pyrolysis has been shown to be one of the most reliable and efficient methods

of recovering both fibre types without any significant effect of their properties compared to the virgin fibres [132]. This involves heating the fibres to similar temperatures to those used in incineration but without the presence of oxygen. This process produces solid char on the fibres and requires a carefully controlled post-pyrolysis oxidation process to treat the fibres before they can be re-used [131]. The recycling process is shown in Fig. 2.19.

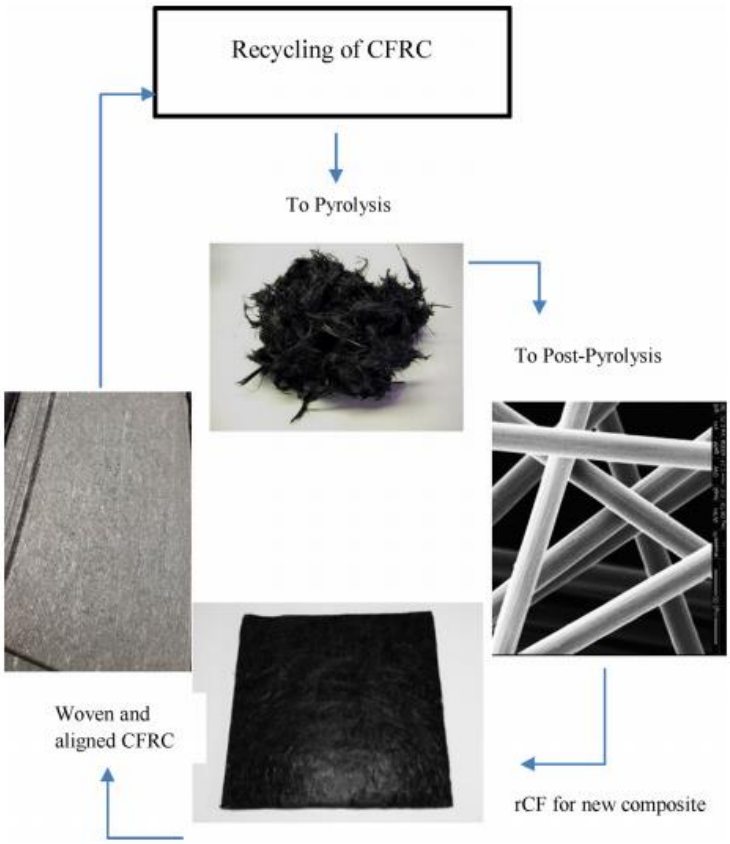

Fig. 2.19: Closed life cycle for CFRP in a circular economy [131].

The advantage of thermoplastic composites is that both the entire product (matrix and reinforcement) can be re-used by shredding/grinding and reforming it into a short fibre composite part as shown in Fig. 2.20. A collaboration involving TenCate and Fokker developed an access door panel by grinding scrap thermoplastic carbon fibre composite using this process for an aircraft elevator and rudder [133]. Such processes can be more cost effective than using new materials and by sourcing the recycled material from within the same industry means that traceability and purity can be monitored. The recycled material can also be sold for use in non-engineering products like crates, furniture and industrial components. Due to the shredding/grinding process, the original continuous fibre composite becomes a discontinuous composite, meaning its mechanical properties are significantly reduced. As such, the process

shown in Fig. 2.19 is technically considered to be a form of *downcycling* from the original product. Due to the high viscosity of thermoplastics, no known methods for recycling both the fibre and matrix by separation currently exist.

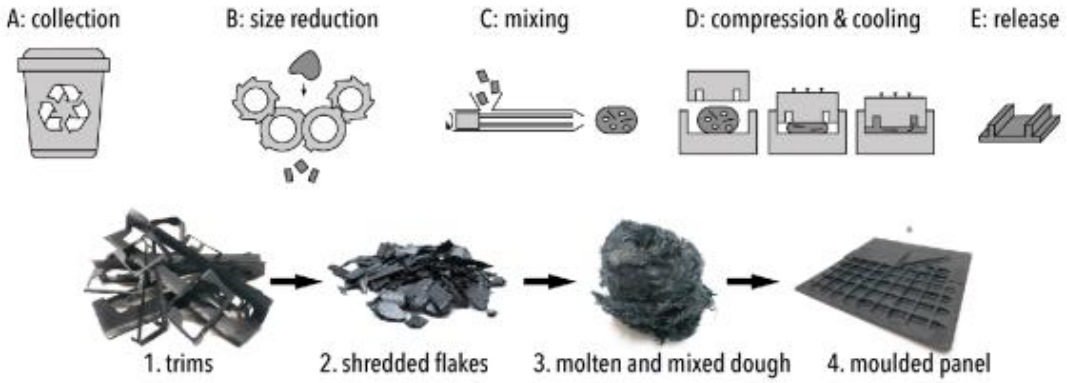

Fig. 2.20: Downcycling process for thermoplastic composites [134].

Chapter 3: Development of TP-RTM Equipment

Summary

This chapter describes the design, build and assembly processes used to develop equipment to manufacture APA-6 composites. Design requirements are outlined, the analysis and tests carried out in advance and the methods used to manufacture the equipment are discussed in detail.

3.1 Chapter Introduction and Overview

In order to manufacture APA-6 composites, the TP-RTM equipment had to be developed. Two different TP-RTM machines were built: the original prototype at The University of Edinburgh and an improved version at The University of Auckland. The chapter breaks down the initial design requirements that were laid out during the design process for the rig in terms of heating, flow/pressure, mixing and purging/flushing. Information from existing technology, literature as well as books on heat transfer, fluid mechanics and chemical engineering were used throughout the definition and design stages.

After final definition of the requirements, individual components were designed and built. The design steps taken involved consideration of fluid dynamics and heat transfer theory. In some cases, small-scale experiments were carried out to measure/determine unknowns throughout the design process. Drawings and 3D models were generated to assist part machining, fabrication and assembly. Temperature measurements were taken inside the TP-RTM machine to see that heat was being transferred sufficiently within the allowable times outlined during the design phase. The controls and operations of the assembled setup are described to give the reader a thorough understanding of how the TP-RTM equipment worked prior to discussing the manufacturing processes further in the coming chapters.

3.2 Design requirements and considerations

3.2.1 Overview of equipment

Like most typical RTM processes, TP-RTM of APA-6 composites involves the mixing of two components and injecting them into a textile, which is contained within a heated mould. Due to the resistance to flow from the reinforcement during injection, some method to drive the mixture into the mould is required to apply pressure. This applied pressure also results in pressures within the mould cavity, meaning that a method is also required to keep the mould closed and prevent leaking. The closed mould is generally constrained between platens of a press so that forces can be applied and released as required. In high speed processes, the mould halves are often fixed to the platens such that the part can quickly be removed by opening the press. After mould filling, the injected mixture often requires application of heat to allow the curing process (or polymerisation) to occur. The basic setup for a twin component RTM system is shown in Fig. 3.1. The equipment can be broken down into four separate systems for simplification of explanation: the heating system, the flow & pressure system, reactive mixing system and electrical systems. Each are described separately in this section even though in reality, there are overlaps between many of them.

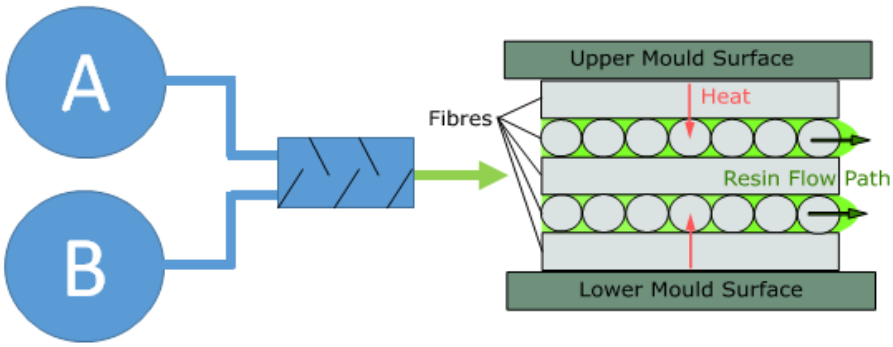

Fig. 3.1: Basic schematic diagram of a twin component RTM system

3.2.2 Heating and mixing

The raw precursor materials have to be heated above their melt temperature such that they can be processed. These three materials are the monomer, the activator and catalyst. A more holistic discussion of the choice of reactants and their chemical properties is covered in Chapter 4 but in this section, we mainly consider properties which are relevant to the design of the heating components. These properties were taken from supplier datasheets and literature for each and are summarised in Table 3.1 [135]. Where data was unavailable for the activator and catalyst, mixtures containing either were assumed to have the same thermal properties of the pure monomer. This was considered a fair assumption considering the mixture was more than 97% caprolactam by weight and was similar in terms of other properties.

Table 3.1: Thermal and ignition properties of raw materials.

Material	Melt temp. (°C)	Ignition temp. (°C)	Bulk density (g/cm^3)	Density (g/cm^3)	Specific heat @80°C (kJ/kg.°K)	Specific heat @150°C (kJ/kg.°K)	Heat of fusion (kJ/kg)
Monomer	69	375	~0.65	1.01	2.135	2.345	123.5
Activator	61	390	~0.80	1.2	-	-	-
Catalyst	62	390	~0.50	1.124	-	-	-

From Table 3.1, it can be seen that the monomer has the highest melt temperature of the three materials, meaning the precursors must be heated above 69 °C. In order for the mixture to polymerise, the materials need to be heated to temperatures above the 140 °C inside the mould; however, it is not necessary to have such high temperatures during storage and mixing. The lowest ignition temperature of the three precursors is 375 °C and it is therefore important that the material does not risk coming into contact with heating components above this temperature. With regards to boiling, the vapour pressure (P_{vap}) of the mixture is related to its temperature (T). This is defined by the Clausius-Clapeyron relationship [136], given in equation 3.1, where ΔH_{vap} is the molar heat of vapourisation (63713 $J \cdot mol^{-1}$), R is the gas constant (8.3143 $J \cdot K^{-1} \cdot mol^{-1}$) and T_b is the boiling temperature at 1 atmosphere (540 K) [13]:

$$\ln p_{vap} \approx \frac{\Delta H_{vap}}{R}\left(\frac{1}{T_b} - \frac{1}{T}\right) + 11.5261 \tag{3.1}$$

Fig. 3.2 demonstrates this relationship and also presents experimental values obtained from literature [137]. It is clear that anywhere where vacuum is used, the operating vacuum pressure

and temperature should be considered. During polymerisation, the mixture undergoes an exothermic reaction, at which point the highest temperatures are reached and where the mixture is most prone to boiling.

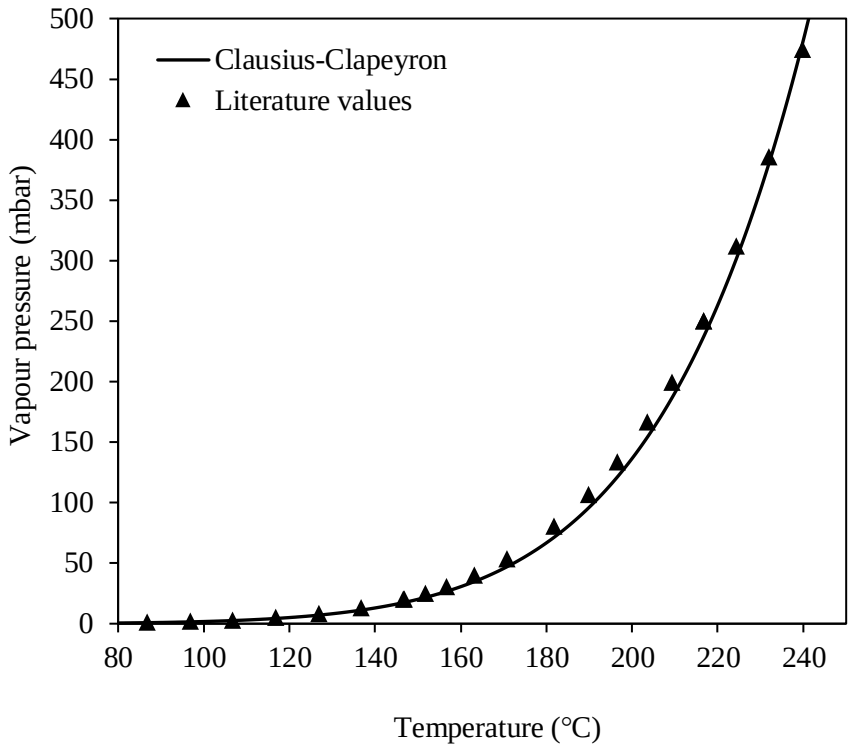

Fig. 3.2: Theoretical and experimental plot of the relationship between temperature and vapour pressure for the ε-caprolactam monomer [137].

When the raw materials are placed into the A and B component vessels, they are in solid granule form as provided by the supplier. In this case, the bulk density (or packing density) needs to be considered. The values in Table 3.1 show that the effective density for each case is approximately half of that for the actual density due to the air between granules. Therefore, only half the capacity amount of material can be contained in vessels in frozen form. This also reduces the heat transfer in frozen form due to overall reduced conductivity with the air. The mechanism of heat transfer would change over time from when the granules begin to melt and come into more intimate contact with one another until the mixture is fully melted. Where the component vessels are heated, the rate of heat transfer to/within the mixture can be increased by using dynamic stirrers to induce convection. Using too high a rotational speed, however, could cause the air between granules to become dissolved in the mixture. In order to determine the effective thermal conductivity of the bulk material in solid form, it was firstly assumed

that in terms of conduction, the material acted like a porous medium. The effective void volume fraction V_v was found to be approximately 0.36 based on the difference from the density of solid caprolactam and its bulk density. Loeb's relation assumes that if the thermal conductivity of a porous media is significantly larger than the gas/liquid filling the pores (nitrogen in our case), the relationship between the two is linearly related by V_v [138]. Where k_c is the thermal conductivity of caprolactam and k_n is that of nitrogen, the effective thermal conductivity for the bulk material can be defined as follows:

$$k_m = k_c(1 - V_v) + k_n V_v = 0.38\ W/mK \tag{3.2}$$

With the two components now heated sufficiently, they must be mixed for injection and then transferred to the mould. In order to do so, they must leave their respective heated vessels. All interconnecting parts between the vessels and mould should be maintained at temperatures above 69 °C at all times to prevent freezing, and hence, blockages. It is important that the mixture isn't heated so much that it begins to polymerise within the delivery system as such blockages could be detrimental to machine components. In order to remove PA-6, it would require melting or burning it out at temperatures above the melt temperature of the polymer (>218°C); however, this would be extremely inconvenient and most non-metallic parts in the system such as seals are not generally rated to such temperatures.

Finally, when the molten mixture reaches the mould, it would once again undergo a heating process as it comes into contact with the mould surfaces, which will be at temperatures above 140 °C. Note that as the front flow of the molten mixture fills the mould, it increases in temperature due to heat transfer from the cavity walls. Due to this effect, the hottest temperatures would be towards the outlet. In order for the mould temperature not to change dramatically, the mould would require a large thermal mass so that the temperature can be maintained as closely as possible. However, it should also be noted that doing so will also decrease the mould's ability to dissipate exothermic heat during the reaction. It is important that the temperature of the mould does not exceed the degradation temperature of the fibre sizing as doing so would hinder the benefits of sizing. Throughout the design process, two of the three modes of heat transfer were considered: conduction and convection. Due to the relatively low temperatures used, the effects of radiation were considered to be negligible.

3.2.3 Flow and Pressure (including Permeability testing)

For a closed mould cavity with fixed thickness, the main factor influencing the injection pressure of the system is the permeability of the textile as dictated by Darcy's law. The permeability κ of the textile within the mould depends on the fibre volume fraction, the orientation of the fibres and the surface treatment of the fibres. In addition to the resistance caused by the textile, friction losses and differences in elevation will also contribute to the pressure required to inject.

As the reaction time of the mixture is fast, the mixture must fill the mould before there is a large increase in viscosity at the onset of polymerisation. This also coincides with the needs of high volume production where short cycle times are necessary, so fast injection times are desirable. To meet these requirements, it is preferable that the mixture fills the cavity in 10-15 seconds to allow the remaining cycle time for polymerisation, cooling and demoulding. The back pressure experienced at the mould inlet is mainly dictated by Darcy's law, as faster injection rates would result in higher back pressures in the system. Where t is the injection time, h the cavity thickness, b the cavity width and l the length of the mould cavity, the flow rate through the mould (Q_m) is described using equation 3.3.

$$Q_m = \frac{V}{t} = \frac{hbl}{t} \tag{3.3}$$

Where the cross sectional area of the mould cavity $A_{cs} = hb$, Darcy's equation can be written in both forms shown in equation 3.4 where μ is the dynamic viscosity of the mixture (~ 3 x 10^{-3} Pa.s for mixture @ 80 °C).

$$P_m = \frac{\mu l Q_m}{\kappa A} = \frac{\mu l^2}{\kappa t} \tag{3.4}$$

Equation 3.4 demonstrates that the injection pressure is directly proportional to the cavity length squared. As the viscosity, permeability and infusion time are all known (or determined experimentally), the theoretical injection pressure at the mould inlet can be calculated. Permeability measurements are generally taken using either a constant flow rate or constant pressure. The textile is laid up in a fixed thickness cavity and the resin is infused either rectilinearly or radially [139]. Flow rate and pressure are then monitored and recorded during infusion. This data combined with viscosity measurements from rheometry of the resin, allow determination of permeability of a given textile and layup.

Working backwards from the mould inlet, head losses due to friction in pipes between the drive and inlet have to be considered. This increased back pressure P_p can be determined from

the Hagen–Poiseuille relationship given in equation 3.5 where L is the length of the pipe and Q_p is the flow rate through the pipe. Note that by using this equation, it is assumed that the pipe flow is laminar and fully developed. Flow rates less than 1l/min result in Reynolds numbers (Re) of around 1,800 which is less than the critical limit for pipe flow (~2,400), meaning that the flow should be laminar. It should also be noted that pressure drops due to bends in the pipe have been neglected in this analysis as they are not significant.

$$P_p = \frac{128\mu l Q_p}{\pi d^4} \tag{3.5}$$

Pressure drops across tubular devices with obstructions (such as those in a static mixer) can be calculated by multiplying equation 3.5 by a flow coefficient K_v [140]. The K_v values can be obtained experimentally by comparing measured pressure values with those generated using equation 3.5; however, K_v values can often be obtained from supplier datasheets.

Pressure drops due to an orifice valve can also be determined using a flow coefficient K_v value for a device. This pressure drop can then be expressed as in equation 3.6 where SG is the specific density with respect to water (~1.01 for caprolactam) and Q is the flow rate through the device [140]. Note that there is a squared relationship between the flow rate and pressure, and so, the effects are often negligible at low flow rates.

$$P_{ov} = \frac{SG \cdot Q^2}{{K_v}^2} \tag{3.6}$$

Pressure due to a difference in elevation between the injection drive and mould inlet are negligible as both should be positioned at approximately the same height. Check valves are often used in flow systems where back flow cannot be allowed. These valves usually contain a spring loaded sealing system which require a minimum *cracking pressure* P_{CV1} to open the valve. In addition to the cracking pressure, the obstruction caused within a check valve will result in a subsequent back pressure P_{CV2}.

The force required to keep the mould closed and prevent leaking during and after injection is the sum of that required for compaction of the preform F_c (if required), elastic deformation of the seal F_s and that required to counteract the fluid pressure at the mould inlet where it is highest F_m. While the pressure distribution across the length of the mould varies, it is a safer and more conservative method to assume that the pressure across the cavity is that at the inlet. Where F_c and F_s can be determined experimentally, the clamping force F_p required to close the press during injection can then be determined by equation 3.7.

$$F_p = F_m + F_c + F_s = P_m bl + F_c + F_s \tag{3.7}$$

3.2.4 Reactive mixing

Prior to injection, the A and B components must be mixed in a 1:1 ratio. As the melt viscosity of the precursor materials is low, the amount of mixing required to gain a homogenous mixture in the individual tanks is not very high. In most typical RTM processes, mixing is carried out using a static mixing head. The mixing head, either disposable or reusable, often contains complex internal geometry which causes intimate integration of the two components [141]. A static mixing head such as that shown in Fig. 3.3 consists of a number of elements which mix the components in three steps:

(a) Flow division: Each time a stream passes an element, it splits into two separate streams. *n* number of elements results in 2^n number of flow streams.
(b) Flow conversion: the spiral walls cause the product in the centre to spread radially towards the walls and that on the outside to do the opposite, causing shearing between the products.
(c) Flow inversion: at each element, the direction of flow rotation is rapidly inverted, causing agitation.

The degree of mixing based on samples taken from the outlet of a mixing head would present a Gaussian distribution. Where the coefficient of variation (standard deviation/mean) for this distribution is less than 0.05, the homogeneity of the mixture is 95.5 %. This is widely considered an acceptable level of mixing in such processes [142][143].

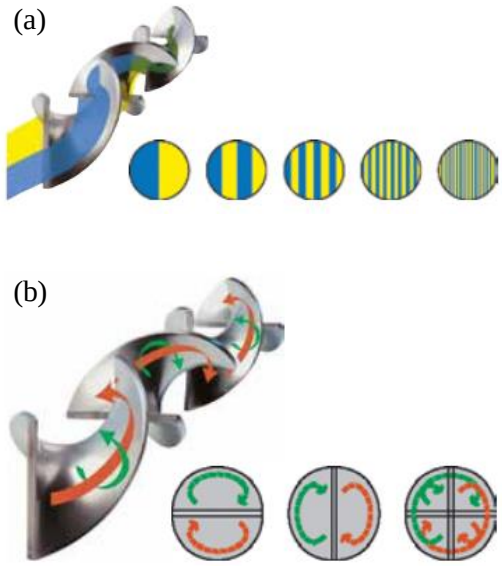

Fig. 3.3: Internal geometry of a static mixing head showing (a) flow division and (b) flow conversion and inversion [144].

3.2.5 Moisture control

As discussed in Chapter 2, the anionic polymerisation will terminate in the presence of moisture [56]. Coinciding with the fact that the precursor materials used are hygroscopic, it is important that they are protected from moisture during processing. Due to the presence of moisture in air, it is important that the moisture is curtailed in the circulatory and storage networks of the TP-RTM system. This can be done by either evacuating the air present or using an inert gas such as nitrogen or argon with a controlled moisture content to create a gas blanket in the system. Evacuation of air alone will not, however, get rid of water condensation residing in parts at temperatures below boiling point, nor will creating a blanket of inert gas achieve this. In order to minimise water particles, application of a high pressure blast of inert gas would be required to flush/purge the parts. While the gas purge should clear a significant amount of moisture from parts, a follow up flush run of the system with a small batch of caprolactam would further reduce the amount of moisture residing in parts. These purge and flush processes may only need to be carried out once per day just before the production of the first batch. From then on, however, blanketing of the system with inert gas should be maintained. This should be constant in the storage tanks and should be supplied to the remaining components prior to flow of the mixture. An additional effect of blasting the system with inert gas would be to flush the molten mixture from the system immediately after injection, in order to clear the mixing head and other parts. While polymerisation of high quality polymer is only achieved at temperatures above ~140 °C, low molecular weight polymer/oligomer can cause solidification in parts at much lower temperatures. Purging the system after each run with gas would prevent this from occurring.

3.3 Final design

3.3.1 Systems overview

A schematic diagram of the flow network design for the TP-RTM system is shown in Fig. 3.4. The system contains two individual lines for the A and B components, which meet at the mixing head. Each component line has a heated tank with stirrers, fixed with a valve for draining and another directed towards the pumps. The pumps drive each molten component to separate junctions, each with 3 solenoid valves. Depending on the opening/closing sequences of these valves during pumping, the components can either be recirculated or injected. Recirculation is where the contents from the heated tanks are pumped back into the tanks in a continuous loop. Recirculation allows the machine components to be cleaned with caprolactam before the first batch of the day is produced. Use of recirculation prior to injection also ensures that the flow front of each component is at the mixing head and ready for injection.

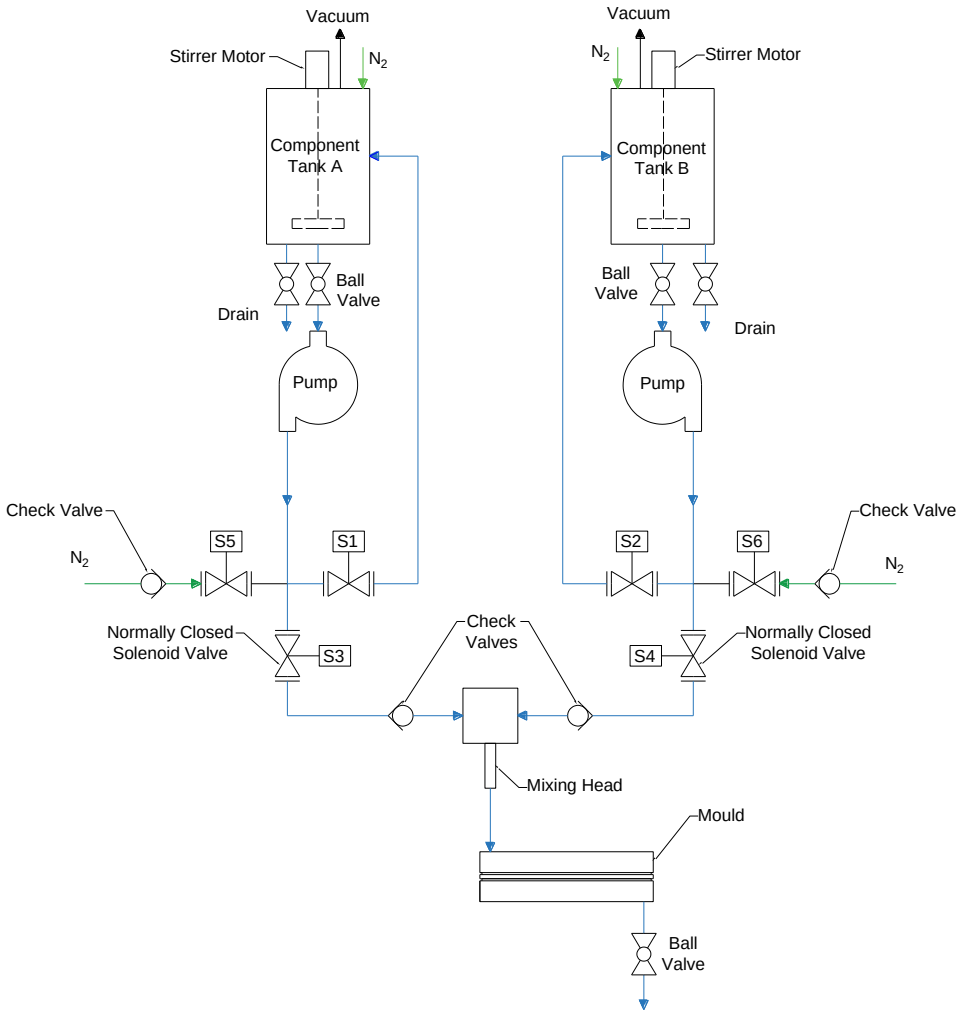

Fig. 3.4: Schematic diagram of the flow network for the TP-RTM system.

During injection, the components are directed to the mixing head, where they finally meet and mix prior to entering the mould. Even though both pumps should always function simultaneously, in case of a fault in the system, a set of check valves were used in each line to prevent backflow from A into B or vice versa. The components mix intimately as they pass through the mixing head.

It can be seen in Fig. 3.4 that a nitrogen gas supply is connected to each component junction. This is used for purging of moisture from both the recirculation and injection lines and to flush the system just after injection to prevent polymerisation occurring within the heated parts. A nitrogen gas pressure of approximately 2 bars was used during these steps. Check valves were situated on each nitrogen line to prevent resin flowing into the nitrogen line. A separate supply of nitrogen goes to the component tanks for maintenance of a nitrogen blanket which is controlled manually by a ball valve.

As previously mentioned, in order to control the flow path of the molten components and nitrogen in the system, a number of solenoid valves were used. Two normally closed solenoid valves for each component were used to change the flow path between the recirculation and injection lines. Another normally closed solenoid valve was used on each line to control the nitrogen supply to the system during purging and flushing. Activation of the solenoids in different arrangements allowed for different operations to be carried out. For example, to flush the system after injection, the pumps are turned off with the injection line closed, the recirculation line open and the nitrogen line open. This allows nitrogen to flow into the recirculation line, flushing all the resin in the line back into the tank. Then the injection line is opened and the recirculation line and nitrogen lines closed. The pumps are then turned on to drive the remaining contents out from the tanks through the injection line. The nitrogen valves are then opened to further purge any contents remaining.

After exiting the outlet side of the mixing head, the molten mixture is then transferred to the heated mould contained within a pneumatic press, via aluminium tubing. An in-line pressure transducer and 3-way valve were later introduced to the injection line and a vacuum pump introduced at the mould outlet line, but these will be discussed in more detail in Chapter 4.

3.3.2 Mould design

According to Darcy's law (equation 3.5), the back pressure required at the mould inlet to inject into a textile is related to the length of textile (cavity length) squared so it is important that the cavity length is kept to a minimum where possible to avoid unnecessary large injection pressures. The mould cavity had to be large enough to produce mechanical test samples in compliance with various test standards. As different tests recommend different laminate thicknesses, a three part aluminium mould using interchangeable cavity frames was designed and built in-house. Images of a 3D model and actual pictures of the mould are shown in Fig 3.5. The mould halves were machined from two 450 mm x 400 mm x 40 mm aluminium blocks and a number of 390 mm x 350 mm cavity frames with different thicknesses were machined (1, 2, 4, 6 mm).

(a)

PARTS LIST		
PART NAME	ITEM	QTY
Bottom	1	1
Cavity	2	1
Top	3	1
Inserts	4	20
Dowel Pins	5	4
Inlet/Outlet block	6	2

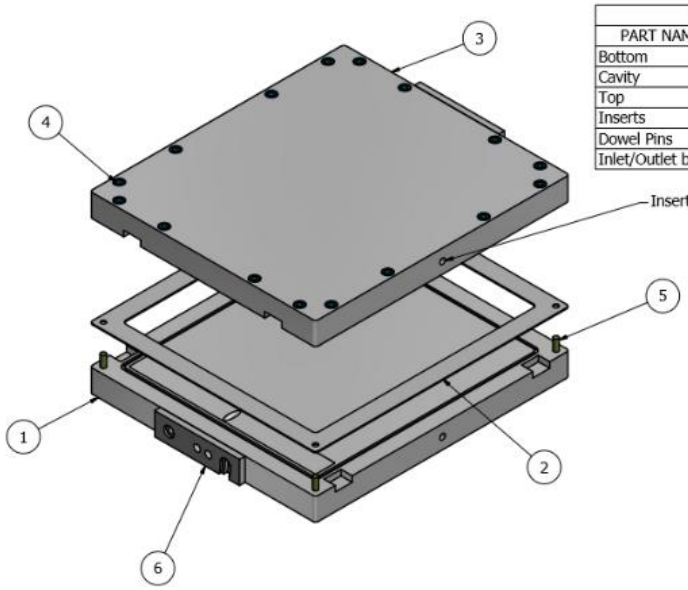

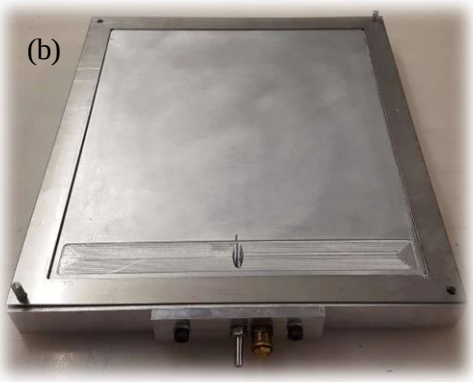

Fig. 3.5: (a) 3D model of the mould (exploded view), (b) lower mould half with 2 mm cavity plate and (c) upper mould half fitted with handles.

A line injection gate was machined into the lower half on the inlet side to encourage rectilinear filling of the cavity. The mould consisted of removable pieces at the inlet and outlet to make demoulding easier. The inlet and outlet holes were placed at angles so the runners could easily slide out with parts during demoulding. Swagelok stainless steel tube fittings (¼'' BSP) were used with PTFE tape to achieve airtight seals in joining interconnecting tubing at the inlet and outlet. Due to the high temperature range used for polymerisation of APA-6 (140 °C – 160 °C), silicone rubber seals were used as they can operate at temperatures up to around ~300 °C. Aluminium was chosen over stainless steel as the mould material due to mostly practical reasons such as lower cost, easier machinability and lighter weight. Aluminium (tool grade alloy) is known for its high thermal conductivity (~205 W/m.K) compared to stainless steel (~13 W/m.K) [145]. As a result, aluminium would be better suited to conducting heat away from the cavity during the exothermic reaction, compared to stainless steel. Disadvantages associated with aluminium are also due to the high thermal conductivity, which causes heat energy to get lost to the environment. While this might not be a concern at lab scale, it can be costly in large scale production in terms of heating power. Aluminium also has a lower hardness than stainless steel, meaning that dents and scratches can be more easily caused during part removal etc.

3.3.3 Flow and back pressure

Prior to choosing a suitable set of pumps, the required flow rate and subsequent driving pressure had to be determined. The highest load experienced by the pumps would be during injection into the textile, after the mixture reaches the outlet. The theoretical injection pressure required at the pumps can be calculated by taking the sum of the pressure drops across the system. This value would be the minimum pressure required to infuse a part. In order to compress voids and improve wet-out, additional pressure would be required.

In order to write equation 3.4 in terms of flow rate, the permeability κ had to be determined. An experiment was carried out to measure the recti-linear permeability across a layup of 4 plies of UD glass fibre with a 2 mm cavity in the mould. A constant flow rate was used and the pressure was measured on the inlet side using an inline pressure gauge. The permeability κ for this layup across the mould was found to be approximately 2.86 x 10^{-10} m^2. The flow rate beyond the mixing head (Q_m) is double that experienced before it (Q_p) due to the combined flow of the A and B components. The pressure drop across the mould due to the fabric was then rewritten in terms of Q_p and is given in equation 3.8.

$$P_m = 11.69 \times 10^9 Q_p \tag{3.8}$$

During injection, the flow passes through both stainless steel check valve and solenoid valves in each component line. The check valves chosen (Swagelok 4CPA2) had a variable cracking pressure and could be adjusted to a desired setting. While a higher cracking pressure requires more work by the pump to open the valve, it also means that the valve will seal more tightly in the event of back flow. The valves were set to have a cracking pressure P_{CV1} of ~50,000 Pa each. The relationship between the pressure drop in the valve and the flow rate Q_p is given in equation 3.9. This equation was derived in Appendix A using supplier datasheet information and interpolation.

$$P_{CV2} = 1.59 \times 10^9 Q_p + 126{,}000 \tag{3.9}$$

The solenoid valves chosen (Shako JA2EE/24V/18) were 2/2 way normally closed valves, made from stainless steel and with a 4 mm orifice. Pressure drops in the solenoid valves were considered negligible due to the low flow rates used, which resulted in relatively low pressure drops across the device.

Between each pump and the mixing head, there was approximately 500 mm of aluminium tube with an inner diameter of 4.6 mm to transport the individual components. The same tubing was used between the mixing head and mould to transport the combined mixture with a length of around 1500 mm. Using the Hagen–Poiseuille relationship given in equation 3.5, the pressure loss across tubing for the individual and combined tubing can be rewritten as follows:

$$P_{ind} = 45.5 \times 10^6 Q_p \tag{3.10}$$

$$P_{comb} = 136.5 \times 10^6 Q_m = 273.0 \times 10^6 Q_p \tag{3.11}$$

The mixing head used (Stratos™ Static Tube Mixer) consisted of 21 elements and had an inner diameter of 4.93 mm, length of 178 mm and flow coefficient K_v of 7. By factoring K_v into the Hagen-Poiseuille relationship, the pressure drop across the mixing head in terms of flow rate is:

$$P_{MH} = 515.63 \times 10^6 Q_p \tag{3.12}$$

For two identical pumps in parallel, the overall flow rate doubles from the mixing head onwards but the pressure remains the same. The pressure required by each pump can then be expressed in terms of flow rate by adding the pressure drops in each part. The total pump pressure in terms of flow rate through the pump is given as:

$$P_{p\,min} = P_{ind} + P_{CV1} + P_{CV2} + P_{MH} + P_{comb} + P_m$$

$$P_{p\,min} = 13.84 \times 10^9\, Q_p + 126{,}000 \tag{3.13}$$

Due to their ability to provide continuous flow accurately, stainless steel gear pumps were chosen to drive each component. In order to fill the mould, the entire volume of all flow paths and the cavity would have to be filled between the pumps and the mould outlet. For a 2 mm mould cavity containing a textile with ~50% fibre volume fraction, the total volume of the cavity and tubing was found to be around 166 x 10^{-6} m^3 (166 ml). To fill this volume in ~10s, a volumetric flow rate Q_m = 16.6 x 10^{-6} m^3/s (996 ml/min) through the mould would be required. To meet this demand, a flow rate Q_p = 8.3 x 10^{-6} m^3/s (498 ml/min) would be required by each of the 2 pumps. Inserting this value into equation 3.13 shows that this would require a pressure of 240,872 Pa (~2.41 bar) to be supplied by the pump.

3.3.4 Pump and drive

The pump chosen (Beinlich ECO.pump) was an external gear pump with a rotational displacement V_g of 3 x 10^{-3} l/rev and volumetric efficiency η_v of 94%. The chosen drive for the pumps (Mellor DC geared motor) had a rated rotational speed n of 160 rev/min when run at 24V but could be changed by varying the voltage. Use of this combination would result in a flow rate and back pressure of 451 ml/min and 2.30 bar, found using equations 3.14 and 3.13 respectively. This flow rate would result in a mould filling time of approximately 11s, which was deemed close enough to the desired fill time outlined.

$$Q_p = \eta_v V_g n \tag{3.14}$$

Where η_m is the mechanical efficiency and f_v is the viscosity factor, the torque required to drive the pump shaft was determined using equation 3.15 [146]. The η_m value at the specified pressure range is around 96% and the f_v value for viscosities less than 10 mPa.s is approximately equal to 1. At a flow rate of 451 ml/min, the torque was found to be 1.92 Nm. The motors chosen had a rated torque of 2 Nm which meant the pumps had enough torque to deal with filling in the specified time.

$$T_p = \frac{P_p Q_p f_v}{\eta_m \eta_v} \tag{3.15}$$

DC motors are characterised by their linear torque-speed relationship, which controls the pressure-flow relationship of the pump. As more torque (higher pressure) is applied, the speed (flow rate) reduces in a linear manner. In order to reduce voids after mould filling, it was decided that additional pressure may be required. This would ultimately result in a reduced injection flow rate; however, at this point the mould would have already been filled, so it is

not an issue if the motors stall at this point. To prevent the motors burning out during stall (while maintaining excess pressure), a current limit could be set on the power supply. In summary, the torque/pressure is limited by the current supply and the speed/flow is governed by the voltage. A quick experiment was carried out to determine the relationship between the voltage and flow rate (see Fig 3.6) and a linear relationship was derived from the data points, given in equation 3.16. It was later discovered that better rectilinear flow could be achieved in the mould using a lower flow rate, and so, a component flow rate of ~416 ml/min was used at a supply voltage of 20 V to the motors. This would result in a back pressure of approximately 2.22 bars and a fill time of ~ 12 s.

$$Q_p = 0.0208\,V \tag{3.16}$$

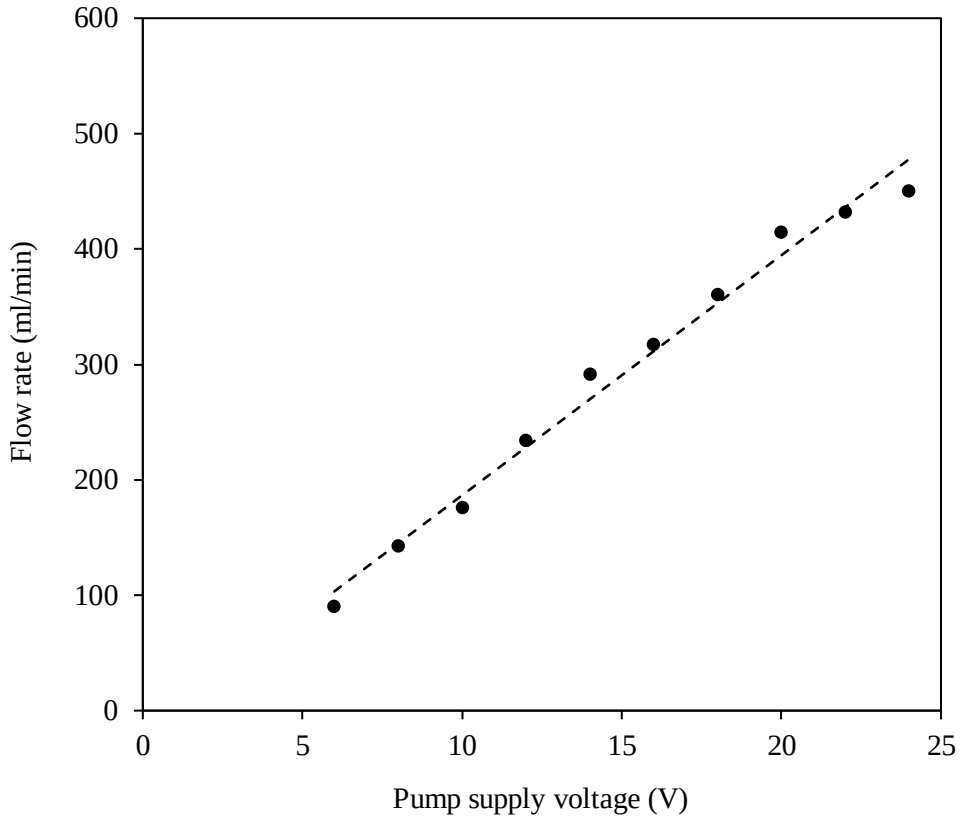

Fig. 3.6: Experimental data points for voltage versus flow rate.

It should be noted that Kalrez® perfluoroelastomer (FFKM) was used as the sealing material in all O-rings which came in contact with the materials. Nitrile, EPDM and FKM were all trialled in the seal of solenoid valve plungers and deteriorated over time due to the aggressive nature of the reactants at the temperatures encountered (~90°C). PTFE was trialled but was too rigid to provide a good seal given the particular elastic constant of the plunger spring. Silicone

rubber was also trialled but experienced significant swelling (as did the FKM material) which caused jamming of the valves. A quick experiment was carried out by placing an FKM O-ring in a flask containing the reactant materials heated to 90°C. It was found that significant swelling, weight gain and permanent deformation occurred in the O-ring. Examples of observations are shown in fig. 3.7.

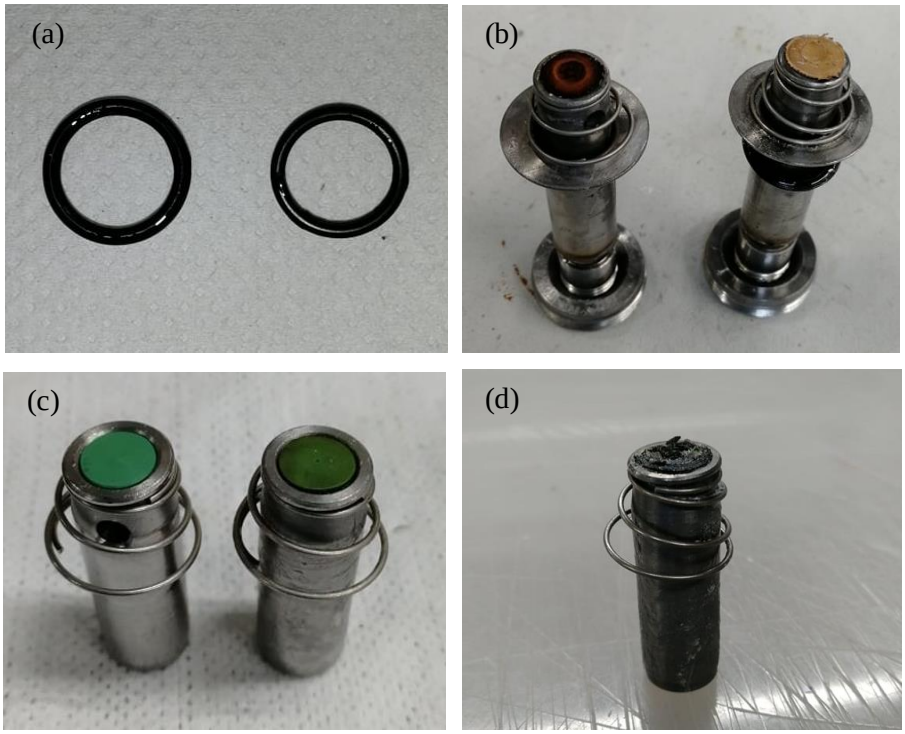

Fig. 3.7: (a) FKM O-ring before (left) and after (right) 1 hour immersion, (b) valve plungers with seals made from silicone rubber which have swollen, (c) valve plungers with FKM seals before (left) and after (right) one injection run, and (d) valve plunger with FKM seals after several injection runs.

3.3.5 Heating System

It was decided that all the components shown in Fig. 3.4 down to the mixing head would be contained within a heated enclosure maintained at temperatures above the melting point of the raw materials. A separate method for heating the component tanks was required due to their large thermal mass and that of the raw materials after pouring. High power heating would be required here in tandem with the stirrers to quickly heat the materials. Quicker heating would reduce the residence time of the component materials in the tanks, minimising their exposure time to moisture and increasing the confidence levels in the quality. The heating system consisted of silicone heater mats for the tanks and a ceramic heater in the enclosure. To analyse

the heating affects in the system, thermal resistance networks are modelled in this section. Both transient and steady state cases were considered. While a lot of the complex equations discussed in this section are difficult to solve, contain many unknowns and have many solutions; they demonstrate understanding of the system and provided methods for approximating design values to a satisfactory level. The values sought after mainly were power requirements for heaters given the designed enclosure geometry/properties and the amount of material required to heat in a fixed time. The following three heating scenarios were considered:

(i) Transient heating of the machine parts before the addition of the materials.
(ii) Steady state heating in the enclosure.
(iii) Transient heating of the materials in the tanks.

For cases (i) and (iii), the desired time to heat the parts and materials will have to be determined for each. Three heating sources were used in total: two heating mats on the tanks providing heat flow Q_{hm} and one ceramic heater in the enclosure providing heat flow Q_{ch}. For all three cases mentioned, heat is lost to the surroundings with a flow rate of Q_{loss}. When the machine is first turned on, heat flow Q_{parts} is required for heating the internal parts of the machine. When the raw component materials are placed in the tanks, additional heat flow Q_{mat} is required to melt them. The three cases can now be rewritten mathematically as in equations 3.17, 3.18 and 3.19 respectively.

$$2Q_{hm} + Q_{ch} = Q_{loss} + Q_{parts} \tag{3.17}$$

$$2Q_{hm} + Q_{ch} = Q_{loss} \tag{3.18}$$

$$2Q_{hm} + Q_{ch} = Q_{loss} + Q_{mat} \tag{3.19}$$

While the aluminium surface is more conductive than the surrounding air, an amount of heat flow from the heating mats would be lost to the air in the enclosure. The two heating mats combined with the ceramic heater would effectively work in parallel to heat the air in the enclosure as well as the tanks. Firstly, the enclosure and the tanks will be dealt with separately in terms of heat transfer. A way of solving such problems one dimensionally involves determining a thermal resistance network for each stage of heat transfer and adding them in parallel or series prior to solving, analogous to electrical resistances [145]. To help with solving the equations, some boundary conditions can be identified. A reasonable time for all these parts to heat could be ~30 min. The temperature of both the parts and the materials initially is that of the lab (~20°C/293.15K) and after 30 min is 90°C/383.15K. The temperature can be written as a function of time T(t) and with boundary conditions given in SI units as:

$$T(0) = 293.15\text{K} \tag{3.20}$$

$$T(1800) = 383.15\text{K} \tag{3.21}$$

The enclosure, with dimensions 700 mm x 600 mm x 500 mm, consisted of 6 walls. The wall panels were each 30 mm thick, consisting of inner and outer aluminium sheets with glass wool insulation sandwiched between the two. A fan was used to induce convection currents within the enclosure in order to increase the heat transfer rate and improve the temperature distribution. Heat transfer through the enclosure walls was assumed to be due to conduction, and that transferring to/from the air on the inner/outer surfaces due to convection. While the upper and lower walls of the enclosure would have differing heat transfer coefficients than the side walls, they were assumed to be the same for simplification of the analysis. It was assumed that the three heat sources were evenly distributed within the enclosure and that parts didn't obstruct air flow. The original resistance network diagram for the enclosure is shown in Fig 3.8 (a).

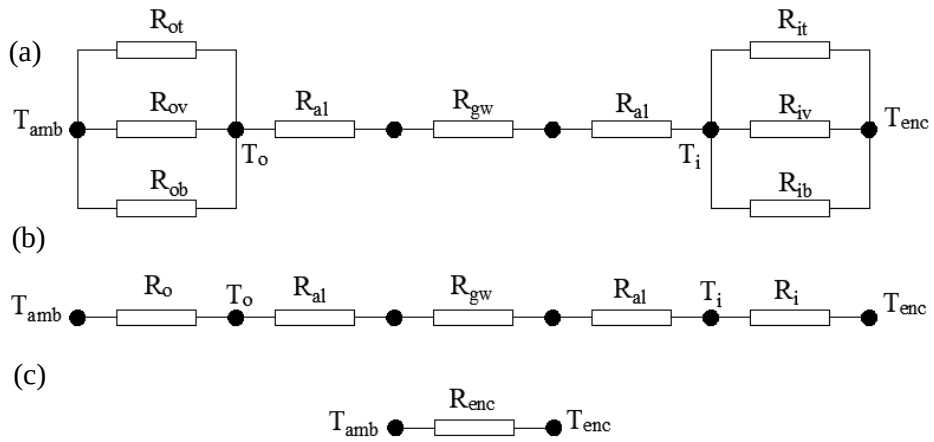

Fig. 3.8: (a) Thermal resistance network diagram for walled enclosure (b) reduced network after parallel addition, and (c) final reduction after series addition.

The internal convection was forced due to the assistance by the fan while that on the external walls was natural. The heat transfer coefficients (h) for each wall panel were unknown but generally for convection of air, these values are between 0.5 and 1000 W/m^{2}K. As shown in Fig 3.8, the thermal resistances of the walls act in parallel, and should therefore be added inversely. Assuming a similar outer and inner aluminium surface area (A) for each wall, the equation for resistance loss from the enclosure (R_{loss}) can then be compiled as in equation 3.19 where k is thermal conductivity and t is the thickness of the walls. The subscripts *o*, *al*, *gw*, *i* and *t* represent the outer wall, aluminium, glass wool, inner wall and total respectively.

$$R_{loss} = R_o + 2R_{al} + R_{gw} + R_i$$

$$R_{loss} = \frac{1}{A_t h_{to} + A_v h_{vo} + A_b h_{bo}} + 2\frac{t_{al}}{k_{al} A_t} + \frac{t_{gw}}{k_{gw} A_t} + \frac{1}{A_t h_{ti} + A_v h_{vi} + A_b h_{bi}} \quad (3.19)$$

To more clearly observe the relationship between the heat transfer coefficient values and R_{loss}, it was assumed that the heat transfer coefficients for all inner walls (h_i) were the same and all outer walls (h_o) were the same. Outer values ranging from 0.5 to 20 W/m^{2}K were inserted into the equation and plotted against R_{loss} as in Fig 3.9. Curves were generated for different h_i/h_o values with respect to the average h_o value. It can be noted that above outer values of 10 W/m^{2}K, the difference in resistance for all cases becomes almost negligible as the values plateau.

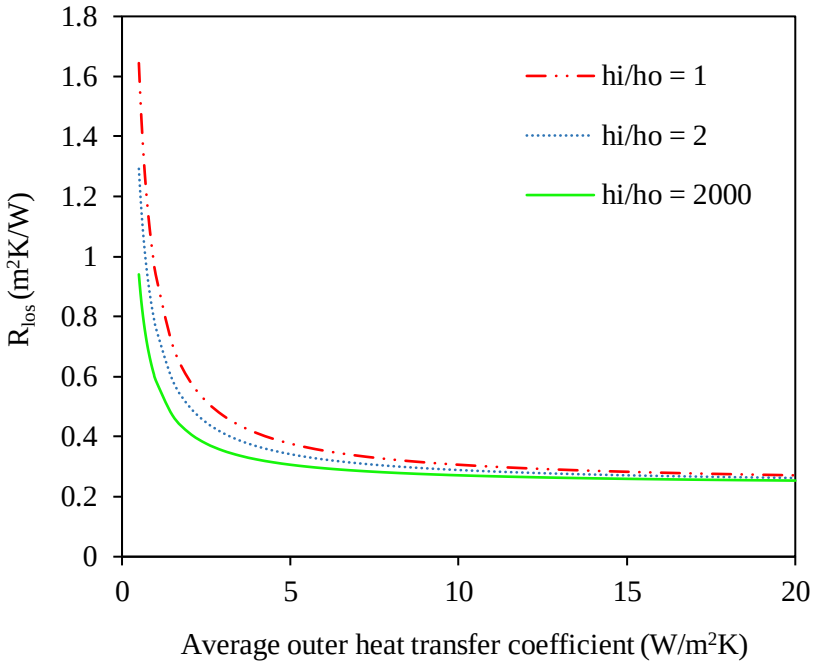

Fig. 3.9: Thermal resistance plotted against the outer heat transfer coefficient for the enclosure (h) values where all the outer h values are the same.

Assuming an average enclosure temperature of T_{enc} = 90 °C and an ambient temperature in the lab of T_{amb} = 20 °C, the heat loss at steady state can be written as in equation 3.20.

$$Q_{loss} = \frac{T_{enc} - T_{amb}}{R_o}$$

$$Q_{loss} = \frac{70}{\frac{1}{A_t h_{ot} + A_v h_{ov} + A_t h_{ob}} + 2\frac{t_{al}}{k_{al} A_t} + \frac{t_{gw}}{k_{gw} A_t} + \frac{1}{A_t h_{it} + A_v h_{iv} + A_t h_{ib}}} \quad (3.20)$$

It is also known that the heat flow due to convection away from the outer walls is the same as that due to conduction through the wall and that due to convection to the inner wall. Equation 3.21 expresses Q_{loss} in terms of convection from the outer wall. The heat flow as expressed in both equations 3.20 and 3.21 can be plotted against the average outer heat transfer coefficient. The temperature of the outer surface T_o was not known; however, mock values were chosen. The values chosen were 30°C, 40°C and 50°C as they fall between the ambient and enclosure temperatures and seem realistic. Equation 3.20 was plotted in Fig 3.10 using the same h_i/h_o values used in Fig 3.9.

$$Q_{loss} = Q_o = h_o A_o (T_o - T_{amb}) \tag{3.21}$$

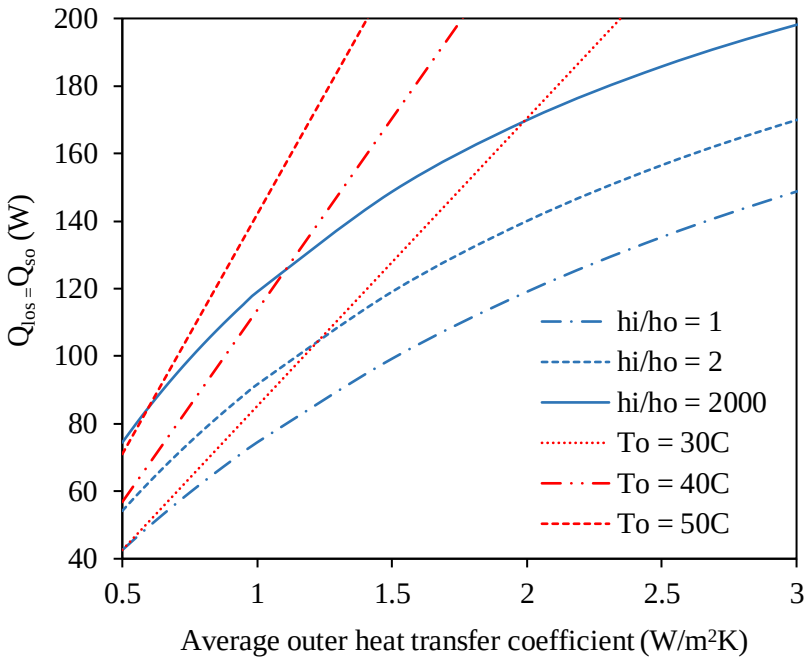

Fig. 3.10: Heat flow plotted against the outer heat transfer coefficient for the enclosure (h) values where all the outer h values are the same.

The lines generated at three different temperatures intersect the three curves, determining heat values that satisfy both equations. A minimum design limit value was defined where the $T_0 = 30℃$ line intersects with $h_i/h_o = 2000$ at ~170W. The upper limit value of 170 W was used as a worst case scenario heat loss during steady state conditions. This value was considered conservative as it seemed highly unlikely that the outer temperature of the enclosure at steady state would be less than 30°C; and, it was likely that the h_i/h_o value was much less than the 2000 value assumed here.

When the machine is first turned on, the parts (and air) have to be heated. If there are ~3 kg of steel (m_{st}), ~9 kg of aluminium (m_{st}) and ~0.25 kg of air, the heat flow required to increase their temperature from 20°C to 90°C in 30min (1,800s) is defined by equation 3.22.

$$Q_{parts} > \frac{\Delta T(m_{al}C_{p\ al}+m_{st}C_{p\ st}+m_{air}C_{p\ air})}{t} = 353\ W \tag{3.22}$$

It is desirable that the raw materials in the tanks are heated within about 10 min (600s). The heat required is that to heat the solid components up to 69 °C, provide further latent heat for melting and then heat them up to 90 °C. For a material batch of m_{mat} = 0.6 kg in each tanks, the heat required to raise its temperature to 90 °C was defined by equation 3.23.

$$Q_{mat} > \frac{\Delta T(m_{mat}C_{p\ mat})+m_{mat}l_{mat}}{t} = 273\ W \tag{3.23}$$

As mentioned, the heating mats would contribute towards the heating of the enclosure as well as the tanks. Due to the much higher conductivity of the tank compared to the air, and assuming a highly conductive adhesive bond between the tank and mat, most of this heat goes to the material. Even if the entire heat loss from the enclosure was provided by the tanks alone (85W each), a 358W (273W + 85W) heating mat would account for a worst case scenario.

400W heating mats were chosen for each tank and are often considered close to 100% efficient, therefore allowing for heating of a 0.6 kg batch in just over 9 minutes with constant supply of power in the worst case scenario. Heating at a constant rate up to 90°C would result in a temperature overshoot in the tanks, and so, a PID (proportional integral derivative) controller was used. Based on the controller's settings, it controlled the output to the heater in a binary on/off manner to reduce overshoots in the system but at the expense of time.

Out of the three heating cases discussed, cases (i) and (iii) are the most demanding in terms of power consumption. In reality, the losses for case (i) are initially zero and increase over time until steady state. Therefore, the minimum designed heat flow required from the heaters are described as:

$$2Q_{hm} + Q_{ch} > Q_{loss} + Q_{parts} > 523\ W \tag{3.24}$$

A 600 W ceramic heater was used, combined with the fan to heat (mainly) the enclosure.

3.3.6 Tank Design

The component tanks were designed to heat, mix and store the individual components under inert conditions. Each tank was designed such that disassembly could be carried out easily for cleaning. The tanks with a storage capacity of 1.8 litres each were made from hollow

aluminium tube with flanges, a removable base containing the feed to the pumps and a removable lid containing a mechanical stirrer and ports for recirculation, nitrogen and vacuum (shown in Fig. 3.11). The stirrers consisted of 3 sets of impellers. Baffles were not used in the tanks as they would act as an obstruction for the material in solid form which could cause jamming. The vacuum port in the tanks was not used during this project but was designed for degassing of components if necessary.

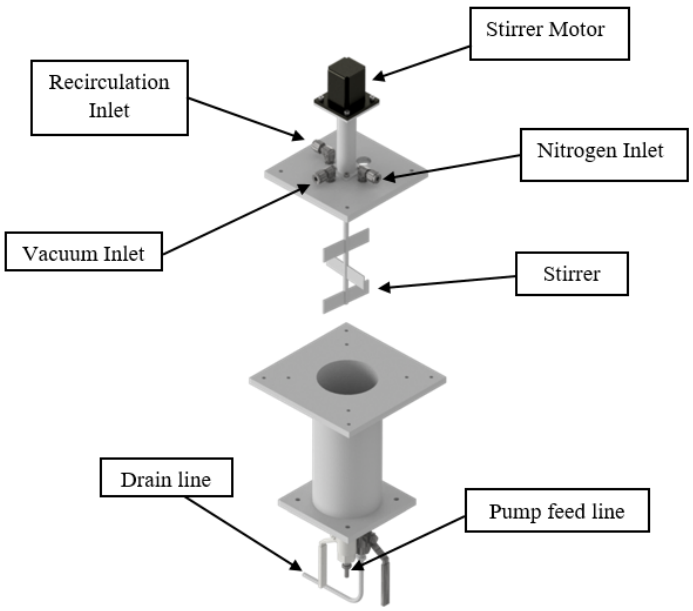

Fig. 3.11: Exploded view of the different tank parts.

3.3.7 Pressure transducer

In order to measure the pressure at the inlet of the mould, a pressure transducer was positioned just before the inlet. A block was machined so that the transducer could be placed in-line as shown in Fig. 3.12. Pressure transducer readouts were recorded using an Arduino Uno microcontroller. The output voltage range of the transducer was between 0 and 10V, while the input voltage range of the microcontroller was only between 0 and 5V. The voltage divider rule as given in equation 2.25 was applied to the circuit by using a set of resistors to halve the values for reading. To get half the voltage, the resistance rating of each was the same. As well as providing a live data output over time, the circuit also illuminated a set of LEDs which signalled to the user when the pressure had exceeded a pre-set value and when it was below. This was required during the later stage of the infusion process where flow restriction was used at the outlet to increase the pressure in the cavity. This will be described in more detail in Chapter 5.

$$V_{out} = V_{in}\left(\frac{R_2}{R_1+R_2}\right) \tag{2.25}$$

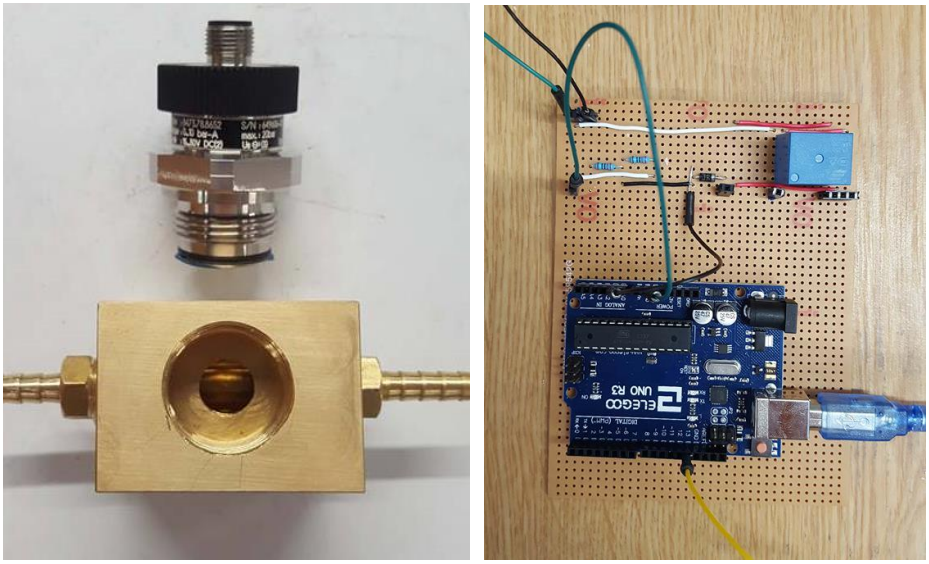

Fig. 3.12: Pressure transducer, in-line pressure block and Arduino microcontroller/circuit.

3.3.8 Electrical systems

The electrical power systems were subcategorised into two groups: those which drew current from the mains (~230 VAC) and those which drew current from remote power supplies (20-24 VDC). The former included the two heating mats, ceramic heater and convection fan while the latter included the two stirrers, two pumps and six solenoid valves. All the heaters were connected to a multi-channel PID controller with binary on/off control via activation/deactivation of solid state relays (SSRs) which opened/closed circuits as required (dependent on settings) such that the measured temperatures reached the set value of 90°C. Temperature feedback measurements were recorded using K-type thermocouples, whose location was important. Bolted thermocouples were screwed into the bottom of each tank. They were positioned such that the temperature measuring surface was flush with the inner surface of the tank. For feedback to the ceramic heater, the thermocouple was placed close to the tubing used to transfer the molten materials; however, it was measuring air temperature as opposed to the part temperature. Had the thermocouple been located in the parts themselves, the temperature response time within the part would be slow. This would initially cause an oversupply of heat in the enclosure (fire hazard), and later causing massive temperature overshoots. The AC fan could be turned on/off by a manual switch located on the side of the machine. A switch control box was made in-house to control the DC components. With regards to the solenoid valve control, a 3-way switch was used. When in its central position, all valves were deactivated. When switched to recirculation, the circuit to the solenoid of the two

recirculation line valves was closed, causing the valve to open. When switched to injection, this circuit was opened while that for the solenoids of the two injection line valves were activated. A separate switch was used to blast the lines with nitrogen gas by activating the solenoid of the nitrogen valves. The switch control box contained 2 more 2-way switches to turn on/off the pumps and stirrers. In order to decide on the types of wires, switches, relays etc. to use, the current drawn by each component had to be considered such that thick wires would not melt from overheating.

3.3.9 Second prototype

It is important to clarify at this stage that two different versions of the system were built: the original at The University of Edinburgh and the second at The University of Auckland, New Zealand. While the two systems were very similar, there was one key difference. The drive used for the pumps in the original version was a set of DC motors whereas the drive for the second system used stepper motors. The flow rate in the former design had a linearly inverse relationship with pressure, which was troublesome. While the pressure (and hence, pump torque) in both component lines should be equal theoretically, it was not guaranteed. For variations in pressure between the two, the flow rate would vary correspondingly which would affect the mixing ratio. Experiments to measure the rotational speed of each were carried out and it was shown that a variation of ~2% occurred. The benefits of the DC drive was that high pressures were avoided by the flow rate adjusting in response to reduce the pressure, meaning that wet-out was always achieved. The second system in Auckland used stepper motors instead to drive the pumps. So long as they were operated below their torque limit, the stepper motors ensured a constant flow rate in both lines as they rotate in signalled steps which were controlled by an Arduino microcontroller. The disadvantage of using this system is that the back pressure in the system varied massively from run to run. This was due to variations in the highly sensitive permeability of the layup, which typically varies a lot depending on the compaction and fibre volume fraction of the textile in the cavity.

3.4 Fabrication and assembly of TP-RTM equipment and controls

After the design of each system was complete, the parts and components were either built in house or sourced externally. To ensure correct alignment of the parts of the frame, enclosure, pump supports and tanks, a 3D model of the assembled parts was generated as shown in Fig. 3.13. This helped with determining dimensions, fits, clearances and alignment of parts.

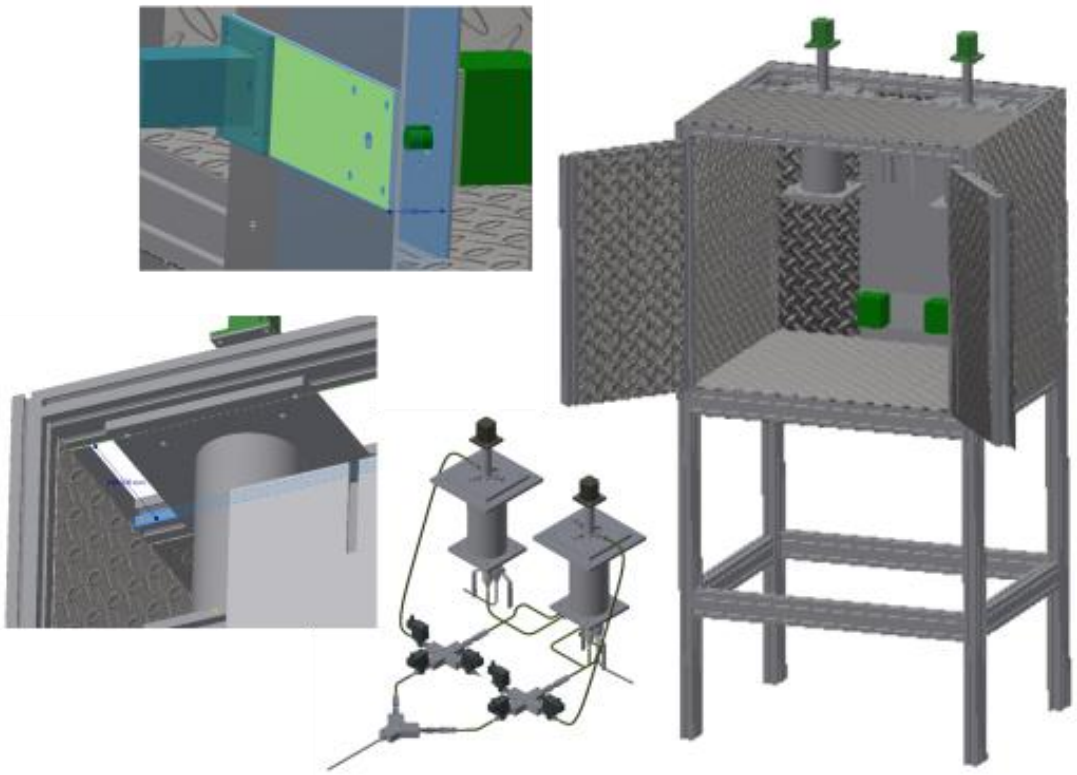

Fig. 3.13: 3D models of TP-RTM assemblies and sub-assemblies.

The frame of the TP-RTM machine was built from aluminium extrusion (30 mm x 30 mm cross section) such that the enclosure area would be 700 mm x 600 mm x 500 mm, assembled with brackets and T-nuts. The tanks were fabricated in-house from aluminium, and 3D printed high temperature reinforced polymer was used to produce the stirrer motor supports as shown in Fig. 3.14(a). The heating mats shown in red in Fig. 3.14 (b) were bonded to the tanks and the tanks were fixed to the frame. 4 mm aluminium plates were fixed to the inside (Fig. 3.14 (b)) and outside (Fig. 3.14 (c)) of the frame to support the pumps and their motors respectively. The alignment of shaft holes for these parts was important as the shafts of the pumps and motors had to be connected. Couplings with keyways and grub screws were used to transmit the torque required to drive the pumps. The convection fan was also connected to the inner plate with a 50 mm clearance between the two to allow the fan to draw air from behind. As shown in Fig. 3.14 (c), the wiring for all the electrical components passed through a slot in both plates. 1.6 mm thick aluminium sheets made up the outer and inner sides of the enclosure walls with glass wool insulation placed between the two. The wires from the stepper motors were connected to the Arduino microcontroller and motor driver as shown in Fig. 3.14 (d). Fig. 3.14 (e) shows the inside of the TP-RTM machine after the addition of the tubing, mixing blocks, check valves and solenoid valves. Thermally insulated doors were placed on the front of the machine, acting similar to the walls when closed as shown in Fig. 3.14 (f).

3.5 Heat distribution testing in enclosure

Initial tests were carried out to monitor the effects of different factors on the heating in the original TP-RTM machine. K-type thermocouples were placed at various locations in the machine to monitor temperature changes at various locations in the enclosure over time. The results are shown in Fig. 3.15. All the heaters were turned on at the same time with the PID temperature set to 100°C initially; however, the convection fan was not turned on at this point. At the time when this test was carried out, the mechanisms for sealing the doors was different to that finally used. It was suspected that large amounts of heat were escaping due to a gap. To test the effects of this, after about 700s when the temperature reached 100°C, this area was sealed using glass fibre insulation and light pressure was applied. There was a sudden jump in temperature as a result. When the fans were turned on, the enclosure temperature at the measured location fell dramatically, as colder air moved in from other areas. Even with the fan off for the first 700s, the solenoid valves farthest from the ceramic heater (purge valves A and B) reached 69°C within 30 min, as desired.

An FLIR infrared camera was used to try and identify any cold spots in the machine and some of the images captured are shown in Fig. 3.16. To take these images, the enclosure doors had to be opened and shots captured quickly prior to major temperature drops in components. The measurements taken confirmed that the enclosure was suitable for purpose and identified areas for concern, which were then addressed. Changes to the original machine at The University of Edinburgh were made incrementally to improve its heating performance. These issues were all taken into account in the second prototype design at The University of Auckland.

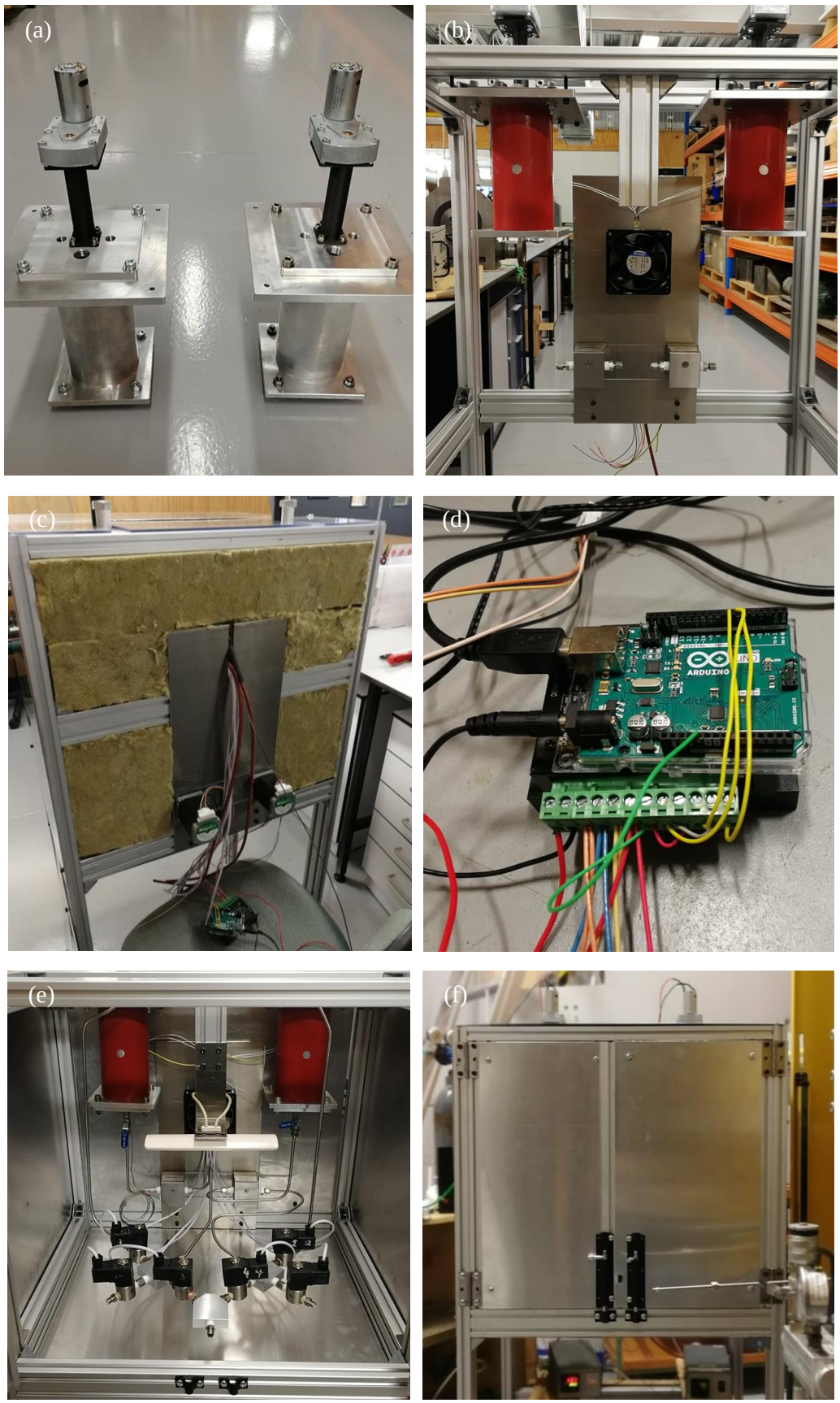

Fig. 3.14: TP-RTM machine at various points in the build phase.

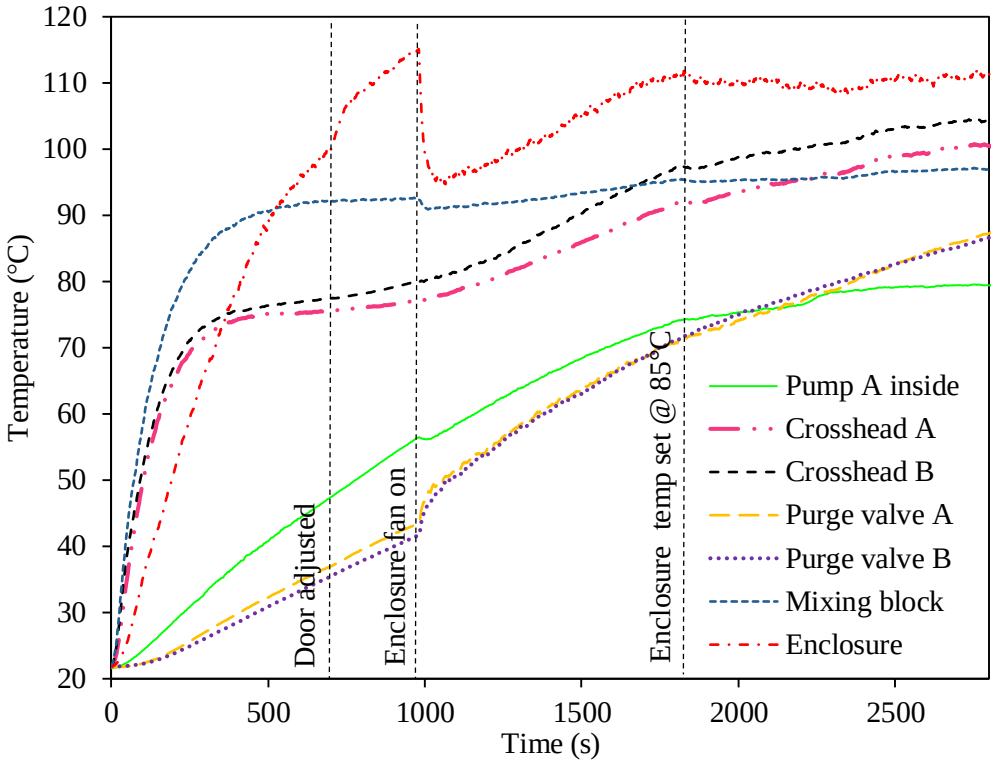

Fig. 3.15: Time-temperature data in enclosure

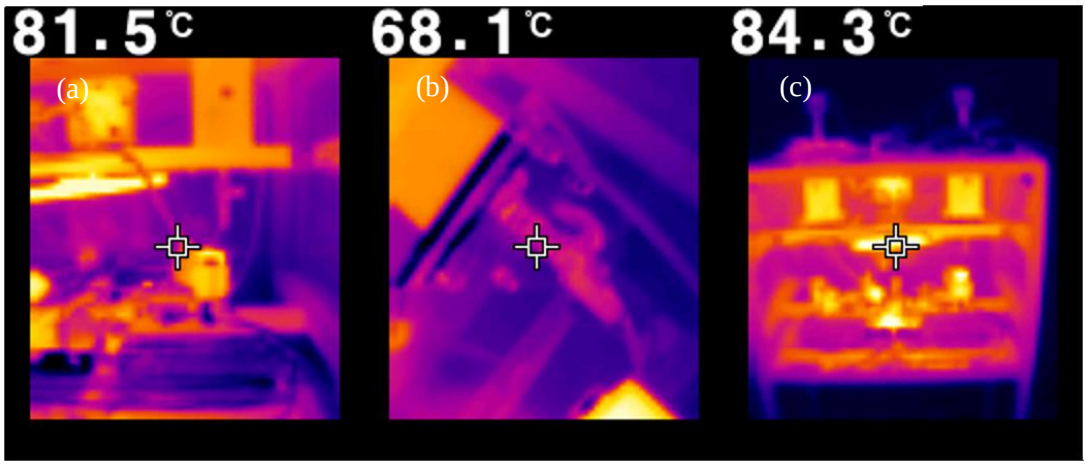

Fig. 3.16: Temperature distribution within the enclosure.

3.6 Operations for manufacturing

The system used for manufacturing consisted of the TP-RTM machine, press, mould and other interconnecting parts as shown in Fig. 3.17 The 3-way valve was introduced to bleed any air/nitrogen from the system prior to injecting into the mould. Originally, there was a regular 2-way valve as shown in Fig. 3.18 (a). This was opened as the pumps were turned on, causing a sudden change in the vacuum pressure and affecting the fine control required to find the balance between minimising voids while preventing the molten materials from boiling. To avoid this, a three way valve was introduced, as shown in Fig. 3.18 (b). The third port allowed for bleeding of the mixture into a bucket until there was consistent flow, while simultaneously bridging the air gap to the mould which previously existed. When rotated, the valve directed the flow towards the mould for injection. As can be seen at the inlet side of the mould, there was a U-bend in the pipe which was used to supply additional feedstock to the mould during shrinkage within the cavity. On the outlet side, there was a 2-way valve which would be used to restrict flow by partially closing it after filling. A vacuum catch pot was used at the outlet to prevent molten mixture entering the vacuum pump. The use of the vacuum, as well as other manufacturing details will be discussed further in section 4.2.4.

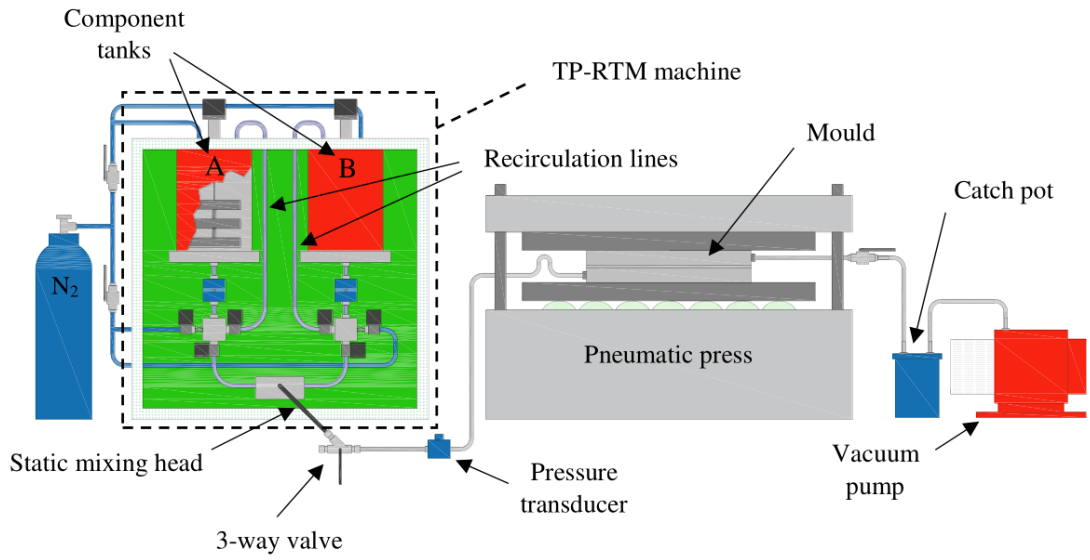

Fig. 3.17: Assembled TP-RTM setup for polymer/composite manufacture.

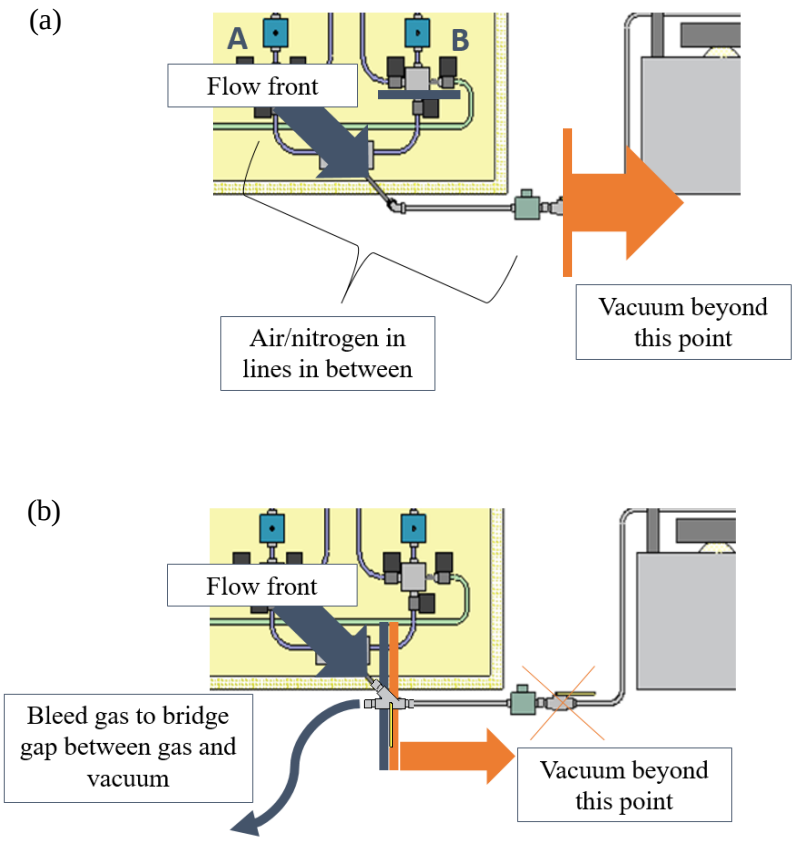

Fig. 3.18: Tubing between the enclosure and mould using (a) 2-way valve and (b) 3-way valve with bleeding.

3.7 Conclusions

Two different TP-RTM systems were designed and built to manufacture APA-6 composites. The design requirements were outlined and an analysis of the pressure and heat requirements was carried out to help make design choices. While some crude assumptions had to be made, they were sufficient from a design point of view, considering the low risk in the economic cost of trialling components. Changes to the original design were made incrementally to improve the system's performance, whereas for the second prototype, most of these changes were taken into account from the beginning. Drawings and 3D models were generated to assist with the machining, fabrication and assembly of parts. Initial testing of the equipment showed that the conservative design choices made had succeeded in allowing for composites to be manufactured with sufficient pressures and temperatures where required. One important note to be pointed out is the relatively low cost of the parts which cost ~£5000 in total; however, this does not account for technician's time and machining costs as it was built in house.

Chapter 4: APA-6 manufacture & characterisation

Summary

This chapter focuses on the manufacture and characterisation of unreinforced PA-6 produced using anionic polymerisation (APA-6). The chapter discusses the materials and methods used to produce the material as well as the chemical, thermal and mechanical analytical techniques used to characterise the polymer before progressing to manufacturing composites.

4.1 Chapter Introduction and Overview

Prior to manufacturing and investigating the behaviour of APA-6 composites, it was important to firstly consider the pure APA-6 in terms of processing and characterisation. Due to the many sensitivities of the anionic polymerisation to moisture, temperature, the reactants used and their mixing ratios, it was necessary to carefully consider which conditions were most suitable based on the desired application of APA-6 as a tough matrix. Based on literature and trial experiments carried out using the TP-RTM system, specific process parameters were decided upon such that the material's performance could be optimised.

While there is a lot of information in the literature about manufacturing APA-6 in terms of the most suitable temperatures, reactants and mixing ratios, there is a limited amount of knowledge on the effects of moisture on the mechanical performance. An initial study was carried out to determine how purging the mould with nitrogen gas affects the material performance at temperatures of 160, 170, 180 and 200 °C. The performance was measured in terms of degree of conversion, average molecular weight and tensile strength.

The distribution of thickness and density of material produced using the TP-RTM setup was determined to demonstrate shrinkage and flow effects during polymerisation within the cavity. The thermo-morphological behaviour of the material was investigated using differential scanning calorimetry. This determined the degree of crystallinity as well as the melt and crystallisation temperatures of the material. Dynamic mechanical analysis was used to determine the glass transition temperature in the material.

Finally, mechanical testing was carried out in tension, compression and flexure to determine the behaviour and performance of APA-6 compared to other materials in terms of strength, strain-to-failure, modulus and toughness.

4.2 Materials and manufacturing

4.2.1 Choice of materials and storage

The storage of the raw materials is so important in the production of APA-6 that it is discussed in depth to precisely demonstrate the measures taken in terms of quality to control a consistent process. Due to the sensitivity of the anionic polymerisation to moisture and the hydrophilic nature of the APA-6 precursor materials, extreme caution was taken to limit the exposure of the raw materials to moisture. The main component in the production of cast polyamide is the caprolactam monomer, which was kindly supplied by Brüggemann GmbH & Co. KG (Heilbronn, Germany) under the brand name AP-NYLON® Caprolactam. The caprolactam, contained within aluminium lined sacks had a water content of <100ppm in its supplied form, making agglomeration less likely. Each 25 kg caprolactam sack, once opened, was stored in a large HDPE drum with a silicone sealed airtight lid. Upon sealing, the drum was purged with nitrogen gas to replace air present. A perforated container with silica desiccant beads was placed alongside the bag in the sealed drum to dominate the uptake of moisture so as to keep the caprolactam dry. The other reactants used in the production of APA-6 were the activator and catalyst which were also provided by Brüggemann GmbH & Co. KG. The activator component (brand name BRUGGOLEN® C20p) is a bi-functional activator/caprolactam blend supplied in pellet form, consisting of ~80: 20 wt% hexamethylene-1,6-dicarbamoylcaprolactam (HDCL) : caprolactam. The catalyst component (brand name BRUGGOLEN® C10) is a catalyst/caprolactam blend supplied in flake form, consisting of consisting of ~20:80 wt% sodium-caprolactamate (NaCL):caprolactam. The choice of activator and catalyst was based on literature, their suitability for fairly rapid polymerisation and suitability for RTM style processes [35]. Both of these were stored in sealed aluminium lined sacks, contained in a glass desiccator at room temperature. Quantities of caprolactam, activator and catalyst for between 4 and 8 injections were weighed out at a time to reduce the exposure time of each to moisture. The measured quantities were stored in sealed glass powder jars with small silica bags. The chemical structure of each component is given in figure 4.1. The various reactions involved in polymerisation are given in Appendix B.

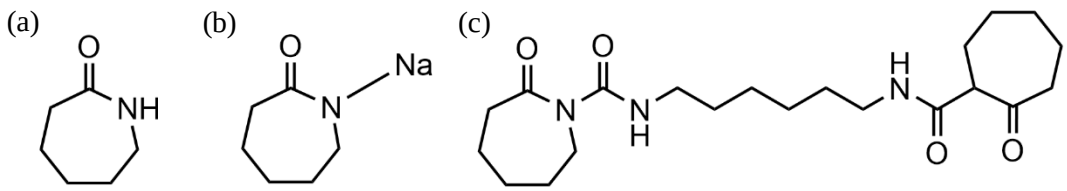

Fig. 4.1: Chemical structure of (a) caprolactam, (b) catalyst and (c) activator.

Table 4.1: Raw material components used in APA-6 polymerisation.

Matrix System	Component Brand Name	Component Type	Molecular weight (g/mol)	Density (g/cm^3)
APA-6	AP-NYLON® Caprolactam	Monomer	113.160	1.01
	BRUGGOLEN® C20p	Activator	394.508	1.2
	BRUGGOLEN® C10	Catalyst	135.139	1.124

4.2.2 Choice of mixing ratios and processing temperatures

The concentration of the monomer, catalyst and activator used during polymerisation massively affects the average molecular weight, rate of reaction, degree of conversion and degree of purity. The effects of changing the concentrations of each component is demonstrated in Fig. 4.2 with each case described below.

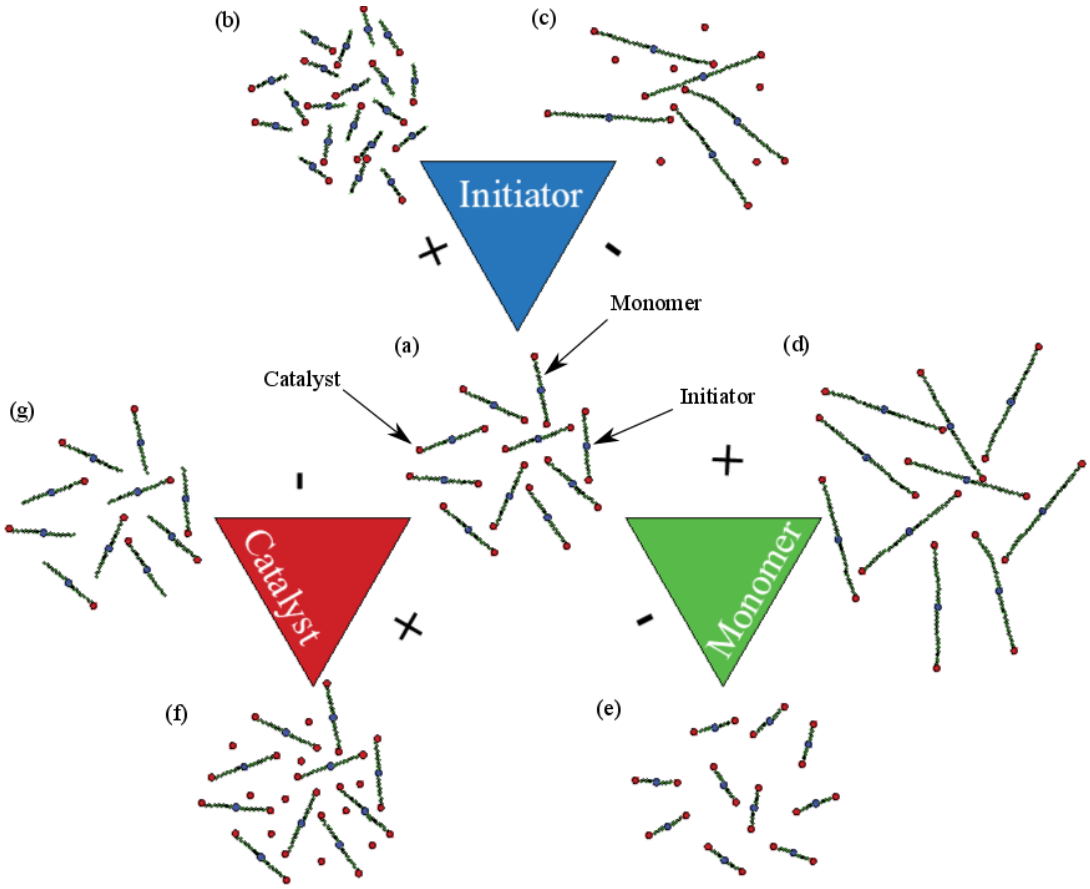

Fig. 4.2: Theoretical demonstration of how changing the mixing ratio of monomer, catalyst and activator affects the product in an ideal scenario.

Activator:

- Higher concentrations → larger number of chains, lower average molecular weight, slower reaction speed due to lower C:A ratio (Fig 4.2 (b)). This is associated with reduced material toughness [27], [55], [58], [111], . Higher quantities are also associated with increased amounts of oligomer content which is an impurity and so, reduces the degree of conversion slightly [56].
- Lower concentrations → reduced number of chains, higher average molecular weight, faster reaction speed due to higher C:A ratio (Fig 4.2 (c)). This is associated with higher material toughness.

Monomer:

- Higher concentrations → No change in number of chains, higher average molecular weight, longer time required for full conversion to occur (Fig 4.2 (d)).
- Lower concentrations → No change in number of chains, lower average molecular weight, less time required for full conversion (Fig 4.2 (e)).
- In reality, the longer the polymer chain, the more inhibited further chain growth becomes due to increasingly restricted mobility of reactants.

Catalyst:

- Higher concentrations → No change in number of chains, slightly lower degree of conversion, slightly lower molecular weight, faster reaction speed due to higher C:A ratio (Fig 4.2 (f)).
- Lower concentrations → No change in number of chains, slightly higher degree of conversion, slightly higher molecular weight, slower reaction speed due to lower C:A ratio (Fig 4.2 (g)).
- As the catalyst isn't consumed in the reaction, it doesn't make up part of the polymer structure and such, excessive concentrations result in a higher level of impurity in the product. This includes quantities of cationic sodium from dissociation of the catalyst. These sodium cations react with caprolactam anions (H- atoms), which transform the caprolactam to catalyst [13]. This causes a higher reaction rate, an even further reduction in conversion due to the higher amount of impurities in the product and causes a reduced average molecular weight due to less caprolactam available for chain growth. Contrary to this however, a deficiency in catalyst levels could cause premature termination, resulting in lower conversion.

Note that the above is a general rule-of-thumb and in reality, other effects come into play when the mixing ratio concentrations are varied significantly. The reaction is autocatalytic in nature and as a result, too high a catalyst concentration can result in excessive heat which can hinder the polymer quality during polymerisation.

Project partners, Johns Manville, carried out trial tests on APA-6 properties using fibre reinforcements which indicated that a mixing ratio of 98.2 mol% caprolactam, 0.6 mol% bi-functional activator and 1.2 mol% catalyst produced the most desirable results at a mould temperature of 160°C. This temperature value was also shown by van Rijswijk to offer high strength and high strain-to-failure, indicating good toughness [13], [35]. With regards to mixing ratios, it would make sense theoretically that there are double the number of catalyst-to-activator molecules. The bi-functionality of the activator allows chain growth from both ends of the molecule. Having one catalyst molecule for each growing chain end at any given time means conversion can happen at the highest rate possible without using excess catalyst and hence, reducing the purity of the polymer. While the concentration of both activator and catalyst are slightly less than those reported in much of the literature discussed in section 2.5.1, it would theoretically result in less impurities in the material.

4.2.3 Gravitational casting of APA-6

Prior to the development of the TP-RTM machine and mould described in Chapter 3, a simple setup was used to cast pure APA-6 plates for the determination of nitrogen effects on properties. A three-part gravitational mould shown in Fig. 4.3 was used and consists of two aluminium mould surfaces and a cavity frame all held together by 16 fastened bolts along the periphery of the mould. Electrical heaters are fixed to the back of each mould surface and are controlled by a PID controller. The mould frame allows it to be positioned at a 45° angle during processing. Inlet and outlet feed spouts are fixed to the mould such that the inner spout is elevated higher than the outlet spout, indicated by Δh in Fig. 4.3. This allows for any air present in the cavity to be evacuated ahead of the flow front rising from the lower side of the mould. The mould temperature was set and time was given to allow the spouts to heat sufficiently so that the molten mixture wouldn't freeze during filling.

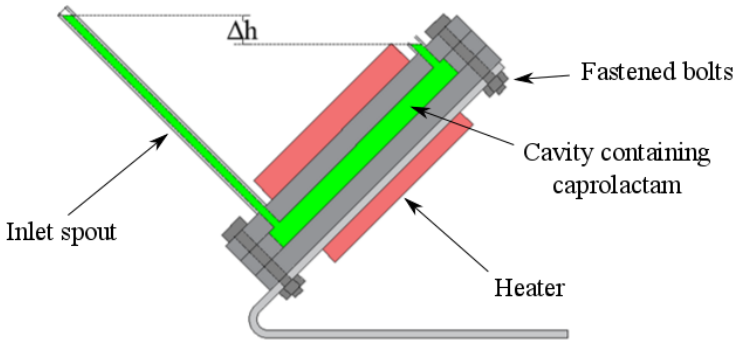

Fig. 4.3: Three-part gravitational mould for casting of APA-6.

The precursor materials were split in a 1:1 ratio by volume to form an A and B component so that the activator and catalyst could be separated in a mixture of caprolactam respectively during heating. In order to measure the quantities, weight measurements were taken based on known material densities. Each of the two components were crushed using a pestle and mortar into a fine powder in order to increase conductivity through the materials such that exposure times could be reduced during heating. The components were poured into glass vials with aluminium covers and each heated in an oven up to 110°C. Boiling water vapour (steam) from the air was allowed to escape through a vent in the oven, and this, to a large degree, protected the components from moisture absorption. As such, nitrogen was not required at this stage.

Many polymerisation permutations were carried out to determine polymer quality at mould temperatures of 160, 170, 180 and 200°C, both with/without nitrogen purged through the mould system. The A and B components were mixed in the oven using a stirrer for several seconds and then poured into the inlet spout to fill the mould from the bottom up until the molten mixture was seen at the outlet of the mould. At this point, both the inlet and outlet spouts were bunged to reduce air exposure during polymerisation. The mixture was then held to temperature for 15 minutes during polymerisation, after which, the heaters were turned off to allow the mould to cool.

4.2.4 TP-RTM casting of APA-6

With the exception of the study on the effects of nitrogen, all remaining polymer panels were manufactured using the TP-RTM setup described in Fig. 3.17. The TP-RTM mould surfaces, inlet and outlet were cleaned using acetone, and two layers of mould release agent (Loctite Frekote 55NC) were applied. All monomer residue from previous runs was dissolved from the aluminium tubes and ball valves using hot water at around 90 °C followed by air drying in an oven at 110 °C. A 4 mm cavity piece was used such that the thickness of the material produced

would be in line with test standards. The upper mould surface was placed on top of the other mould parts to close the cavity. The gap created by the seals was investigated along the perimeter to ensure that the flat surfaces were clear of any foreign objects which could prevent full contact between them after application of pressure. The assembled mould was placed between the platens of the pneumatic press, and the aluminium tube for the outlet was secured to the mould with the valve and vacuum accessories connected. The aluminium tube, sensor, and 3-way valve were connected at the inlet side of the mould. The valve was initially positioned to shut off flow such that the cavity could be used as a vacuum chamber during drying. The vacuum pump with a pump rate of 330 l/min was turned on, pressure was applied to the mould, and the platens were heated to 160 °C. The cavity now acted like a vacuum chamber, such that moisture was eliminated sufficiently for polymerisation. The vacuum pressure was monitored with the sensor at the inlet and from the pressure gauge on the catch pot at the outlet. Typical gauge pressure readings of around - 990 and -980 mbar respectively indicated that a sufficient vacuum was achieved. A bigger difference between the 2 readings often indicated leaking across the mould/tubing. Leaks may occur if the silicone seals are worn, fittings aren't tightened correctly or if foreign objects get trapped between the mould surfaces. Leaks present in the mould would lead to air entering the cavity and cause voids in the final part as a result.

The local tank temperatures were set to 90 °C and the global temperature of the enclosed parts was set to 90 °C. The system was flushed with caprolactam before each run to remove any moisture that may have been present on the inner walls of the machine components. Precursor materials consisting of 98.2 mol% caprolactam, 0.6 mol% bi-functional activator and 1.2 mol% catalyst were poured into the component tanks. The stirrers were turned on and the tanks were purged with nitrogen gas to create an inert atmosphere while heating. The vacuum was then reduced such that the absolute pressure in the mould was just higher than the vapour pressure (53 mbar) of the precursor components at the exothermic temperature peak (~170 °C), but sufficiently low to prevent large amounts of air entering the mould and hence oxidising the sizing [137].

The effects of not reducing the pressure causes the mixture to boil and significantly hinders (or completely terminates) polymerisation. Examples of this are demonstrated in Fig. 4.4, in which case it is believed that partial conversion occurred while boiling, leaving behind residue. Nitrogen was purged through the component lines and the mixing head and exited through the bleed port of the 3-way valve in order to purge the liquid precursor carrying components which were not under vacuum. The components that were now melted in the tanks were then recirculated, followed by injection at a flow rate of 820 ml/min. In order to bridge the gap

between the liquid precursor flow front and the vacuum, the air/nitrogen gas mixture in front was bled through the bleed port of the 3-way valve until a consistent flow was observed, at which point the valve was adjusted such that the flow was directed into the mould. When the mixed liquid precursors reached the mould outlet, the ball valve at the outlet was manually adjusted to partially restrict the flow such that the pressure increased to ~4 bars while still flowing. After holding for several seconds, the valve at the outlet was shut, then the inlet valve was closed, and finally the pumps were turned off.

15 minutes after injection, the heating to the platens was turned off but the pressure was maintained such that both sides would cool naturally at the same initial rate of approximately 2.7 °C/min to minimise thermal stresses.

Fig. 4.4: Example of boiling mixed precursor residue caused by cavity pressure drops below that of the caprolactam vapour pressure at ~ 170°C.

4.2.5 TP-RTM process improvements

Visual observation of earlier parts produced showed a number of shrinkage induced voids across the material even though the surface was generally very smooth otherwise. These were distinguishable by their shape and size. Those on the right hand side of the plate shown in Fig. 4.5 (a) were due to a lack of available molten feedstock locally during polymerisation as the surrounding areas had already polymerised first. It should be noted that a larger number of smaller voids occurred at the inlet side of the mould, shown in Fig. 4.5 (b). These were due to polymerisation within the inlet itself which dragged material from the mould cavity back as feedstock, resulting in a poorer surface. This was clear from the high degree of directionality of these voids towards the inlet. An initial attempt to overcome this issue involved introducing a U-bend at the inlet side as shown in Fig. 3.17. Because the crest of the U-bend was at a higher elevation than the inlet, it was believed that this would supply the feedstock required in the inlet rather than dragging it back from the cavity. This didn't solve the problem alone, however, as the feedstock froze before polymerisation was complete as the U-bend wasn't

heated or insulated. The problem was mostly improved by adding layers of insulation to the tubes transferring the liquid precursors and maintaining the application of pressure until polymerisation was complete. Because the mixture was heated to 90 ℃ prior to injection, the material had a 31°C temperature window to fall before freezing. Fig. 4.5 (c) shows what occurred when entrapped gas is present in the liquid precursors. This however, only occurred when air leaked into the filled cavity while under vacuum. When leaks were sealed completely, this didn't occur, hence discounting the theory that the voids may be due to the release of dissolved gases.

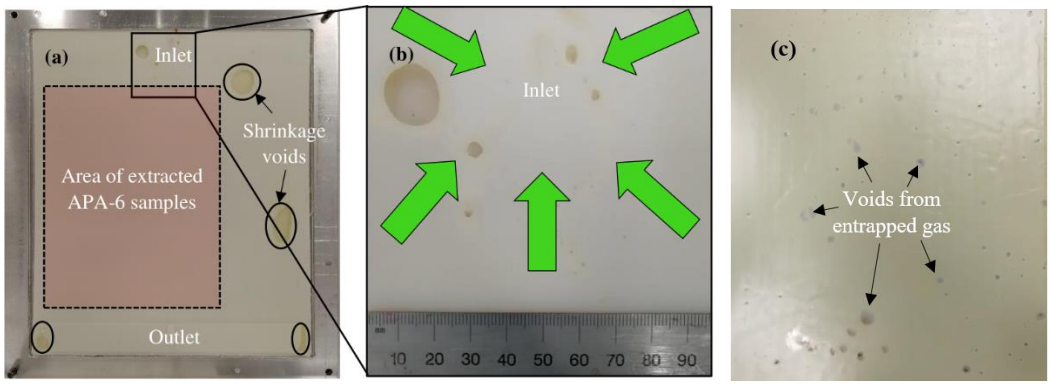

Fig. 4.5: (a) Image of an APA-6 plate in the mould cavity, (b) a close-up view of voids due to shrinkage around the inlet of the mould and (c) voids due to entrapment of gas.

4.3 Analysis and testing

4.3.1 Quality improvement

A particular emphasis was placed on quality control and improvement in terms of accuracy and consistency of the process. During a six-sigma style improvement process, a thorough method for establishing quality was put in place. These were measured in terms of part thickness, density, void content and glass transition temperature. For every part manufactured, a quality assurance form (see Appendix C) was completed after a range of these less time consuming tests were carried out, quoting the average result and standard deviation for each. Due to the complexity of the setup, measurements such as degree of conversion and viscosity average molecular weight were not taken for all samples.

4.3.2 Sample preparation

Due to the complex dumb-bell shape of the tensile specimens, a computer numerical control (CNC) machine was used to cut the specimens. A spindle speed of 5000 RPM was used. Initially a solid carbide cutter was used at a feed rate of 60 mm/min, however due to the

toughness of the polymer, melting occurred even with the application of coolant, causing the cutter to jam. To solve the problem, an increased feed rate of 230 mm/min was used with a high speed steel cutter which gave a clean finish without indications of melting. The rough edged surface resulting from the lower cutting speed is shown in Fig. 4.6 (a) and that of a finely cut specimen is shown in Fig. 4.6 (b).

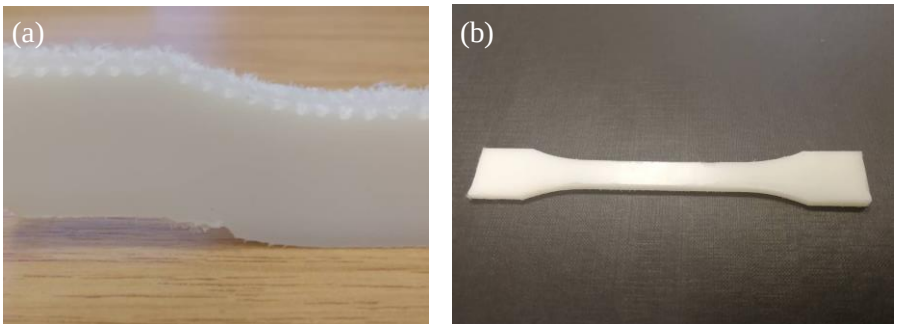

Fig. 4.6: APA-6 parts cut using (a) a low feed rate, which resulted in a rough surface and (b) a high feed rate, which resulted in a smooth surface.

Due to their simple rectangular geometry, samples for all other test types were cut using a diamond blade cutting saw with coolant at a feed rate of ~300 mm/min with the exception of differential scanning calorimetry (DSC) samples, which were cut using a Stanley knife blade. All samples were then dried under vacuum for 24 h at 50 °C and stored in polybags with desiccant until testing.

4.3.3 Thickness and density distribution

Thickness measurements were taken at 25 points distributed evenly in a 5 x 5 pattern across each part produced. Measurements were taken using a Kroeplin Digital C450 thickness gauge, accurate to 0.02 mm. Density measurements were taken for 15mm x 15mm samples extracted from 9 locations evenly distributed across each part in accordance with *ISO 1183-1:2019 Method A.* To measure the density, the mass of each sample was recorded using an OHAUS AX324 analytical balance. This was followed by measuring the apparent mass in water using a density determination apparatus as shown in Fig. 4.7. The setup consists of beaker of distilled water placed on a platform. An overhanging bracket is supported by the scale so that any vertical loading to the bracket is measured by the scale. From this, a sample holder was hung with its free end submerged in the distilled water. After zeroing the setup, each sample was added to the holder and the apparent mass of each was recorded from the scale. Archimides' Principle was used to determine the density of the material based on apparent mass in water, actual mass (in air), air density and water density. As the density of the water is dependent on the temperature, a thermometer was placed in the water and the temperature was monitored.

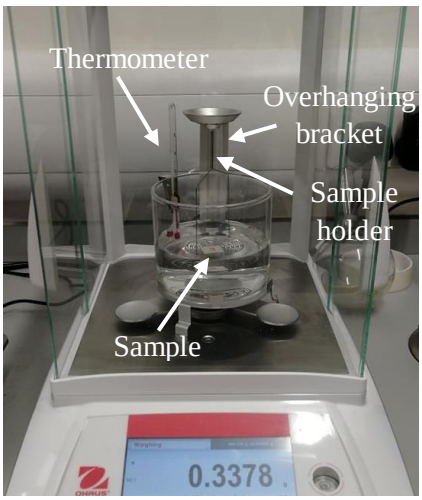

Fig. 4.7: Setup for measurement of apparent mass in water for polymer specimens, a key step required for determination of density.

4.3.4 Degree of conversion

While the product is referred to as PA-6, the material is not 100% polymer and in reality, contains a degree of impurities in the form of unreacted monomer, low MW oligomer and residue catalyst which isn't consumed in the reaction. This occurs for reasons mentioned in section 4.2.2 as well as the presence of small amounts of moisture which hinder the degree of conversion to polymer. In order to determine the amount of monomer converted to polymer, a reflux method was used to extract unreacted impurities from the product. As the reactant materials can be dissolved in water but PA-6 cannot, water can be used to extract or "wash out" the remaining reactants from the product. Firstly, the manufactured parts were ground into small shavings using a CNC machine such that the surface area to volume ratio was maximised. The ground particles were then placed under vacuum in an oven for 24 hrs at 50 ℃ to remove moisture. A round-bottom flask was placed in the analytical balance and zeroed. Approximately 10 g of the dried shavings were placed into the flask and the mass recorded. The flask was then filled with distilled water above the level of the shavings and was placed in a heating mantle to boil the water. A condenser was connected to the flask to prevent evaporation of the boiling water and maintain the reflux cycle. In the meantime, a bowl with a filter was weighed and zeroed on the balance. The reflux sample was removed after 24 hours and poured through the filter which allowed the water solution to pass into the bowl but not the solid material. The impurities extracted during this process are dissolved in the water and so are removed in the process. The sample was then oven dried to remove the remaining moisture after draining. Where m_m is the mass lost during extraction and m_t is the mass before

extraction, the degree of conversion can be calculated using Equation 4.1. The process steps are shown in Fig. 5.8.

$$DC \approx 100 \times \{1 - [m_m/m_t]\} \quad (4.1)$$

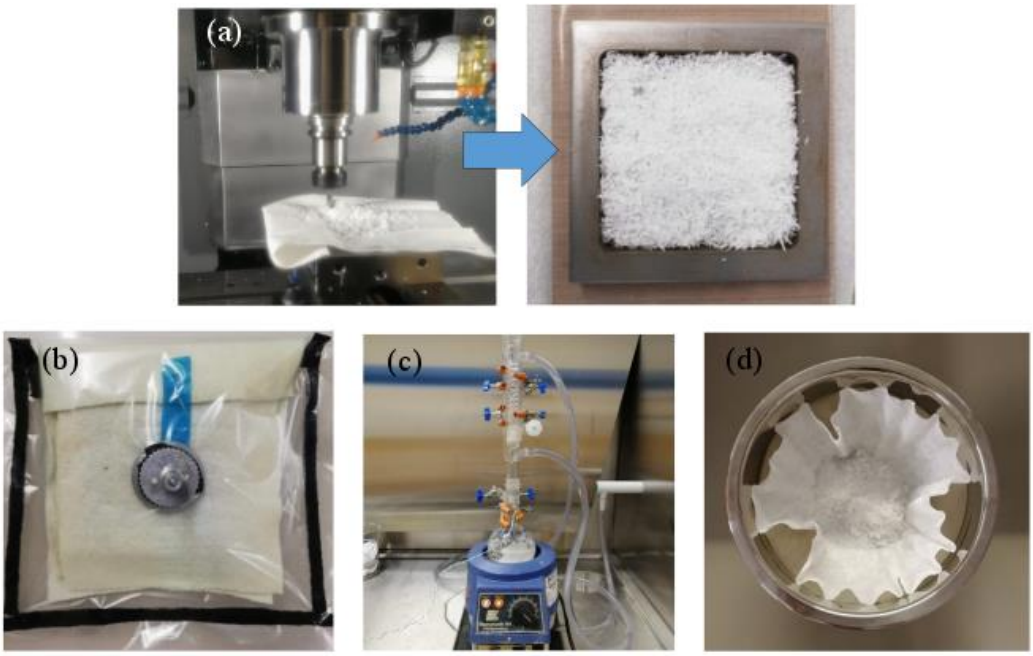

Fig. 4.8: Images of some of the the main procedures required in determining the degree of conversion including (a) grinding, (b) vacuum bagging, (c) refluxing and (d) filtering.

4.3.5 Dilute solution viscometry

For most standard thermoplastics, the average molecular weight (MW) and polydispersity (Đ) can be determined using a technique known as gel permeation chromatography (GPC). For this process, the polymers are typically dissolved in an appropriate solvent and passed through columns which separate chains based on their size (MW). However, due to the chemical resistance of PA-6 to most solvents which are compatible with GPC apparatus, this method cannot be used. As such, dilute solution viscometry (DSV) was used to approximate the *viscosity average molecular weight* (M_v). The technique involves measuring the change in viscosity of a solvent due to the addition of the polymer and determining the time (t) taken for the solution to pass through a glass capillary viscometer compared to that of the pure solvent (t_0). Where c is the concentration of the polymer solution, the inherent viscosity (η_{inh}) can be defined as given in Equation 4.2 [147].

$$\eta_{inh} = \frac{ln\left(\frac{t}{t_0}\right)}{c} \quad (4.2)$$

The intrinsic viscosity, which measures the polymer's contribution to the viscosity of a solution is related to M_v by the Mark-Houwink relationship given in Equation 4.3. The $K'$and p terms are the Mark-Houwink constants given as 5.92×10^{-4} dl/g and 0.69 respectively [58].

$$\eta_{int} = K' M_v^p \tag{4.3}$$

It is assumed that the intrinsic and inherent viscosities are approximately equal and therefore, the viscosity average molecular weight can be calculated using equation 4.4.

$$M_v = \left[\frac{ln\left(t/t_o\right)}{c}\right]^{1/p} \tag{4.4}$$

Preparing the polymer solution involved taking a batch of pure polymer, having removed the impurities using the reflux method described in section 4.3.2, and drying for 24 hrs under vacuum at 50 °C to remove moisture. The pure polymer sample was weighed in a glass beaker on an analytical balance. Sulphuric acid with a concentration of 40 w/w % in water was added to the beaker such that the concentration of polymer in the solution was 0.5 g/dl and the solution was mixed thoroughly with a glass rod until fully dissolved.

The setup for the solution viscometry measurements is shown in Fig. 4.9. The ubbelohde viscometer was cleaned with acetone which was allowed to evaporate prior to use. Using a pipette, the solution was transferred to the viscometer. The digital timer assembly was attached to the viscometer and it was then placed in a tank of water to maintain a constant temperature. The experiment was initiated and the t values were recorded for each run. This was repeated for the 40 w/w % sulphuric acid without the polymer dissolved in order to calculate t_0.

Fig 4.9: Setup for viscometry measurements.

4.3.6 Differential scanning colorimetry

Differential scanning calorimetry (DSC) was used to determine the degree of crystallinity of the polymer product, the melt temperature and the crystallisation temperature range. Due to the difference in properties between the amorphous and crystalline phases, it was important to measure the degree of crystallinity. When semi-crystalline polymers are melted, their highly structured crystalline phase comes apart allowing the chains to move freely, causing the polymer to flow [58]. When this phase change occurs, additional energy is absorbed which causes a noticeable spike in the relationship between endothermic heat flow and temperature. This is the phenomenon on which the concept of differential scanning calorimetry is based to measure the degree of crystallinity. A sample is placed in a pan, while another pan containing no polymer is used as a reference. Both are placed in a DSC apparatus which heats the samples at a constant temperature rate, providing the heat energy required to maintain this rate. Both temperature and heat flow are measured. The difference in behaviour between the pans can be attributed to phase changes in the polymer. The degree of crystallinity (X_c) in the material can be determined from the ratio of the polymer's enthalpy of fusion (ΔH_m) to that for pure crystalline PA-6 (ΔH_c). Taking into account the fact that the product is not 100% pure polymer, the degree of conversion should be considered. The corrected method for determining the degree of crystallinity is given in Equation 4.5.

$$X_c = \frac{\Delta H_m}{\Delta H_c} \times \frac{1}{DC} \tag{4.5}$$

A Perkin Elmer DSC was used to determine the degree of crystallinity of APA-6. Small samples of approximately 5 mg were used, each weighed and then placed in pans which were crimped prior to being placed in the DSC pan holder along with the reference pan. The test began with a 2 min isotherm at 25 ℃ followed by heating at a rate of 10 ℃/min up to 250 ℃. The samples were then cooled at a constant rate of 10 ℃/min such that the recrystallisation temperature range could be observed. An enthalpy of fusion value of 190 J/g for 100% crystalline PA-6 was used in Equation 4.5 as reported in the literature [65].

4.3.7 Dynamic mechanical analysis

Dynamic mechanical analysis (DMA) was used to determine the glass transition temperature (T_g) of the polymer. This can be determined by applying sinusoidal displacement to a material as it is heated while monitoring the modulus of the material. The viscoelastic properties of a polymer change above a specific temperature known as the glass transition. This change occurs as a result of increased chain mobility in the amorphous phase, which causes the material to

go from a hard glassy state to a soft rubbery state [58]. The storage modulus (E') is a ratio of a material's elastic stress to strain, while the loss modulus (E") is a ratio of a material's viscous (out of phase) component of stress, which is related to its ability to dissipate that stress in the form of heat. The degree of damping is indicated by the ratio of E" to E', otherwise known as Tan δ as given in Equation 4.6. By plotting Tan δ with respect to temperature, the glass transition temperature (T_g) can be identified by a noticeable peak in the relationship, at which point the storage modulus has dropped and the loss modulus has increased.

$$Tan\ \delta = \frac{E''}{E'} \tag{4.6}$$

A single cantilever bending configuration was used for the APA-6 samples in accordance with ISO 6721-5:1996 on a Triton 2000 DMA. Three 10 mm x 35 mm samples from each plate were tested using a 20 mm free-length for the polymer samples with a displacement of 0.05 mm. The samples were dried under vacuum for 24 hours at 50 °C prior to testing. The test was run at frequencies of 1Hz and 10 Hz from room temperature up to 180 °C at a ramp rate of 5 °C/min. The T_g was determined by the peak in loss modulus as opposed to the storage modulus inflection point as the latter was difficult to define accurately from the test data. The temperature at which the Tan δ peak occurred ($T_{tan\,\delta}$) was also recorded.

4.3.8 Tensile testing

Tensile tests were carried out in accordance with BS EN ISO 527-1:2012 using type 1B dumb-bell shaped specimens. The tests were carried out on a screw-driven Instron 3369 test machine with a 10 kN load cell and mechanical wedge grips as shown in Fig. 4.10 (a). A crosshead speed of 1 mm/min was used and an IMETRUM video gauge was used to track strain. In order to track change in length using the video gauge, a speckled pattern was dotted along the gauge length of the specimen with a fine black marker to optimise the contrast. Due to the high strain to failure of the polymer, strain could not be tracked far into the plastic region. Nominal strain values at break had to be determined from crosshead extension measurements with respect to gauge length. These values were correlated with those measured using the video gauge in the linear region such that a compliance factor could be used to more accurately approximate strain at failure.

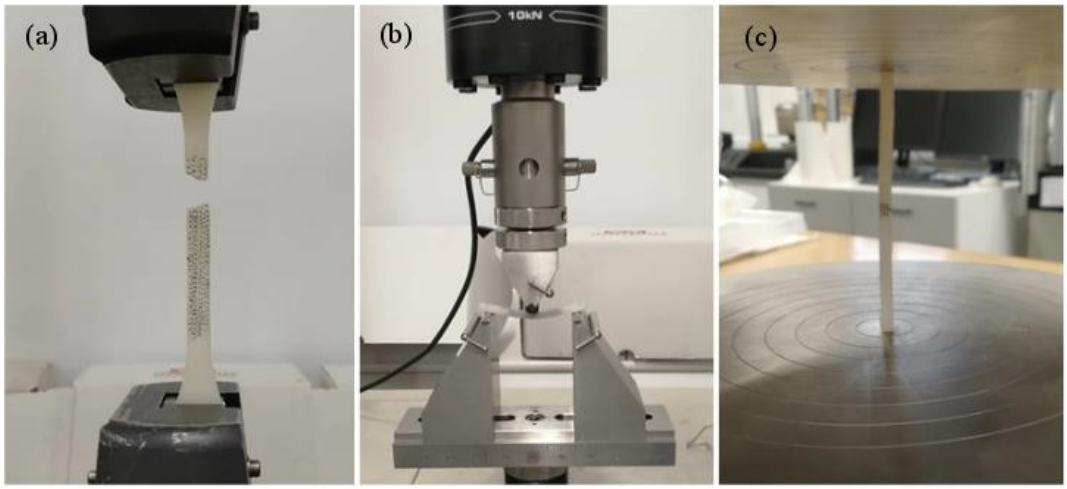

Fig. 4.10: Mechanical test setup for (a) tension, (b) flexure and (c) compression.

4.3.9 Flexural testing

Three-point bending tests were carried out in accordance with BS EN ISO 178:2010+A1:2013 using the recommended loading support and nose radii of 5 mm for specimens greater than 3 mm in thickness. A span of 64 mm was used between the two supports and the specimens were 80 mm long and 10 mm wide. The tests were carried out on a screw-driven Instron 3369 test machine with a 10 kN load cell as shown in Fig. 4.10 (b). The mid-span deflection was tracked using the IMETRUM video gauge. To do so, a tracking point was marked on the front edge of samples at their centre and a reference point was taken on the lower fixture. The change in distance between the two over time was used to determine the mid-span deflection. These values were used to determine the flexural modulus. A crosshead speed of 2 mm/min was use and samples were tested to approximately 9 % flexural strain, at which point the samples came into contact with the fixture. It should be noted however that the stress-strain data isn't valid beyond 5 % flexural strain according to the standard, however the tests were continued to observe failure progression.

4.3.10 Compression testing

Compressive tests of the pure polymer were carried out in accordance with BS EN ISO 604:2003 using type A (50mm x 10mm x 4mm) and type B (10mm x 10mm x 4mm) specimens for determining modulus and strength respectively. The tests were carried out on an MTS C45.305 machine between compression plates. Modulus specimens were coated with a speckled pattern using a fine black marker to create contrast to the cream coloured specimens

such that strain measurements could be measured using an IMETRUM video gauge and were tested at 1 mm/min in the elastic region. The strength specimens were tested at 5mm/min. until maximum strength was reached, at which point their load bearing capacity dropped until the test was stopped. Nominal strain values at break were determined from crosshead extension measurements with respect to gauge length.

4.4 Results and discussion

4.4.1 Thickness and density distribution

Measurements taken at 25 locations in laminates used in this study determined a thickness of 3.83 ± 0.07 mm using the thickness gauge excluding the areas with shrinkage voids. Even though the cavity was 4 mm thick, the final part size was less due to shrinkage, especially towards the centre of laminates as shown in Fig. 4.11 (a). This was possibly due to two different reasons. Firstly, the areas close to the edges were more likely to polymerise first as they were in contact with the cavity frame walls, particularly towards the outlet side which was heated first [148]. It is possible that the polymer from the centre fed into these areas initially as shrinkage occurred, leaving less material when the centre polymerised. Secondly, the thickness is less around the inlet which is a clear indication of drag towards the inlet due to reasons described in 4.2.4. It also seems that there was a slight change in thickness diagonally from position (0, 0) mm to (200, 200) mm. This was likely due to the mould not being perfectly level.

The density was measured in 9 locations across laminates, showing an average values of 1.147 ± 0.002 g/cm^3. Generally, a higher density would indicate a higher molecular weight and/or degree of conversion. It seems from Fig.4.11 (b) that the material towards the outlet side, is that with the lowest density while the opposite is true towards the inlet side. It should be noted that the precursor material temperature was at 90 °C while the mould temperature was 160 °C. It is possible that even though the thermal mass of the mould is much greater than that of the precursors, the temperature on the mould's inner walls is likely to drop to a degree due to contact with the flow of the mixture as it passes. As such, the material towards the inlet side likely experiences slightly lower temperatures initially. Even though the rate of chain growth is higher at higher temperatures, crystallisation is less. Because the density of crystalline PA-6 is higher than that of amorphous PA-6, the higher material density in the cooler areas can be explained.

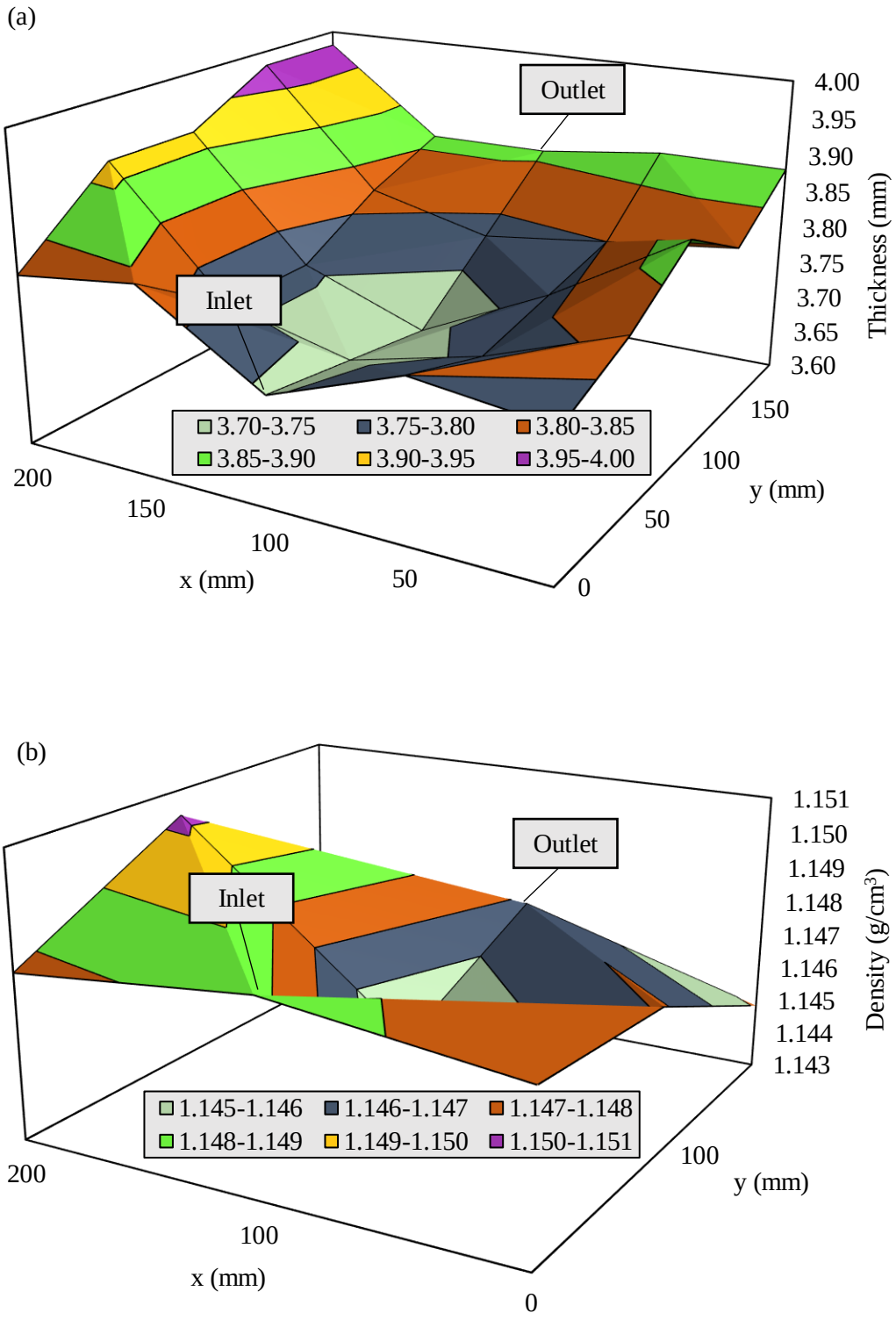

Fig. 4.11: Distribution of (a) thickness and (b) density with (x, y) co-ordinates given.

4.4.2 Effects of nitrogen and temperature on APA-6 properties

The effects of nitrogen purging in the mould cavity and interconnecting parts on the degree of conversion and viscosity average molecular weight was studied in samples manufactured using the gravitationally filled casting approach described in section 4.2.3. The results are presented in Fig. 4.12. Theoretically a living anionic polymerisation such as this one has no formal termination step but growth is restricted by depletion of monomer locally. The presence of water molecules in the air due to moisture can react with the active chain ends or caprolactam to terminate chain growth or prevent available monomer respectively. The nitrogen purge replaces the air which contains water, and so, chain growth is less likely to be hindered by moisture before reaching depletion. The results indicate that there is a clear increase in both the average molecular weight and degree of conversion with increased temperature. The effects of the nitrogen purge on both properties is apparent, particularly at 160 °C which shows a difference of almost 3% in conversion. It seems that the effects of purging however are not as significant above 180 °C. This may be due to the fact that at higher temperatures, polymerisation occurs exponentially faster due to the autocatalytic effect and so, there is less time for interactions with moisture. While the mould and delivery system used for the TP-RTM setup is different, this indicates the importance of nitrogen purging.

With regards to the tensile strength results shown in Fig. 4.13, there is a clear difference in strength between the samples purged with and without nitrogen at 160 °C but not so much at higher temperatures. This matches with observations seen in Fig. 4.11 with the exception of the strength values at 170 °C. While the molecular weight and conversion for the samples produced at 170 °C are lower than at 180 °C and 200 °C, the reason for the increased strength is likely due to a higher degree of crystallinity at lower temperatures.

While a mould temperature of 170 °C was shown to have the highest strength for the gravitational mould setup, this was not necessarily the best temperature to process at. It was found from trial mechanical tests carried out on materials manufactured using the TP-RTM system that a mould temperature of closer to 160 °C was required to deliver sufficient toughness (based on area under the stress-strain curves) to justify using a thermoplastic matrix, without significantly sacrificing the strength.

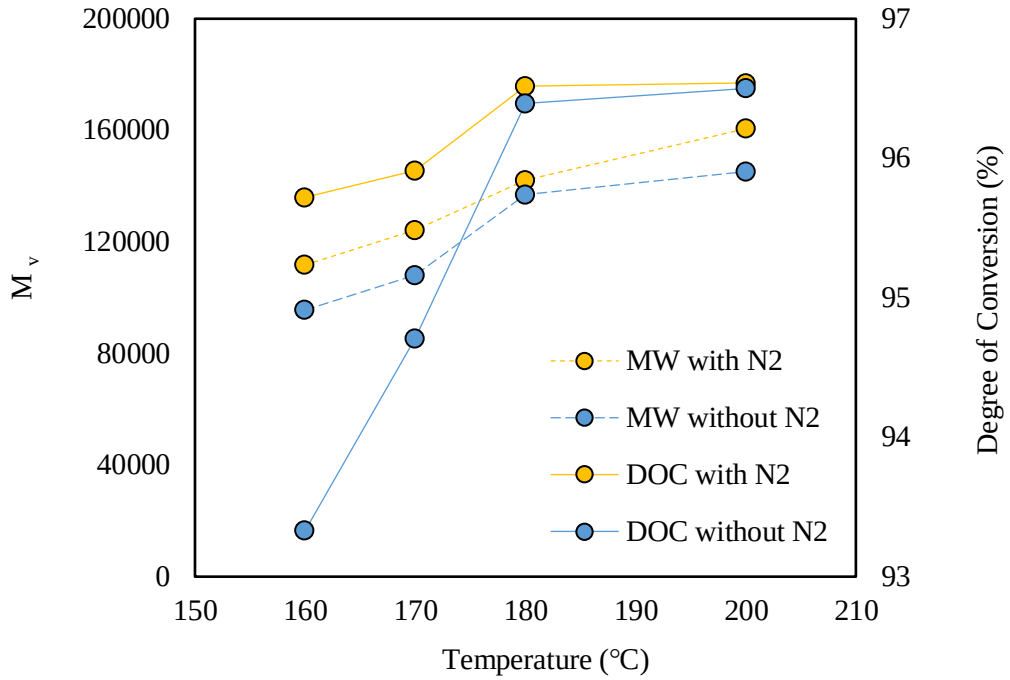

Fig. 4.12: Temperature sweep of viscosity average molecular weight and degree of conversion for samples both with and without nitrogen purging in the cavity.

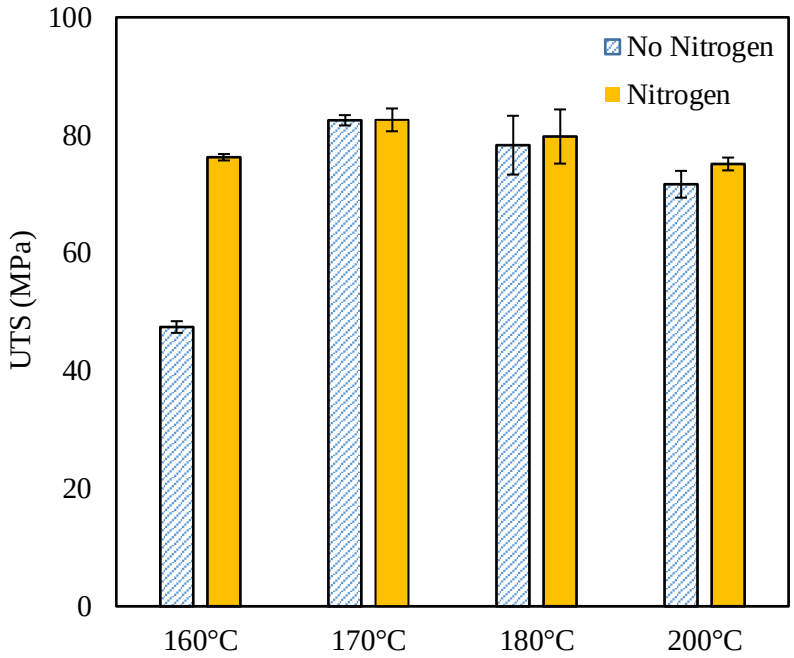

Fig. 4.13: Results from tensile tests presenting the ultimate tensile strength of APA-6 produced at different temperatures both with and without nitrogen.

4.4.3 Differential scanning calorimetry

Differential scanning calorimetry determined the melt temperature, recrystallization temperature and degree of crystallinity for both the product as moulded and that recrystallized after melting. The heating and cooling curves are presented in Fig. 4.14 and the results presented in Table 4.2. The degree of crystallinity of the polymer is similar to that in literature for APA-6 using the same mould temperature, reactants and activator content [87]. However in this study, the M_v value given is noticeably less but this may be due to poor moisture control. When cooled at a rate of 10 °C/min after melting, the resulting crystallinity is reduced significantly, indicating effects which would be important for recyclability of the material.

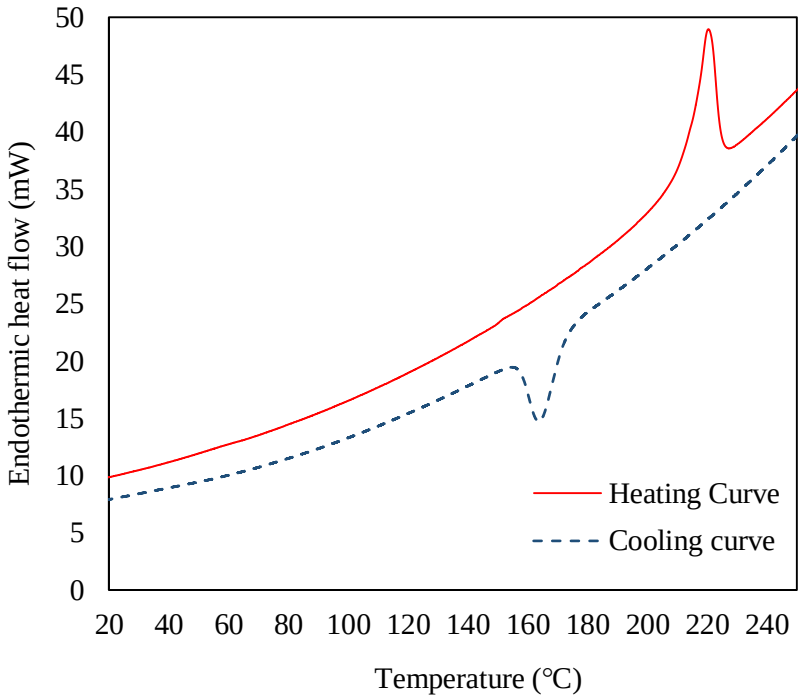

Fig. 4.14: DSC heating and cooling curves at 10 °C/min

Table 4.2: Results from DSC testing

Plate	Melt peak temperature	Enthalpy of fusion	Degree of crystallinity as processed	Degree of crystallinity after 10 °C/min. Cooling
	T_m (°C)	ΔH (J/g)	X_{c1} (%)	X_{c2} (%)
APA-6	219.4 ± 1.0	75.3 ± 5.5	42.2 ± 3.1	20.5 ± 1.0

4.4.4 Dynamic mechanical analysis

The DMA curves for the polymer are shown in Fig. 4.15 and the values for the glass transition temperature (T_g) and tan δ peak ($T_{tan\delta}$) are given in Table 4.3. The T_g at both frequencies is in the higher range of those reported in literature [149]. This can be explained by the influence of the molecular weight of the APA-6. High molecular weight polymers have a lower number of chain ends per unit volume. As these ends are not restrained to the same degree as the core, they allow for greater mobility [150]. The higher the molecular weight, the more mobility is restricted as a result, hence increasing the glass transition temperature. The relation between molecular weight and T_g is characterised by the Flory-Fox equation [151], $T_g = T_{g,\infty} - k/M_n$ where $T_{g,\infty}$ is the glass transition temperature that can be obtained at the highest theoretical molecular weight, M_n the number-average molecular weight, and k, an empirical constant. This relationship however is more relevant to low molecular weight polymers because long chains in high molecular weight polymers tend to interfere with one another and entangle, hence creating a much more complex system to analyse.

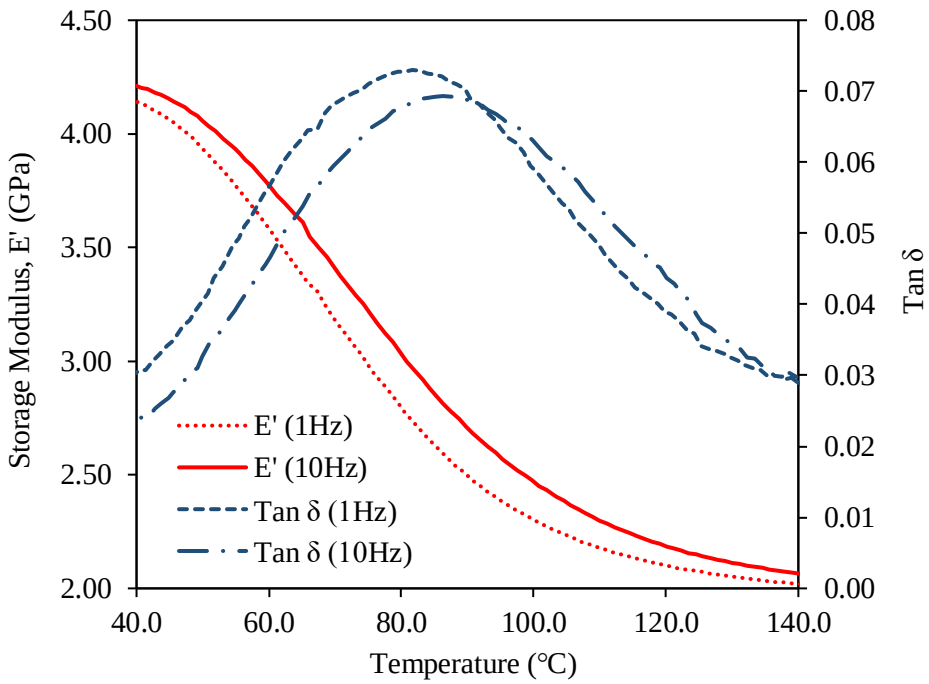

Fig. 4.15: DMA curves for storage modulus and tan δ at 1 Hz and 10 Hz.

Table 4.3: Glass transition temperatures from DMA tests as determined from the peak in loss modulus (T_g) and peak in tan δ ($T_{tan\ \delta}$).

	1Hz	10Hz
T_g	70.0 ± 0.8	75.8 ± 1.1
$T_{tan\ \delta}$	79.8 ± 2.1	84.5 ± 2.0

4.4.5 Mechanical properties

Representative stress-strain data for tension, compression and flexure is given in Fig. 4.16 and the mechanical properties are summarised in Table 4.4. The behaviour of the tensile curve is typical for a high molecular weight thermoplastic such as PA-6. This is characterised by the large plastic region with a high strain-to-failure compared to most thermosets. Compared to a standard RTM resin such as Gurit PRIME™ 27, the ultimate strength of the APA-6 is about 12 % more. The ultimate strength values are 7 - 30% higher than those reported in another study for anionically polymerised PA-6 over a wide range of polymerisation temperatures (140 °C - 170 °C) [38] and those produced by hydrolytic polymerisation [30]. Strength in polymers is mainly related to molecular weight, cross-linking and crystallinity [152]. While there is no cross-linking in the APA-6, its high molecular weight results in long chains, causing a larger number of entanglements. The high degree of crystallinity of the APA-6 in this case causes more significant intermolecular bonding. Deformation may lead to orientation of such structured chain phases in favour of increasing the material's strength. However, due to the plastic behaviour of the material, APA-6 has a yield strength, above which, deformation is no longer elastic. The tensile yield strength was determined where the change in stress with respect to strain ($d\sigma/d\varepsilon$) reached its minimum prior to necking. For each sample set, the stress at the lowest average $d\sigma/d\varepsilon$ over a 100 data-point moving average was used to determine the yield point. Based on the results for density and melt temperature, the molecular weight of the polymer synthesised in the current study is suspected to be slightly higher than that in literature for APA-6 which would partially explain this. The yield strength value for APA-6 however is similar to the ultimate strength of the Gurit epoxy even though the modulus is about 13 % less. While the modulus of the epoxy is poorer in flexure than in tension, the opposite is true for the APA-6. The large strain-to-failure combined with the capability of APA-6 to withstand high loading throughout, demonstrates high toughness. The higher flexural strength values compared to tensile strength is typical for polymers as the upper part of the specimen is in compression and the compressive strength is higher [30]. The results are in the range of those for hydrolytically polymerised PA-6. Overall, the results relate quite well to one another. The

low standard deviation in tension and flexure gives high confidence in the test methodology. The same can be said for compression up to yield but beyond this point, the failure strength and mode of failure varies significantly. As plastic deformation progresses in compression, the samples become unstable and eventually buckle which is the reason for the high standard deviation shown in Table 4.4.

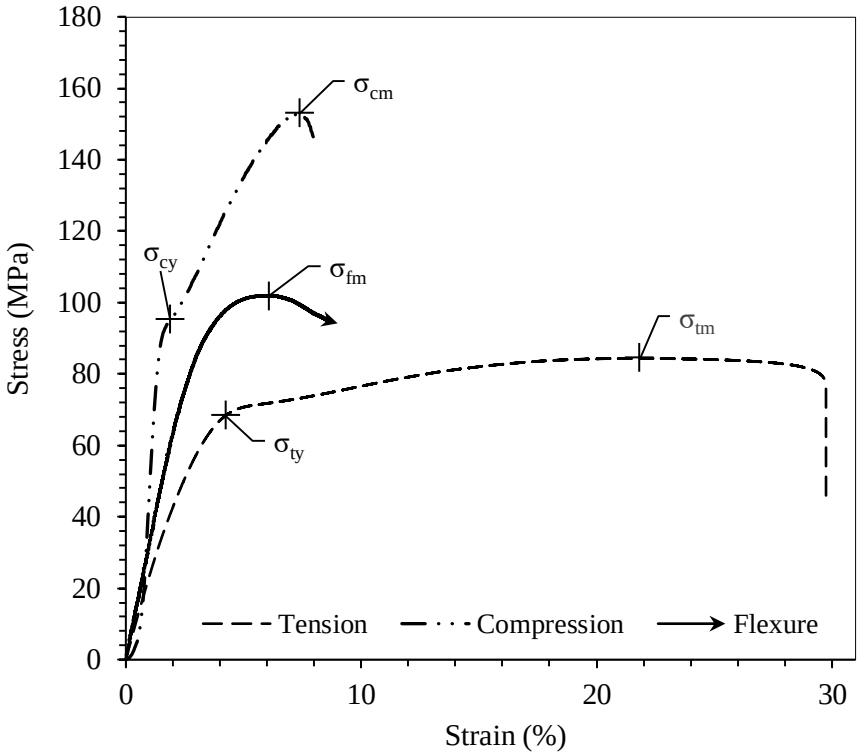

Fig. 4.16: Stress-strain data for mechanical testing in tension, flexure and compression.

Table 4.4: Mechanical properties determined from testing in tension, flexure and compression.

Test type	Maximum Strength (MPa)	Yield Strength (MPa)	Modulus (GPa)	Strain at maximum strength (%)	Strain at break (%)
Tension	83.2 ± 1.3	69.2 ± 2.4	2.8 ± 0.2	22.0 ± 0.5	29.5 ± 2.6
Compression	157.1 ± 37.1	92.4 ± 1.8	3.4 ± 1.6	8 ± 3	-
Flexure	102.7 ± 1.6	-	3.2 ± 0.2	6.2 ± 0.2	-

4.5 Conclusions

A fast acting catalyst and activator combination was chosen as the most suitable for an RTM style process for high rate production. The measures taken in storing the material and the importance of moisture reduction were discussed in depth. The effects of different mixing ratios of the three reactant materials (monomer, activator and catalyst) was considered, concluding that the most suitable mixing ratios would be 98.2 mol% caprolactam, 0.6 mol% bi-functional activator and 1.2 mol% catalyst for a mould temperature of 160 °C. While higher molecular weight is achieved at higher temperatures, the degree of crystallinity is reduced. Both molecular weight and crystallinity are factors which generally contribute positively towards strength so there is a crossover point at which a highest strength is achieved. Tests carried out on samples produced at mould temperature increments of 10 °C showed that the highest strength occurred at 170 °C. However, due to the difference in thermal mass of the mould used in the TP-RTM setup, a temperature of 160 °C resulted in more similar results. It was also shown that nitrogen purging can enhance both the degree of conversion and molecular weight of the material, particularly at lower temperatures.

Higher density and lower thickness were generally observed in areas of the part where there was either higher molecular weight and/or a higher degree of crystallinity. Material closer to the outlet was exposed to lower temperatures over time in the cavity compared to that towards the inlet, and so was slightly thicker and less dense due to a presumably lower molecular weight.

DSC results showed that the APA-6 material produced using the TP-RTM setup had a melt temperature of ~219.4 °C and a degree of crystallinity of ~42.2 % while DMA determined a glass transition temperature range of around 70-85 °C, depending on which frequency was used to determine this value.

Mechanical testing of the final products indicated that overall, the APA-6 material demonstrated excellent properties for its proposed application. The material demonstrated strength and modulus values close to that of a typical RTM epoxy but with a significantly higher strain-to-failure, indicating superior toughness. The conclusion is that the material retains comparable static properties to conventional resins but with the addition of greater energy absorption properties which could make it a highly suitable candidate as a matrix in high impact applications.

Chapter 5: Process optimisation & static properties of APA-6 composite

Summary

This chapter focuses on the manufacture and characterisation of reinforced APA-6 produced using TP-RTM. The chapter discusses the raw materials and methods used to produce the composite material as well as the physical, chemical, thermal and mechanical analytical techniques used to characterise the composite. The chapter shows that the manufacturing process used, results in a material with competitive physical and static mechanical properties compared to alternative RTM materials using similar textiles. The flow behaviour during mould filling and its effects on porosity and mechanical properties were studied.

5.1 Chapter Introduction and Overview

Having decided the most suitable temperatures, reactants and their mixing ratios for APA-6 in Chapter 4, the aim of this chapter was to focus on processing of APA-6 composites. A glass fibre non-crimp fabric was used to manufacture composite laminates with fibre volume fractions ~51-52 %. One of the key challenges in processing composites is controlling the flow rate and dispersion during filling; and the pressure required to gain optimal properties given the processing window available. The chapter focused heavily on reducing voids, both within fibre bundles (intra-bundle or micro voids) and between fibre bundles (inter-bundle or macro voids).

The distribution of thickness and density of material produced using the TP-RTM setup was determined to demonstrate shrinkage and flow effects with the reinforcement. The fibre volume fraction of the material was determined using burn-off and SEM. Thermo-morphological behaviour of the material was investigated using DSC to determine the degree of crystallinity as well as the melt and crystallisation temperatures of the material. Dynamic mechanical analysis was used to determine the glass transition temperature in the material.

Mechanical testing was carried out in tension, compression and flexure to determine the behaviour and performance of APA-6 composites and was compared to other similar materials in terms of strength and modulus. The effects of voids and stitching on the mechanical performance were discussed in depth. SEM was carried out on fractured surfaces to look at the nature of failure in the thermoplastic composite.

5.2 Materials and manufacturing

5.2.1 Materials and storage

The matrix material used in the manufacture of composites was the APA-6 used in Chapter 4. In the manufacture of composites, the effects of the reinforcement material on the matrix properties must be considered. For this study, a 640 g/m^2 unidirectional stitched glass fibre non-crimp fabric (NCF) was used. The rovings (brand name StarRov® 871), provided by Johns Manville (CO, USA) consisted of glass fibre filaments (ø ~17 μm) coated with a silane agent compatible with in-situ polymerisation of APA-6. The rovings were held together by polyester stitches in 5 mm increments along the fibre length as shown in Fig. 5.1. The rovings were stitched by DITF (Denkendorf, Germany) to make a fabric. The fibre reinforcement material was supplied on spools and wrapped with plastic film when in storage at room temperature.

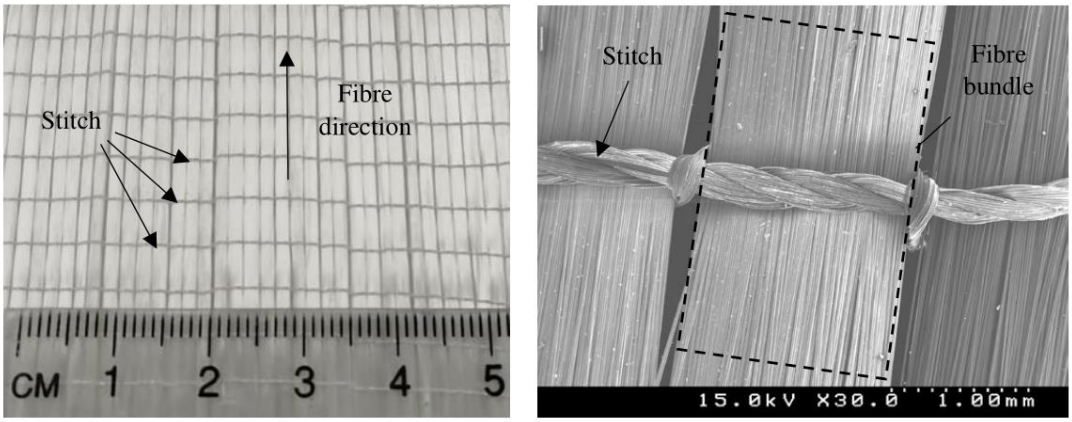

Fig. 5.1: Images of the stitched glass fibre NCF with polyester stitching.

5.2.2 Manufacture of APA-6 composites by vacuum infusion

Prior to using the TP-RTM equipment, a vacuum infusion style process was used for the manufacture of composite laminates. The work was carried out at James Walker Devol (Gourock, Scotland), a manufacturer of engineering thermoplastic parts made mainly from nylons. The precursor materials were heated, stirred and dispensed using a Bronk Industrial nylon casting unit (NCU 50/6). The casting unit consisted of two tanks like that for the TP-RTM equipment: tank A for a caprolactam/activator solution and tank B for a caprolactam/catalyst solution. The contents of both tanks were heated to 110°C with continuous stirring above melting point under a nitrogen atmosphere. The contents of each

tank were dispensed in a 1 : 1 ratio by volume into a pre-heated glass beaker at 140°C sitting in a heating mantle. A two-sided electrically heated stainless steel mould was used to cast the polymer composite. Four plies of the stitched fabric were laid up in the mould with the fibres aligned in the direction of flow. The fibres were dried for at least 4 hours at 100°C in a vacuum oven prior to layup. The outlet was connected to a vacuum pump via a resin catch pot and pressure was recorded from a pressure gauge. Silicone rubber tubing was used between the vacuum pump, resin catch pot, mould and beaker. A needle valve was used between the vacuum pump and catch pot to control the flow rate and a ball valve was used at the inlet to turn the flow on and off. All silicone rubber piping and valves were dried and heated prior to use to prevent inhibition of the reaction and/or freezing during injection. The vacuum infusion setup is shown in Fig. 5.2.

After dispensing into the heated beaker, the mixture was stirred. All ball valves were opened and the open end of the silicone inlet pipe coming from the catch pot was submerged in the mixture. The vacuum pump was turned on and the resin travelled via the inlet pipe, into the mould to infuse the fabric. When the resin reached the outlet port, the inlet ball valve was shut, followed by immediately shutting the outlet ball valve. The mould temperature was left at the pre-set value for 15 minutes to allow polymerisation to occur. After 15 minutes, the heating was turned off and the mould was left to cool by natural convection. When sufficiently cool to handle, the composite panels were demoulded.

Fig. 5.2: Image of vacuum infusion setup

5.2.3 Manufacture of APA-6 composites by TP-RTM

The manufacturing procedure for composites using TP-RTM was very similar to that in chapter 4, except with the addition of the textile in the mould. Initially, the electrically heated mould described in section 4.2.3 was used for composites manufacture, but its use was later discontinued. While peripheral clamping with bolts along the edges kept the mould parts together, it didn't prevent deflection of the centre of the mould when under pressure. This deflection resulted in a variation in thickness across the laminate, and therefore, a variation in fibre volume fraction. Even though the laminates manufactured using this method weren't used for characterisation of the material, the process was used as a stepping stone in learning to troubleshoot flow issues, most of which are typical for RTM processes.

The final system used for material characterisation in this chapter was that shown in Fig. 3.17 using the pneumatic press. For the 2 mm cavity, 4 plies of stitched unidirectional fabric were laid up with final dimensions of 350 mm x 390 mm. Due to open stitches along the ply edges from cutting, additional material in the width-wise direction was allowed to account for lost fibre bundles during handling. After placement of the four plies, excess bundles were removed and the overhanging stitches were trimmed so that they would not act as a pathway for leaking between the seal and cavity plate. Due to the ease of fabric handling and the guidance of the cavity edges, good fibre alignment was achieved. The upper mould surface was placed on top of the other mould parts to close the cavity. The gap created by the seals was investigated along the perimeter to ensure that it was consistent and that there were no fibres or stitches to be seen. After placement of the mould in the press, the vacuum pump with a pump rate of 330 l/min was turned on, pressure was applied to the mould, and the platens were heated to 130 °C for at least 90 minutes for sufficient drying of the fabric to occur. All other steps in the manufacturing process were carried out as in section 4.2.4.

5.2.4 TP-RTM defect reduction measures

The aim during RTM style processes is to fully fill the mould cavity, wet out the textile completely and yield a high degree of cure (or polymer conversion in this case). In reality, dry patches and voids can result in part defects which limit material performance. While such defects are undesirable and can be reduced to a large degree with sufficient process controls in place, it is often practically impossible to eliminate them entirely.

One of the initial flow problems experienced during manufacturing was race tracking. This occurs when the textile doesn't cover the full width of the mould cavity, leaving channels for

the molten pre-polymer to travel along the side walls. The pre-polymer will always take the path of least resistance, traveling faster along these channels than through the textile. The pre-polymer travelling around the periphery reaches the outlet before that travelling through the textile, and so, results in a large dry area in between like that shown in Fig. 5.3. Continuation of flow through the cavity doesn't really solve this issue as it may be at an equilibrium, as the liquid continues to travel around the edges. To solve this, the edges were packed out with fibre to create resistance in the side channels, and hence, create more uniform flow across the laminate.

Another problem during filling is leakage of air into the cavity. Leaking air entered the mould either when seals were worn, fibres were caught between mould sealing surfaces, insufficient pressure was applied by the press to keep the mould sealed or interconnecting parts weren't tightened sufficiently. Such leaks can destroy parts with entrapped air causing unacceptably large void volumes. A vacuum drop check was carried out prior to infusion to prevent this from occurring during processing.

The application of a vacuum on the outlet reduced the amount of air in the mould cavity, and hence, that available for the formation of voids. However, even where vacuum was applied, voids could still occur due to entrapment when surrounded by crossing flow paths. However, application of a vacuum pressure greater than that of the vapour pressure of the liquid, can result in boiling as was discussed in section 4.2.4. Positive pressure was applied to not only fill the mould but also reduce the volume of trapped air already in the mould. The effects of pressure (both vacuum and positive) are discussed in great detail in section 5.4.

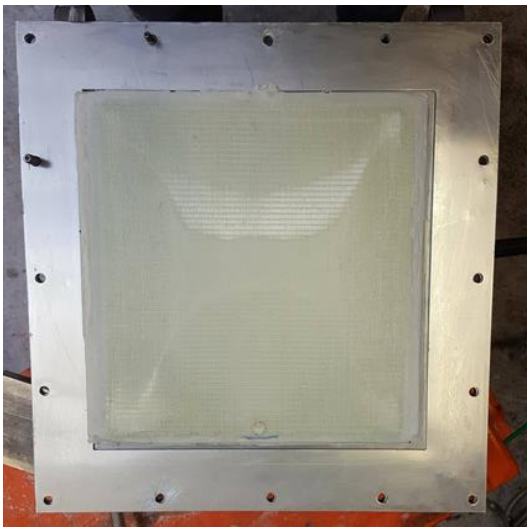

Fig. 5.3: Example of laminate where race tracking occurred.

5.3 Analysis and testing

5.3.1 Quality improvement

As in section 4.3.1, a six-sigma style improvement process was used to analyse the quality of composite parts based on part thickness, density, fibre volume fraction, void content and glass transition temperature. The average values and standard deviation of each metric was recorded in a quality assurance form (see Appendix C). Notes on visual observations were also recorded in the form. Fig. 5.4 shows an example of a typical laminate manufactured using the final TP-RTM process parameters and measures.

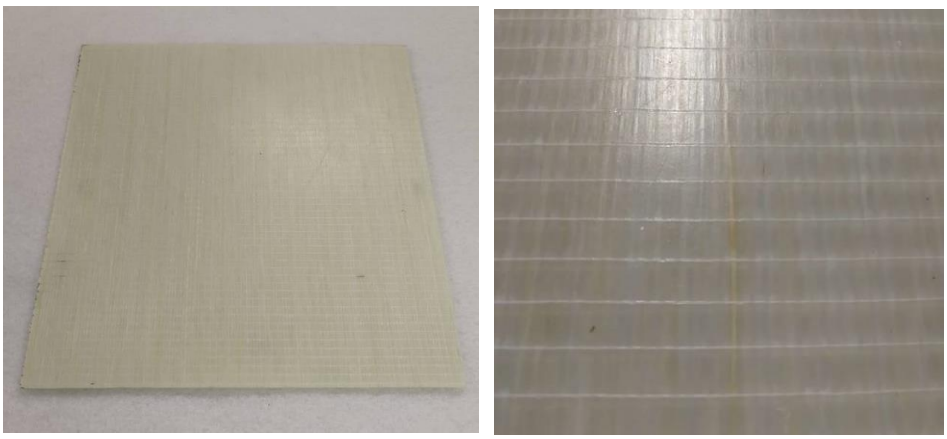

Fig. 5.4: Image of a typical laminate produced from TP-RTM.

5.3.2 Sample preparation

Due to their simple rectangular geometry, all composite samples were cut using a diamond blade cutting saw with coolant at a feed rate of ~300 mm/min with the exception of DSC samples, which were cut using a Stanley knife blade. All samples were then dried under vacuum for 24 h at 50 ℃ and stored in polybags with desiccant until testing. For each test type, samples were extracted from 2 laminates in locations shown in Appendix D.

5.3.3 Distribution of thickness and density

The same methods as those in 4.3.3 were used to determine the thickness and density of samples at 9 different locations in each laminate.

5.3.4 Burn-off

To determine the fibre volume fraction (V_f) of composite samples, the 9 samples from the density measurements were used for burn off in accordance with *ISO 7822:1999-Method A*. The composite samples with mass w_c were placed in ceramic crucibles, and the total weight of each was measured. Lids were put on the crucibles, and they were placed in the furnace. The samples were heated from room temperature to 560 °C over the course of an hour and were held at this temperature for 5 h to allow burn off of the matrix. After completion of the heating cycle and cooling back to room temperature, the crucibles containing the fibres only were weighed. The mass of the polymer matrix (w_m) was defined as the mass lost during burn off, and that of the fibres was defined as the remaining sample mass (w_f). V_f was determined using known fibre and matrix density values, ρ_f and ρ_m respectively using the following equation:

$$V_f = \frac{V_f}{V_c} = \frac{{}^{w_f}/_{\rho_f}}{{}^{w_c}/_{\rho_c}} \tag{5.1}$$

With knowledge of these properties and the composite density (ρ_c), the void content (V_v) was calculated using equation 5.2.

$$V_v = \rho_c \left[\frac{w_f}{\rho_f} + \frac{1-w_f}{\rho_m}\right] \tag{5.2}$$

5.3.5 Optical and scanning electron microscopy of polished surfaces

Both optical microscopy and scanning electron microscopy (SEM) were used to study the fibre distribution and voids within composite samples. The former was mainly used to demonstrate the effects of injection pressure on macro voids across a large sample, while the latter was used to take a closer look for micro voids and determinine the fibre volume fraction visually. Rectangular samples (~15 mm x 15 mm) were placed in polishing moulds, embedded with epoxy and cured overnight at room temperature. The samples were ground using a rotational grinder, using sandpaper of various grit sizes (P240, P1200, P2500) in a water suspension. This was followed by cleaning and polishing using a smooth polishing cloth and diamond suspension of various sizes (9µm, 3µm, 1µm). Optical microscopy of samples was carried out on a Zeiss Axioskop 2 MAT microscope with an AxioCam MRc5 5MP camera. The camera shots were stitched together using the Inkscape graphics editor to look at macro voids across samples. SEM samples were prepared in the exact same manner and were observed using a

Hitachi TM4000Plus SEM with an accelerating voltage of 15 kV. Images across the full thickness of samples at a magnification of 100 were taken to determine the fibre volume fraction while images at a magnification of 1,200 were used to observe wet-out of fibres within bundles. *ImageJ* was used to analyse the images using thresholding segmentation to differentiate between fibres and matrix as shown in Fig. 5.5.

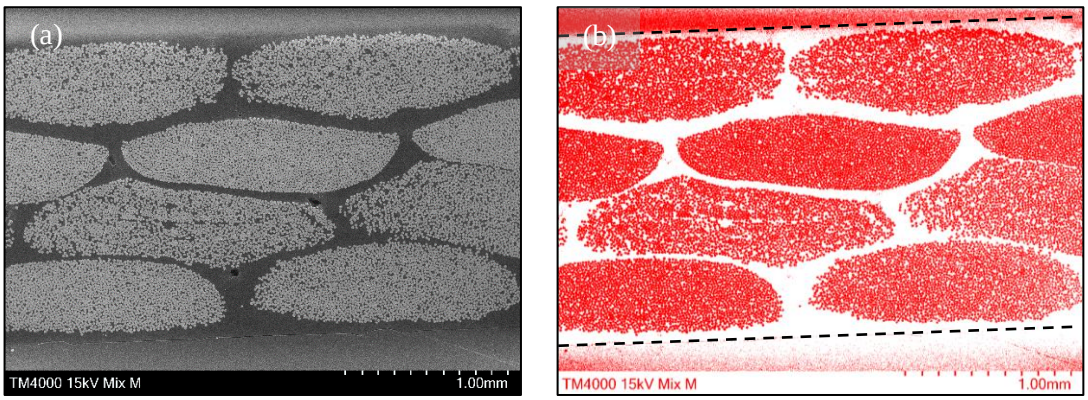

Fig. 5.5: (a) an original SEM image of a composite cross-section and (b) an edited SEM image where thresholding was used to determine the fibre volume fraction.

5.3.6 CT Scan

In addition to the measurement of the void content by volume, knowledge of the distribution of voids and their significance was required to later explain mechanical test results. To do so, one-off computerised tomography (CT) scans were carried out on 9 composite samples (dimensions: 15 mm x 15 mm). It should be noted that the CT samples were extracted from a different laminate to those used for mechanical testing but were manufactured using the same system and setup. The 9 samples were split into 2 batches for scanning and were stuck together with double sided tape to form blocks. The two batches were scanned separately using a CT scanner in the School of GeoSciences at The University of Edinburgh. 3D representations of the samples were produced by stacking the individual CT images (~80 per sample) using *ImageJ* software. The brightness of the stack was increased to filter out the visible range dominated by the fibres, such that greater contrast could be presented in the resin-rich inter-bundle trenches where the macro voids were located. The macro void content by volume was determined using thresholding segmentation on *ImageJ*. The image processing steps are presented in Fig. 5.6.

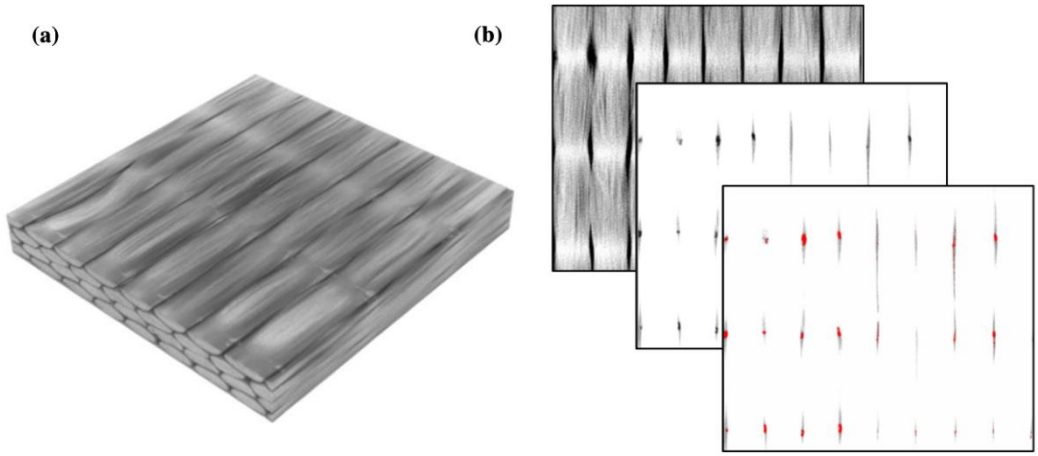

Fig. 5.6: (a) Stacked 3D view of one of the 15 mm x 15 mm CT samples and (b) visual representation of the image processing steps used to analyse the void content and distribution.

5.3.7 Degree of conversion

To measure the degree of conversion of the composite, a grinding and reflux process was carried out almost identically to that in section 4.3.4. At the end of the process however, a burn-off of the product was carried out in a similar fashion to that described in section 5.3.4 to determine the fibre volume fraction. This is taken into account when determining the conversion as follows, where m_m is the mass of the matrix burnt off, m_t is the mass of the sample prior to burn-off and m_f is the mass of the fibres:

$$DC \approx 100 \times \{1 - [m_m/(m_t - m_f]\} \tag{5.3}$$

5.3.8 Differential scanning colorimetry

DSC was used to determine the degree of crystallinity of the polymer product, the melt temperature and the crystallisation temperature range for the composite. For the most part, the methods used are very similar to those in section 4.3.6. The degree of crystallinity (X_c) in the matrix part of the material can be determined from the ratio of the polymer's enthalpy of fusion (ΔH_m) to that for pure crystalline PA-6 (ΔH_c). Taking into account the mass of the fibres (m_f), which don't take part in the phase change and the degree of conversion (DC), the degree of crystallinity can be determined as follows, where m_s is the mass of the sample.

$$X_c = \frac{\Delta H_m}{\Delta H_c} \times \frac{m_s}{m_s - m_f} \times \frac{1}{DC} \tag{5.4}$$

The value for m_f can be determined from burn-off of the sample post DSC testing.

5.3.9 Dynamic mechanical analysis

DMA was used to determine the glass transition temperature (T_g) of the composite. A three point bending configuration for composites was used in accordance with *ISO 6721-11:2012* on a Triton 2000 DMA. Three 10mm x 35mm samples from each plate were tested using a 30 mm span with a displacement of 0.05 mm. The samples were dried under vacuum for 24 hours at 50°C prior to testing. The test was run at frequencies of 1Hz and 10Hz from room temperature up to 180°C at a ramp rate of 5°C/min. The glass transition temperature was determined using the same methods described in section 4.3.7.

5.3.10 Tensile testing

Tensile tests for the composite case were carried out in the longitudinal and transverse directions in accordance with *BS EN ISO 527-5:2012*. Type B specimens (250 mm x 25 mm x 2 mm) were used for transverse testing using an Instron 3369 screw-driven machine with a 10 kN load cell and a crosshead speed of 1 mm/min. In order to keep the thickness in line with other test types, the dimensions of the longitudinal specimens used were 250 mm x 15 mm x 2 mm. The gripping ends of the specimens were sand blasted and cleaned with acetone prior to applying glass fibre end tabs which were bonded using a cyanoacrylate adhesive (Loctite 406) and polyolefin primer (Loctite 770). The samples were tested on an MTS C45.305 machine using a 300 kN load cell and a crosshead speed of 2 mm/min. A clamping pressure of ~70 bar was used to hydraulically grip the specimens. The strain for both the transverse and longitudinal samples was measured using the video extensometer and a speckled pattern. The setup for each tensile test type is show in Fig. 5.7.

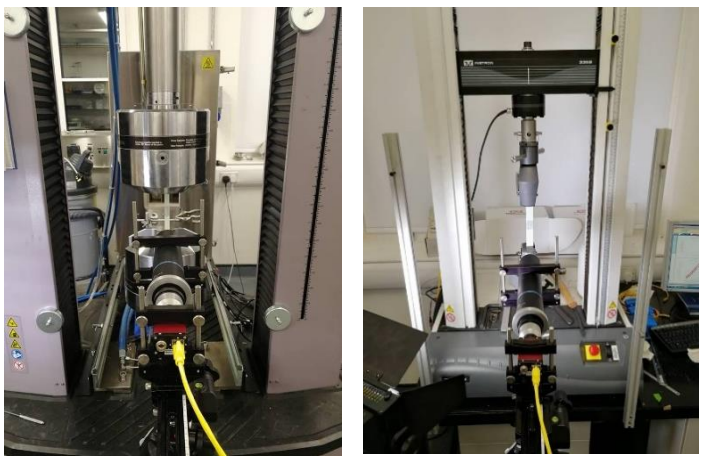

Fig. 5.7: Tensile test setup for composites in the (a) longitudinal direction and (b) transverse direction.

5.3.11 Flexural testing

Flexural testing of the composite were carried out in the transverse and longitudinal directions in accordance with *BS EN ISO 14125:1998+A1:2011* in four-point bending using the preferred loading support/nose radii, specimen dimensions (60 mm x 15 mm x 2 mm) and span of 45 mm as shown in Fig.5.8. An Instron 3369 screw-driven machine was used with a 50 kN load cell. The midspan deflection of specimens was tracked using the video extensometer by tracking a speckled pattern on the edge of samples. A crosshead speed of 1mm/min was used and samples were tested to failure. The setup for flexural tests is shown in Fig. 5.8.

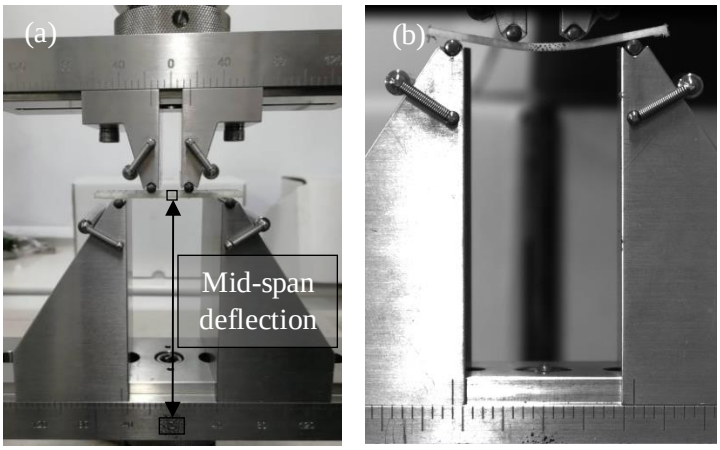

Fig. 5.8: Flexural test setup for four-point bending showing (a) the reference regions for tracking mid-span deflection and (b) a deflected sample during testing.

5.3.12 Compression testing

Compression tests were carried out in the transverse and longitudinal directions in accordance with *ASTM D6641/D6641M* using a combined loading compression (CLC) fixture using *Procedure A* as shown in Fig. 5.9. The fixture used in this test subjects the specimens to combined end- and shear-loading [153]. The specimens used were approximately 140 mm x 13 mm x 2 mm for both the transverse and longitudinal cases. They were placed in the fixture and tightened by applying a torque of 4 Nm to each of the 8 clamping screws. The fixture was placed between two compression platens fixed to the grips of an MTS C45.305 machine using a 300 kN load cell. A crosshead speed of 1.3 mm/min was used and strain was measured on one side by tracking a speckled pattern previously applied to the surface along the gauge length of the specimens.

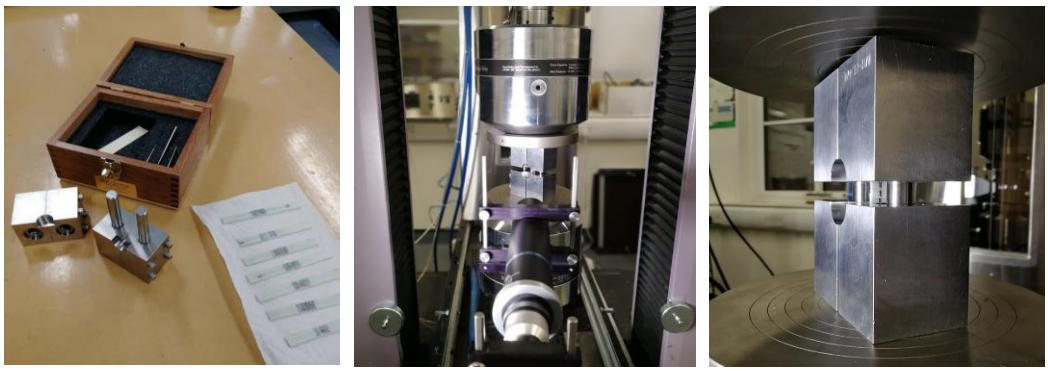

Fig. 5.9: Compression testing using a combined loading compression fixture.

5.3.13 Scanning electron microscopy of fractured surfaces

SEM was used to study the fracture surface topography of failed flexural specimens as they had been subject to both compressive and tensile fracture. In order to separate the two halves of the specimens, the tests carried out in section 5.3.11 were continued by further loading/deflecting the samples until significant tensile fracture occurred on the bottom surface. At this point, the deflections became so large that loading and support fixtures risked coming in contact with one another so the final separation was carried out by hand. The samples were firstly sputtered with a 200 Å thick gold coating to improve surface conductivity. A JEOL JSM-6010PLUS/LV SEM was used to observe samples at magnifications between 300 and 1,200 at an accelerating voltage of 20 kV. A Carl Zeiss SIGMA HD VP Field Emission SEM was used to observe finer morphological features (<100 nm) at higher magnifications between 4,800 and 60,000 with an accelerating voltage of 2 kV.

5.4 Results and discussion

5.4.1 Effects of processing techniques and pressure

The vacuum infusion process used in section 5.2.2 resulted in composite parts with extremely poor quality. Fractured parts demonstrated that the fibre bundles were dry and observation using optical microscopy showed that there was a significant number of macro voids in the material. This was similar to reports from literature which indicated void contents ranging between 3 and 10 % by volume for the same process technique [39]. Due to the low viscosity of the precursors, it is extremely difficult to control the flow rate using standard valves. Fine control needle valves were used in this current study but still resulted in poor regulation of flow. The porosity varied from lay-up to lay-up so the pressure differential required for each run was inconsistent. TP-RTM on the other hand, though assisted by vacuum at the outlet side,

was driven by the pumps. The system was controlled using a flow rate which was constant, regardless of the back pressure experienced in the mould (up to a limit). Having established a more consistent TP-RTM setup, the vacuum infusion process was discontinued. The use of positive pressure from the inlet side and vacuum pressure from the outlet in the TP-RTM setup allowed for optimisation of quality. Fig. 5.10 (a) shows a stitched micro-section image for a part using neither vacuum nor any additional pressure other than back pressure due to the textile and pipe friction (~0.8 bar) during filling. Fig. 5.10 (b) shows a similar type of image where additional back pressure (~4 bar) was introduced but without vacuum at the outlet. This back pressure was created by restricting flow at the outlet. This resulted in a significant reduction in voids in the part down to levels ~1.5 %. The quality was further improved by using vacuum at the outlet, which saw almost complete elimination of intra-bundle voids. Microscopic images of these parts with optimised quality are shown in section 5.4.4.

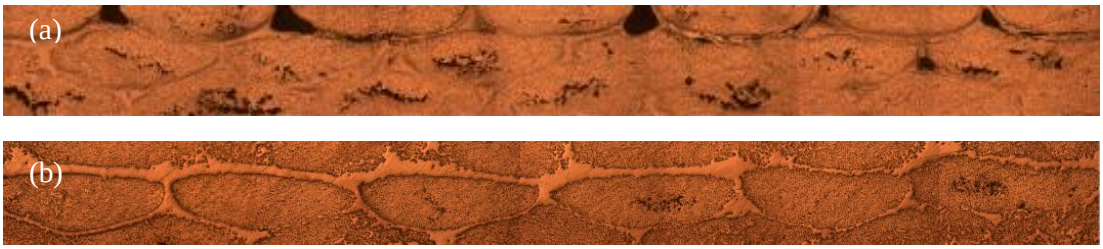

Fig. 5.10: Stitched micro-section images for composites produced by TP-RTM using (a) back pressure due to the textile and pipe friction only and (b) additional pressure due to restricted flow at the outlet.

5.4.2 Thickness and density distribution

Measurements were taken from 2 laminates (referenced A and B) at 25 locations for thickness and 9 locations for density. Their distribution is shown in Fig. 5.11 and their average values ± SD are given in Table 5.1. While the distribution is given for one laminate only, similar observations were made across other laminates, making the results representative for all composite samples produced using the 2 mm cavity and TP-RTM setup. The thickness is higher towards the outlet while the opposite is true for the density, similar to results in section 4.4.1 for the pure polymer. Once again, this is likely due to a temperature gradient across the mould during filling, which affects the crystallinity, and hence, the density and thickness. The drop in density and thickness towards the centre seen in Fig. 4.11 was not observed here. This makes sense as the textile, which is preheated, reduces the difference in conductivity between peripheral regions and those towards the centre, as well as reducing mobility of the matrix.

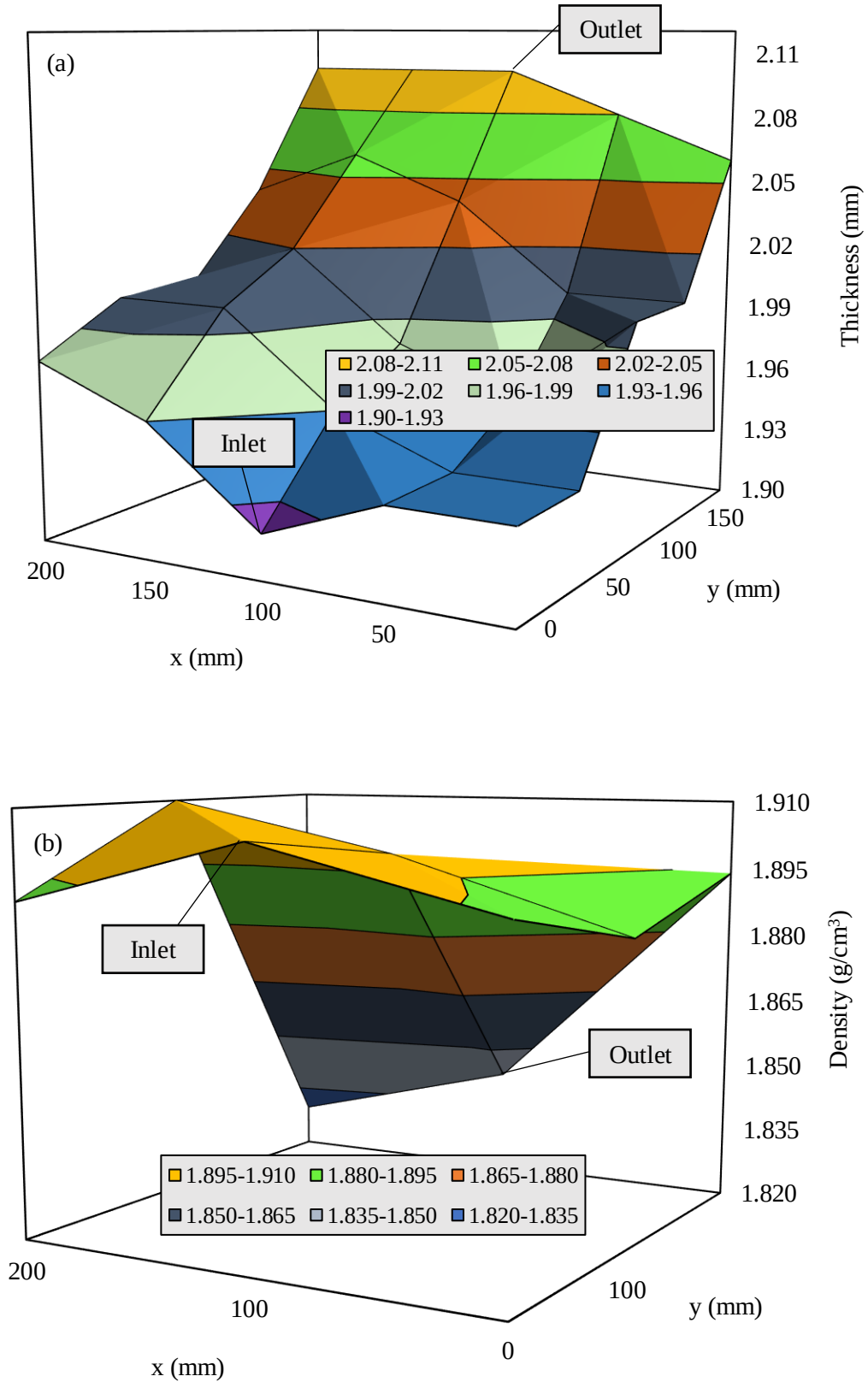

Fig. 5.11: Representative distribution of (a) thickness and (b) density with of a composite laminate with an (x, y) co-ordinates given.

5.4.3 Fibre volume fraction and void volume from burn-off

Measurements of fibre volume fraction and void volume were performed using equations 5.1 and 5.2 respectively. The results are summarised in table 5.1 along with those from section 5.4.1. The results show little difference between the two laminates. The standard deviations in void volume values are extremely high relative to the average values. This is typical for the method used, which has a high margin of error, particularly where the void volume is low [65]. To further look at voids and their distribution, CT and SEM images were also used.

Table 5.1: Average values ± SD for thickness, density, fibre volume fraction and voids in GF/APA-6 laminates.

Plate	Thickness t (mm)	Density ρ (g/cm^3)	Fibre volume V_f (%)	Void volume V_v (%)
GF/APA-6 A	1.97 ± 0.07	1.883 ± 0.028	51.4 ± 2.0	0.8 ± 1
GF/APA-6 B	1.99 ± 0.06	1.882 ± 0.025	51.8 ± 1.9	1.1 ± 0.4

5.4.4 Two-dimensional (cross sectional) inspection

Both optical and scanning electron microscopy of polished surfaces showed the distribution of fibres through the thickness of the composite. Due to the stitched fibre bundles, there are large fibre rich regions and pure polymer regions as shown in Fig. 5.12 (a). Generally there weren't many inter-bundle voids observed, except for areas at stitches. SEM images were taken parallel to the fibre direction to observe defects caused by the stitching as shown in Fig. 5.12 (b). This is looked at in greater detail in section 5.4.4 using three-dimensional CT scanning.

Analysis of SEM cross-sectional images on *Image J* showed a fibre volume fraction of ~52 %, similar to that determined by burn-off. Analysis of individual fibre bundles such as that in Fig. 5.12 (c) showed that the bundles had local fibre volume fractions varying from ~ 66 - 70 %, depending on how far from a stitch the cross section is. The bundles were most densely packed with fibres at each stitch (every 5mm) and were least densely packed halfway between two stitches where they aren't restricted from spreading radially. SEM images at high magnifications inside bundles such as that in Fig. 5.12 (d) showed excellent wet-out with no significant indications of intra-bundle voids.

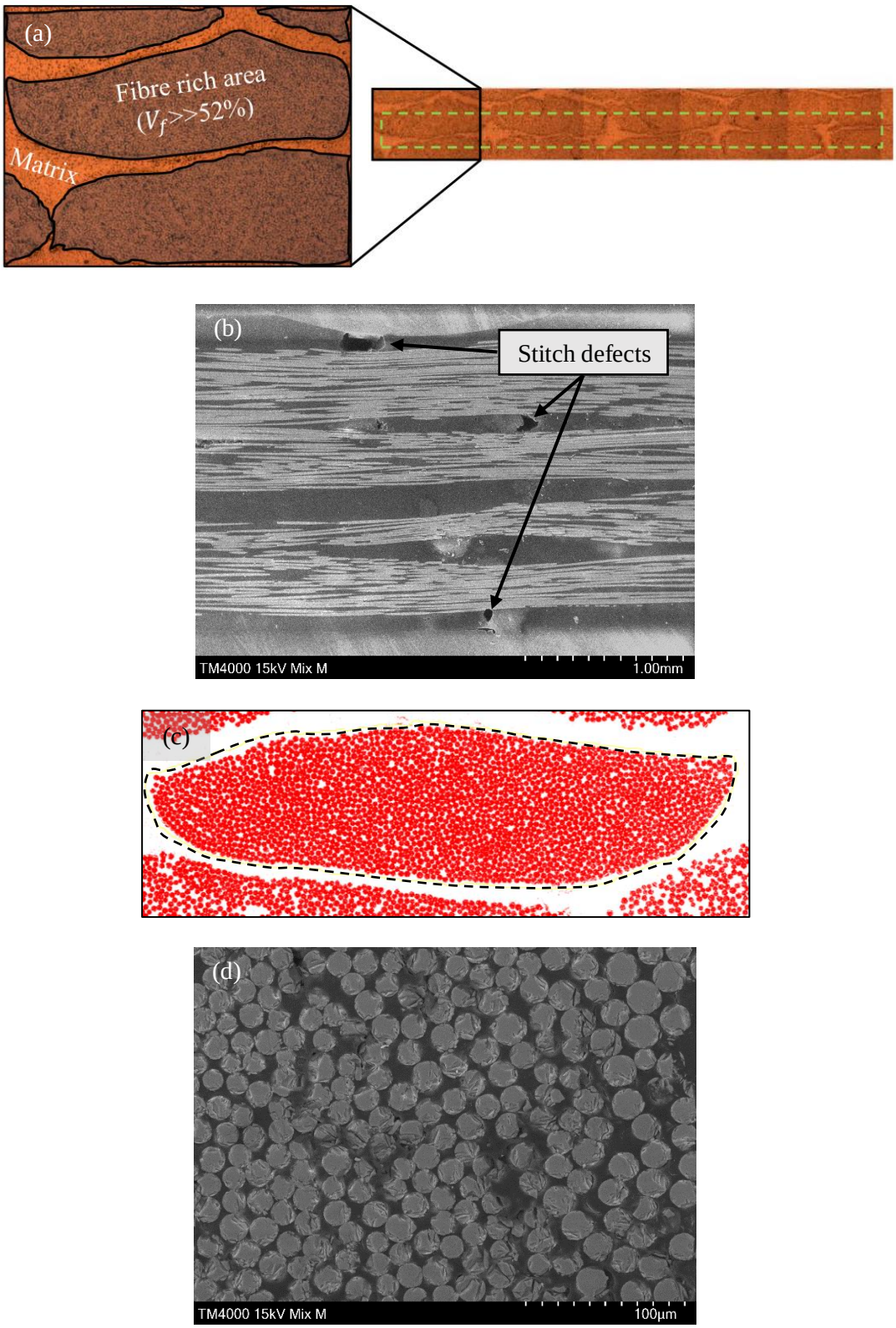

Fig. 5.12: (a) Stitched image of a cross-section from optical microscope images, (b) SEM image perpendicular to the fibre direction, showing stitches and the defects that they cause within the material, (c) threshold segmentation of an individual fibre bundle and (d) view inside a fibre bundle where complete wet-out can be observed.

5.4.5 Three-dimensional void distribution from CT

The inter-bundle void content of one laminate was measured using CT and compared to burn-off methods carried out on the same samples. Due to the low resolution of the scans, intra-bundle voids could not be observed whereas the burn-off method accounts for all voids. As suspected from visual observation of Fig. 5.12 (b), macro-voids were seen to be present in areas along the stitch (shown in Fig 5.13) but otherwise, there were few voids observed.

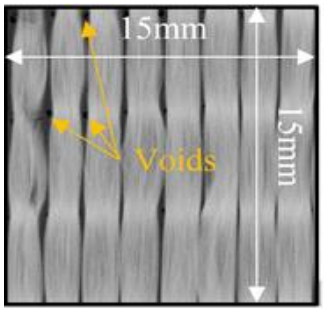

Fig. 5.13: CT Image prior to stacking, demonstrating through-thickness macro-voids at stitch.

Their presence can be explained by entrapped air in the fabric during processing. A small amount of air enters the mould when the vacuum is reduced just prior to injection to prevent the liquid precursors boiling. The volume of air in the mould during injection can be determined from Boyle's law (given in equation 5.5), where V_m is the volume of the mould and inlet tube, and P_{atm} and P_{vac} are the atmospheric pressure and vacuum pressure, respectively.

$$V_a = P_{vac}/P_{atm} \times V_m \tag{5.5}$$

For a 5.3 kPa pressure under vacuum, this results in around 5.2% air inside the cavity and tubing which is available for entrapment. In the case where no fibres are present, such as that for the pure APA-6 plate, this gas would be evacuated during injection as it is pushed out in front of the liquid precursors. The flow is much more complex for the composite case as air already exists within fibre bundles and becomes entrapped. As the macro-flow between the bundles moves forward, it is speculated that the flow also infiltrates radially into the fibre bundles, but at a slower rate. This infiltration would occur primarily in the areas of least resistance where the fibres are less densely packed, i.e., at inter-stitch areas away from the fibre-stitch interfaces, where permeability is lower. This would be followed by capillary action, which would drive the intra-bundle flow from the inter-stitch regions towards the stitched regions. Because the fibre bundles are tightly packed at the stitch, it is likely that the

intra-bundle flow would get choked. The capillary pressure would expel some of this air into the inter-bundle regions as the pressure in these regions would be less than that required to penetrate the stitched areas. The result is areas of both macro and micro voids in laminates at 5 mm increments. When the cavity pressure is then increased to 4 bars, the volume of these voids decreases. The steps of void formation are summarised in Fig. 5.14.

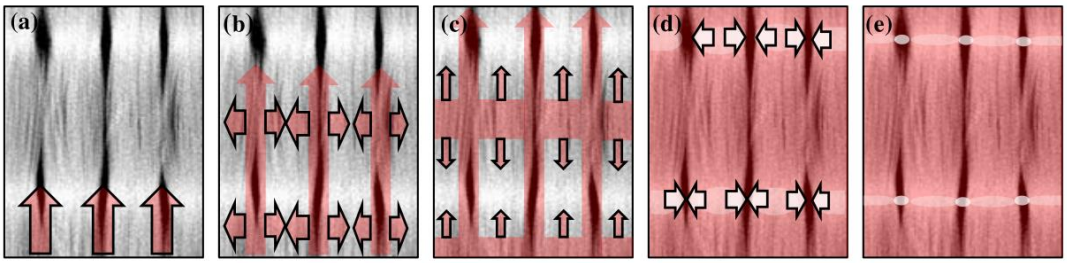

Fig. 5.14: Suspected formation of voids during injection where red indicates the liquid flow and white indicates gas. The steps include (a) Macro-flow making its way through a ply, (b) radial flow into fibre bundles, (c) capillary driven intra-bundle flow towards the stitched areas, (d) expulsion of air into inter-bundle regions, (e) resulting macro and micro voids after application of ~ 4 bars of pressure.

A possible solution to reduce this effect would be to use a greater vacuum to reduce the amount of air available for this phenomenon to occur. While this can easily be accomplished, it is limited by the boiling of caprolactam at lower pressures, and reaction temperature is also a key factor. For example, at 163 °C, the vapour-pressure of caprolactam is ~ 4 kPa but at 147 °C, this is ~ 2 kPa, indicating that a lower injection temperature would allow a greater vacuum to be used and hence, greater void reduction would be achieved [137]. Though CT scanning is often considered the pinnacle of void content determination methods, a sufficiently high resolution is required to observe the distribution of inter-bundle voids. Micro CT with higher resolution would render superior image quality allowing for segmentation within bundles, but at the expense of sample size.

5.4.6 Degree of conversion & differential scanning calorimetry

The degree of conversion for samples was calculated using equation 5.3. Values ranged from 95-98% for laminates produced using TP-RTM in general. Samples taken from laminates which were used for tests results presented in this chapter had an average conversion of 96.9%. The DSC curves for the composite are shown in Fig. 5.15. Due to the composites consisting

of ~52% fibres, the apparent enthalpy of fusion results were lower than those for the pure polymer. The fibre content was taken into account in equation 5.4 when calculating the degree of crystallinity and the results are shown in Table 5.2. This analysis shows that the degree of crystallinity is slightly higher for the composite compared to that for the pure polymer (shown in Table 4.2). As the thermal conductivity of the fibres is about 1/5th that of the pure APA-6, their presence in the composite during processing possibly slows down the transfer of heat during crystallisation, thus resulting in a higher degree of crystallinity. When cooled at a rate of 10°C/min after melting, the resulting crystallinity is reduced significantly. The difference in the degree of crystallinity between the polymer and composite is reduced as a result. This indicates that historical morphological effects, which occurred upon cold crystallisation, and caused a difference between the two due to the presence of fibres; has mostly been eliminated.

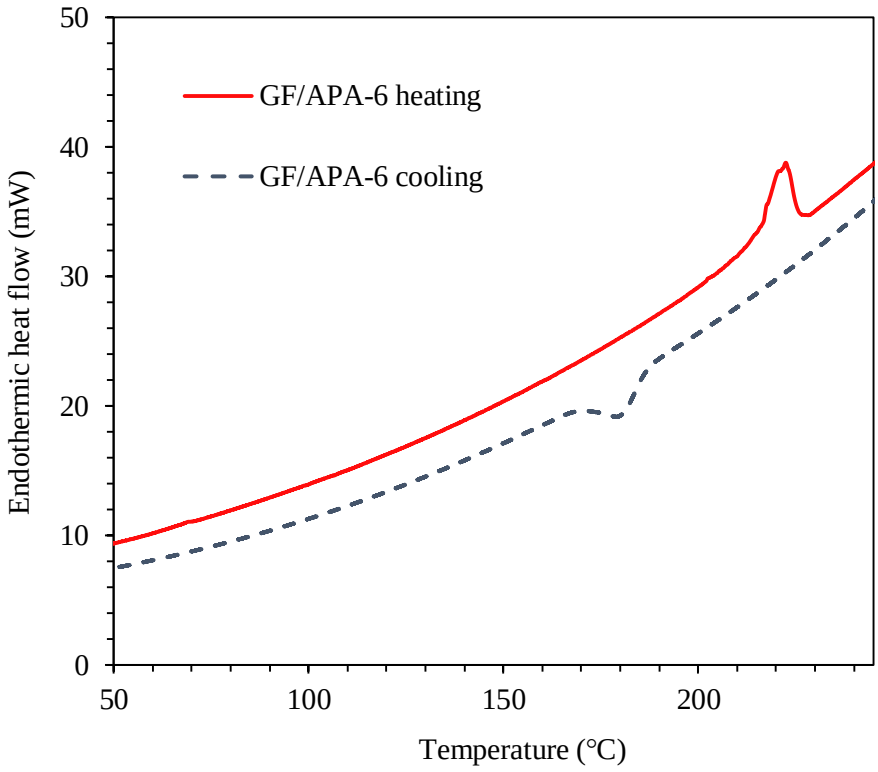

Fig. 5.15: Typical heat flow-temperature curves for the glass fibre reinforced APA-6.

Table 5.2: DSC results for the GF/APA-6 composite samples.

Plate	Melt peak temperature T_m (°C)	Enthalpy of fusion ΔH (J/g)	Avg. resin weight fraction W_p (%)	Degree of crystallinity as processed X_{c1} (%)	Degree of crystallinity after 10 °C/min. cooling X_{c2} (%)
A	221.7 ± 0.9	23.2 ± 0.9	29.0	44.8 ± 1.7	20.2 ± 1.1
B	221.4 ± 0.9	23.7 ± 0.9	28.4	45.7 ± 1.7	19.9 ± 1.1

5.4.7 Dynamic mechanical analysis

Results for DMA testing of the composite are shown in Fig. 5.16 and Table 5.3. The results show that the glass fibres significantly increase the T_g when compared to the pure polymer (shown in Table 4.3). The bonding of APA-6 hydrogen groups to the silane agent on the fibre surface would likely cause a reduction in mobility, hence increasing the T_g. Furthermore, a trans-crystalline interphase due to a local increase in the degree of crystallinity close to the fibre surface may further reduce mobility in this region [154].

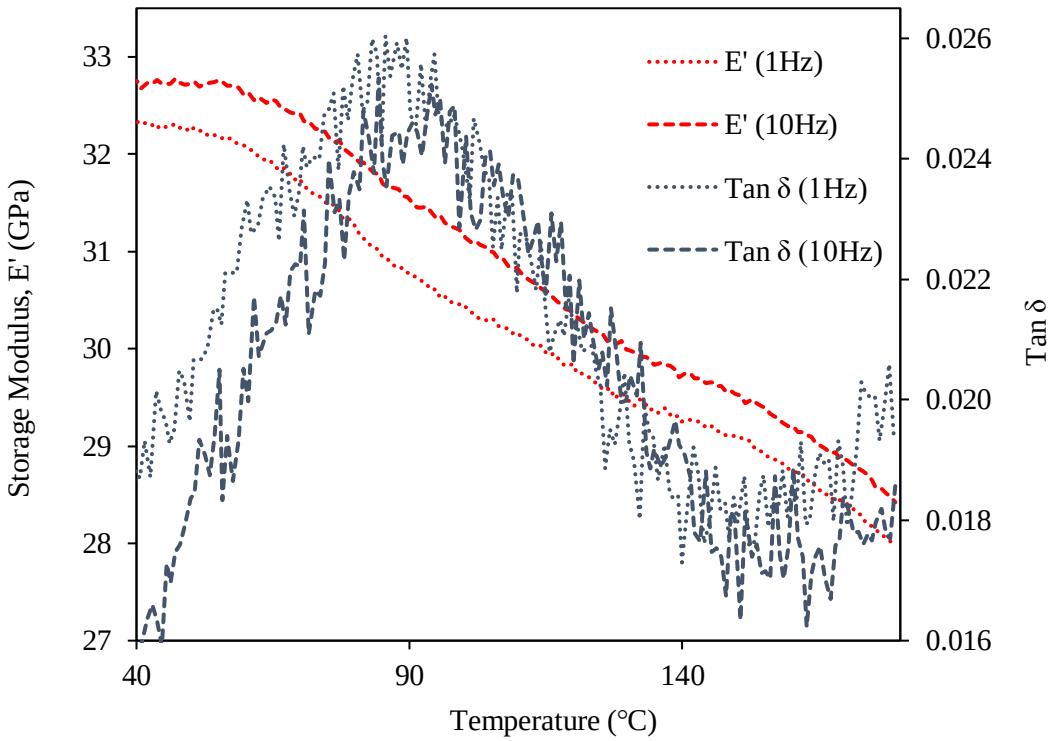

Fig. 5.16: DMA curves for storage modulus and tan δ at 1 Hz and 10 Hz.

Table 5.3: Glass transition temperatures from DMA tests as determined from the peak in loss modulus (Tg) and peak in tan δ ($T_{\tan\delta}$).

Plate	Tg	
	1Hz	10Hz
A	84.6 ± 1.9	87.0 ± 2.3
B	81.9 ± 5.6	85.5 ± 2.0

5.4.8 Mechanical properties

5.4.8.1 Transverse properties

The transverse properties of the GF/APA-6 composite determined from testing are summarised in Table 5.4 and representative stress-strain curves are presented in Fig. 5.17.

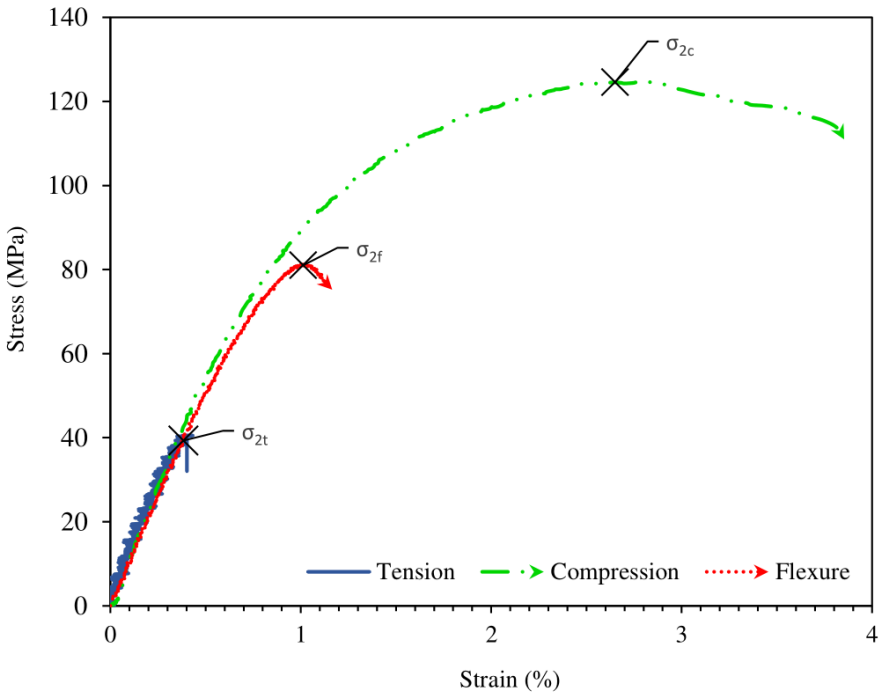

Fig. 5.17: Transverse mechanical test results of GF/APA-6 composite where $\boldsymbol{\sigma_{2t}}$, $\boldsymbol{\sigma_{2c}}$ and $\boldsymbol{\sigma_{2f}}$ represent the maximum transverse strength in tension, compression and flexure respectively.

Table 5.4: Transverse test results for the GF/APA-6 composite.

Test type	Maximum Strength (MPa)	Modulus (GPa)	Strain at break (%)
Tension (90°)	37.8 ± 2.4	10.6 ± 0.6	0.4 ± 0.0
Compression (90°)	134.7 ± 5.3	12.3 ± 0.9	2.7 ± 1.0
Flexural (90°)	82.8 ± 9.8	10.3 ± 0.5	1.1 ± 0.1

Transverse properties in unidirectional composites are dependent on a variety of factors including matrix and fibre properties, interfacial bond strength, the volume and distribution of voids, internal stress-strain distribution and in this case, the stitching [155]–[157]. The transverse tensile strength for the composite falls well below the tensile strength of the pure matrix. This can be explained by stress concentrations due to the fibres which peak midway between two fibres in the matrix. UD composites with fibre volume fractions of ~50% typically have a transverse strength reduction by a factor of ~2 with respect to the matrix tensile strength [155]. Due to high fibre volume fractions locally within bundles (as shown in Fig. 5.12), this factor must have an effect. The transverse strength is further reduced by material flaws, and for polymer matrices with non-linear stress-strain relationships (such as that of the pure APA-6 as shown in Fig. 5.17), the high strain at failure may cause other phenomena to occur which haven't been considered. In the areas where there is stitching every 5 mm along the ply width (~4/5 per ply per sample), the fibres are even more tightly packed. This, combined with a reduced local load bearing area due to voids at these bundle-stitch intersections, would likely act as an initiation point for failure (as demonstrated in Fig. 5.18). After initiation, it is likely that these cracks propagate along the fibre-matrix interface [155]. While the void content is below the critical value (~2%) mentioned in literature [158] at which transverse strength drops off significantly, the bulk distribution of voids occurs along the planes at the mentioned intersections. It is clear from Fig. 5.12 (a) that the stacking of bundles between plies is not staggered and it would be impractical to purposely do so in reality. Where bundles between plies are aligned, so are the voids along the same plane and as a result, the load bearing area is further reduced, resulting in weak regions in specimens.

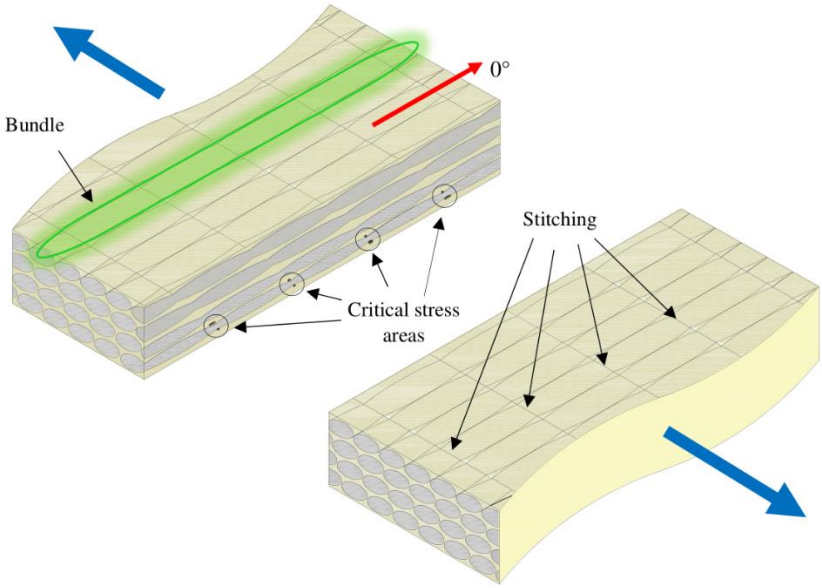

Fig. 5.18: Sketch of specimen loaded in tension in the transverse direction, demonstrating critical stress areas at stitch locations where the fibres are densely packed.

In compression, the transverse specimens mostly failed in shear along the gauge length. This failure is typical in unidirectional composites in the transverse direction [155]. In all cases, the shear plane of failure seems to have initiated between bundles on the outer surface and from there on, propagating both through and between bundles showing slight bias towards the latter path.

Flexural testing in the transverse direction resulted in failure occurring from the lower side of the specimen in tension at various locations showing bias towards inter-bundle failure in some cases. The flexural strength falls somewhere between the tensile and compressive strength values as expected.

5.4.8.2 Longitudinal properties

The longitudinal properties of the GF/APA-6 composite determined from testing are summarised in Table 5.5 and representative stress-strain data is presented in Fig. 5.19.

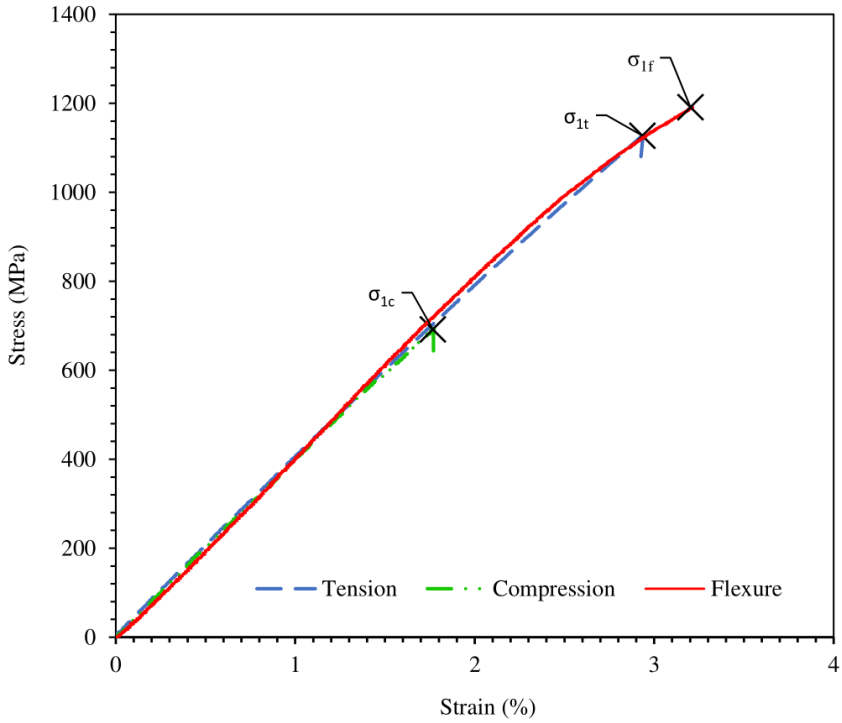

Fig. 5.19: Longitudinal mechanical test results of GF/APA-6 composite where $\boldsymbol{\sigma_{1t}}$, $\boldsymbol{\sigma_{1c}}$ and $\boldsymbol{\sigma_{1f}}$ represent the maximum longitudinal strength in tension, compression and flexure respectively.

Table 5.5: Longitudinal test results for the GF/APA-6 composite.

Test type	Maximum Strength (MPa)	Modulus (GPa)	Strain at break (%)
Tension (0°)	1108.9 ± 66.3	40.8 ± 1.3	2.9 ± 0.1
Compression (0°)	691.1 ± 70.3	42.2 ± 1.7	1.7 ± 0.2
Flexural (0°)	1148.8 ± 54.5	37.8 ± 1.8	3.2 ± 0.1

Compared to organo-sheet produced from GF/APA-6 tapes with ~50% fibre volume fraction [159], the tensile longitudinal modulus of the equivalent composite in the current study is lower by about 14% but its strength is higher by about 2%, and the strain-to-failure is higher by about 21%. The difference in modulus may be attributed to the fibre crimp introduced by the polyester stitching, which would also explain the higher strain-to-failure for the current study. At each stitch, the fibres are tightly packed**,** which causes a local reduction in fibre straightness. During extension of the samples in the longitudinal direction, straightening of these fibres may occur due to the allowance of transverse strain by the matrix, hence causing

larger composite strain and a reduction in modulus. In a study comparing UD carbon fibre epoxy composites manufactured from straight fibre tows versus those manufactured from an NCF, but using fibres with a similar modulus, it was shown that the modulus for the stitched case was inferior by ~ 10 % [160].

Consistent initial failure occurred across the entire sample set with either splitting through the laminate thickness or from an individual ply (i.e. delamination) such as that in Fig. 5.20 (a). In all cases, the cracks followed clear inter-bundle pathways through the matrix. In some cases, the samples were left in the grips at constant load after initial failure to observe failure progression across the entire specimen without applying any further load. Generally, this occurred within seconds after initial failure in an explosive fashion, though all breakage still occurred around bundles such as that shown in Fig. 5.20 (b). Due to their lower strain-to-failure, it is likely that the failure initiated in a fibre or across a bundle first, followed by propagation along an inter-bundle pathway. Due to voids at the bundle-stitch intersections, it is understandable that failure propagated along these pathways.

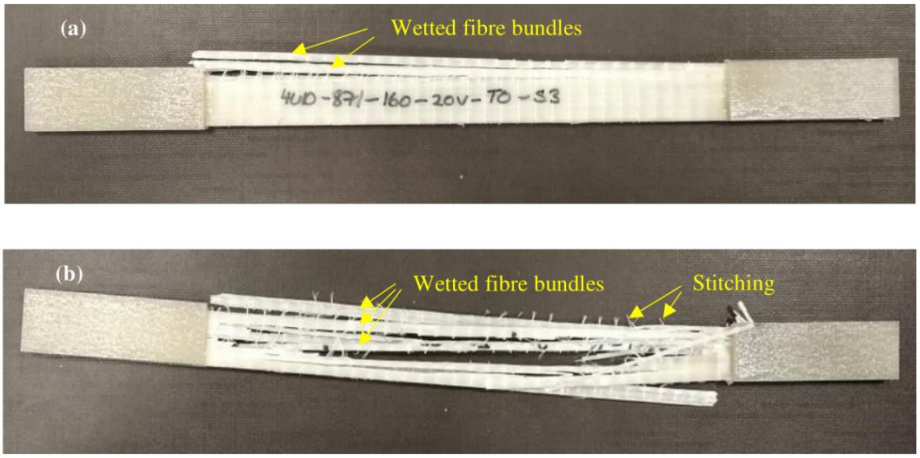

Fig. 5.20: Images of failed longitudinal tensile specimens after (a) initial failure, and (b) complete failure. In both cases, failure propagated along the matrix between wetted fibre bundles.

Compressive failure occurred mainly along the net section of specimens due to kinking. A closer observation revealed that the planes of kinking showed bias towards stitched areas where the voids were aligned. Due to the lack of local fibre straightness at stitched locations, the compressive strength is likely reduced; thus, the compression strength is dominated by the

shear modulus of the matrix, which is heavily dependent on the degree of crystallisation in the case of the APA-6 matrix [27].

The flexural samples failed at first in compression on the upper surface, which was expected as the compressive strength of the material is lower. Compared to commercial organo-sheet produced from GF/PA-6 tapes with ~50% fibre volume fraction, the mean compressive strength of samples in this work is slightly higher but the mean modulus when normalised is 12.4% less. It is suspected that the lower modulus is due to preliminary straightening of fibre bundles in the lower (tensioned) surface in a similar manner to that described for the tensile 0° samples, so the fibre bundles did not reinforce the specimens to their potential for the initial part of the test.

Scanning electron microscopy images taken of the specimens show the fracture surface in more detail and are described in Section 5.4.5. A summary of normalised composite mechanical properties are compared to those from commercial organo-sheet in Table 5.6.

Table 5.6: Average mechanical test results compared to commercially available PA-6 organo-sheet where the 0° results only have been normalised to 50% fibre volume fraction. The organo-sheet values are from various sources: * SGL GF-PA6 UD-tape [159], **Evonik VESTAPE [161], ***TenCate TC910 [162] normalised to a fibre volume fraction of ~50%.

	Strength (MPa)			Modulus (GPa)		
Mode	Organo-sheet	Normalised GF/APA-6	Increase	Organo-sheet	Normalised GF/APA-6	Increase
Tension (0°)	1050*	1070.4	+1.9%	46*	39.4	-14.3%
Tension (90°)	40**	37.8	-5.5%	7.1**	10.6	+49.3%
Compression (0°)	431***	667.1	+54.8%	-	40.7	-
Compression (90°)	-	134.7	-	-	12.3	-
Flexure (0°)	1085*	1117.5	+3%	42*	36.8	-12.4%
Flexure (90°)	65*	82.8	+27.4%	10*	10.3	+3%

5.4.9 Scanning electron microscopy

SEM images of the fractured surface of flexural specimens are shown in Fig. 5.21. The images clearly show the distinct inter-bundle matrix areas and intra-bundle fibre rich areas previously described. The former demonstrates ductile behaviour of the APA-6 polymer. There are signs of both clean fibre pull-out and remnants of polymer on the surface throughout samples, indicating a satisfactory degree of interfacial adhesion at the fibre-matrix interface. Interestingly, web-like networks were observed in areas across the fracture surfaces, which are believed to be polymer chain entanglements that were stretched during failure. The diameter of the entanglements were measured using *ImageJ* in various locations at higher magnifications and were shown to be in the nanoscale.

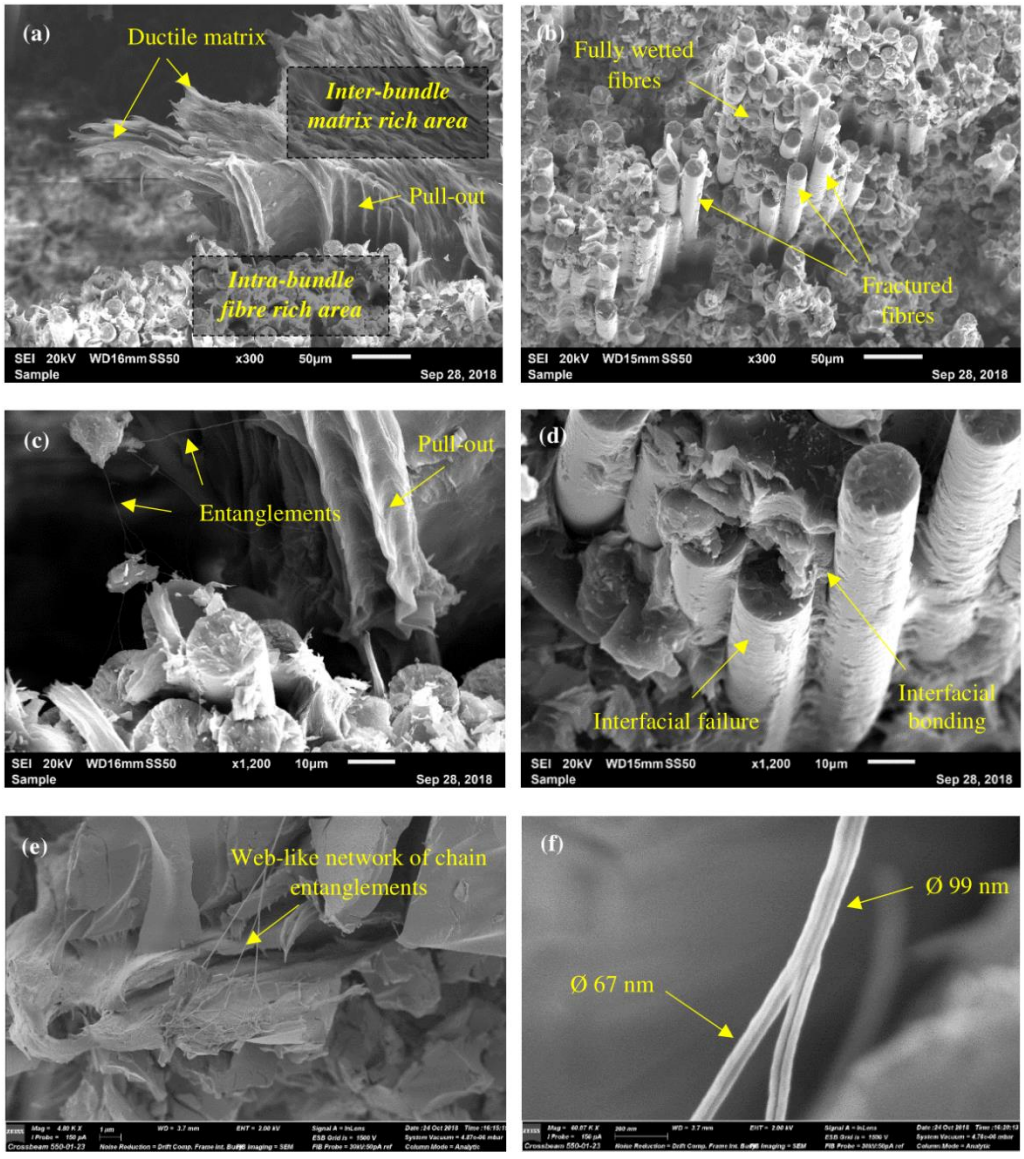

Fig. 5.21: SEM images of the fractured surface of GF/APA-6 flexural samples.

5.5 Conclusions

Glass fibre composite laminates were successfully manufactured using TP-RTM with fibre volume fractions ~51-52 %. One of the key challenges was the reduction of voids in the material. This was unachievable for vacuum infusion with the available resources, which resulted in poor wet-out of the fibre bundles. The fixed volumetric displacement of the gear pumps in the TP-RTM machine allowed for control of the flow rate through the textile. By restricting flow at the outlet, a sufficiently high back pressure was achieved in the cavity during filling. This, combined with the use of vacuum at the outlet, resulted in almost full wet-out of bundles; however, macro voids were present in the material due to the stitching.

The degree of crystallinity in the composite is higher than that for the pure polymer, possibly due to the presence of the fibres which conduct heat away from the polymer matrix during crystallisation. The glass transition temperature is also higher for the composite, likely due to the decreased mobility of chains as a result of bonding to the fibre sizing.

With the exception of transverse tensile strength, the mechanical properties of the GF/APA-6 material compared excellently with commercially available alternatives. The reason for the lower transverse strength is likely due to the high local density of fibres in the tightly packed bundles (due to stitching), which results in significant stress concentrations. SEM of the fractured surfaces revealed the ductile nature of the matrix during failure, suggesting promising behaviour for the composite in terms of fracture toughness and impact. These properties are discussed in depth in Chapters 6 and 7.

Chapter 6: Fibre-matrix interface

Summary

This chapter focuses on the interface between the fibres and the polymer matrix. Two different types of coatings on the surface of the fibres are studied using microscopic and pyrolytic techniques. Their effects on the composite properties are then investigated using mechanical testing.

6.1 Chapter Introduction and Overview

Up to this point, the polymer and composite cases were investigated. With the quality of the composite process optimised, a closer look was then taken at the interfacial adhesion between the fibre and matrix in the composite. This chapter focuses on fibre sizings used to improve this adhesive bond and how they affect the composite properties. Two different sizing cases were investigated using the same type of fibres. One of these contained a standard silane agent and the other contained a reactive agent which promotes chain growth from the fibre surface during polymerisation. This would theoretically improve the interfacial adhesion of the composite. This chapter discusses a number of techniques used to study the fibre sizings and determine their effects on the interfacial adhesion.

Scanning electron microscopy and atomic force microscopy were used to observe the distribution of sizing at both the micro-scale and nano-scale respectively. In some cases, the sizing was removed and the de-sized fibre looked at for comparison. Thermogravimetric analysis was used to determine the relationship between mass loss and temperature. In order to more accurately determine the amount of sizing on the fibres, larger quantity batches were used and mass loss was determined after burn-off and reflux extraction.

Composites were manufactured from both sizing types. Extensive quality assurance measures were put in place to compare the two cases in terms of voids and fibre packing density. This was considered important because these variables must be fixed so that the difference between the two cases can be almost exclusively attributed to the sizings. Transverse mechanical tests were carried out for each composite case and results were compared in terms of strength, stiffness and strain to failure. Double cantilever beam tests were conducted to determine the mode I fracture toughness of each. SEM images of the fractured surfaces were captured and the surface roughness across them identified. Short beam shear tests were carried out for each case in order to determine the interlaminar shear properties.

6.2 Materials and manufacturing

6.2.1 Materials and storage

The matrix material used in the manufacture of composites was the same as that used in Chapters 4 and 5. For this study, two different 640 g/m^2 unidirectional stitched glass fibre non-crimp fabrics (NCFs) were used. The fabrics, both provided by Johns Manville, were identical in terms of fibres, polyester stitching and areal weight. The only difference between the two was the sizing on the fibres' surface. The first contained rovings with a reactive sizing with the brand name StarRov® 886 RXN. The reactive sizing consisted of functional groups bonded to the fibre surface which act as initiation sites for chain growth during polymerisation. This would result in strong covalent bonding along the fibre-matrix interface which would theoretically result in superior mechanical performance for the composite. The control fabric used for comparison was that used in Chapter 5 (StarRov® 871) which consisted of rovings containing a standard silane agent compatible with APA-6. Both fabrics were supplied in the same form and stored in the same environment at room temperature. From now on, *886* and *871* will be used to denote the reactive and non-reactive sizings respectively.

6.2.2 Manufacture of APA-6 composites by TP-RTM

Composite laminates for tensile, flexural and short beam shear samples were manufactured using both the 886 and 871 fabrics with the exact same procedures as those described in section 5.2.3 using the final TP-RTM setup (shown in Fig. 3.17) at The University of Edinburgh. The measures taken in section 5.2.4 to minimise voids were implemented such that optimum conditions would be achieved. The same injection and vacuum pressures were used for both cases. The samples for the double cantilever beam tests were extracted from laminates manufactured using the same TP-RTM machine and mould but using a 4 mm cavity instead of the 2 mm used for all previous laminates. These laminates consisted of 8 plies for each case. A non-adhesive insert was placed at the mid-plane through the thickness to act as a delamination initiator. The insert material used was a Teflon PFA film supplied by Lohmann Technologies with a thickness of 12.7 μm.

6.2.3 Sample preparation

Due to their simple rectangular geometry, all composite samples were cut using a diamond blade cutting saw with coolant at a feed rate of ~300 mm/min with the exception of DSC

samples, which were cut using a Stanley knife blade. DCB specimens were prepared in accordance with *ASTM D5528 – 13* using bored loading blocks to apply the opening force. Each sample (~3.8 mm x 25 mm x 170 mm) was cut such that the bore at the centre of the loading block (load line) would be 50 mm from the insert tip (crack initiation site) as shown in Fig. 6.1. The blocks were 25 mm x 25 mm x 15 mm, made from stainless steel and bored in the centre with a 6.1 mm diameter hole for a 6.0 mm pin. The bonding surfaces of the blocks and specimens were sanded using rough grit size sandpaper and cleaned with acetone prior to adhesion to the specimens. Polyolefin primer (Loctite 770) was applied to the surfaces, followed by bonding using a cyanoacrylate adhesive (Loctite 406). All samples were then dried under vacuum for 24 h at 50 °C and stored in either sealed polybags or tupperware with desiccant until testing.

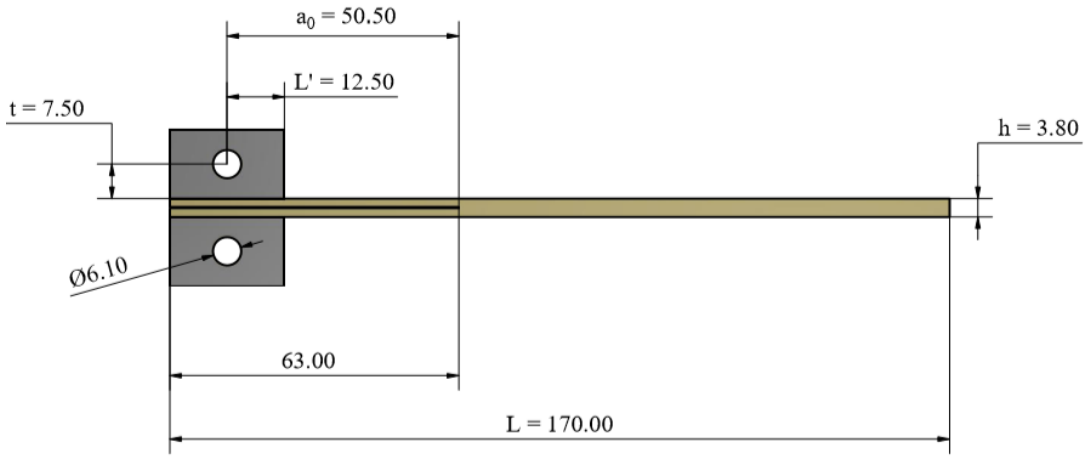

Fig. 6.1: Dimensions of the DCB specimens and loading blocks. Note that the width of specimens was 25 mm (into the page).

6.3 Analysis and testing

6.3.1 Fibre and sizing analysis

6.3.1.1 Thermogravimetric analysis

Thermogravimetric analysis (TGA) was completed using a Mettler Toledo TGA/DSC1. The experiment was completed in air and repeated in nitrogen using approximately 30 mg of fibres chopped into 5 mm long pieces. The temperature cycle selected was a constant ramp rate of 10 °C/min from 30 °C to 600 °C. Thereby, the mass of the sizing (and any other agents) present on the glass was found.

6.3.1.2 Burn-off of sizing

Approximately 10 g of conditioned fibres for each fibre type was subject to incineration with a temperature ramp of 10 °C/min from 30 °C to 600 °C followed by an isotherm at 600 °C for 30 mins. Following this, the samples were cooled in the furnace to a temperature of 110 °C, after which the new mass was recorded. This ensured the specimens did not have enough time to absorb moisture at any point prior to weighing. An analytical balance was used to record masses and a Nabertherm Muffle Furnace was used to complete the incineration.

6.3.1.3 Condensation reflux extraction

Prior to studying the effects of the fibre sizing on the composite properties, it was first necessary to view the nature of the fibres and the distribution of sizing on their surface using scanning electron microscopy and atomic force microscopy. In addition to the fibres with the two different sizings (871 and 886), microscopy was also carried out on de-sized fibres to allow for a more robust comparison. The de-sized fibres were prepared by dissolving the sizing from the fibre surface using condensation reflux extraction. The apparatus for extraction consisted of a round-bottom boiling flask containing a solvent and a condenser with a heat-exchanging element. The boiling flask was heated using a heating mantle such that the solvent was excited to a vigorous boil and evaporated into the condenser, whereupon it condensed on contact with the cold heat exchanger. In this experiment, approximately 10 g of fibre cut into 50 mm long tows was added to the flask for each batch. 250 ml of acetone was used as the solvent, water was used as the cooling medium in the condenser and the reflux was run for 24 h. As well as being used for preparing de-sized sample for microscopy, this method was also used to deduct the mass of the sizing on fibres. In doing so, the fibres were dried and weighed using an analytical balance both before and after extraction to determine the mass loss which was attributed to the sizing.

6.3.1.4 Scanning electron microscopy of fibres

For each of the fibre sizing cases, individual fibres were carefully removed from bundles using a tweezers and cut to lengths of ~20 mm using a scissors. The unsized fibres were prepared by burn-off using methods described in section 6.3.1.2. The stage for the SEM was removed and cleaned with acetone which was allowed to evaporate. A number of fibre samples for each case were placed on the SEM stage in separate batches. The stage was placed in the Hitachi TM4000Plus SEM and the samples were viewed at magnifications of 4,000 x using an accelerating voltage of 2 kV.

6.3.1.5 Atomic force microscopy of fibres

Atomic force microscopy (AFM) was utilised to image the surface of each of the three fibre cases at the nanoscale. All imaging was performed in tapping mode using a Bruker-JPK Nanowizard 4 (Bruker, Santa Barbara, CA, USA) in air at ambient conditions. Bruker RTESPA cantilevers with a spring constant of 40 N/m and a nominal tip radius of 2 nm were used for all imaging. As the fibres had relatively small diameters, the scan size for each image was 1 μm^2. Height and 3D images were obtained for the three fibre types. Furthermore, profile plots were obtained from the height images which showed the surface topography of each fibre in greater detail. The average arithmetic surface roughness (Ra) was calculated from at least four separate images for each fibre type. The profile plots and surface roughness values were obtained after the AFM images had undergone flattening in order to reduce any influence from the fibre curvature.

6.3.2 Composite analysis

6.3.2.1 Geometric characterisation and density

In order to carry out a fair comparative study between the two different cases, it was important to ensure that all other factors were as close to constant as practically possible. The quality assurance methods used in section 5.3.1 were used to measure these. Thickness, density, fibre volume and void volume fraction/distribution were determined using the exact methods described in sections 5.3.3, 5.3.4 and 5.3.6. Due to the effects of fibre packing density in bundles, it was essential to make sure that the staggering of bundles in both cases was similar before comparing transverse properties.

6.3.2.2 Polymer matrix characterisation

The quality of the polymer matrix was monitored in a similar manner to the geometric properties. It was characterised by the degree of conversion, degree of crystallinity, melt temperature and glass transition temperature; determined using experimental techniques described in sections 5.3.7, 5.3.8 and 5.3.9. It was important to study the polymer quality as it was likely to be affected by the reactive sizing on the fibres' surface. It should be noted that a cyclic loading frequency of only 10 Hz was used for DMA testing to determine the glass transition temperature due to the lower standard deviations in general compared to those tested at 1 Hz.

6.3.2.3 Transverse properties

One of the best ways to determine the interfacial performance in unidirectional composite is by testing samples in the transverse direction to the fibres. Transverse testing takes practical problems previously discussed into account such as the fibre packing density and voids due to stitching. Transverse testing was carried out for both cases in tension and flexure using the procedures described in sections 5.3.10 and 5.3.11 respectively.

6.3.2.4 Double cantilever beam testing

Double cantilever beam (DCB) tests are mainly used to measure the Mode I fracture toughness of a composite or other adhesively bonded material. While fracture toughness is something of interest in general for the GF/APA-6 material, the DCB test can also be used as a method for measuring the strength of the interface. The tests were carried out in accordance with *ASTM D5528 − 13* on an Instron 3369 using a 1 kN load cell. Loading pin fixtures were tightened in the wedge grips of the machine and checks were carried out to ensure they were correctly aligned and that 5 degrees of freedom were constrained, only allowing movement in the vertical direction. The specimens used in these tests were fully consolidated at one end but split in two halves at the other end, separated during manufacture by a thin insert as described in section 6.2.2. During bonding, the 25 mm wide loading blocks were aligned flush with the outer split end of the specimen, 63 mm from the initial crack tip at the insert. With the bore hole positioned 12.5 mm away from the split end, the initial delamination length was ~50.5 mm for all specimens with respect to the load line. As a result of small variations in this length due to combined errors in manufacturing, cutting, boring and positioning during bonding; it was necessary to locate the exact length for each specimen. To do so, the samples were placed

under a stereo microscope and the insert tip was located and marked on both sides. A line was drawn across the top of specimens joining the two and the variation in delamination length between the sides was recorded (less than 0.5 mm in all cases). To track the crack length during testing, the IMETRUM video gauge was used. As with previous tests using this equipment, it was required to create visual contrast on samples, and so, a white marker was used to paint the edges prior to application of a black speckled pattern. Unlike strain measurements which are dimensionless, for crack length, it was necessary to calibrate the system input from the camera and output to the Intron machine such that exact measurements for crack length could be recorded. The crosshead was positioned such that the distance between pins was the same as that between the specimen holes. The samples were placed on the pins and the displacement was jogged until the load cell reading was ~ 0 N. The samples were tested at a crosshead speed of 1 mm/min. Due to the large opening displacements (δ) with respect to crack length, correction factors (F and N) were incorporated in the data reduction in accordance with Annex A1 in the test standard. F and N were defined by equations 6.1 and 6.2 where g and L' are the distances of the bore hole from the bottom and side of the block respectively as shown in Fig. 6.1. The modified beam theory was used to account for rotation at the delamination front. This required definition of a value Δ by generating a relationship between the modified compliance ratio (C/N) and the crack length (a) as discussed in the test standard using Annex A1. The corrected fracture toughness (G_1) was then calculated using equation 6.3.

$$F = 1 - \frac{3}{10}\left(\frac{\delta}{a}\right)^2 - \frac{3}{2}\left(\frac{\delta g}{a^2}\right) \tag{6.1}$$

$$N = 1 - \left(\frac{L'}{a}\right)^3 - \frac{9}{8}\left[1 - \left(\frac{L'}{a}\right)^2\right]\left(\frac{\delta g}{a^2}\right) - \frac{9}{35}\left(\frac{\delta}{a}\right)^2 \tag{6.2}$$

$$G_1 = \frac{F}{N} \times \frac{3P\delta}{2b(a+|\Delta|)} \tag{6.3}$$

Toughness at crack initiation was determined visually ($G_{1c\,VIS}$) with the camera and at maximum load ($G_{1c\,Max}$). Due to seemingly complete linearity in the load-displacement relationship up to the point where crack initiation was observed visually, the fracture toughness at deviation from linearity ($G_{1c\,NL}$) was not the most conservative of the methods prescribed in the test standard. For this reason, combined with the large error in determining its location, it was left out of the analysis. Average crack propagation values ($G_{1p\,Avg}$) were taken beyond the maximum load over a crack length of 10 mm for each.

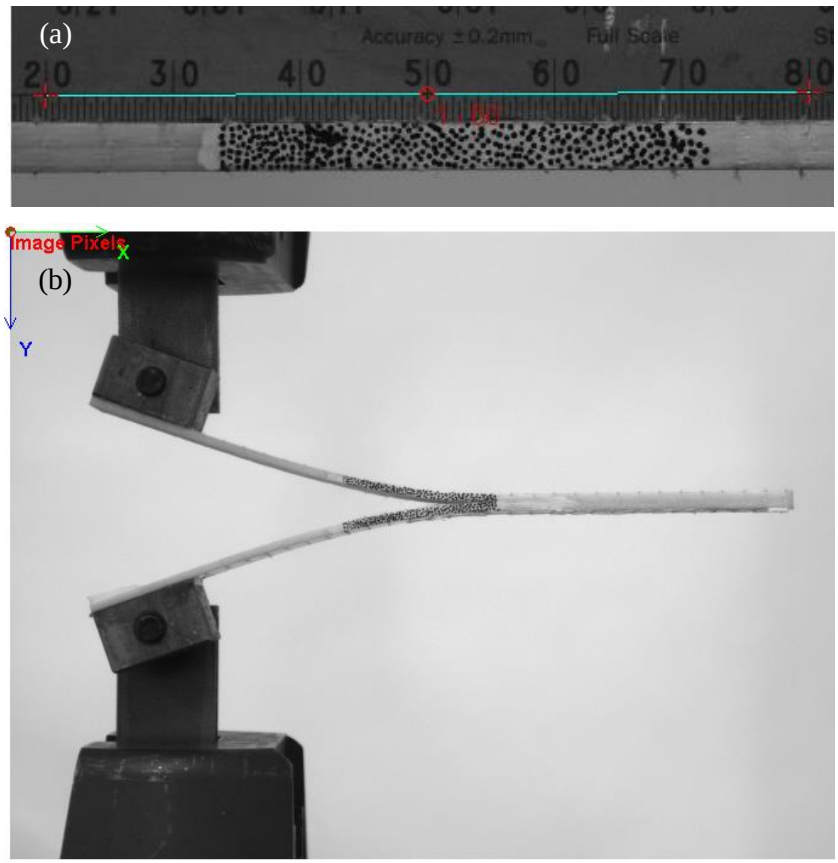

Fig. 6.2: (a) Calibration of length values on camera for tracking crack length and (b) Image of a DCB test running.

6.3.2.5 Surface Roughness

The surface roughness of tested DCB specimens was measured using a Keyence VHX 7000 digital microscope by taking multiple images and stitching them together. Multi-focus image fusion (or 3D depth composition) was used to obtain optimum focus at different depths and a 3D image was generated. Imaging was carried out over a focused area of 4 bundles (shown in Fig 6.3 (a)) at high magnifications and was carried out over the entire sample width (shown in Fig 6.3 (b)) at lower magnifications. Surface plots were generated at various cross sections across specimens at both magnifications (shown in Fig. 6.3 (c)-(d)), both in the tested crack area and in the area where the insert was placed. The surface roughness was plotted over a width of three bundles from crest to crest with the "zero height" datum positioned at the average height for each case. The surface roughness was defined using two parameters: Ra, the mean deviation from the average and Rq, the root mean square parameter.

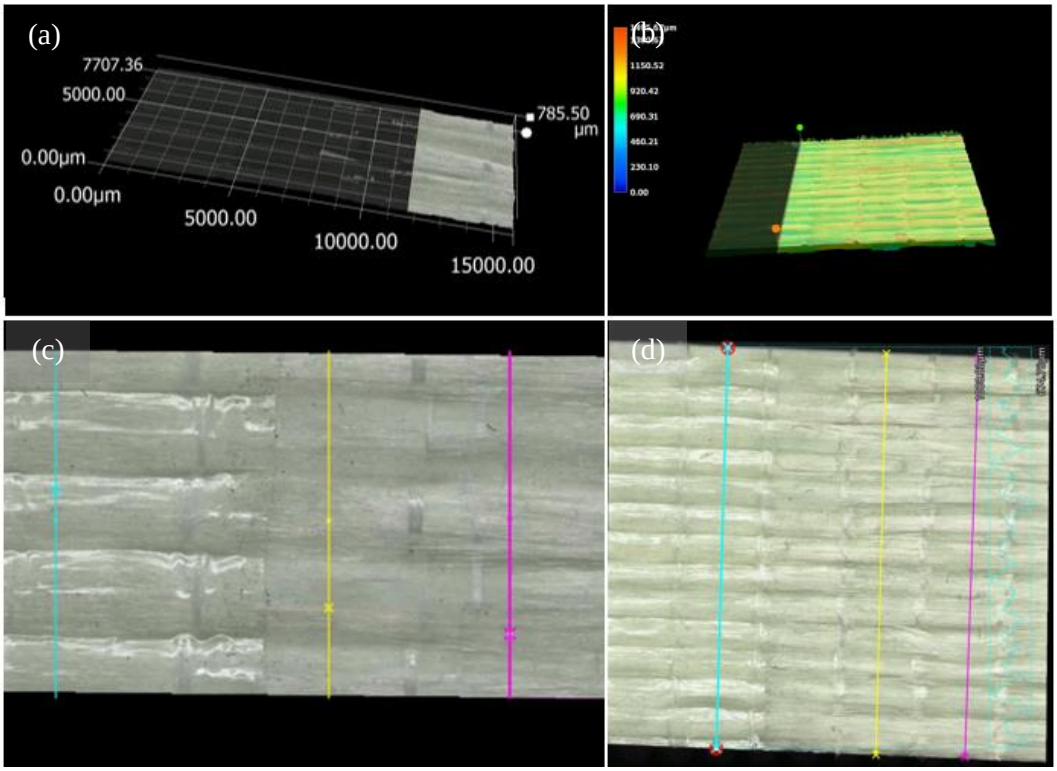

Fig 6.3: Surface roughness techniques applied to stitched images with multi-focus image fusion.

6.3.2.6 Short beam shear testing

Short beam shear tests were carried out in an attempt to determine the apparent interlaminar shear strength (ILSS). The tests were carried out in accordance with *ASTM D2344/D2344M – 16* using a three-point bending fixture with the preferred loading support/nose radii, specimen dimensions (24 mm x 8 mm x 4 mm) and span of 10 mm as shown in Fig. 6.4. The tests were carried out on an Instron 3369 screw-driven machine with a 10 kN load cell. A crosshead speed of 1 mm/min was used and samples were tested up to the limits of the load cell (~10 kN).

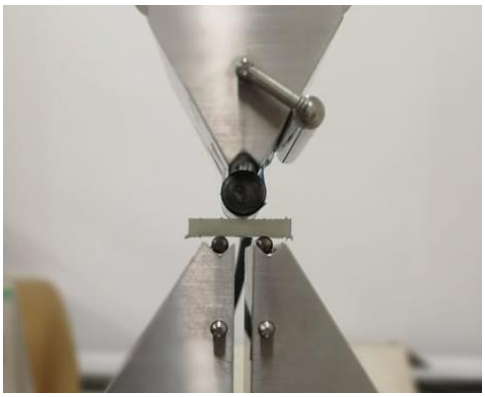

Fig 6.4: Setup for short beam shear testing.

6.4 Results

6.4.1 Fibre and sizing results

6.4.1.1 Mass loss

The results for TGA are shown in Fig. 6.5. There is no volatile mass loss in the water vaporisation region (~100 °C) which proves that the specimens were appropriately conditioned prior to the experiment. In this case, the measured change in mass can be attributed to the mass of the sizing and other relevant agents. Based on how small the mass losses are as a percentage of the sample size from TGA, the error is likely to be quite large using this technique; however, the sample size cannot be increased due to the limited amount of material that the crucibles can hold. For this reason, TGA may not be the most accurate for determining the amount of sizing on each fibre but is good at identifying the temperatures at which mass loss changes occur. This was captured much more accurately by burn-off as much larger samples were used.

The mass loss over time from TGA can be observed in Fig. 6.5. The main area of interest is that between 130 °C and 200 °C as this is the temperature range where polymerisation occurs. Initially, both lose very little mass; however, the rate of loss in the 886 RXN in air increases above ~ 178 °C and that for the 871 in air increases above ~ 190 °C. If the exotherm in the mould causes temperatures to rise to this degree, there is a possibility that the sizing may become damaged. If this is the case, it would reduce the sizing's effectiveness in increasing the interfacial strength. The mass loss for both cases was observed to be marginally smaller in the nitrogen environment, which suggests there is minor oxidation occurring in both cases in air. The conditions in nitrogen would be more similar to the conditions in the mould cavity under vacuum during processing as oxygen isn't available for oxidation to occur. Due to the flow of nitrogen into the TGA chamber, the mass loss readings fluctuated a lot, leading to the noisy data in Fig. 6.5 for the fibres in nitrogen.

The total mass loss after TGA, Burn-off and reflux extraction are given in Table 6.1. All techniques showed that the amount of 886 on fibres by mass was less than that on the 871 but only by a small fraction. The mass loss using burn-off was noticeably greater than that using reflux extraction. It is possible that the acetone can't dissolve the sizings in full. Overall, the analysis would suggest that the amount of 886 sizing on fibres is slightly more by mass than the 871. The sizing makes up ~0.5 % of the total weight on fibres. This is slightly more than the 0.3 % value stated for each in the Johns Manville data sheets. It is likely that the distribution varies for different test samples and that the different test methods used have different errors.

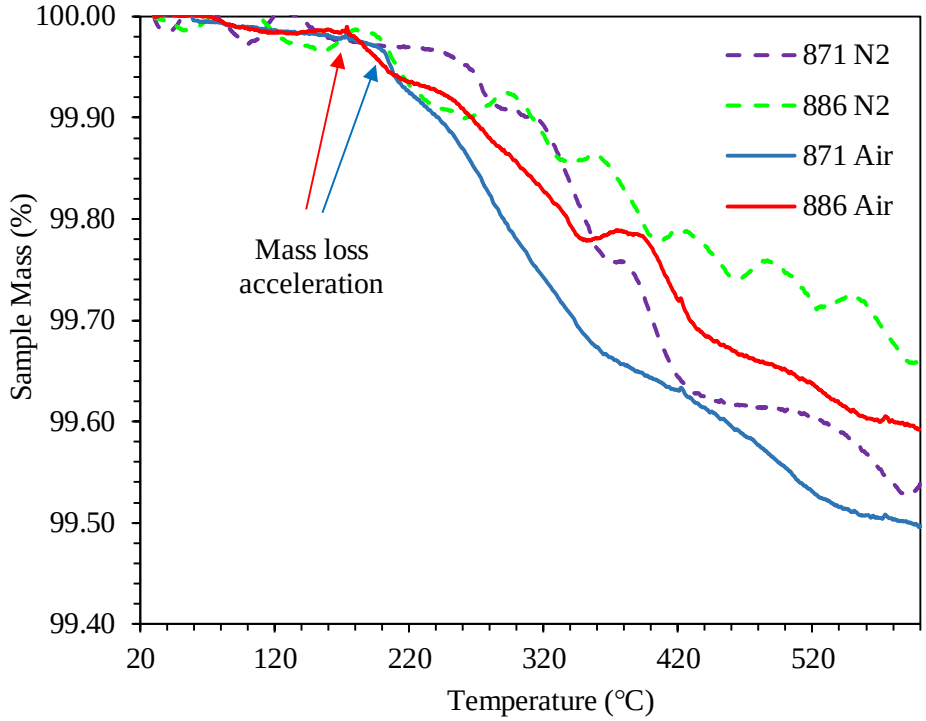

Fig. 6.5: TGA curves for the 871 and 886 RXN sizings in air and nitrogen.

Table 6.1: Mass loss determined using TGA (in air and nitrogen), burn-off and reflux.

Sizing	M_{loss} (%)			
	TGA (air)	TGA (N_2)	Burn-off	Reflux
871	0.49	0.45	0.50 ± 0.03	0.32 ± 0.11
886	0.38	0.35	0.45 ± 0.09	0.29 ± 0.15

6.4.1.2 Scanning electron microscopy

Representative SEM images of the 871, 886 and unsized fibres are shown in Fig. 6.6. Differences in topography (surface roughness) of the sizings can be observed from the three images. It is clear from observation of Fig. 6.6 (a) that the distribution of sizing on the 871 is discontinuous and contains agglomerations, whereas that for the 886 shown in Fig. 6.6 (b) is even and overall, very smooth. The discontinuous distribution on the former may cause non-uniform interfacial interactions which could negatively affect the adhesion strength of the composite; however, the strength on average may be improved due to mechanical interlocking caused by the surface roughness [163]. The diameter of the fibres (and sizing) was measured from 5 samples for each case. The measured diameter of the 871 was 15.94 ± 1.18 µm, that for the 886 was 17.70 ± 0.07 µm and that for the unsized was 15.62 ± 0.79 µm. Admittedly,

there was no certainty as to how flat each of the fibres were lying on the stage. Visual perspective would present deceptive results where fibres are at different elevations from the stage. Unsurprisingly, the 871 has the highest standard deviation as a result of the discontinuous spread on the fibres. The unsized fibres had the lowest diameter as expected. The amount of sizing on the 886 fibres was more than that on the 871 which was surprising based on the mass loss results. Perhaps the 871 sizing is more dense than that the 886 sizing.

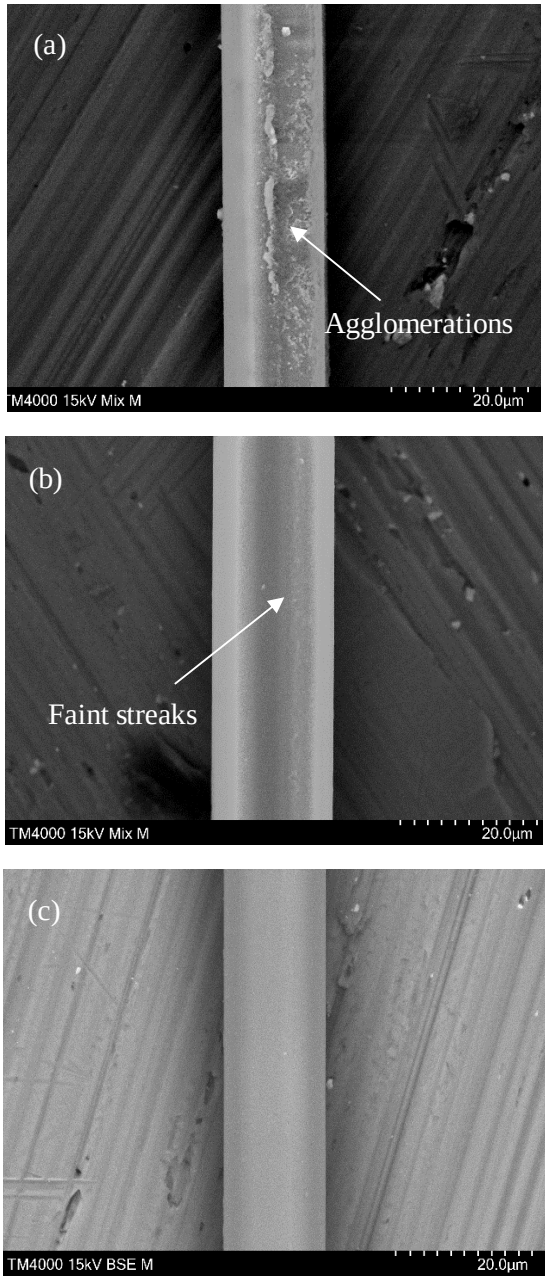

Fig. 6.6: SEM images of fibre sizing distribution on (a) 871, (b) 886 RXN cases and (c) unsized case.

6.4.1.3 Atomic force microscopy

Fig. 6.7 shows representative AFM height images for each fibre type with corresponding profile plots (represented by the two horizontal lines across each image) which show the surface of the fibres in greater detail. Additionally, Fig. 6.7 also presents corresponding 3D images (not flattened) which clearly show the surface topography of the sizing on the curved fibres. It demonstrates that the topography of the sizing was very different on each fibre type. On the unsized fibres (Fig. 6.7 (a) – (c)), the topography is mostly smooth with only a few discernible features which have a maximum height of around 10 nm. These features are possibly small remnants of the original sizing. The unsized samples were prepared using the reflux condensation method described in section 6.3.1.3 and perhaps not all the sizing was removed during extraction. However, despite this, the unsized fibres were still extremely smooth with an average surface roughness of 0.8 nm. The sizing on the 871 fibres (Fig. 6.7 (d) – (f)) formed a distinct dendritic structure with a height that generally ranged from 5 – 15 nm. The dendritic structure was very homogeneous across large areas of the fibre surface (see Appendix E) and the average surface roughness of the 871 fibres was 3.5 nm. In contrast, the sizing on the 886 fibres (Fig. 6.7 (g) – (i)) had a very different surface topography. The sizing appeared to form fairly large aggregates which were sporadically located across the fibre surfaces. Elsewhere, the distribution was relatively smooth and therefore, the surface in these areas was very flat. This is clearly observed in the 3D image (Fig. 6.7 (i)) which shows a few large aggregates located on an otherwise fairly smooth fibre surface. The average surface roughness of the 886 fibres was 2.7 nm. The AFM results suggests that the nature of the 886 sizing and 871 sizing are quite different on the fibres. The 871 sizing has a very distinct pattern whereas the 886 sizing forms irregular aggregates with larger heights which are sporadically positioned on the surface. AFM phase images for each of the fibre types which provide qualitative information regarding the viscoelastic properties of the fibre surfaces are included in Appendix E.

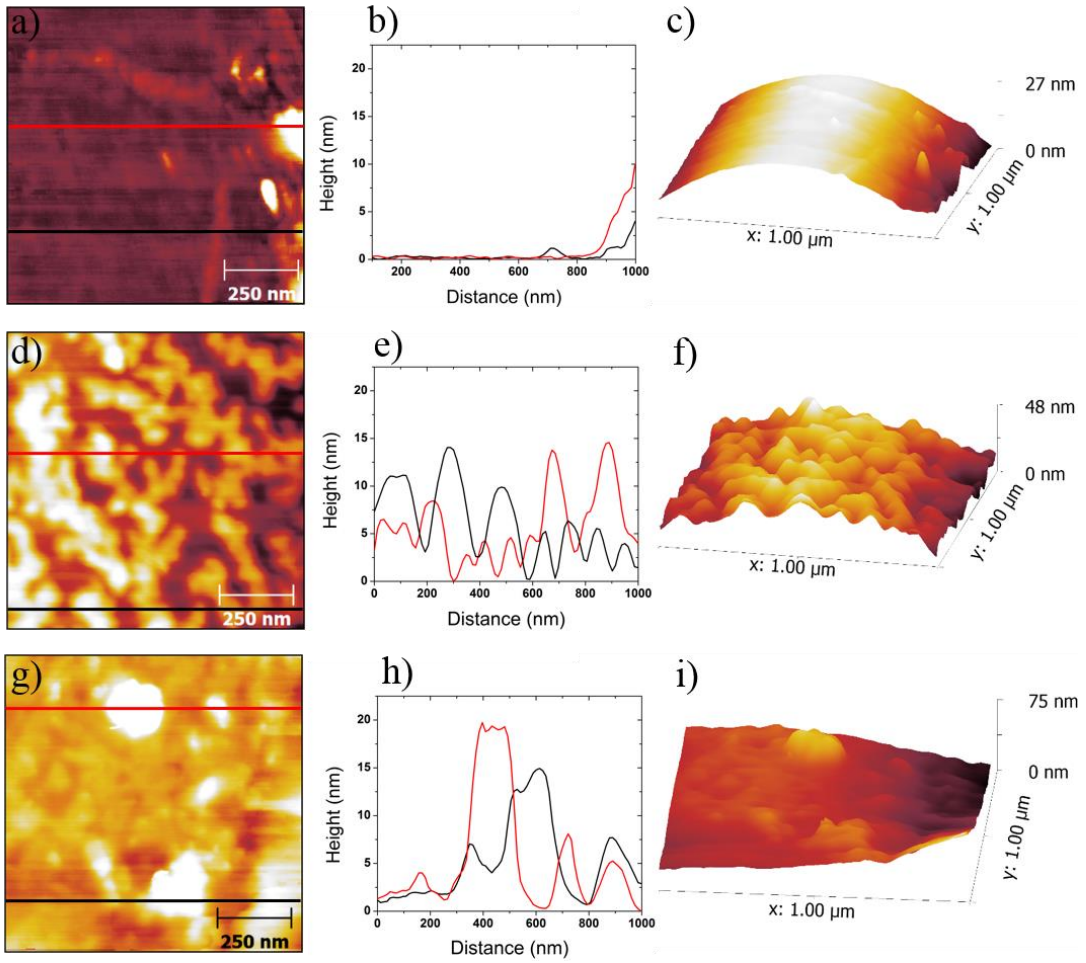

Fig. 6.7: Typical flattened AFM height images of each fibre type with corresponding profile plots and non-flattened 3D height images. (a) Height image of the desized fibre, (b) profile plot of the desized fibre, (c) 3D image of the desized fibre, d) height image of the 871 fibre, (e) profile plot of the 871 fibre, (f) 3D image of the 871 fibre, (g) height image of the 886 fibre, (h) profile plot of the 886 fibre, (i) 3D image of the 886 fibre.

6.4.2 Composite analysis

6.4.2.1 Geometric characterisation and density

The quality assessment results for composites manufactured using the 886 and 871 fabrics are summarised in Table 6.2. Firstly, there is a clear difference in the thickness between the two composites. This was noticed in almost all manufactured composites. This was attributed to the sizing on the 886 fires, which contained initiating agent. This would have caused an additional number of chains to grow; particularly at the interface, which might be the cause for the higher density in the 886 composite.

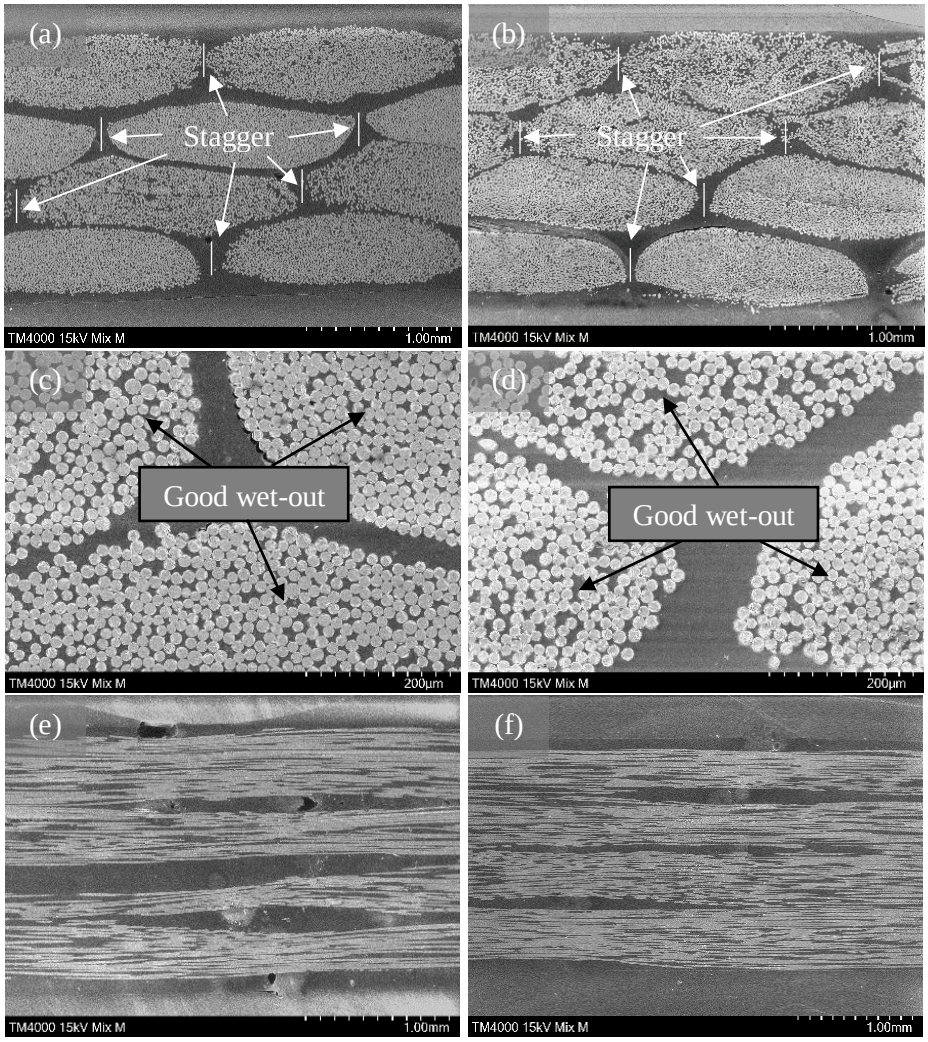

Fig. 6.8: SEM of the 886 (left) and 871 (right) composites cases taken at surfaces perpendicular to the fibre direction [(a), (b), (c) and (d)] and parallell to the fibre direction [(e) and (f)].

The results from SEM carried out on cross-sections of each are shown in Fig. 6.8. It is clear from Fig. 6.8 (a) and (b) that the staggering of the bundles for the 886 and 871 is almost identical for both. The reason for the less densely packed bundles in the upper plies of the 871 case is due to their distance from the next stitch. There is only indication of very minor macro voids in each case, which occurs at the stitching while Fig. 6.8 (c) and (d) show the wet-out of bundles is excellent with no indication of any significant micro voids in either. Fig. 6.8 (e) and (f) is a view which observes the fibre in the transverse direction. The former indicates macro voids but only at the stitch. The reason this is observed in the former but not in the latter is due to the depth (into the page) that the sample were cut/polished. The former shot has been taken at a section which is close to resin rich trenches for most of the bundles as described in section 5.3.6. This is indicated by the relatively low fibre volume fraction in the image compared to the equivalent for the 871 case.

Table 6.2: Quality assessed results in terms of thickness, density, fibre and void fractions for the 886 and 871 composites.

Material	Thickness (mm)	Density (g/cm^3)	Fibre volume fraction (%)	Void volume fraction (%)
APA-6/871	1.93 ± 0.02	1.882 ± 0.025	51.8 ± 1.9	1.1 ± 0.4
APA-6/886	1.86 ± 0.03	1.906 ± 0.018	53.7 ± 1.0	1.3 ± 0.6

6.4.2.2 Polymer matrix characterisation

The results for degree of conversion, degree of crystallinity, melt temperature and glass transition temperature are presented in Table 6.3. The average value of conversion for the 886 is 2 % less than that for the 871 material. This drop is possibly due to the reactive sizing which acts as an initiation site for chain growth. The effects of the sizing on the matrix properties would be similar to adding additional initiator to the system as described in section 4.2.2; however, these effects would only apply to the polymer right at the fibre surface, creating a sort of interphase, with chains growing radially from the fibre surface. The initiation process involves the addition of impurities to the matrix in the form of oligomers, and so, would likely reduce the degree of conversion [56]. Due to the larger number of chains but unchanged amount of monomer available during polymerisation, the chain length is likely shortened, reducing the average molecular weight. Ironically, this would result in a lower polymer toughness which would partly go against the reason for using it in the first place. The average

glass transition temperature is only slightly higher for the 886 case, though barely significant statistically. Even though lower molecular weight is generally associated with a lower T_g in accordance with the Flory-Fox relationship [164], the increased restriction in mobility may counteract this with an upward shift in the temperature required for mobilisation. Typical DSC curves for both cases are shown in Fig. 6.9. The degree of crystallinity for both cases are similar and considering the large error (due to numerous dependencies) in the method to calculate values, greater conclusion from these results would be rudimentary. Overall, no significant differences were identified between the matrix in the 886 and 871 composite.

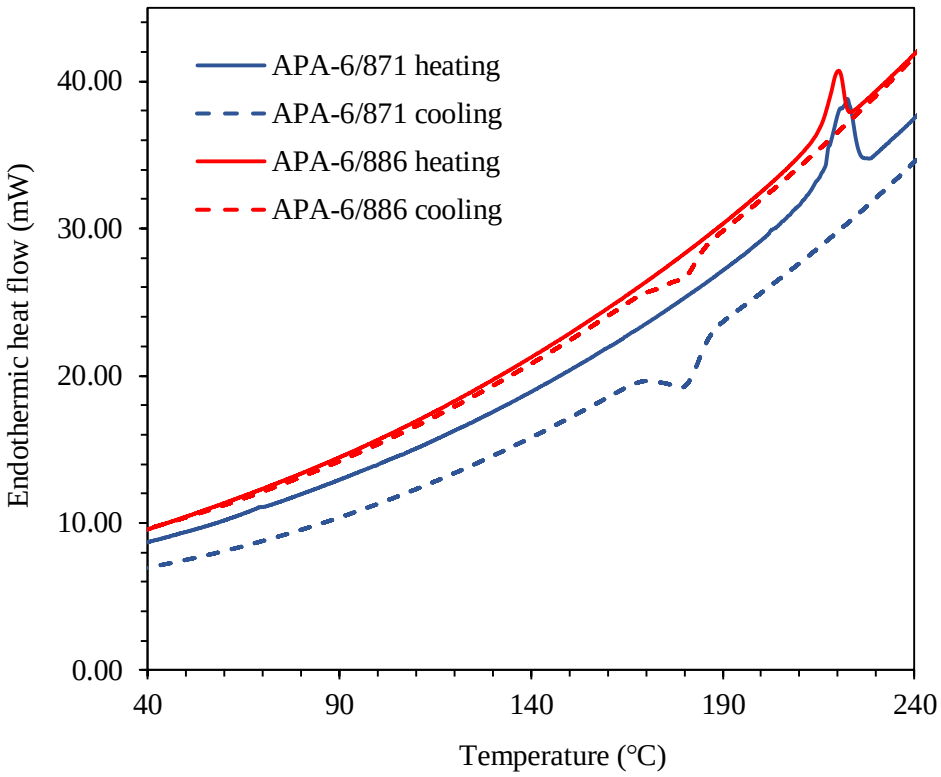

Fig. 6.9: DSC curves for the 871 and 886 composites.

Table 6.3: Matrix properties for 886 and 871 composites.

Material	Average degree of conversion (%)	Average degree of crystallinity (%)	Melt temperature (°C)	Glass transition temperature (°C)
APA-6/871	96.9	44.8	221.4 ± 0.9	85.5 ± 2.0
APA-6/886	94.9	43.3	219.8 ± 0.3	87.5 ± 2.1

6.4.2.3 Transverse properties

Results from transverse tensile and flexural tests are presented in Table 6.3 and Fig. 6.10 in terms of strength, modulus and strain at maximum strength. Properties for the pure matrix and a commercial organosheet are included to contextualise results. The tensile strength of the 886 composites was higher than the 871 composite. While the difference in modulus between the two was practically negligible, the increased strength and slight increase in strain to failure indicate possible signs that the reactive sizing in enhancing performance. The flexural strength was notably higher for the 886 case compared to the 871. It is believed however that undesired effects due to the stitching have a greater influence in flexure due to the dependency of flexural properties on the distance of fibres from the neutral axis. For example, a composite with fibres towards the outer surface (where the highest stresses and strains are experienced) result in a higher performing composite than one with the exact same fibre fraction but with fibres more concentrated towards the neutral axis. As such, the tensile results likely give a clearer indication as to which sizing performs better. Further investigation of the bundle/sizing effects was beyond the scope of this project. Fig. 6.13 (a) and (c) show SEM images of representative transverse tensile fracture surfaces for the two cases. Overall, there isn't a big difference in appearance between the two. Fibre tracks are more visible in the 871 case which indicates cleaner pull-out, and hence, adhesive failure. The agglomerations of ductile matrix drawn from around the fibre surface are smaller for the 886 but have a more fibrous nature, possibly indicating more local sites with superior bonding.

Table 6.3: Summary of transverse mechanical properties for the 886 and 871 composites cases. Matrix properties from chapter 4 and properties of commercially available UD glass fibre PA-6 organosheet are given as a reference [159][161].

Transverse Property	Reference materials		Comparative study		
	Matrix	Organosheet	APA-6/GF 871	APA-6/GF 886 RXN	Average Increase
Flexural strength (MPa)	102.7 ± 1.6	65	82.8 ± 9.8	101.0 ± 4.6	22
Flexural modulus (GPa)	3.2 ± 0.2	10	10.3 ± 0.5	14.5 ± 1.0	29
Flexural strain at max strength (%)	6.2 ± 0.2	-	1.09 ± 0.12	0.97 ± 0.11	-11
Tensile strength (MPa)	83.2 ± 1.3	40	37.8 ± 2.4	43.9 ± 5.1	16
Tensile modulus (GPa)	2.8 ± 0.2	7.1	10.6 ± 0.6	10.7 ± 2.0	1
Tensile strain at max strength (%)	22.0 ± 0.5	-	0.41 ± 0.02	0.49 ± 0.08	20

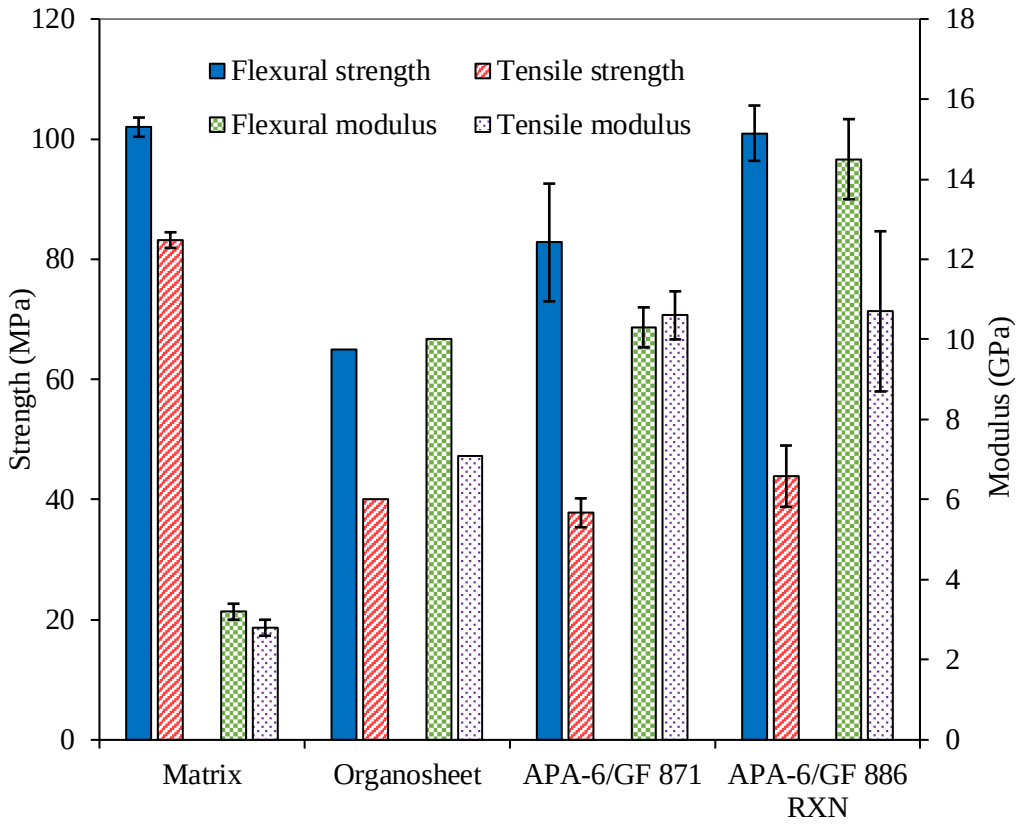

Fig. 6.10: Comparison of 871 and 886 composite cases with properties of the pure APA-6 matrix material and commercial organosheet given as references [159][161].

6.4.2.4 Fracture toughness

Values for mode I fracture toughness (G_1) were calculated from DCB test data for both the 871 and 886 cases and are given in Table 6.4 and Fig. 6.12. In general, the results have a large amount of scatter, even though it is reported in the standard that this is expected due to the large number of factors to be accounted for. In terms of the average mode I fracture toughness across sample sets, the 886 outperforms the 871 in using all three methods of determination, even though the standard deviations overlaps between the two. Fibre bridging occurred in samples but only in the immediate area up to approximately 10 mm behind the crack as it grew (see Fig. 6.12). This, combined with plastic deformation along the cracked region may explain the reason for such large difference between initiation values determined visually and at maximum load.

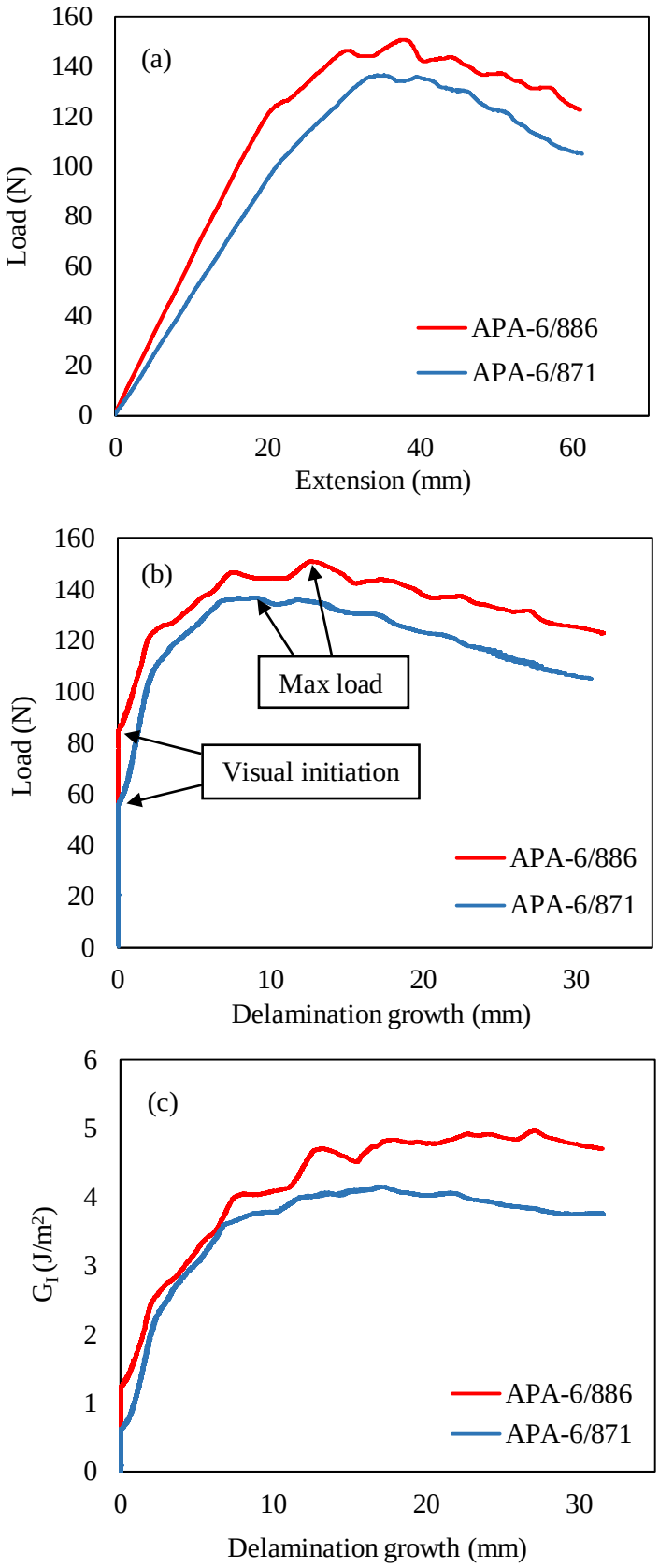

Fig. 6.11: DCB plots of (a) load-extension, (b) load-delamination and (c) G_I-delamination.

Table 6.4: Mode I fracture toughness values for initiation by visual observation ($G_{1C\ VIS}$) and by maximum load ($G_{1C\ Max}$); and for propagation over an average range of values ($G_{1C\ Avg}$).

Material	Initiation		Propagation
	$G_{1C\ VIS}$ (J/m^2)	$G_{1C\ Max}$ (J/m^2)	$G_{1C\ Avg}$ (J/m^2)
APA-6/871	1013 ± 422	3527 ± 626	3684 ± 518
APA-6/886	1303 ± 461	4005 ± 449	4037 ± 394

Ductile fibrillation in SEM images of fractured surfaces in Fig 6.13 (b) and (d) indicates that significant plastic deformation occurred for both cases at the fibre-matrix interface. The images show a high degree of adhesive failure in both cases but with cleaner pull-out of fibres in the 871, leaving a smoother surface. The nature of the matrix in each case is different. The 886 has a more fibrous appearance as was seen in the SEM images of the transversely tested samples. It is likely that due to the higher strength of the interfacial bonding in the 886 samples (shown in Table 6.3), the material is allowed to experience higher strains to failure before finally failing at the interface.

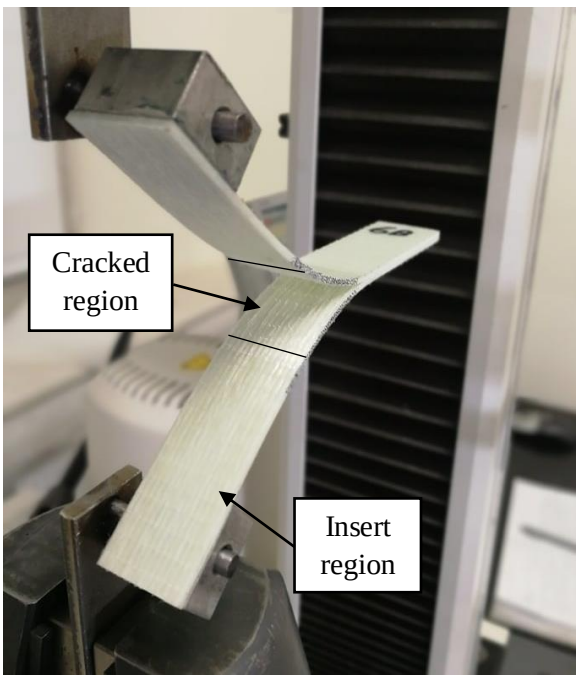

Fig. 6.12: DCB specimen being tested.

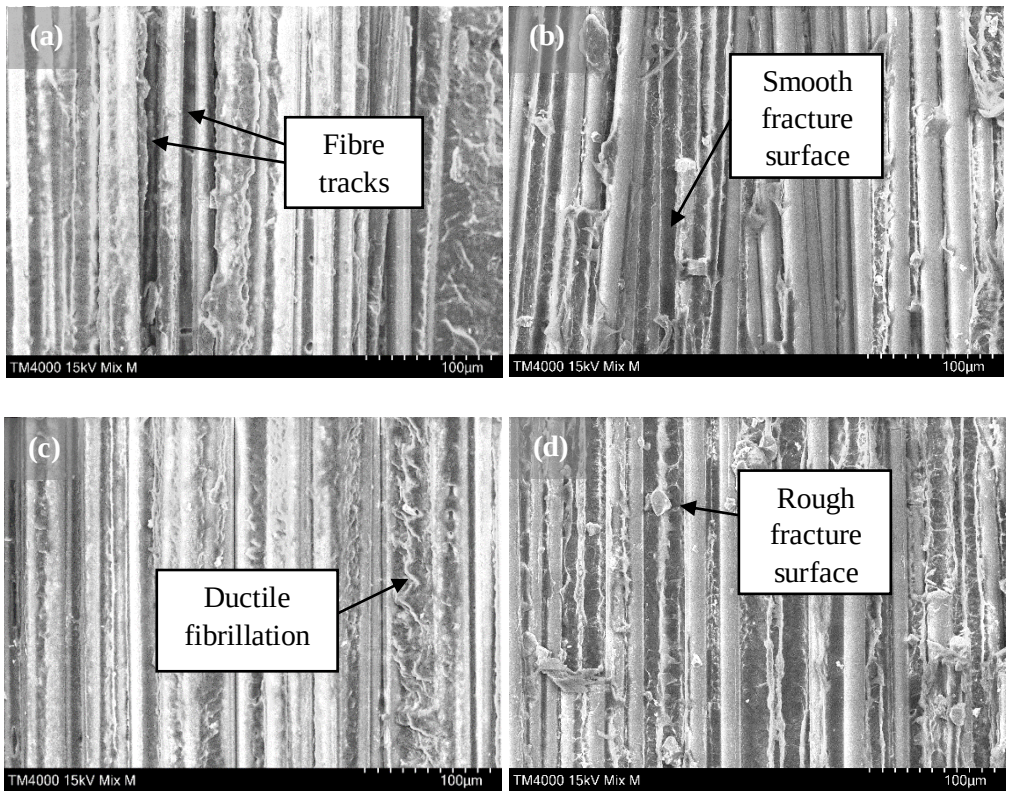

Fig. 6.13: SEM images of fracture surfaces of tested DCB and transverse tensile specimens for the 871 composite, (a) and (b) respectively; and the 886 composite, (c) and (d).

The surface plots for both cases are shown in Fig. 6.14 and the roughness values are summarised in Table 6.5. The surface roughness values in the cracked region for the 886 are higher than those for the 871 in terms of Ra and Rq. The large jagged peaks and crests on the 886 cracked surface plot indicate that large amounts of plastic deformation occurred prior to separation of the surfaces. This may be due to fibre bridging or higher strain in the matrix, however both indicate a superior bond at the interface. This reinforces the aforementioned explanation as to why the 886 cracked surface appears to be more fibrous. High strength and strain both contribute towards the calculation of G_1 by increasing the force and displacement terms in equation 6.3, and so, it is unsurprising that the values for the 886 case are greater than those for the 871 case.

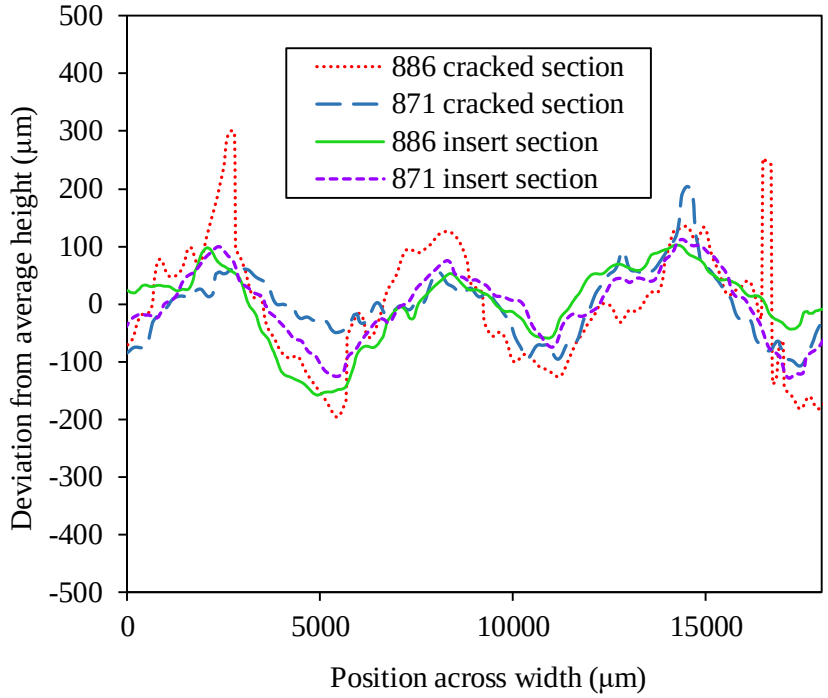

Fig 6.14: Surface roughness techniques applied to stitched images at high magnifications with multi-focus image fusion.

Table 6.5: Surface roughness values for 871 and 886 cases in terms of Ra and Rq.

Material	Ra		Rq	
	Cracked	Insert	Cracked	Insert
APA-6/871	53.2	51.3	302.5	170.8
APA-6/886	81.1	53.6	353.6	242.5

Due to the large deflections observed in Fig. 6.12, it would be fair to question if plastic deformation occurred in the sample itself in the split ends (cantilevers). After unloading of specimens, these ends didn't fully close to their original position, indicating a degree of plastic deformation. Looking back at Fig. 5.20, it can be seen that while bending in the longitudinal was very elastic, a small degree of non-linearity was observed, indicating an amount of plastic deformation. However, the test standard states that small amounts of plastic deformation are acceptable. In hindsight, thicker specimens with an increased number of plies would have been more suitable for this test type as they would have been stiffer. The large deflections as a result of the low stiffness made it necessary to apply the correction factors (F and N) which added to the complexity of the test. More importantly, thicker specimens would have resulted in lower flexural stresses, hence less plastic deformation within the cantilevers.

6.4.2.5 Short beam shear testing

Representative curves for interlaminar shear stress versus extension for the 871 and 886 cases are shown in Fig. 6.15. Interlaminar shear failure did not occur for either case throughout the test. The interlaminar shear stress (ILSS) was so high relative to the flexural yield strength that flexural deformation occurred first such that the ILSS could not be determined. The legitimacy of interlaminar shear stress values in Fig. 6.15 beyond plastic deformation is questionable. As plastic deformation occurs, the neutral axis can shift away from the mid-plane, rendering the data obsolete beyond this point. The tests were allowed to progress up the point where local crushing began to occur between the loading supports and nose after approximately 1 mm extensions. An attempt to overcome both issues involved using different sample sizes and span lengths to encourage interlaminar failure, however this resulted in either the same problem, or local plastic deformation on the upper surface of samples. As such, it can be concluded that the window for the desired failure type is non-existent due to the plasticity of the material. Even though the ILSS values could not be determined, this in itself is a conclusion.

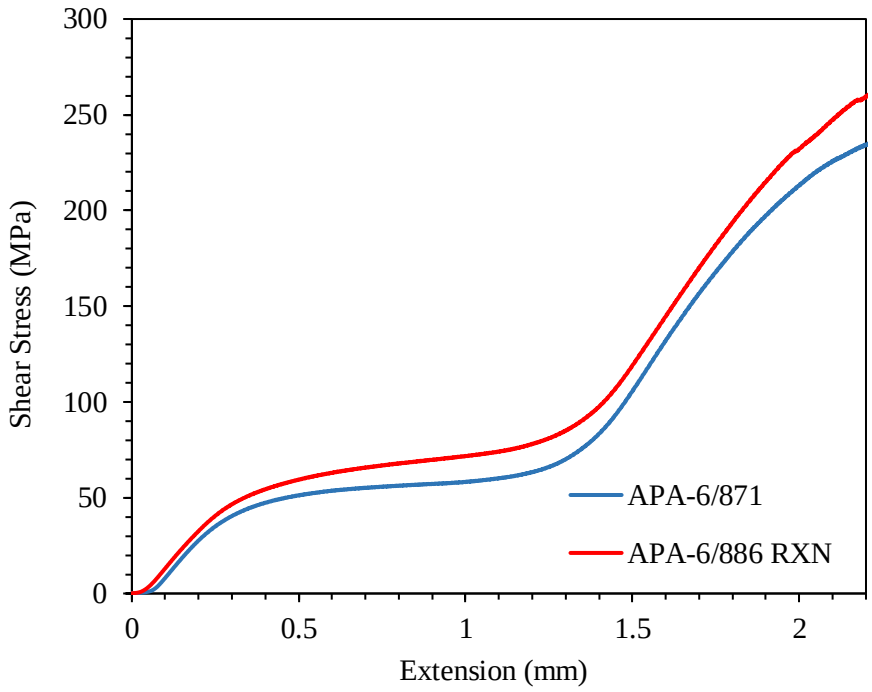

Fig. 6.15: Short-beam shear curves for 871 and 886 composites cases.

6.5 Overall Discussion

It was noted that the average diameter of the 886 fibres (+ sizing) was greater than the 871, indicating a larger volume of sizing on the former. However, the mass loss indicated that there was more sizing on the 871. If both of these were to be true, the obvious conclusion is that there is a difference in density between the sizings. The difference in coverage by volume is so much greater in the 886 compared to the 871 that it would mean the difference in density would have to be extremely large (by greater than a factor of 5). It is more likely that experimental error in one of the techniques occurred. Due to the fact that all three mass loss methods showed similar results, it is more likely that SEM imaging did not give representative measurements for diameter. This may also be due to a variation in the raw fibre diameter. Perhaps the batches used in the mass loss experiments were different in size to those used in SEM. This would need to be investigated further in partnership with the fibre manufacturer (Johns Manville).

SEM showed that the distribution of sizing across the 871 fibres varied a lot, which was also indicated in the standard deviation of diameter measurements. This was in contrast to the 886 which appeared to be smoother overall. AFM also confirmed this to be the case, showing that the surface roughness (Ra) of the 871 fibres was ~ 30 % higher than the 886. The strength on average may be superior as a result of mechanical interlocking caused by the surface roughness [163]. At a smaller scale, the 871 is more ordered, forming clear dendritic structures, whereas the 886 shows no signs of order at the same level of magnification.

It was observed that almost all composite laminates manufactured with the 871 material had a higher thickness and lower density. It is believed that this is due to the additional activator on the fibres. A small increase in the fibre volume fraction, especially at these higher values (>50%), can have a significant impact on the transverse properties. This was demonstrated in Chapter 5, where the local average fibre volume fraction in bundles was in the 66-70 % range. Increasing the average fibre volume fraction in the composite by ~ 2 %, could mean that these local values increase by ~ 4 %. It is likely at these values, that a significant number of fibre are touching one another. Where this occurs, the load bearing capacity drops to zero [155]. This is a secondary effect of the sizing on the material's properties which to a degree means that the comparative study is not entirely fair. Perhaps a reduced concentration of sizing in the APA-6 mixture should be used to minimise these effects; however, this would also result in changed matrix properties in the matrix rich regions. Therefore, there is no perfect comparison.

In addition to these effects, the degree of conversion for the 886 case is lower, presumably due to the presence of the additional initiator which produces more oligomer (impurity).

Regardless of the previously mentioned points, the transverse strength for the 886 case is still superior by a noticeable degree. It is important to note though that it is unlikely that this would have been the case had the bundles not been staggered perfectly. It is unlikely that staggering is practically possible to do manually at an industrial scale, and so, the results here are an ideal case. One possible way of overcoming this challenge would be to have the fabric supplied with multiple plies stitched together in a perfectly staggered form. At fibre volume fractions of >50%, staggering of the plies and fibre volume fraction play as important a role on the transverse properties as the sizing.

The average Mode I fracture toughness value for the 886 material was higher than the 871 by 10-30%, depending on which method was used for its determination. The difference in values between the two was less than the standard deviation for all three methods. It is believed that the additional oligomer would have reduced the toughness of the matrix. This would mean that the toughness of the matrix is sacrificed to a degree in order to toughen the interface. The fracture toughness for both cases is significantly higher than most thermoset composites and competes well with PEEK composites [165][166]. Surface roughness measurements showed that there was much greater distortion in the cracked region of the 886 material compared to the 871. This is thought to be due to the larger strains to failure, allowed by the greater interfacial strength.

In addition to the testing described in this chapter, several other testing techniques were used to compare the 886 and 871. These were mostly incomplete/inconclusive studies carried out from side projects by undergraduate students. Some important results from these studies are given in the Appendices section to support this work. Additional mechanical tests to those mentioned were carried out on the composites made using the 886 fibres; however, due to some uncertainties, they were omitted from Table 6.3. Four laminates for each composite case (871 and 886) had been manufactured at around the same time. All these laminates were manufactured using the same process and the parameters used were identical. The 871 and 886 results presented in the comparative study and summarised in Table 6.3, were tested at the same time. For this reason, it is believed that the comparison is valid. Some of the additional 886 composite samples were tested almost 1 year later and showed poorer results. It is believed that this was due to water absorption over this extended time and an insufficient drying period of 24 hours before testing. The absorbed water likely caused plasticisation in the material,

which resulted in a reduction in strength and modulus [90]. Also, SEM analysis wasn't carried out on this batch of specimens to observe the amount of staggering. The results for all 886 and 871 tests are given in tabulated form in Appendix F.

Additional SEM images were taken of the 886 composite fracture surface after longitudinal flexural testing and are shown in Appendix G. The longitudinal fracture surface exposes the difference between the 886 and 871 more clearly than the transverse fracture surfaces. These images show the effectiveness of the 886 sizing more clearly and can be compared to SEM images of the 871 fibres in Fig. 5.21. The fibres are barely visible in Fig. G.1 (a), meaning that cohesive failure occurred and it indicates that the fibre-matrix interface is strong. Fig. G.1 (b) shows ductile drawing of the matrix from the fibre surface. The matrix seems to have undergone a lot of plastic deformation but still remained bonded to the surface which is further evidence that the interface is strong.

A side project was carried out to measure the debond strength of the 871, 886 and unsized fibres. Firstly, the fibres were tested such that their strength and modulus could be determined. These methods and results are discussed in Appendix H. The unsized fibres were found to be very brittle and weak and the 886 outperformed the 871. This demonstrated the protective effect of sizing on fibres, in addition to other purposes which they served. Single fibre pull-out tests were carried out for each case where fibres had been embedded in an APA-6 matrix. These methods and results are discussed in Appendix I. Unfortunately, only a limited number of 871 and unsized fibres failed at the interface. Most samples failed along the fibre length; however, of the 871 samples which failed at the interface, their values were lower than that for the 886. While this study was not entirely conclusive, there are indications that the 886 performed better but further investigation would be required to determine this.

Overall, there are strong indications that suggest that the 886 fibres result in greater composite strength and fracture toughness compared to the 871. For greater certainty, some of these tests would need to be repeated with large specimen batches. The samples would need to be manufactured with perfectly staggered plies and a prudent conditioning regime would be required before testing.

6.6 Conclusions

TGA showed that oxidation occurs at ~178 ℃ in the 886 sizing and at ~190 ℃ in the 871 sizing. It was shown using SEM that on the micro-scale, the distribution of sizing on the fibre surface of the 886 was less consistent than the 871. The same was shown on the nano-scale where the 871 structure was shown to be dendritic while that of the 886 was more heterogeneous.

Transverse testing in tension and flexure showed that the composite manufactured using the 886 fibres outperformed those manufactured using the 871 in terms of strength. DCB testing showed that the Mode I fracture toughness for the 886 was slightly higher than for the 871 case. It was shown that the surface roughness of the 886 was higher in the cracked region after testing and more sporadic. This matches the observations seen from microscopy of the fibres and indicates that although the distribution of sizing isn't uniform in the 886 case, the bonding where present is significant. Short beam shear tests showed that it was not possible to make the materials fail in interlaminar shear. In all cases, plastic deformation occurred before that in interlaminar shear.

Chapter 7: Impact Properties

Summary

This chapter focuses on the behaviour of APA-6 and their composites when exposed to high strain rate loading. Three distinct study cases were investigated to determine (a) the impact performance of APA-6 compared to a commercially available RTM thermoset resin, (b) the impact and post-impact performance of APA-6 composites compared to thermoset composites and (c) the effect of different fibre sizings on impact and post-impact performance of composites.

7.1 Chapter Introduction and Overview

Knowledge of the impact behaviour of materials is important where their applications in components could potentially be subject to high strain rate loading. High molecular weight thermoplastics are generally tougher than thermosets and therefore, it would be expected that their use as a matrix material in composites would also result in higher impact damage resistance. Improving the energy absorption of a component without significantly sacrificing the static properties may prevent the spread of damage to other, more critical components and potentially save lives as a result. Additionally, improving the energy absorption over a greater amount of time can result in reduced projectile deceleration forces, which in the case of vehicles, can reduce the injuries caused to passengers. As such, energy absorption per unit force (in J/kN) induced during impact is a good measure when comparing material performance.

This chapter consists of three different comparative studies related to the impact performance of thermoplastic RTM materials, describing the experimental procedures and results for each case.

The first study compared the impact performance of pure APA-6 with pure epoxy at two different energy levels (3J & 6J). Due to the brittle nature of the epoxy, the samples were either unaffected or completely shattered such that compression-after impact tests could not be performed.

The second study compared the impact performance of APA-6 composites to epoxy composites using the same fibres and layup at an energy level of 40J. In this case however, carbon fibre textiles were used due to the availability of two similar fabrics but with different sizings tailored for each resin system.

The third compared the performance of glass fibre/APA-6 composites at three different energy levels (25J, 50J & 150J) using the 871 and 886 sizings discussed in chapter 6. The performance of the material after impact was also measured in terms of compression strength to determine how significant the impact damage was to the structural properties.

7.2 Materials and Methods

7.2.1 Materials and Storage

Throughout this chapter, four different textiles were used and two different polymer systems. Unidirectional non-crimp stitched fabrics were used for all the composite cases and their details are summarised in Table 7.1. The two glass fibre fabrics used were the same as those used in chapter 6 with the 871 and 886 sizings. Both carbon fibre fabrics consisted of the same Zoltek PANEX 35 50K fibres but with different sizings tailored for each matrix system. The areal weight and fabric architecture varied slightly however. The fabric sized for the APA-6 system had a total areal weight of 300 g/m^2 and consisted of a single layer of carbon fibres, with PA 6,6 fibres as stitching in the warp direction. The fabrics sized for the epoxy system had a total areal weight of 314 g/m^2 and consisted of 2 layers of carbon with a number of glass fibre rovings in between the two layers at angles of +/- 85° to the carbon fibres, held together by a polyester stitch in a tricot pattern as show in Fig. 7.1.

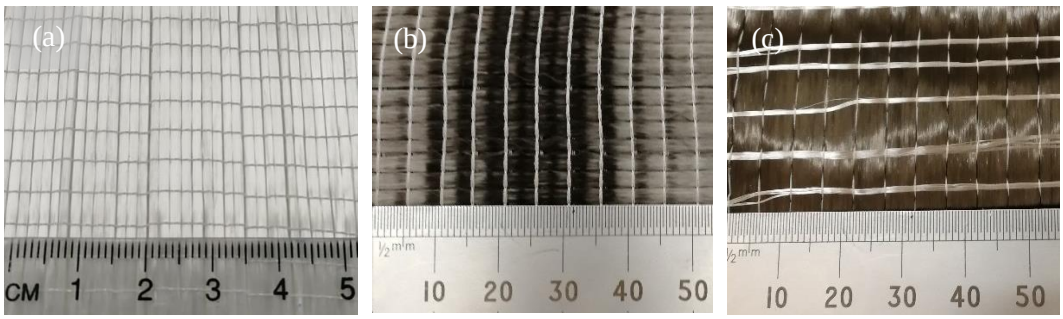

Fig. 7.1: Fabric form and stitching pattern for the (a) Glass fabric StarRov®871/886 RXN, (b) Carbon fabric PANEX 35-61 A 50K and (c) Carbon fabric PANEX 35-13 50K.

Table 7.1: Reinforcement textile material details, each supplied in a unidirectional non-crimp stitched fabric.

Material	Fabric Architecture	Fibre rovings	Supplier
871	640 g/m^2: 1 layer 0° GF (635 g/m^2), PES warp stitch (5 g/m^2)	StarRov®871	Johns Manville
886	640 g/m^2: 1 layer 0° GF (635 g/m^2), PES warp stitch (5 g/m^2)	StarRov®886 RXN	Johns Manville
APA-6 sized CF	300 g/m^2: 1 layer 90° CF (295 g/m^2), PA 6,6 warp stitch (5 g/m^2)	PANEX 35-61 A 50K	SAERTEX
Epoxy sized CF	314 g/m^2: 2 layer 0° CF (300 g/m^2), 1 layer 85° GF (11 g/m^2), PES tricot stitch (3 g/m^2)	PANEX 35-13 50K	SAERTEX

The AP-NYLON® system and additives described in Chapter 4 were used as the raw materials for the APA-6 polymer. As this research was carried out at the University of Auckland during winter, the environmental conditions and storage were slightly different to that at The University of Edinburgh. It should be noted that the relative humidity (RH) in the city of Auckland during this time of year was typically in the 80-90% range. Fig. 7.2 shows the average RH in both cities, with Phoenix, USA shown for comparison as it is an example of a place with particularly low RH values. The RH in the lab varied in/around the critical level for caprolactam (~65%) [167]. On humid days, it was observed that caprolactam flakes exposed to the general lab conditions overnight had become a liquid solution as a result of absorbed moisture. An RH meter was placed in the airtight drum used to store the caprolactam to monitor the conditions. After closing the lid for 1+ hours, this generally levelled off in the 30-35% RH range and was checked each day before weighing the material batches.

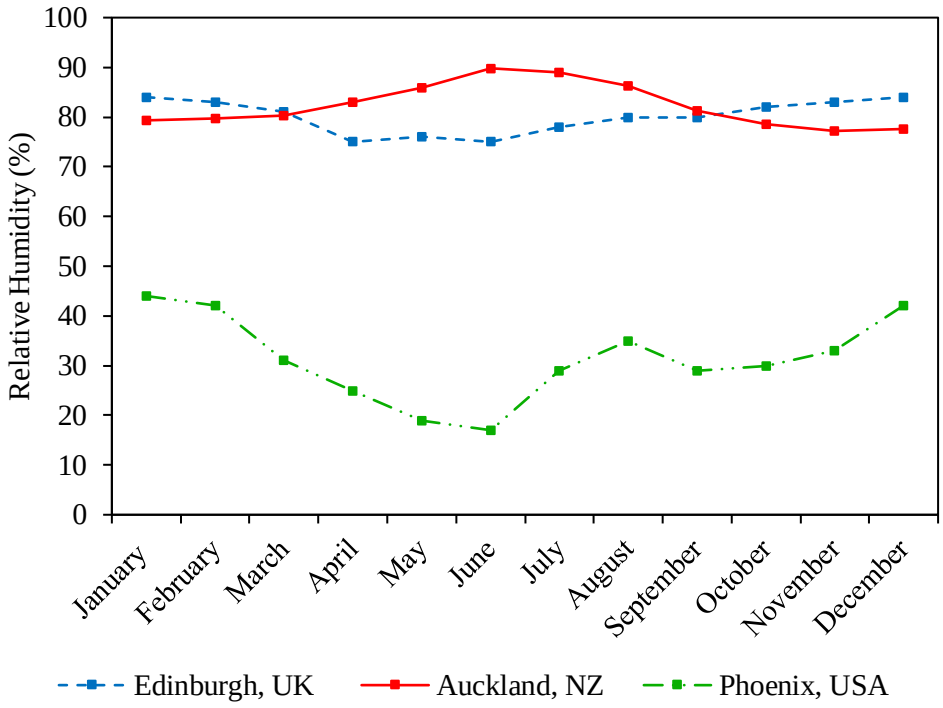

Fig. 7.2: Graph showing average recorded relative humidity (RH) values in Edinburgh, Auckland and Phoenix throughout the calendar year [168][169][170].

The epoxy resin used was Gurit PRIME™ 27, a low viscosity system for infusion of textiles. The resin was mixed with a Gurit *Slow* PRIME™ 20 HARDENER in a 100:28 by weight mixing ratio, using a sufficient volume to fill the mould. The components were degassed under vacuum in an airtight chamber, both before and after mixing, to extract any dissolved moisture or gas present in the system either prior to or during mixing. The details of the raw materials for both the APA-6 and epoxy matrix systems are summarised in Table 7.2.

Table 7.2: Summary of the raw precursor materials for the APA-6 and epoxy polymer matrix systems.

Matrix System	Component Brand Name	Component Type	Supplier
APA-6	AP-NYLON® Caprolactam	Monomer	Brüggemann
	BRUGGOLEN® C20p	Activator	Brüggemann
	BRUGGOLEN® C10	Catalyst	Brüggemann
Epoxy	PRIME™ 27	Resin	Gurit
	PRIME™ 20 HARDENER	Hardener	Gurit

7.2.2 Manufacture

7.2.2.1 Manufacture of GF/APA-6

Different manufacturing setups were used for the polymers, the CFRP and the GFRP; and so, each is described in individual sections. The injection/mould setup used in Chapter 5 with a 350 mm x 390 mm mould cavity was used for the GFRP work but using a 4 mm thick cavity and different layup due to the nature of the test specimens required for impact testing. The ASTM D7136/D7136M – 15 test standard suggests layups for UD tape and woven fabric. Due to the fact that the glass fibre fabrics used in this study are UD, a $[45/0/-45/90]_s$ layup like that suggested for UD tape was used with a cure ply thickness of 0.50 mm. The injection steps and process parameters using the TP-RTM machine were otherwise identical to those in Chapter 5.

7.2.2.2 Manufacture of epoxy and CF/epoxy laminates

A 340 mm x 440 mm cavity with a 3.12 mm thickness was used for the neat polymer and CFRP work. The cavity had a 2.34 mm pinch-off around the periphery to reduce race tracking during filling. The mould contained a single centred inlet and two outlets in the corners. The two mould halves were sealed using a nitrile O-ring and the application of pressure in a 200 ton heated hydraulic press. A vacuum pump was connected to the mould outlet via a catch pot to prevent resin entering the pump. The vacuum was used to evacuate air from the cavity so that the formation of voids was reduced. Though assisted by the vacuum, the epoxy resin was mainly driven by a ~ 4 bar over-pressure supplied to a pressure reservoir from a compressed air line. The regulator was used to control the pressure and it was recorded using an Impress IMP-G1002 0-5 bar digital pressure transducer.

Manufacturing of the pure epoxy began by heating the mould to a steady state temperature of 40 °C and applying approximately 100 tons to properly seal the mould. The valve at the inlet was then closed and a dry vacuum test was carried out to ensure that a sufficient vacuum (>20 mbar) was drawn and that there was no air entering the mould which could cause voids to form during filling and curing. The resin and hardener were degassed individually to remove any dissolved gas present and were then mixed according to the supplier's recommended guidelines. The mixture was degassed once again and placed in a sealed pressure reservoir. The pressure reservoir contained water at room temperature so that exothermic heat from the mixed epoxy (in a container) could be transferred more easily to increase the pot life of the mixture by delaying the onset of cure. A valve in the pressure reservoir was opened so it would remain at atmospheric pressure and allow the pressure differential between it and the vacuum to drive the resin. To begin mould filling, the inlet valve was opened. When resin exited both outlets and passed the outlet valve, the inlet valve was closed first followed by the outlet valve. The valve on the pressure reservoir was then closed, 4 bars of pressure supplied and the mould inlet valve opened again to maintain pressure in the cavity.

For the CFRP-epoxy laminates, 10 plies were required to achieve the desired fibre volume fractions (~57 %) using the epoxy sized CF fabric. The ASTM D7136/D7136M – 15 standard only gives recommended layups for multiples of 8 plies which would result in a fibre volume fraction too low (~46 %) for the fabric. Instead, a $[45/-45/0/90/0]_s$ layup was used, though it should be noted that this resulted in bias in the 0° direction. Manufacturing of the CFRP-epoxy laminates began with placing the lay-up in the mould, applying 100 tons and heating to 40°C. The vacuum was applied to the outlet and tested. The resin and hardener were mixed, degassed and placed in the pressure reservoir in a similar manner to the pure epoxy panels, but this time

the valve on the pressure reservoir was closed and an over-pressure of 4 bars was supplied to the reservoir. This had not been done previously as the lack of resistance in the mould cavity without the reinforcement would have resulted in the mould filling too quickly to practically take responsive action. The inlet was then opened to begin injection. When the resin passed the outlet valve, it was closed and the inlet valve was left open to maintain pressure within the cavity. The process setup for manufacturing epoxy and CF/epoxy are shown in Fig. 7.3.

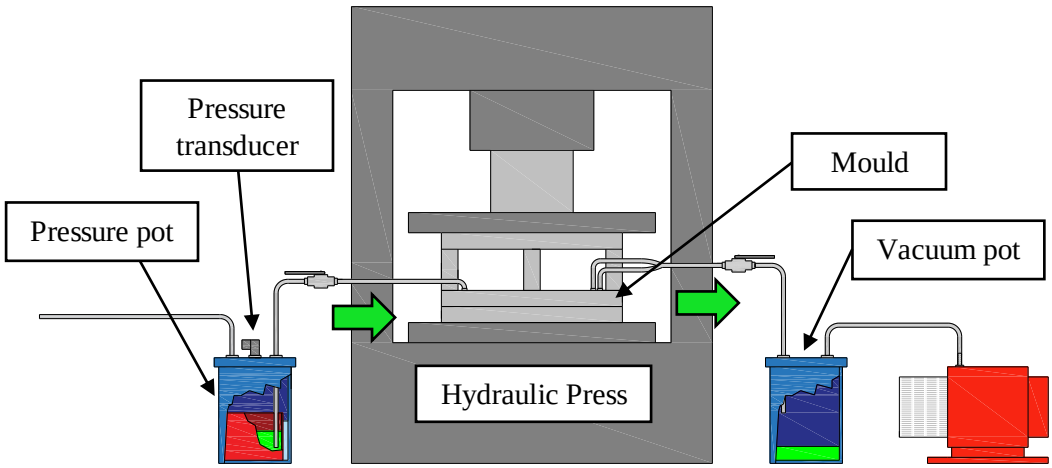

Fig. 7.3: Schematic of the manufacturing process setup for epoxy and CF/epoxy.

7.2.2.3 Manufacture of APA-6 and CF/APA-6

The same mould cavity, hydraulic press and vacuum setup was used for manufacture of the APA-6 and their CFRP composites as that used in section 7.2.2.2. Due to the higher temperatures required for polymerisation of APA-6, silicone rubber O-rings were used to replace the nitrile rubber. Due to the more difficult processing of the APA-6 precursor materials, the TP-RTM machine built for the University of Auckland described in Chapter 3 was used. An in-line pressure transducer was used to measure the pressure at the inlet side but was only useful during injection as the mixture froze after approximately 1 minute because the heat was not maintained in this location. A three-way valve placed between the machine and the mould allowed the application of a vacuum between the mould outlet and machine mixing head while also allowing bleeding of gas between the resin flow front and the vacuum to bridge the gap between the two prior to injection.

To manufacture the APA-6 panels, the mould was heated to 160 °C and a pressure of 100 tons and a vacuum were applied. The vacuum served an additional purpose for APA-6 processing as it aided in removing moisture from the cavity and interconnecting parts. The components were heated and mixed using the TP-RTM machine exactly as described in Chapter 4. Just

prior to injection, the vacuum pressure was increased above the vaporisation pressure of caprolactam (53 mbar) at the exothermic peak temperature (~170 °C) to prevent boiling in the cavity. The resin was pumped into the cavity under the reduced vacuum and when the resin passed the outlet valve, the valve was shut and a pressure of 4 bars was maintained at the inlet until the resin in the feed line had frozen, by which point polymerisation onset may have occurred. 10 plies of fabric with a $[45/-45/0/90/0]_s$ layup were also used to achieve the desired fibre volume fraction using the APA-6 sized CF, so that it would more closely resemble the fibres in the CF/epoxy laminates. To begin manufacturing, the layup was placed in the mould under 100 tons of force with a vacuum applied at 160 °C. The remaining steps were almost identical to those described for the pure APA-6 panels except a higher injection pressure of ~12 bars was applied to overcome the reduced permeability due to the carbon fibres and their tight compaction. The manufacturing cases for impact testing are summarised in Table 7.3.

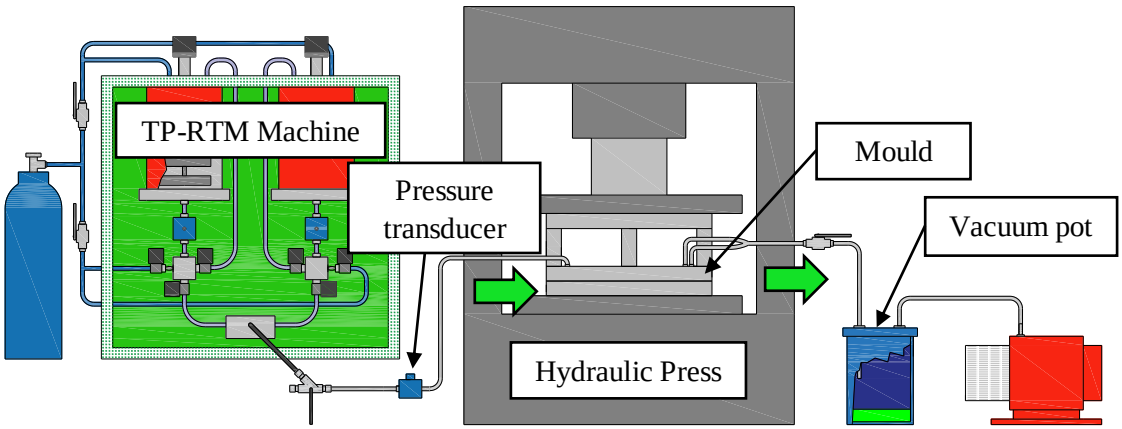

Fig. 7.4: Schematic of the manufacturing process setup for APA-6 and CF/APA-6.

Table 7.3: Summary of manufacturing cases showing whether they were manufactured at The University of Edinburgh (UoE) or The University of Auckland (UoA).

Material	Fabric	Fibre rovings
APA-6	n/a	UoE
GF/APA-6	886 & 871	UoE
CF/APA-6	APA-6 sized CF	UoA
Epoxy	n/a	UoA
CF/Epoxy	Epoxy sized CF	UoA

7.2.3 Sample Preparation

The impact specimens for the pure polymer and composite were extracted from panels manufactured using both the TP-RTM system at The University of Auckland and The University of Edinburgh respectively. The specimen preparation and testing was carried out in accordance with the test standard using 6" x 4" samples. The pure polymer and CFRP samples were cut using a plate saw at the University of Auckland. All glass fibre composite specimens were cut in Edinburgh from 6 laminates with very similar thickness, density and fibre volume fraction; 3 laminates with the 871 sizing and 3 with the 886 sizing. The samples were cut using a diamond blade cutting saw with coolant at a feed rate of ~300 mm/min. All samples were dried in an oven at 50°C overnight and stored in a desiccator until testing.

7.2.4 Impact Testing

Low velocity impact tests were carried out using an Imatek IM10-20 instrumented drop weight impact test machine as shown in Fig. 7.5 (a). Initial trial tests which were carried out at various energy levels showed that penetration of the GFRP occurred at ~ 60+ J, and so, 25 J and 50 J were chosen as the two sub-penetration energy levels while 150 J was chosen as a safe value that would ensure full penetration of all specimens.

A Phantom high speed video camera was used to capture the impact on the lower surface of the specimens and was synchronised to the same software used to monitor velocity (from which the actual measured energy was calculated) and force such that the visual damage could be matched with both properties at various time intervals. The velocity was measured with an instrumented laser detector immediately prior to impact and a 60 kN load cell mounted to the back of the striker was used to determine the impact force.

The samples were held to the rigid stage of the test machine with four rubber tipped toggle clamps. A 16 mm hemispherical striker was used in accordance with the test standard and a total carriage mass of 9.756 kg was used. The machine was fitted with an anti-rebound system which arrested the carriage after impact to prevent further impact from occurring.

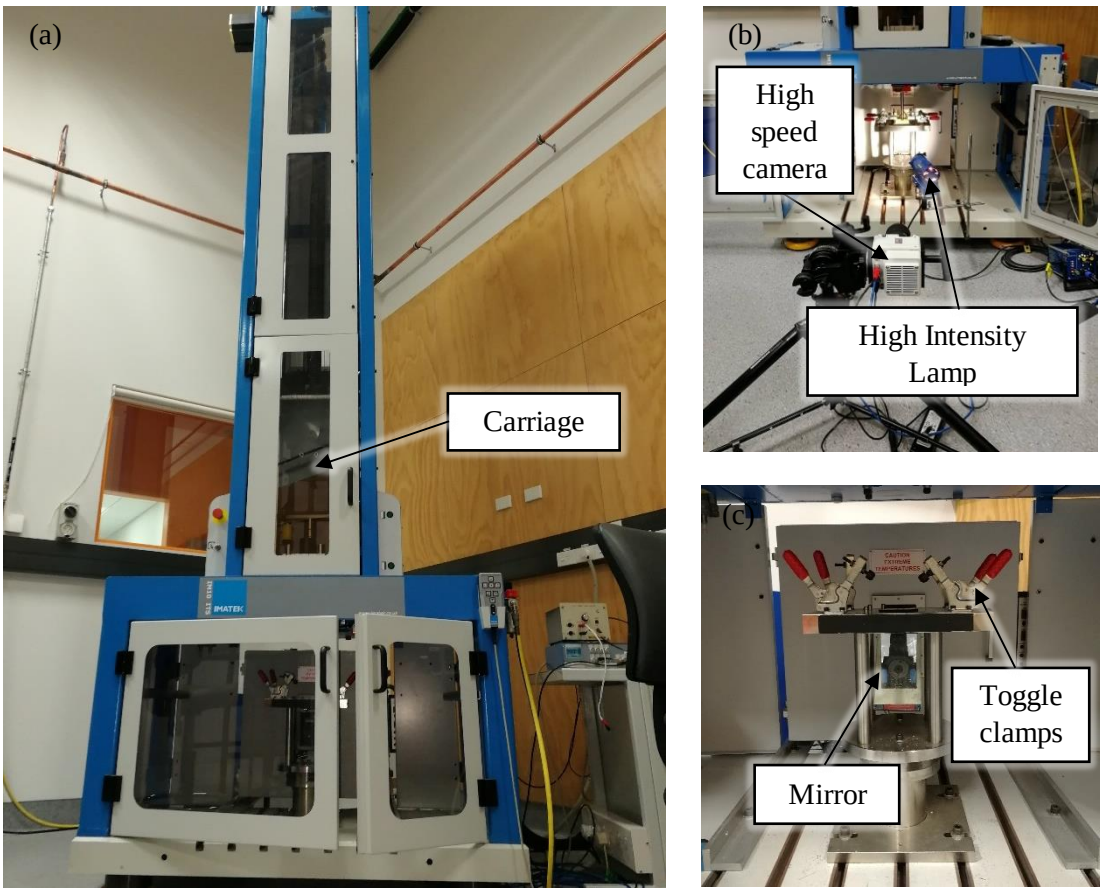

Fig. 7.5: Image of the impact test machine and its parts: (a) the Imatek IM10-20 drop weight impact test machine, (b) the camera and light setup and (c) the stage and toggle clamps used to fix the sample in place during impact.

7.2.5 Damage analysis

Ultrasound NDT was used initially to determine the post-impact damage area of specimens using 5 MHz and 2.4 MHz probes. However, due to the voids at the fibre-stitch intersections, combined with the large number of plies (8 in total) and their orientations, it was difficult to locate a consistent back wall to reflect the signal, and hence, determine the location of damage. GF/APA-6 samples with the same number of plies, thickness and process conditions but manufactured using a UD layup did not experience the same issue, presenting a consistent back wall.

Due to the partial translucency of the glass fibre/APA-6 composite, a high intensity white light was used to observe the damage area. A camera was used to capture this damage on both the upper and lower sides of the specimens. For the penetrated specimens tested at 150 J, additional side shots were taken to capture the out-of-plane damage. The images were then

edited on ImageJ so that the damage area could be isolated for thresholding and analysis. Similar image processing techniques were used to determine the amount of voids in each material. Flaws in this technique were due to the assumption that voids could be calculated by area. This results in surface voids being given the same treatment as internal voids which affect the material through the thickness. For the CF/APA-6, it was not possible to determine the damage using either of the above methods, so an outline of the damage area on the outer surface was drawn using a white marker and determined as a fraction of the entire specimen on ImageJ. In all cases, the damaged area was clearly distinguishable from the undamaged but only on the surface.

7.2.6 Compression after Impact Testing

Compression after impact (CAI) tests were carried out on GFRP specimens impacted at all three energy levels and were compared with un-impacted specimens. The tests were carried out in accordance with ASTM D7137/D7137M – 17 using a specific Compressive Residual Strength Support Fixture for the test as shown in Fig. 7.6 (a). The thickness, width and length dimensions of each sample were taken using a micrometre and Vernier callipers prior to placement in the fixture. The fixture consisted of adjustable retention plates to prevent buckling of the specimens. A feeler gauge was used to ensure a consistent gap of 0.05 mm between the samples and the retention plates. The upper piece of the fixture was placed on top of the sample and the entire sample and fixture was placed between a set of flat and parallel platens in an Instron 1185 universal test machine as shown in Fig. 7.6 (b).

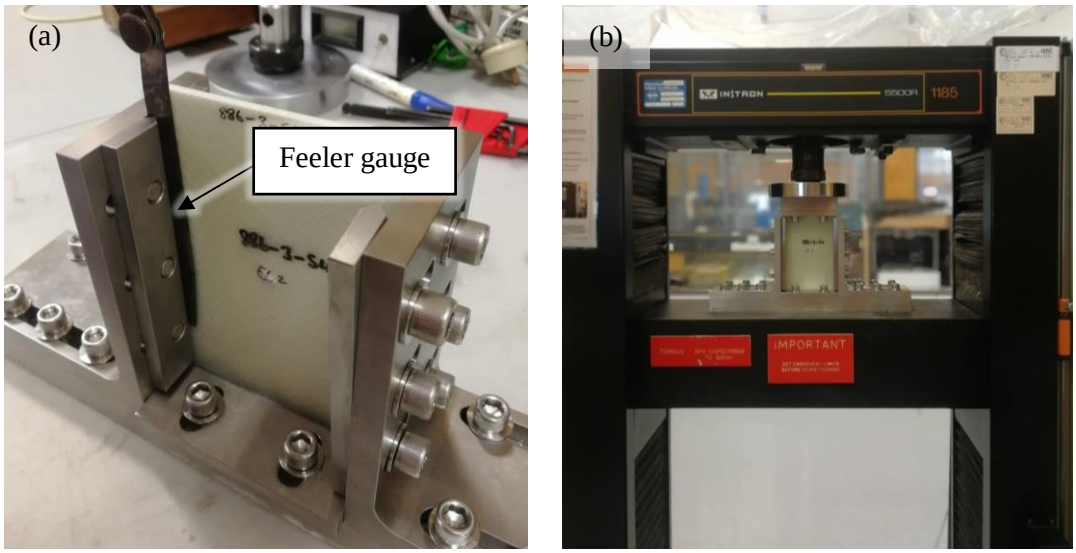

Fig. 7.6: (a) loading of fixture used for compression-after-impact testing and (b) the fixture positioned between platens of test machine during testing of a GF/APA-6 sample.

7.3 Results and Discussion

7.3.1 Pure APA-6 versus pure epoxy

There was a significant difference between the impact performance of the pure APA-6 and epoxy materials. The summarised data is presented in Table 7.3. At an impact energy of 3 J, all the epoxy specimens failed while barely any damage was observed for the APA-6 at the same energy level. Data gathered indicated an average failure energy of 2.58 ± 0.80 J for the epoxy. All but one sample from the APA-6 withstood impact at 6 J without any indications of significant damage. Where failure did occur, there was a noticeable difference in the manner of break between the two materials. All the epoxy specimens shattered into many small pieces, indicating a very brittle behaviour. Even though the APA-6 failure was relatively brittle, there was only one critical crack splitting the specimen in two. The damage in both types of materials can be seen in Figure 7.7. While other cracks could be seen on the surface throughout the specimen, the more ductile nature of the APA-6 seemed to prevent complete shattering at each crack. The force generated at impact by each was similar. However, when taken as a fraction of the energy absorbed in J/kN, that for the APA-6 shows superior performance by about 27%. This is typical for thermoplastic polymers which experience strain hardening when loaded and generally have superior crack resistance, even for a semi-crystalline polymer such as PA-6 [171]. It is important to mention that both the epoxy and APA-6 samples contained a noticeable number of voids as can be seen in Fig. 7.7. Image processing determined a similar amount of voids in each so while they are not negligible, the two cases are somewhat comparable.

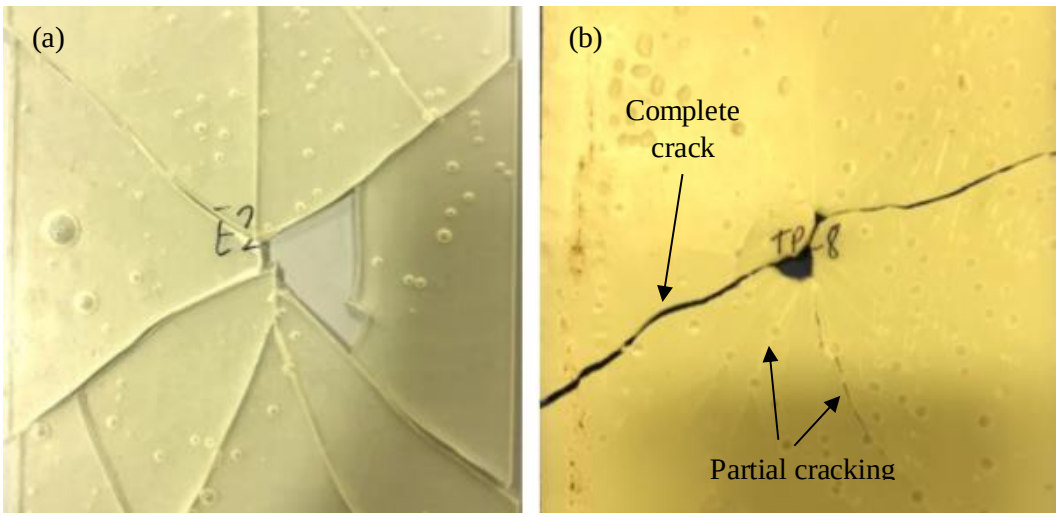

Fig. 7.7: (a) epoxy specimen tested at 3 J shattered into many pieces and (b) APA-6 specimen tested at 6 J with one critical crack splitting the sample in two and several other non-critical cracks.

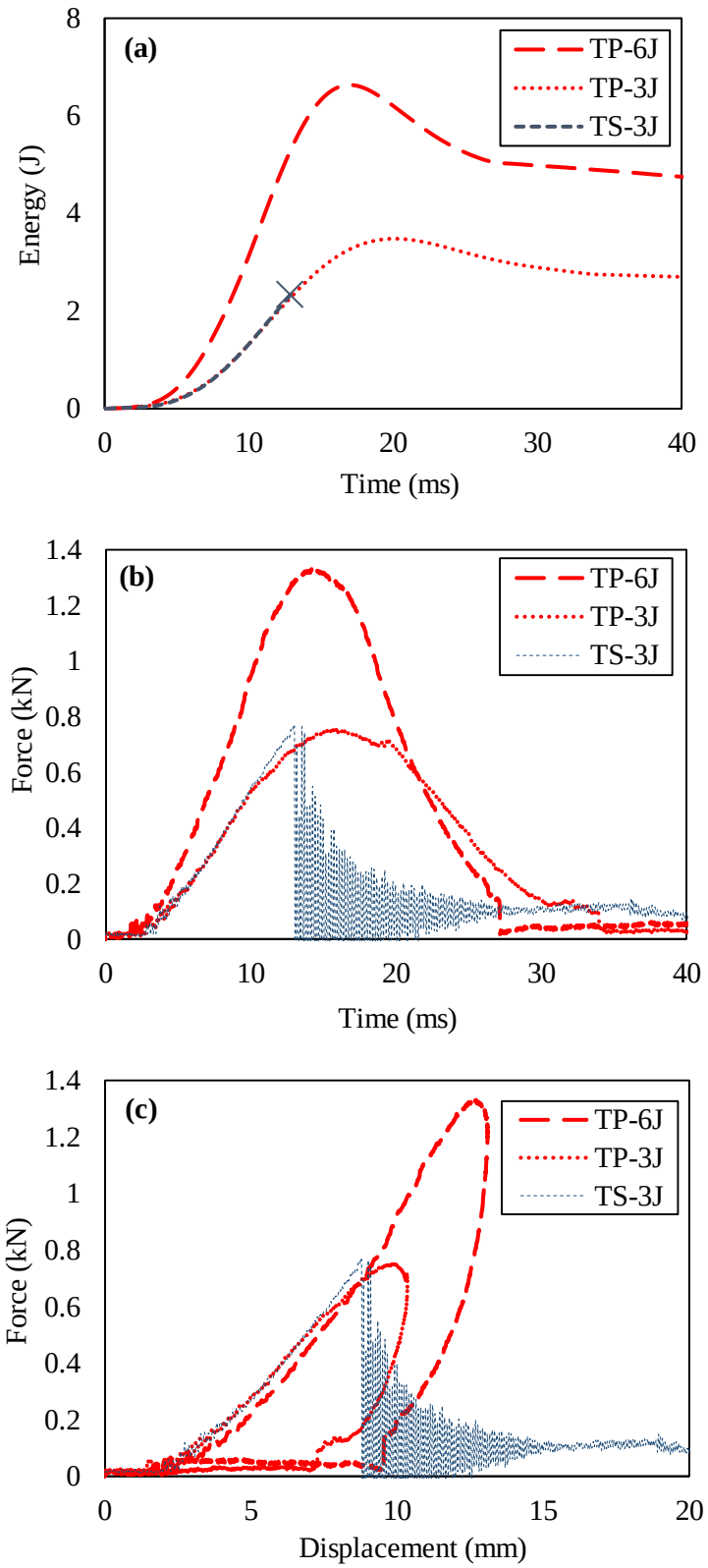

Fig. 7.8: Data recorded during impact testing of the APA-6 and epoxy: (a) energy and (b) force experienced by the striker during impact over time and (c) force plotted against displacement of the striker.

Table 7.3: Summary of results from impact testing of the APA-6 and epoxy at 3 J and 6 J. No tests were conducted at 6 J for the epoxy as all specimens from the testing at 3 J showed failure below the target energy.

	Peak Energy (J)	Peak Force (kN)	Peak Energy/Force (J/kN)	Average Void Content (%)
APA-6 – 3 J	3.00 ± 0.35	0.80 ± 0.04	3.75 ± 0.53	3.66
APA-6 – 6 J	5.91 ± 0.34	1.25 ± 0.10	4.75 ± 0.24	2.19
Epoxy – 3 J	2.58 ± 0.80	0.75 ± 0.14	3.28 ± 0.61	2.56

7.3.2 Impact test results for CFRP

Both the CF/epoxy and CF/APA-6 experienced penetration of the striker on impact at 40 J. After removal of the striker, there was a clear visual difference in the damage due to impact on the outer surfaces of the two specimen types. When analysed on ImageJ, the damaged region was determined to have a surface area of 3.3 ± 0.17 % for the CF/APA-6 and 10.8 ± 3.04 % for the CF/epoxy. The damage in the former is more uniform and distributed radially from the centre while that in the latter showed significant bias in the fibre direction as shown in Fig. 7.9. It is very possible that the damage to the CF/epoxy samples was mainly limited to the lower surface and that the through thickness damage wasn't as large as indicated by the technique used. It should be noted that the small number of glass fibres in the CF/epoxy samples may also have limited the amount of delamination by confining growth in the direction transverse to the carbon fibre direction.

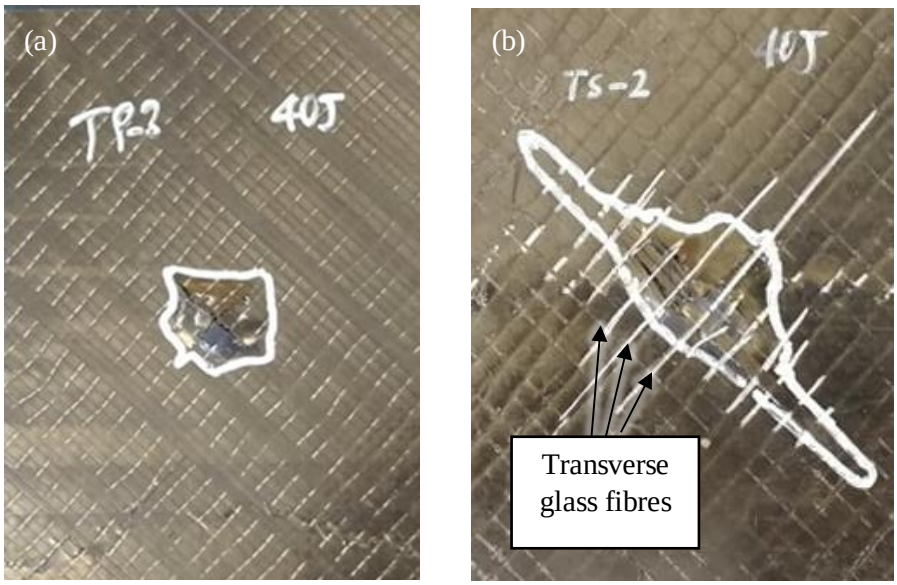

Fig. 7.9: Representative impacted specimens for CFRP with an (a) APA-6 matrix and (b) epoxy matrix. The surface damage is outlined in white marker, demonstrating the difference in size and shape of the impact.

Impact results for both materials are shown in Fig. 7.10. The peak energy absorbed before break can be identified by firstly determining the time at which the maximum load in kN was reached in the time-force curves in Fig. 7.10 (b). The corresponding energy value at this time in the time-energy curves in Fig. 7.10 (a) is that of the energy at break. On average, the CF/APA-6 absorbed ~21 % more energy at break than the CF/Epoxy. The magnitude of the force impacted on the CF/APA-6 was consistently less than the CF/Epoxy, though not by a significant amount. As a result, the impact energy absorbed with respect to the induced force for the CF/APA-6 was higher than the CF/Epoxy by about 28 %. This occurs by transfer of the impacted energy to plastic deformation over time as can be observed in the Fig. 7.10 (c). The relationship between force and displacement for both cases is linear initially but then becomes plastic for the CF/APA-6 as the force plateaus to a degree. These general trends are similar to those observed in section 7.3.1 for the pure polymer cases, as expected. It should also be noted that the maximum displacement of the striker with the CF/APA-6 specimens overall is less than that with the CF/epoxy ones and may be the reason why less surface damage resulted. Though the peak reaction force induced by the CF/epoxy is higher, it suddenly drops after failure allowing the striker to pass through more easily. While the peak reaction force is not as high in the CF/APA-6, a larger force is maintained over time (see Fig. 7.10 (b)) which slows down the striker during penetration due to the less sudden and more ductile failure.

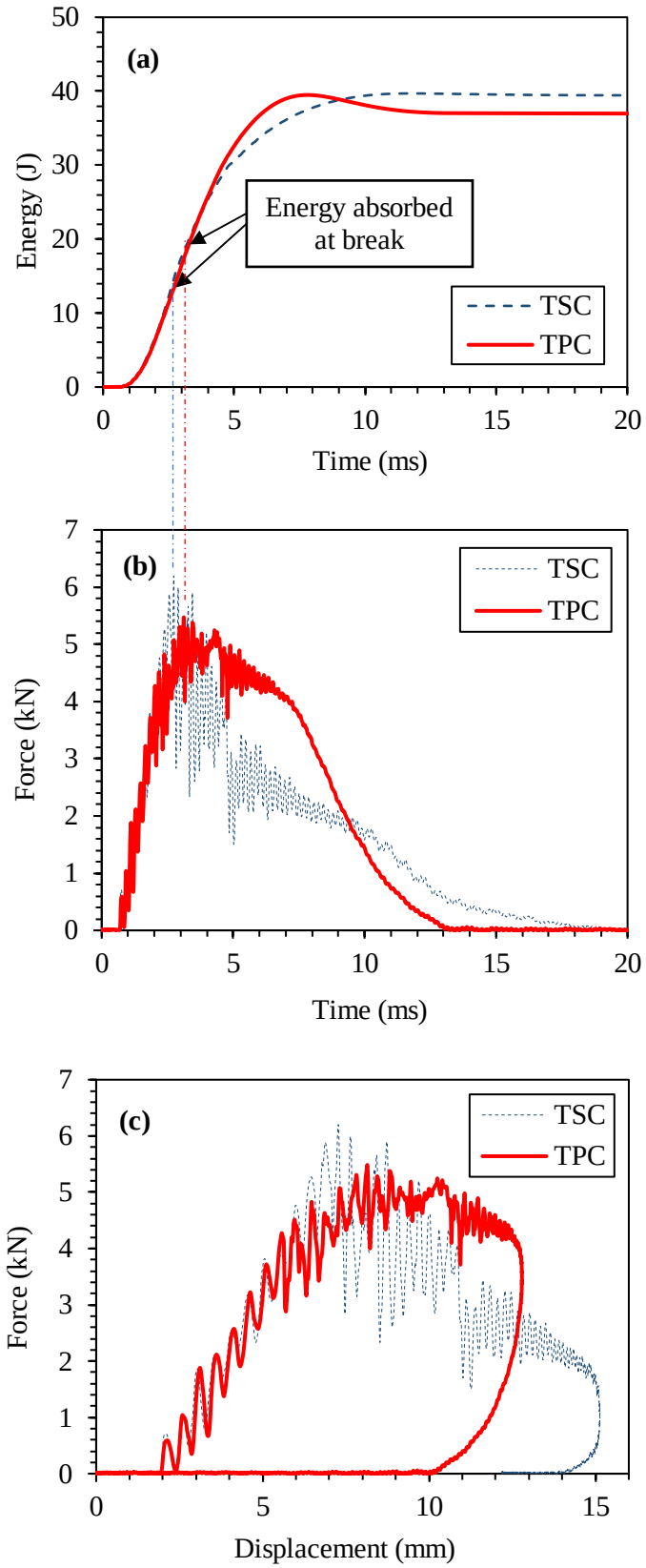

Fig. 7.10: Representative plots of the (a) energy and (b) force experienced by the striker during impact over time and (c) force plotted against displacement of the striker.

Table 7.4: Summary of results from impact testing of the CF/epoxy and CF/APA-6 at 40 J.

	Peak Energy (J)	Peak Force (kN)	Peak Energy/Force (J/kN)	Damage Area (%)
CF/epoxy	14.42 ± 1.65	6.07 ± 0.27	2.37 ± 0.17	10.8 ± 3.04
CF/APA-6	17.24 ± 1.72	5.65 ± 0.25	3.04 ± 0.26	3.3 ± 0.17

7.3.3 Glass fibre composites: comparison of effects of sizings

Photographs of the damaged glass-fibre/APA-6 composites manufactured using both different sizings are shown in Fig. 7.11 and the impact curves are given in Fig. 7.12. From visual inspection, it was clear that the damage incurred by the glass fibre/APA-6 composite at 25 J and 50 J wasn't significant and was localised to the area surrounding that in immediate contact with the striker. While the samples tested at 150 J experienced full penetration, the damage was reasonably localised and partial elastic recovery occurred around the damaged area after removal of the striker from the specimens.

In terms of energy absorption and maximum force experienced during impact, there was no clear difference between the two cases up to the point of break (Fig. 7.12). The energy required for penetration was 64.2 ± 3.7 J for the 871 and 63.3 ± 8.1 J for the 886 RXN. While a similar amount of energy overall was absorbed by both, the method of break was slightly different for each case as seen from visual inspection. The measured damaged area in 886 RXN samples tested at 150 J was approximately 23% higher than that for the 871 case on average. As was the case for the CFRP study, delaminations, which were more prevalent in the 871, were given more weight using this method than the through-thickness damage. Due to improved interfacial adhesion, the 886 RXN material was less likely to suffer delamination to the same degree as the 871, and as a result, the measured damage area was less.

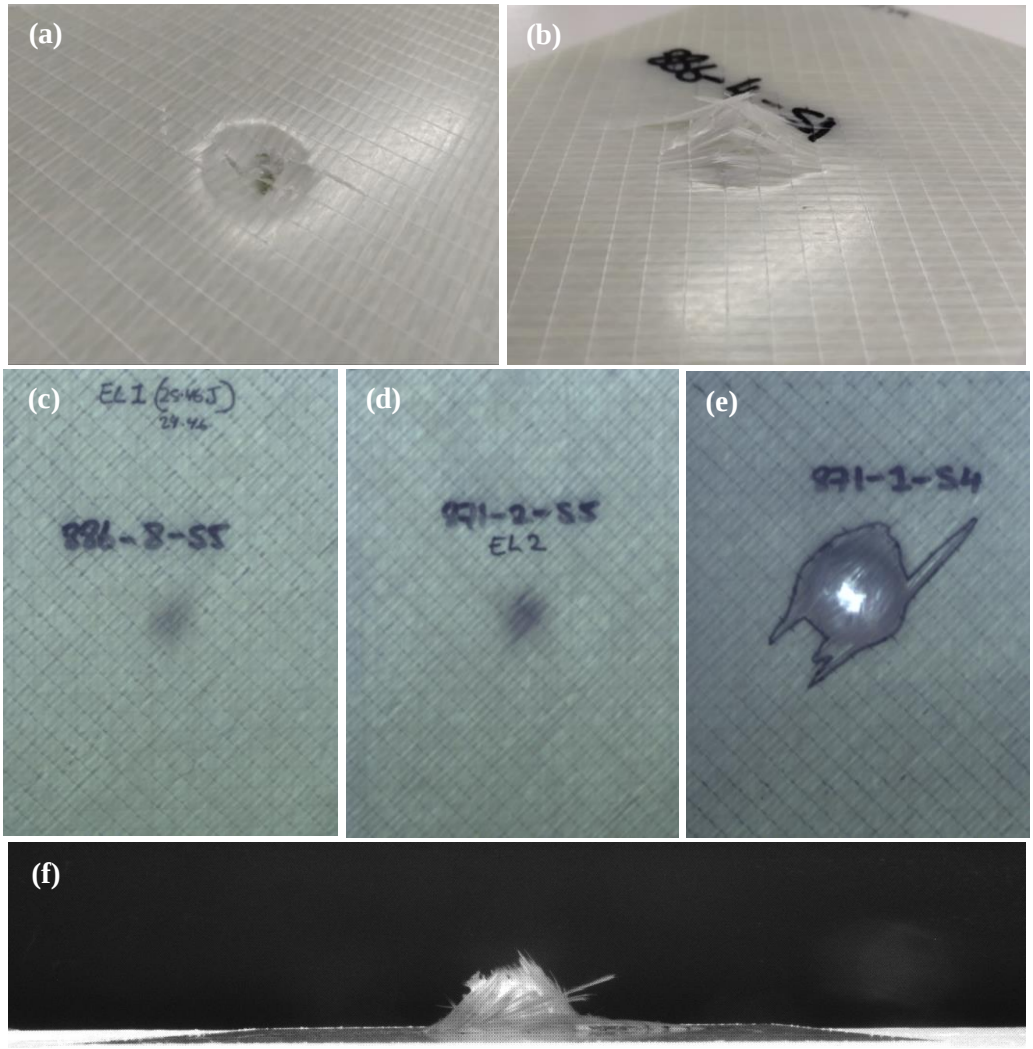

Fig. 7.11: Visual appearance of damage in GFRP specimens after impact testing at 150 J on (a) the upper side (b) the lower side; images taken normal to specimens tested at (c) 25 J, (d) 50 J, (e) 150J; and (f) a side-view of a damaged 150 J specimen.

Compression-after impact results at the three different energy levels for the 871 and 886 RXN cases are presented in Fig. 7.13 and Table 7.5. Due to the low amount of damage caused to the specimens at 25 J and 50 J, its effect on the compressive properties was barely noticeable and in some cases, the average impact strength of the impacted specimens was higher than that of the unimpacted specimens. The scatter is relatively large for the strength values, making it almost impossible to make conclusions about differences between the 871 and 886 RXN cases. It is clear however that the penetration of the specimens at 150 J for both cases caused a significant reduction in strength which was shown to be around 29 ± 8 % from tests results.

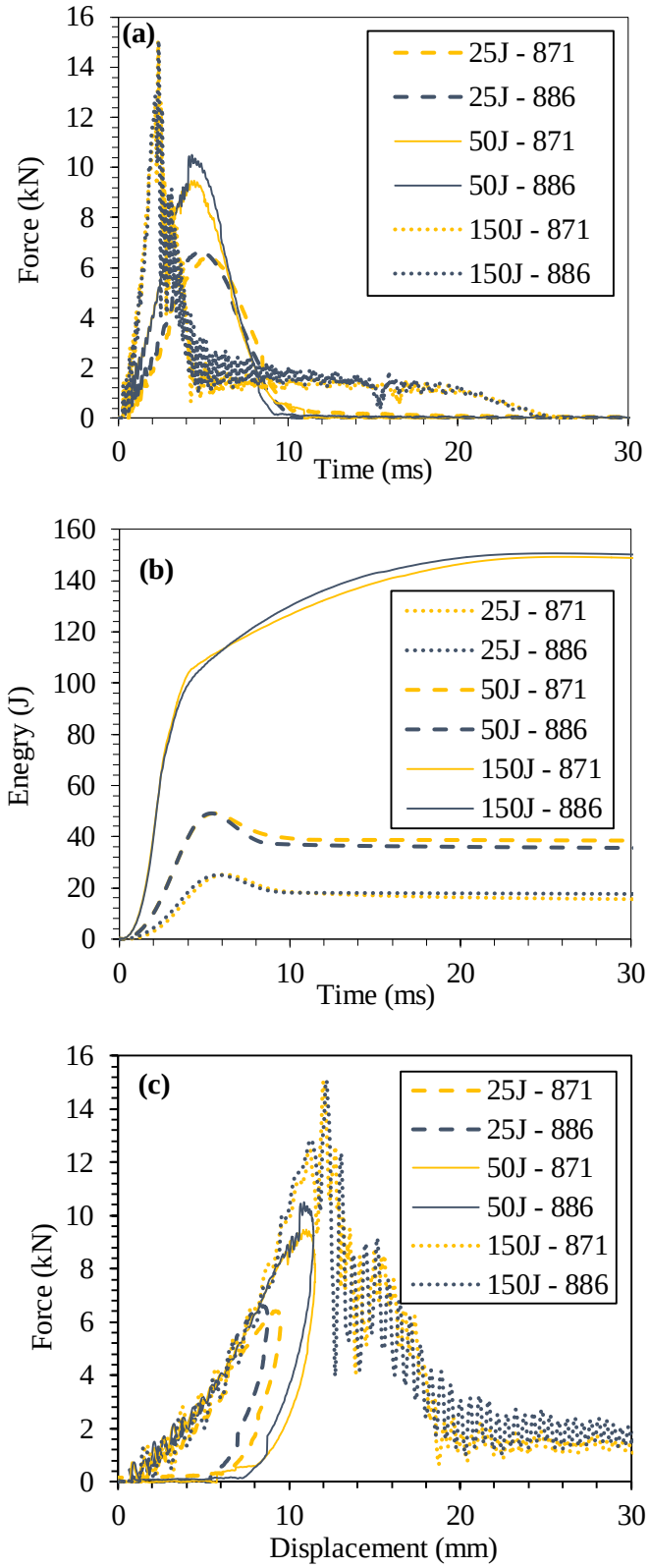

Fig. 7.12: Representative data recorded from impact tests carried out on GF/APA-6 from fibres using both the 871 and 886 RXN fibre sizings.

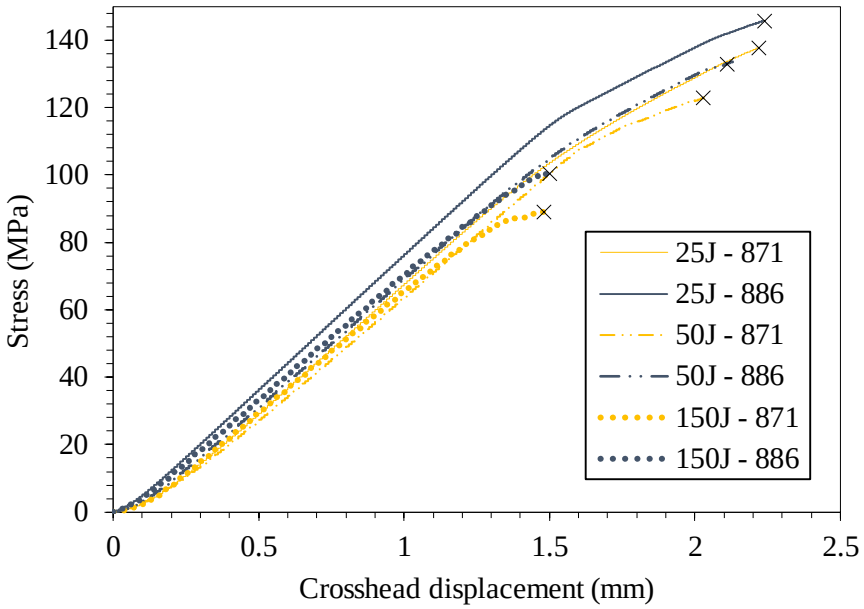

Fig. 7.13: Examples of stress-displacement data from compression-after impact testing of GF/APA-6 using 871 and 886 RXN sizings. Note that while the average values between the 25 J and 50 J energies are very similar, slightly more conservative data is presented for the 50 J in this figure so that the data doesn't visually overlap.

Table 7.5: Summary of the data gathered from analysis and testing of GF/APA-6 material during and after impact. The compression after impact (CAI) data is given as a percentage of the unimpacted strength.

Energy Level (J)	Sizing	Average Damage Area (%)	Peak Energy (J)	Peak Force (kN)	Peak Energy/Force (J/kN)	CAI (%)
25 J	871	1.23	22.3 ± 0.8	6.5 ± 0.3	3.66 ± 0.18	108 ± 6
	886 RXN	1.07	22.8 ± 0.5	6.3 ± 0.4	3.45 ± 0.25	97 ± 10
50 J	871	1.36	44.2 ± 2.5	9.1 ± 1.2	4.95 ± 0.91	96 ± 7
	886 RXN	1.34	45.2 ± 1.5	10.2 ± 1.1	4.47 ± 0.43	100 ± 4
150 J	871	5.69	64.2 ± 3.7	14.2 ± 1.2	4.27 ± 0.27	71 ± 8
	886 RXN	4.61	63.3 ± 8.1	14.8 ± 1.2	4.54 ± 0.43	71 ± 8

7.4 Overall Discussion

The pure APA-6 polymer performs significantly better in impact compared to the pure epoxy. The energy absorbed by the APA-6 before break was more than double that for the epoxy and was able to handle forces around 67% higher. Quite often, crystalline polymers exhibit poor impact performance because of lower visco-elastic behaviour, and hence, low strains to failure. Even though the degree of crystallinity in the APA-6 was high (> 40%), it still performed significantly better than the epoxy. This is unsurprising based on observations demonstrated by Fig. 4.16 which shows that the APA-6 tensile specimens reached ~ 30 % strain before failure while also sustaining high stresses. Even though the failure in the APA-6 wouldn't be described as ductile, it was a much less brittle failure compared to the epoxy. The epoxy shattered into many small pieces upon failure, whereas the APA-6 suffered one major crack and a number of smaller but less critical cracks. This is a result of the damping capabilities of the APA-6 which absorbs the energy in these cracks in the form of plastic deformation, and hence, prevents the cracks from growing further.

As for the pure polymer study, the carbon fibre composite manufactured with the APA-6 matrix was shown to outperform that with an epoxy matrix. The peak energy absorbed by the CF/APA-6 at failure was higher than that for the CF/epoxy. This was due to many of the same reasons discussed for the pure polymer study. The thermoplastic matrix is able to absorb much of the energy, reducing the crack growth across the material. This was observed in the CF/APA-6 specimens post impact where the damage was fairly localised compared to that for the CF/epoxy caused significant damage spread across the surfaces (at least).

In general, non-crimp fabric composites have poorer fracture toughness and impact resistance compared to woven fabric composites [172]. This generally results in a larger damage area too. The non-crimp fabric in the CF/epoxy specimens contained a number of glass-fibres perpendicular to the fibre direction. To a degree, this would have made it act more like a woven fabric compared to the CF/APA-6 specimens and enhance its impact performance. Even with this borne in mind, the damage to the surface in the latter was still less significant.

Study of the 871 and 886 glass fibre composites showed that there was very little difference between their performances. At sub-penetration energy levels, there were signs that the 871 composite performed slightly better than the 886 in terms of energy absorbed per unit force. The opposite seems to be true for penetrated specimens but once again, the difference is slight and within the standard deviation in most cases. There was noticeably more surface damage in the 871 case in the form of delaminations; however, the extent of through thickness damage

is not known as the light method just detects damage without applying weight to severity through the thickness. Both perform similarly in compression after impact, proving that the increased amount of damage observed on the surface of the 871 didn't have profound effects on the mechanical performance.

Overall, it should be noted that this study proved how well the thermoplastic composites perform. The material's ability to limit damage spread from the area of contact with the striker means that a structure can retain a large fraction of its bulk properties after impact. It was shown that these materials can be damaged in the sense that they are plastically deformed but can still uphold extremely high stresses. In contrast, most thermoset composites are brittle and once they are damaged, they serve almost no load bearing capacity.

Even though the 886 composite was shown to have superior Mode I fracture performance in Chapter 6, this had little effect on the impact performance or post-impact performance. This matches with studies in literature which state that Mode I fracture toughness measured by DCB has little effect on the damage caused by impact or compression after impact [173]. On the other hand, the Mode II fracture toughness measured using end-notch testing has been shown to have a direct correlation on damage, which indirectly affects the compression-after-impact performance.

Admittedly, the methods used for determining damage in the composites were crude and unconventional. Ideally, ultrasound would have been used; however, there were issues with using this due to the difficulty in finding a back wall to reflect the waves. This is usually a sign that there are voids through the thickness of the material obstructing the flow from reaching the back wall. This is believed to have been the case and unfortunately due to time constraints, a full investigation into the amount of voids present could not be carried out. The bright light method used for the glass-fibre samples was deemed to be the better of the two as the imaging process was consistent and the damage was easily identifiable. On the otherhand, the CF/APA-6 samples may have had much more damage that was not visible to the eye. For this reason, the damage in the carbon fibre samples should only be seen as an indicator rather than an accurate measure.

Due to the very different layup of the impact samples (quasi-isotropic) compared to the unidirectional layups used in previous chapters, additional pressure would likely have been required to overcome the increased back pressure as a result of the reduced permeability.

7.5 Conclusions

Three separate studies were carried out successfully to compare the impact properties of polymers, composites and sizings.

It was concluded from the polymer testing that the pure APA-6 polymer absorbed over double the amount of energy before break compared to epoxy and its failure was less dramatic due to the material's ductility.

The carbon fibre/APA-6 suffered about 1/3 the amount of surface damage as the carbon fibre/epoxy and absorbed 21% more energy. This was attributed to the ductile behaviour of the APA-6 matrix which absorbs large amounts of energy through plastic deformation locally and hence, reduces the extent of delamination and failure over the overall specimen.

While the surface damage in the glass fibre composite using the standard silane sizing (871) was about 23% higher from penetration than that using the functionalised sizing (886 RXN), the overall energy absorbed and contact force induced was almost identical. Sub penetration energy levels caused barely noticeable effects on compressive strength while the penetrated specimens had a reduced failure load of ~29% for both the 871 and 886 RXN cases.

Chapter 8: Conclusions and Recommendations

Summary

This chapter reviews the project overall, reflecting on the aims and objectives set out in the introduction. The project is concluded in a number of paragraphs and recommendations are suggested for future work. Some of these recommendations aim to address gaps in the current study and others are related to further work required to progress APA-6 composites as a commercially viable manufacturing technique.

8.1 Conclusions

The aim of this project was to assist in the development of tough, recyclable thermoplastic composites suitable for high volume manufacturing of parts. It is believed that this aim was achieved by succeeding to complete the objectives outlined in Chapter 1. These include the following:

Two different TP-RTM systems were designed and built in-house for manufacturing APA-6 composites. Even though the equipment was built at lab scale (~ 3.6 litre capacity), increasing the output would require investment in equipment development and automation but little change in the scientific approach, controls and parameters. The 2 systems used different flow-pressure drive systems and their differences were shown to affect the manufacturing process as outlined in Chapter 3. The TP-RTM machines in both cases cost approximately £5000, which is relatively inexpensive compared to prices being charged by industrial suppliers.

Pure APA-6 was manufactured successfully and its properties were determined. The material produced showed similar strength and modulus to RTM epoxies but had significantly higher strains-to-failure, indicating a much tougher material. For the given mould geometry, material and heating system, a mould temperature of 160 °C resulted in the best properties. Thicker parts produce more exothermic heat due to the nature of the autocatalytic effect. The moulds must either be able to dissipate this heat quickly or the mould temperature needs to be reduced to prevent a temperature surge. The polymer produced had an average melt temperature of around 219 °C, a glass transition range of 70-85 °C and degree of crystallinity of 42%. The average tensile, compressive and flexural strengths and moduli of the polymer were found to be ~ 83, 157 and 103 MPa, and 2.8, 3.4 and 3.2 GPa respectively.

Glass fibre/APA-6 laminates with fibre volume fractions of 51-52% were successfully manufactured with a void content of ~1% by volume. Flow and pressure were optimised to achieve this quality.

A small amount of voids (~ 1 %) in the material were caused by the stitching used in the fabric. The stitching also affected the packing density of fibres throughout laminates which caused local matrix rich and fibre rich areas. Local fibre volume fractions of ~70% were observed in some areas as a result. This was shown to negatively affect the transverse properties. Otherwise, the static properties of the material compared well with commercially available organo-sheet material. The matrix in the composite was found to have a melt temperature of around 222 °C, glass transition range of 82-87 °C and degree of crystallinity of 45%. The average transverse tensile, compressive and flexural strengths and moduli of the composite

were found to be ~ 38, 135 and 83 MPa, and 10.6, 12.3 and 10.3 GPa respectively. The average longitudinal tensile, compressive and flexural strengths and moduli of the composite were found to be ~ 1109, 691 and 1149 MPa, and 40.8, 42.2 and 37.8 GPa respectively.

Two different fibre sizings were compared. One of the sizings contained activator on the coating which caused polymer chain growth from the surface. As suspected, this improved the interfacial adhesion between the fibre and matrix compared to a standard compatible silane agent. The transverse tensile and flexural strength were improved by ~16% and 22% respectively as a result. SEM and surface roughness also indicated signs of greater interfacial adhesion. There were indications that the Mode I fracture toughness may have been improved slightly as a result of the sizing; however, not to a degree which is statistically significant due to large scatter in test data.

Impact testing showed that the APA-6 absorbed significantly more energy than an RTM grade epoxy with the same thickness before fracture. The APA-6 absorbed 5.91 J on average before fracture compared to only 2.58 J for the epoxy. The epoxy shattered into many pieces during failure, demonstrating its brittle behaviour compared to the APA-6 which had one major critical crack during failure in all cases with a number of smaller cracks surrounding it.

The APA-6 composite also absorbed higher energy levels compared to an epoxy composite of the same thickness and experienced less surface damage, with the former absorbing 17.24 J on average compared to 14.42 J for the latter. Due to the out-of-plane local plasticity of the APA-6 composite, the force experienced by the striker on impact was slightly less (by ~7%) as momentum was reduced over a greater amount of time compared to the brittle epoxy composite.

APA-6 composites manufactured from the 2 aforementioned sizings were also tested in impact and showed little difference in terms of energy absorption and post-impact properties. The post-penetration compression strength for both the 886 and 871 cases was ~71% of the original unimpacted compression strength.

8.2 Recommendations

In the earlier stages of this work, changes were implemented continuously to improve the process and quality of the material produced. Eventually a point came where the same procedures had to be maintained without making further improvements such that there was a level playing field for all comparative studies. However, a number of techniques which may further improve the process were noted and are recommended for progression of this work in the future. Also mentioned here are some other areas of research related to this work which would help with its overall commercialisation.

8.2.1 Study of flow through fabric and how it is affected by stitching

In this work, the aftermath of obstructed flow was observed in terms of voids. An interesting follow-up study would be to model this flow based on the stitched fabric geometry to show how the variation in packing density affects the flow. This could be complemented by carrying out an infusion using the same fabric as in this work but with a transparent mould so the wet-out behaviour can be observed using a camera. Perhaps a coloured die could be added to more clearly observe this behaviour.

In addition to being responsible for void formation in the material, the stitching also caused a reduction in tensile properties due to the dense packing of fibres in regions. Very little experimental work exists which show how this packing density in bundles affects the mechanical properties. An interesting study would be to compare the performance of stitched fabrics such as those used in this work with a part manufactured using the same cavity and fibre volume fraction but without the stitching. This would allow the fibres to distribute more evenly within the cavity. It can be foreseen that removing the stitching would cause issues with movement of the fibres during mould filling; however, a slow reacting catalyst could be used instead so that extremely low injection rates can be used to prevent this occurring.

Following on from the two previous points, soluble stitching could be considered. Stitching that is soluble in caprolactam material would allow for handling of the fabric during preparation but would become dissolved in the caprolactam during infusion. This would allow the fibres to disperse evenly after infusion but before the polymerisation onset. This technology could significantly increase the transverse properties of the product.

8.2.2 Thorough investigation of parameters

Admittedly, there was a lack of experimenting with various parameters in this work and an overreliance on findings in literature and industrial recommendations. This was mainly due to time constraints and lack of resources over the prescribed period of the project. Each processing system has different geometry, heating and often different reactants and mixing ratios. In order to properly determine which conditions produce the best properties for this specific system, different permutations should be trialled and tested, mainly temperature and mixing ratios. A study to more thoroughly investigate the effects of moisture content in the precursors and how it affects the polymer should be investigated. This would be an important step for an industrial setup for the production of large parts.

8.2.3 Fill gap in technology readiness for industry

In order for industry to adopt a TP-RTM system, a number of issues need to be addressed. The PA-6 reaction is very temperamental and requires fine control over moisture levels, temperature and pressure in order to achieve sufficient and consistent part quality.

Due to the effects of temperature on the degree of conversion, molecular weight and crystallinity, it is important that the temperature is monitored as closely as possible during the process. With the ability to use dielectric sensing, combined with temperature measurements to monitor the polymer conversion, this can be used to speed up processes. There is slight variation in the time for polymerisation onset to occur between parts. One solution for manufacturers is to be conservative and leave the part in for a longer time to ensure full conversion is achieved; however, this costs time and money. An alternative solution is to use a smart system which senses polymerisation progress and temperature and feeds the information back to the mould controls such that parts are removed as soon as sufficient conversion is achieved. There is work ongoing in this area but more is required before widespread commercialisation of reactive APA-6 composites is possible. This technology combined with measurements of the moisture content of the materials during storage and processing may be the missing link in mainstreaming this process for high volume manufacturing.

8.2.4 Repeat comparative study of sizings

It is recommended that much of the work comparing the composite cases for the two sizings in Chapter 6 is repeated after making some adjustments during processing. It was shown that mass loss in the 886 RXN accelerated at temperatures above 178 °C and that for the 871

occurred above 190 °C. When using a mould temperature of 160 °C, the exothermic heat generated by the reaction likely increases the temperature of the mixture to levels close to that of degradation for the sizings. If this exothermic peak temperature exceeds or comes close to 178 °C, consideration should be given to dropping the mould temperature to ~150 °C. Also, it should be noted that the temperature monitored in this work was actually that of the mould rather than the mixture. Due to the large thermal mass of the mould relative to the mixture, the measurements in the mould don't capture this temperature rise. In hindsight, an embedded thermocouple which is in contact with the mixture (perhaps flush with the inner cavity wall) would have captured this temperature change accurately. This would create better conditions to prepare the 886 RXN and 871 cases for a more fair comparative study. The tests should then be carried out again to more clearly determine to what degree the 886 RXN sizing plays a role, if any, in strengthening the interface. End-notch flexural testing and repeat single fibre pull-out tests should be considered to determine the Mode II fracture toughness and interfacial shear strength respectively. For the single fibre pull-out tests, issues discussed in Appendix I should be addressed.

8.2.5 Toughen APA-6 matrix

It is recommended that different methods of toughening the APA-6 matrix are considered. One of the main reasons outlined for focusing on APA-6 composites in this work was due to the material being tougher than traditionally used epoxy composites. While this was shown to be true, it is also known that the crystallinity of the APA-6 matrix used in this work was on the higher end of the range for PA-6 materials in general, as a result of cold crystallisation. It is well known that while higher degrees of crystallinity affect strength and modulus positively, they negatively affect impact properties. To further toughen the material, there are several known options available. Firstly, higher mould temperatures could be used which would increase the molecular weight and reduce the degree of crystallinity of the material. Another option is to use different additives to improve toughness. For example, the company who supplied the raw materials for this work (Brüggemann GmbH, Germany) also supply a range of impact modifiers. According to the datasheet, the addition of 5% of their BRUGGOLEN® C540 Impact modifier can increase the Charpy impact strength of the material by a factor of 5 without significantly affecting the strength and modulus. When studying the fracture toughness, the Mode II fracture toughness could be determined using end-notch flexural testing, as this was shown to have clear correlations with impact performance. This test type is one of the most tedious but combined with the Mode I fracture toughness, provides the properties required for modelling impact performance.

8.2.5 Investigation of recyclability

Recyclability was also one of the reasons outlined for using APA-6 as a matrix in composites. While PA-6 is recyclable, its use in composites makes recyclability more complex. The problems associated with recyclability are both scientific and economic. The material is only partly recyclable. In order to reuse the continuous fibres without chopping them, the matrix needs to be burned off or dissolved. The viscosity of the melted PA-6 is so high that it can't practically be removed without significantly reducing its quality to a degree that it's no longer structurally sound. A more realistic approach is to reuse the material in chopped form in lower tier applications. This would require grinding into discontinuous particles, mixing with virgin PA-6 and melt processing to generate a new product. The grinding process is energy intensive and as long as it's cheaper to introduce short fibres from off-the-shelf, this may not be economical. Questions about degradation of fibre sizing above melt would also need to be considered during melt processing as the sizing chemistry used in this study is not compatible with melt processing. Perhaps a review or feasibility study of reusing these materials should be considered in future work. If deemed feasible, a study of mechanical properties could be carried out on the product.

8.2.6 Feasibility study for lower volume production

It is recommended that a feasibility study is carried out to determine the suitability of a TP-RTM for low-medium volume production (<50 parts per day). While most RTM processes are only suitable for high volume manufacturing, it is believed that TP-RTM could be used to lower scale volumes of smaller parts. This is mainly down two factors: time and viscosity. Parts which don't require extremely short cycle times, also don't require high injection pressures for wet-out. This is mainly due to the water-like viscosity of the APA-6 precursor materials. This means that more basic (and cheaper) dosing systems could be used. Additionally, if low pressures are used, a smaller sized press or simple clamping mechanism would likely be sufficient. While methods such as vacuum infusion exist for low volume production, the process is labour intensive and requires expensive consumable materials such as vacuum bags. In addition to the aforementioned points, the cost of the APA-6 precursors are relatively cheap compared to many resins on the market, further strengthening the economic case for low-medium volume manufacturing using TP-RTM.

References

[1] R. Hitch, “CFC usage and future strategy at Jaguar Land Rover,” *SAMPE UK and Ireland*. Nottingham, 2016.

[2] D. Berjoza and I. Jurgena, “Effects of change in the weight of electric vehicles on their performance characteristics,” *Agron. Res.*, vol. 15, no. 1, pp. 952–963, 2017.

[3] S. Taillemite, “Thermoplastic Composites for Automotive : meeting the 2 minute challenge,” in *British Plastics Federation*, London, 2015, no. October.

[4] J. H. Schut, “Is Thermoplastic RTM Close to Commercial?,” *Plastics Engineering*, 2014. [Online]. Available: https://plasticsengineeringblog.com/2014/07/02/is-thermoplastic-rtm-close-to-commercial/. [Accessed: 19-Dec-2016].

[5] L. A. Khan and A. H. Mehmood, “Cost-effective composites manufacturing processes for automotive applications,” in *Lightweight Composite Structures in Transport*, Elsevier Ltd, 2016, pp. 93–119.

[6] C. D. Rudd, A. C. Long, K. N. Kendall, C. G. E. Mangin, C. D. Rudd, A. C. Long, K. N. Kendall, and C. G. E. Mangin, “1 – Introduction to liquid composite moulding,” in *Liquid Moulding Technologies*, 1997, pp. 1–37.

[7] M. Deléglise, C. Binétruy, and P. Krawczak, “Solution to filling time prediction issues for constant pressure driven injection in RTM,” *Compos. Part A Appl. Sci. Manuf.*, vol. 36, no. 3, pp. 339–344, 2005.

[8] P. Mitschang and M. Christmann, “8 - Continuous fiber reinforced profiles in polymer matrix composites,” in *Manufacturing techniques for polymer matrix composites (PMCs)*, Woodhead Publishing Limited, 2012, pp. 209–242.

[9] D. E. Davenport, R. Petrovich, and G. Sutton, “Low pressure resin transfer molding for cost effective aircraft quality structures,” in *International SAMPE Technical Conference*, Baltimore, 2007.

[10] R. Chaudhari, P. Rosenberg, M. Karcher, S. Schmidhuber, P. Elsner, and F. Henning, “High-Pressure RTM Process Variants for Manfuacturing of Carbon Fiber Reinforced Composites,” in *19Th International Conference on Composite Materials (ICCM-19)*, Montreal, 2013.

[11] P. Bhat, J. Merotte, P. Simacek, and S. G. Advani, “Process analysis of compression resin transfer molding,” *Compos. Part A Appl. Sci. Manuf.*, vol. 40, no. 4, pp. 431–441, 2009.

[12] A. Vita, V. Castorani, M. Germani, and M. Marconi, “Comparative life cycle assessment of low-pressure RTM, compression RTM and high-pressure RTM manufacturing processes to produce CFRP car hoods,” *Procedia CIRP*, vol. 80, pp. 352–357, 2019.

[13] K. Van Rijswijk and H. Bersee, “Thermoplastic composite wind turbine blades,” TU Delft, 2007.

[14] I. Y. Chang and J. K. Lees, “Recent Development in Thermoplastic Composites: A Review of Matrix Systems and Processing Methods,” *Journal of Thermoplastic Composite Materials*, vol. 1, no. 3. pp. 277–296, 1988.

[15] L. Ye, V. Klinkmuller, and K. Friedrich, “Impregnation and Consolidation in Composites Made of GF/PP Powder Impregnated Bundles,” *J. Thermoplast. Compos. Mater.*, vol. 5, no. 1, pp. 32–48, 1992.

[16] P. McDonnell, K. P. McGarvey, L. Rochford, and C. M. Ó Brádaigh, "Processing and mechanical properties evaluation of a commingled carbon-fibre/PA-12 composite," *Compos. - Part A Appl. Sci. Manuf.*, vol. 32, no. 7, pp. 925–932, 2001.

[17] W. Obande, D. Mamalis, D. Ray, L. Yang, and C. M. Ó Brádaigh, "Mechanical and thermomechanical characterisation of vacuum-infused thermoplastic- and thermoset-based composites," *Mater. Des.*, vol. 175, p. 107828, 2019.

[18] R. E. Murray, D. Swan, D. Snowberg, D. Berry, R. Beach, and S. Rooney, "Manufacturing a 9-Meter Thermoplastic Composite Wind Turbine Blade," *American Society for Composites 32nd Technical Conference*. West Lafayette, Indiana, 2018.

[19] H. Parton and I. Verpoest, "In situ polymerization of thermoplastic composites based on cyclic oligomers," *Polym. Compos.*, vol. 26, no. 1, pp. 60–65, 2005.

[20] J. Baets, A. Godara, J. Devaux, and I. Verpoest, "Toughening of isothermally polymerized cyclic butylene terephthalate for use in composites," *Polym. Degrad. Stab.*, vol. 95, no. 3, pp. 346–352, 2010.

[21] A. Murtagh, S. Coll, and C. Ó Brádaigh, "Processing of Low-Viscosity CBT Thermoplastic Composites : Heat Transfer Analysis," in *The 8th International Conference on Flow Processes in Composite Materials (FPCM8)*, Douai, France, 2006, no. July, pp. 157–164.

[22] C. M. O. Bradaigh, A. Doyle, D. Doyle, and P. J. Feerick, "Electrically-Heated Ceramic Composite Tooling for Out-of-Autoclave Manufacturing of Large Composite Structures," *SAMPE J.*, vol. 47, no. 4, pp. 6–14, 2011.

[23] T. Ageyeva, I. Sibikin, and J. Karger-Kocsis, "Polymers and related composites via anionic ring-opening polymerization of lactams: Recent developments and future trends," *Polymers*, vol. 10, no. 4. p. 357, 2018.

[24] J. Šebenda, "Anionic Ring-opening Polymerization: Lactams," in *Comprehensive Polymer Science and Supplements*, 1989, pp. 511–530.

[25] K. Udipi, R. Dave, R. Kruse, and L. Stebbins, "Polyamides from lactams via anionic ring-opening polymerization: 1. Chemistry and some recent findings," *Polymer (Guildf).*, vol. 38, no. 4, pp. 927–938, 1997.

[26] S. Russo and E. Casazza, "4.14 – Ring-Opening Polymerization of Cyclic Amides (Lactams)," in *Polymer Science: A Comprehensive Reference*, 2012, pp. 331–396.

[27] R. S. Davé, R. L. Kruse, K. Udipi, and D. E. Williams, "Polyamides from lactams via anionic ring-opening polymerization: 2. Kinetics*," *Polymer (Guildf).*, vol. 38, no. 4, pp. 939–947, 1997.

[28] R. S. Davé, R. L. Kruse, K. Udipi, and D. E. Williams, "Polyamides from lactams via anionic ring-opening polymerization: 3. Rheology," *Polymer (Guildf).*, vol. 38, no. 4, pp. 949–954, 1997.

[29] J. A. N. Šebenda, "Lactam Polymerization," *J. Macromol. Sci. Part A - Chem. Pure Appl. Chem.*, vol. A6, no. 6, pp. 1145–1199, 1972.

[30] M. I. Kohan, *Nylon Plastics Handbook*. Munich: Hanser Pub Inc, 1995.

[31] A. Luisier, P. Bourban, and J. Månson, "In Situ Polymerization of Polyamide 12 for Thermoplastic Composites," *Proceedings of the 1999 International Conference on Composite Materials (ICCM-12)*. Paris, 1999.

[32] L. Zingraff, V. Michaud, P. E. Bourban, and J. A. E. E. Månson, “Resin transfer moulding of anionically polymerised polyamide 12,” *Compos. Part A Appl. Sci. Manuf.*, vol. 36, no. 12, pp. 1675–1686, 2005.

[33] P. Ó Máirtín, P. McDonnell, M. T. Connor, R. Eder, and C. M. Ó Brádaigh, “Process investigation of a liquid PA-12/carbon fibre moulding system,” *Compos. Part A Appl. Sci. Manuf.*, vol. 32, no. 7, pp. 915–923, 2001.

[34] Hexcel Corporation, “HexFlow ® RTM 6 datasheet.” pp. 1–4, 2018.

[35] K. van Rijswijk, H. E. N. Bersee, W. F. Jager, and S. J. Picken, “Optimisation of anionic polyamide-6 for vacuum infusion of thermoplastic composites: choice of activator and initiator,” *Compos. Part A*, vol. 37, pp. 949–956, 2006.

[36] K. van Rijswijk and H. E. N. Bersee, “Reactive processing of textile fiber-reinforced thermoplastic composites - An overview,” *Compos. Part A Appl. Sci. Manuf.*, vol. 38, pp. 666–681, 2007.

[37] K. Van Rijswijk, J. J. E. Teuwen, H. E. N. Bersee, and a. Beukers, “Textile fiber-reinforced anionic polyamide-6 composites. Part I: The vacuum infusion process,” *Compos. Part A Appl. Sci. Manuf.*, vol. 40, no. 1, pp. 1–10, 2009.

[38] K. van Rijswijk, H. E. N. Bersee, A. Beukers, S. J. Picken, and A. A. van Geenen, “Optimisation of anionic polyamide-6 for vacuum infusion of thermoplastic composites: Influence of polymerisation temperature on matrix properties,” *Polym. Test.*, vol. 25, no. 3, pp. 392–404, 2006.

[39] K. van Rijswijk, a. a. van Geenen, and H. E. N. Bersee, “Textile fiber-reinforced anionic polyamide-6 composites. Part II: Investigation on interfacial bond formation by short beam shear test,” *Compos. Part A Appl. Sci. Manuf.*, vol. 40, no. 8, pp. 1033–1043, 2009.

[40] P. Rosso, K. Friedrich, A. Wollny, and R. Mülhaupt, “A novel polyamide 12 polymerization system and its use for a LCM-process to produce CFRP,” *J. Thermoplast. Compos. Mater.*, vol. 18, no. 1, pp. 77–90, 2005.

[41] B. J. Kim, S. H. Cha, and Y. Bin Park, “Ultra-high-speed processing of nanomaterial-reinforced woven carbon fiber/polyamide 6 composites using reactive thermoplastic resin transfer molding,” *Compos. Part B Eng.*, vol. 143, no. February, pp. 36–46, 2018.

[42] S. Pillay, U. K. Vaidya, and G. M. Janowski, “Liquid Molding of Carbon Fabric-reinforced Nylon Matrix Composite Laminates,” *J. Thermoplast. Compos. Mater.*, vol. 18, no. 6, pp. 509–527, 2005.

[43] G. Van Den Broek D’Obrenan, “The Adaptation of the RTM (Resin Transfer Molding) Process to Manufacture Thermoplastic-based Composites,” INSA de Lyon, 2011.

[44] Y. Gong, A. Liu, and G. Yang, “Polyamide single polymer composites prepared via in situ anionic polymerization of ??-caprolactam,” *Compos. Part A Appl. Sci. Manuf.*, vol. 41, no. 8, pp. 1006–1011, 2010.

[45] N. Müller and P. Seinsche, “T-RTM Components from Caprolactam – Performance Characteristics, Processing Aspects and In-line Testing, Employing Active Thermography,” in *SAMPE Europe*, Stuttgart, 2017.

[46] S. Schmidhuber and P. Zimmermann, “It Couldn’t Be More Hybrid. Thermoplastic-Matrix RTM on the Roof Frame of the Roding Roadster,” *Kunstst. Intl.*, no. 1–2, pp. 36–38, 2017.

[47] M. Bitterlich, M. Ehleben, A. Wollny, P. Desbois, J. Renkl, and S. Schmidhuber, "Tailored to Reactive Polyamide 6: Thermoplastic Resin Transfer Moulding," *Kunstoffe Int.*, pp. 47–51, 2014.

[48] A. de la Calle, S. Garcia-Arrieta, and C. Elizetxea, "In-Situ Polymerized Continuous Fiber Thermoplastic Composite Manufactured Through Liquid Molding Processes," *16th European conference on composite materials (ECCM16)*. Seville, pp. 22–26, 2014.

[49] M. Zhang, G. Klaus, Y. Asheber, and A. Jawed, "Structural Thermoplastic Composites from Reactive Resin Systems New Fiber Sizing Developments for Optimized Properties," in *Proceedings of the 13th SPE Automotive Composites Conference Exhibition*, Novi, Michigan, 2013.

[50] P. Matthies and W. F. Seydl, "High Performance Polymers: Their Origin and Development," New York: Elsevier, 1986, pp. 39–53.

[51] D. Heikens, P. H. Hermans, and G. M. van Der Want, "On the mechanism of the polymerization of ε-caprolactam. IV. Polymerization in the presence of water and either an amine or a carboxylic acid," *J. Polym. Sci. Part A Polym. Chem.*, vol. 44, no. 144, pp. 437–448, 1960.

[52] D. J. Lin, M. Ottino, and E. L. Thomas, "A Kinetic Study of the Activated Anionic Polymerization of ε-caprolactam," vol. 25, no. 18, pp. 1155–1163, 1985.

[53] S. Russo, S. Maniscalco, P. Moretti, and L. Ricco, "Fast-activated anionic polymerization of ε-caprolactam in the bulk under quasi-adiabatic conditions: Comparison of different kinetic models," *J. Polym. Sci. Part A Polym. Chem.*, vol. 51, no. 20, pp. 4474–4480, 2013.

[54] A. Maazouz, K. Lamnawar, and M. Dkier, "Chemorheological study and in-situ monitoring of PA6 anionic-ring polymerization for RTM processing control," *Compos. Part A Appl. Sci. Manuf.*, vol. 107, pp. 235–247, 2018.

[55] Ueda Kazue. Yamada Kazunobu. Nakai Makoto. Matsuda Tsunetoshi. Hosoda Masahiro. and Tai Kazuo., "Synthesis of high molecular weight nylon 6 by anionic polymerization of ε-caprolactam," *Polymer journal*, vol. 28(5). pp. 446–451, 1996.

[56] K. Ueda, M. Hosoda, T. Matsuda, and K. Tai, "Synthesis of High Molecular Weight Nylon 6 by Anionic Polymerization of ε-Caprolactam. Formation of Cyclic Oligomers.," *Polym. J.*, vol. 30, no. 3, pp. 186–191, 1998.

[57] J. Kvarda and I. Prokopová, "Polymerization of lactams, 93: Formation of 6-hexanelactam cyclic oligomers," *Macromol. Chem. Phys.*, vol. 199, pp. 971–975, 1998.

[58] R. J. Young and P. A. Lovell, *Introduction to Polymers, Third Edition*. Abingdon: Taylor & Francis, 1991.

[59] T. Ageyeva, I. Sibikin, and J. G. Kovács, "Review of thermoplastic resin transfer molding: Process modeling and simulation," *Polymers (Basel).*, vol. 11, no. 10, p. 1555, 2019.

[60] T. J. Bessell, D. Hull, and J. B. Shortall, "The effect of polymerization conditions and crystallinity on the mechanical properties and fracture of spherulitic nylon 6," *J. Mater. Sci.*, vol. 10, pp. 1127–1136, 1975.

[61] D. L. Wilfong, C. A. Pommerening, and Z. G. Gardlund, "Separation of polymerization and crystallization processes for nylon-6," *Polymer (Guildf).*, vol. 33, no. 18, pp. 3884–

3888, 1992.

[62] K. Khodabakhshi, M. Gilbert, and P. Dickens, “Monitoring of small-scale anionic polymerization of caprolactam; a method to be used in an additive manufacturing process,” *Polym. Adv. Technol.*, vol. 24, no. 5, pp. 503–510, 2013.

[63] J. J. E. Teuwen, A. a. van Geenen, and H. E. N. Bersee, “Novel Reaction Kinetic Model for Anionic Polyamide-6,” *Macromol. Mater. Eng.*, vol. 298, no. 2, pp. 163–173, 2012.

[64] A. Rigo, G. Fabbri, and G. Talamini, “Kinetic study of anionic polymerization of 6-caprolactam by differential calorimetry,” *J. Polym. Sci. Polym. Lett. Ed.*, vol. 13, no. 8, pp. 469–477, 1975.

[65] H. C. Y. Cartledge and C. A. Baillie, “Studies of microstructural and mechanical properties of Nylon/Glass composite Part I The effect of thermal processing on crystallinity, transcrystallinity and crystal phases,” *J. Mater. Sci.*, vol. 34, pp. 5099–5111, 1999.

[66] S. D. Lipshitz and C. W. Macosko, “Kinetics and energetics of a fast polyurethane cure,” *J. Appl. Polym. Sci.*, vol. 21, no. 8, pp. 2029–2039, 1977.

[67] R. A. Cimini and D. C. Sundberg, “A Mechanistic Kinetic Model for the Initiated Anionic Polymerization of ε-Caprolactam,” *Polym. Eng. Sci.*, vol. 26, no. 8, pp. 123–124, 1986.

[68] H. K. Reimschuessel, “Nylon 6 Chemistry and Mechanisms,” *J Polym Sci Macromol Rev*, vol. 12, no. 1, pp. 65–139, 1977.

[69] R. Z. Greenley, J. C. Stauffer, and J. E. Kurz, “The Kinetic Equation for the Initiated, Anionic Polymerization of ε-Caprolactam,” *Macromolecules*, vol. 2, no. 6, pp. 561–567, 1969.

[70] A. Y. Malkin, V. G. Frolov, A. N. Ivanova, and Z. S. Andrianova, “The nonisothermal anionic polymerization of caprolactam,” *Polym. Sci. U.S.S.R.*, vol. 21, no. 3, pp. 691–700, 1979.

[71] M. R. Kamal and S. Sourour, “Kinetics and thermal characterization of thermoset cure,” *Polym. Eng. Sci.*, vol. 13, no. 1, pp. 59–64, 1973.

[72] S. Sourour and M. R. Kamal, “Differential scanning calorimetry of epoxy cure: isothermal cure kinetics,” *Thermochim. Acta*, vol. 14, no. 1–2, pp. 41–59, 1976.

[73] J. J. E. Teuwen, “Thermoplastic composite wind turbine blades-kinetics and processability,” 2011.

[74] S. A. Bolgov, V. P. Begishev, A. Y. Malkin, and V. G. Frolov, “Role of the functionality of activators during isothermal crystallization accompanying the activated anionic polymerization of ϵ-caprolactam,” *Polym. Sci. U.S.S.R.*, vol. 23, no. 6, pp. 1485–1492, 1981.

[75] A. Y. Malkin, V. P. Beghishev, I. A. Keapin, and Z. S. Andrianova, “General treatment of polymer crystallization kinetics—Part 2. The kinetics of nonisothermal crystallization,” *Polym. Eng. Sci.*, vol. 24, no. 18, pp. 1402–1408, 1984.

[76] A. Y. Malkin, V. P. Beghishev, I. A. Keapin, and S. A. Bolgov, “General treatment of polymer crystallization kinetics—Part 1. A new macrokinetic equation and its experimental verification,” *Polym. Eng. Sci.*, vol. 24, no. 18, pp. 1396–1401, 1984.

[77] K. H. Lee and S. C. Kim, “Reaction-induced crystallization kinetics during the anionic polymerization of ϵ-caprolactam,” *Polym. Eng. Sci.*, vol. 28, no. 1, pp. 13–19, 1988.

[78] K. J. Kim, D. S. Hong, and A. R. Tripathy, “Kinetics of adiabatic anionic copolymerization of ε-caprolactam in the presence of various activators,” *J. Appl. Polym. Sci.*, vol. 66, no. 6, pp. 1195–1207, 1997.

[79] C. Vicard, O. De Almeida, A. Cantarel, and G. Bernhart, “TTT diagram of the anionic polymerization PA6 from -caprolactam,” *21st International Conferences on Composite Materials (ICCM-21)*. Xi’an, 2017.

[80] M. Thomassey, B. Paul Revol, F. Ruch, J. Schell, and M. Bouquey, “Interest of a Rheokinetic Study for the Development of Thermoplastic Composites by T-RTM,” *Univers. J. Mater. Sci.*, vol. 5, no. 1, pp. 15–27, 2017.

[81] A. Y. Malkin, S. G. Kulochikhin, V. G. Frolov, and M. I. Demina, “Rheokinetics of anionic polymerization of caprolactam,” *Polym. Sci. U.S.S.R.*, vol. 23, no. 6, pp. 1471–1479, 1981.

[82] K. Taki, N. Shoji, M. Kobayashi, and H. Ito, “A kinetic model of viscosity development for in situ ring-opening anionic polymerization of ϵ-caprolactam,” *Microsyst. Technol.*, vol. 23, pp. 1161–1169, 2017.

[83] M. R. Dusi, W. I. Lee, P. R. Ciriscioli, and G. S. Springer, “Cure Kinetics and Viscosity of Fiberite 976 Resin,” *J. Compos. Mater.*, vol. 21, no. 3, pp. 243–261, 1987.

[84] M. L. Williams, R. F. Landel, and J. D. Ferry, “The Temperature Dependence of Relaxation Mechanisms in Amorphous Polymers and Other Glass-forming Liquids,” *J. Am. Chem. Soc.*, vol. 77, no. 14, pp. 3701–3707, 1955.

[85] P. W. Sibal, R. E. Camargo, and C. W. Macosko, “Designing nylon-6 polymerisation systems for RIM,” in *Proceedings of 2nd Int’l. Conference on Reactive Polymer Processing*, Pittsburgh, 1983.

[86] R. S. Davé, K. Udipi, and R. L. Kruse, “Chemistry, Kinetics, and Rheology of Thermoplastic Resins Made by Ring Opening Polymerization,” in *Processing of Composites*, Munich: Carl Hanser Verlag, 2000, pp. 1–31.

[87] C. Yan, H. Li, X. Zhang, Y. Zhu, X. Fan, and L. Yu, “Preparation and properties of continuous glass fiber reinforced anionic polyamide-6 thermoplastic composites,” *Mater. Des.*, vol. 46, pp. 688–695, 2013.

[88] S. Russo, S. Maniscalco, and L. Ricco, “Some new perspectives of anionic polyamide 6 (APA 6) synthesis,” *Polym. Adv. Technol.*, vol. 26, no. 7, pp. 851–854, 2015.

[89] L. Wang, X. Dong, M. Huang, and D. Wang, “Transient microstructure in long alkane segment polyamide: Deformation mechanism and its temperature dependence,” *Polymer (Guildf).*, vol. 97, pp. 217–225, 2016.

[90] P. Y. Le Gac, M. Arhant, M. Le Gall, and P. Davies, “Yield stress changes induced by water in polyamide 6: Characterization and modeling,” *Polym. Degrad. Stab.*, vol. 137, pp. 272–280, 2017.

[91] J. P. Pascault and R. J. J. Williams, “Thermosetting Polymers,” in *Handbook of Polymer Synthesis, Characterization, and Processing*, Hoboken: John Wiley & Sons, 2013.

[92] R. P. Kambour, “Review of crazing and fracture in thermoplastics,” *J Polym Sci, Part*

D, Macromol Rev, vol. 7, no. 1, pp. 1–154, 1973.

[93] A. Bassani, E. Hage Jr, L. A. Pessan, A. V Machado, and J. A. Covas, "Evolução da morfologia de fases de blendas PA6/AES em extrusora de dupla rosca e moldagem por injeção," *Polímeros*, vol. 15, no. 3, pp. 176–185, 2005.

[94] M. Arhant, P. Y. Le Gac, M. Le Gall, C. Burtin, C. Briançon, and P. Davies, "Modelling the non Fickian water absorption in polyamide 6," *Polym. Degrad. Stab.*, vol. 133, pp. 404–412, 2016.

[95] L. Silva, S. Tognana, and W. Salgueiro, "Study of the water absorption and its influence on the Young's modulus in a commercial polyamide," *Polym. Test.*, vol. 32, no. 1, pp. 158–164, 2013.

[96] H. K. Reimschuessel, "Relationships on the effect of water on glass transition temperature and Young's modulus of nylon," *J Polym Sci Polym Chem Ed*, vol. 16, no. 6, pp. 1229–1236, 1978.

[97] A. Pegoretti and A. Dorigato, "Polymer Composites: Reinforcing Fillers," in *Encyclopedia of Polymer Science and Technology*, 2019.

[98] Y. Nakamura, M. Yamaguchi, A. Kitayama, M. Okubo, and T. Matsumoto, "Effect of particle size on fracture toughness of epoxy resin filled with angular-shaped silica," *Polymer (Guildf).*, 1991.

[99] P. J. Mallon and C. M. Ó Brádaigh, "Compliant Mold Techniques for Thermoplastic Composites," *Compr. Compos. Mater.*, vol. 2, pp. 873–913, 2004.

[100] L. Boogh and R. Mezzenga, "Processing Principles for Thermoset Composites," *Compr. Compos. Mater.*, vol. 2, pp. 671–699, 2000.

[101] E. K. Gamstedt and R. Talreja, "Fatigue damage mechanisms in unidirectional carbon-fibre-reinforced plastics," *J. Mater. Sci.*, vol. 34, pp. 2535–2546, 1999.

[102] P. Brøndsted, H. Lilholt, and A. Lystrup, "Composite materials for wind power turbine blades," *Annu. Rev. Mater. Res.*, vol. 35, pp. 505–538, 2005.

[103] K. Hamad, M. Kaseem, and F. Deri, "Recycling of waste from polymer materials: An overview of the recent works," *Polymer Degradation and Stability*, vol. 98, no. 12. pp. 2801–2812, 2013.

[104] I. Goitisolo, J. I. Eguiazábal, and J. Nazábal, "Effects of reprocessing on the structure and properties of polyamide 6 nanocomposites," *Polym. Degrad. Stab.*, vol. 93, no. 10, pp. 1747–1752, 2008.

[105] D. Stavrov and H. E. N. Bersee, "Resistance welding of thermoplastic composites-an overview," *Compos. Part A Appl. Sci. Manuf.*, vol. 36, no. 1, pp. 39–54, 2005.

[106] A. Offringa, "Thermoplastic composites in aerospace - Breakthrough Technologies for Advanced Manufacture," in *SAMPE UK and Ireland*, Nottingham, 2016.

[107] M. H. Litt and A. W. Brinkmann, "Nylon 6/graphite fiber composites by in situ polymerization," *J. Elastomers Plast.*, vol. 5, no. 3, pp. 153–160, 1973.

[108] J. Horský, J. Kolařík, and L. Fambri, "Composites of alkaline poly(6-caprolactam) and short glass fibers: One-step synthesis, structure and mechanical properties," *Angew. Makromol. Chemie*, vol. 264, no. 1, pp. 39–47, 1999.

[109] G. Engelmann, U. Gohs, and J. Ganster, "Monomer cast polyamide 6 composites and

their treatment with high-energy electrons," *J. Appl. Polym. Sci.*, vol. 123, no. 2, pp. 1201–1211, 2012.

[110] R. J. Crawford and J. L. Throne, *Rotational molding technology*. New York: William Andrew Inc., 2002.

[111] G. H. Rusu, K. Ueda, E. Rusu, and M. Rusu, "Polyamides from lactams by centrifugal molding via anionic ring-opening polymerization," *Polymer (Guildf).*, vol. 42, no. 13, pp. 5669–5678, 2001.

[112] E. Harkin Jones and R. J. Crawford, "Mechanical properties of rotationally molded Nyrim," *Polym. Eng. Sci.*, vol. 36, no. 5, pp. 615–625, 1996.

[113] A. B. Strong, *Fundamentals of Composites Manufacturing*. Dearborn, Michigan: Society of Manufacturing Engineers, 2008.

[114] A. Luisier, "Time–Temperature–Transformation Diagram for Reactive Processing of Polyamide 12," *J. Appl. Polym. Sci.*, vol. 81, pp. 963–972, 2001.

[115] A. Luisier, P. E. Bourban, and J. A. E. Månson, "Initiation mechanisms of an anionic ring-opening polymerization of Lactam-12," *J. Polym. Sci. Part A Polym. Chem.*, vol. 40, no. 20, pp. 3406–3415, 2002.

[116] A. Luisier, P. E. Bourban, and J. A. E. Månson, "Reaction injection pultrusion of PA12 composites: Process and modelling," *Compos. Part A Appl. Sci. Manuf.*, vol. 34, no. 7, pp. 583–595, 2003.

[117] M. Holmes, "Expanding the market for long fiber technology," *Reinf. Plast.*, vol. 62, no. 3, pp. 154–158, 2018.

[118] S. Ringenbach, J. Richeton, and J. Coulton, "Hyundai's breakthrough front bumper crash beam," *JEC Composites Magazine*, vol. 98, pp. 39–41, 2015.

[119] K. Van Rijswijk, S. Lindstedt, H. E. N. Bersee, K. F. Gleich, K. Titzschkau, and E. J. McDade, "Reactively processed polyamide-6 structural composites for automotive applications," in *6th Annual SPE Automotive Composites Conference*, Troy, Michigan, 2006.

[120] E. Cischino, F. Di Paolo, E. Mangino, D. Pullini, C. Elizetxea, C. Maestro, E. Alcalde, and J. D. Christiansen, "An Advanced Technological Lightweighted Solution for a Body in White," *Transp. Res. Procedia*, vol. 14, pp. 1021–1030, 2016.

[121] M. Eberhardt, S. Geinitz, R. Wendel, F. Henning, and K. Drechsler, "Simultaneous multi-frequency dielectric analysis of the polymerisation of anionic polyamide 6," in *Twenty-second International Conference on Composite Materials (ICCM22)*, Melbourne, 2019.

[122] J. Snudden, "Progression to the next industrial revolution: Industry 4.0 for composites," *Reinforced Plastics*, 2019. [Online]. Available: https://www.compositesworld.com/articles/composites-and-industry-40-where-are-we.

[123] R. Akkerman and S. P. Haanappel, *Thermoplastic composites manufacturing by thermoforming*. Elsevier Ltd., 2015.

[124] C. M. O'Brádaigh, R. B. Pipes, and P. J. Mallon, "Issues in diaphragm forming of continuous fiber reinforced thermoplastic composites," *Polym. Compos.*, vol. 12, no. 4, pp. 246–256, 1991.

[125] H. Xiong, N. Hamila, and P. Boisse, “Consolidation modeling during thermoforming of thermoplastic composite prepregs,” *Materials (Basel).*, vol. 12, no. 18, p. 2853, 2019.

[126] B. Jongbloed, J. Teuwen, G. Palardy, I. Fernandez Villegas, and R. Benedictus, “Continuous ultrasonic welding of thermoplastic composites: Enhancing the weld uniformity by changing the energy director,” *J. Compos. Mater.*, vol. 54, no. 15, pp. 2023–2035, 2019.

[127] A. Yousefpour, M. Hojjati, and J. P. Immarigeon, “Fusion bonding/welding of thermoplastic composites,” *J. Thermoplast. Compos. Mater.*, vol. 17, no. 4, pp. 303–341, 2004.

[128] A. Offringa, “New thermoplastic composite design concepts and their automated manufacture,” *JEC Composites Magazine*, 2010. [Online]. Available: http://www.jeccomposites.com/knowledge/international-composites-news/new-thermoplastic-composite-design-concepts-and-their.

[129] G. Gardiner, “Thermoplastic composites gain leading edge on the A380,” *High-Performance Compos.*, vol. 14, no. 2, pp. 50–55, 2006.

[130] A. P. da Costa, E. C. Botelho, M. L. Costa, N. E. Narita, and J. R. Tarpani, “A review of welding technologies for thermoplastic composites in aerospace applications,” *J. Aerosp. Technol. Manag.*, vol. 4, no. 3, pp. 255–265, 2012.

[131] S. R. Naqvi, H. M. Prabhakara, E. A. Bramer, W. Dierkes, R. Akkerman, and G. Brem, “A critical review on recycling of end-of-life carbon fibre/glass fibre reinforced composites waste using pyrolysis towards a circular economy,” *Resour. Conserv. Recycl.*, vol. 136, pp. 118–129, 2018.

[132] R. A. Witik, R. Teuscher, V. Michaud, C. Ludwig, and J. A. E. Månson, “Carbon fibre reinforced composite waste: An environmental assessment of recycling, energy recovery and landfilling,” *Compos. Part A Appl. Sci. Manuf.*, vol. 49, pp. 89–99, 2013.

[133] G. Gardiner, “Recycled thermoplastic composites for production,” *Composites World*, 2019. [Online]. Available: https://www.compositesworld.com/blog/post/recycled-thermoplastic-composites-for-production. [Accessed: 15-Apr-2020].

[134] G. Vincent, “Recycling of thermoplastic composite laminates: the role of processing,” 2019.

[135] G. R. Maxwell, “Synthetic nitrogen products,” in *Handbook of Industrial Chemistry and Biotechnology: Twelfth Edition*, Boston: Springer, 2012.

[136] E. Olsen and F. Nielsen, “Predicting vapour pressures of organic compounds from their chemical structure for classification according to the VOC-directive and risk assessment in general,” *Molecules*, vol. 6, no. 4, pp. 370–389, 2001.

[137] W. V Steele, R. D. Chirico, S. E. Knipmeyer, A. Nguyen, B. D. M. P. Technologies, and P. O. Box, “Measurements of Vapor Pressure, Heat Capacity, and Density along the Saturation Line for E-Caprolactam, Pyrazine, 1,2-Propanediol, Triethylene Glycol, Phenyl Acetylene, and Diphenyl Acetylene,” *J. Chem. Eng.*, vol. 47, pp. 689–699, 2008.

[138] A. L. Loeb, “Thermal Conductivity: VIII, A Theory of Thermal Conductivity of Porous Materials,” *J. Am. Ceram. Soc.*, vol. 37, no. 2, pp. 96–99, 1954.

[139] C. D. Rudd, A. C. Long, K. N. Kendall, and C. G. E. Mangin, “Introduction to liquid

composite moulding," in *Liquid Moulding Technologies*, Sawston: Woodhead Publishing Ltd., 1997.

[140] F. M. White, *Fluid Mechanics, 7th Edition*. New York: McGraw-Hill, 2011.

[141] R. Perry, D. Green, and J. Maloney, *Perry's chemical engineers' handbook*, no. 7th. New York: McGraw-Hill, 1997.

[142] Fluitec, "Static Mixing - Advanced mixing Technology." 2018.

[143] Chemineer, "Kenics ™ Static Mixer Technology," *Kenics™ Static Mixer Technology*. p. 12, 2018.

[144] Verdermix, "Verdermix Static Mixers." 2014.

[145] M. J. Moran, H. N. Shapiro, B. R. Munson, and D. P. DeWitt, *Introduction to Thermal Systems Engineering: Thermodynamics, Fluid Mechanics, and Heat Transfer*. 2003.

[146] Beinlich Pump Systems, "Solutions for Fluid Technology: External Gear Dosing Pumps." 2014.

[147] W. M. Kulicke and C. Clasen, *Viscosimetry of Polymers and Polyelectrolytes*. Berlin: Springer, 2004.

[148] C. D. Rudd, *Liquid moulding technologies : resin transfer moulding, structural reaction injection moulding, and related processing techniques*. SAE International, 1997.

[149] K. van Rijswijk, S. Lindstedt, D. P. N. Vlasveld, H. E. N. Bersee, and a. Beukers, "Reactive processing of anionic polyamide-6 for application in fiber composites: A comparitive study with melt processed polyamides and nanocomposites," *Polym. Test.*, vol. 25, no. 7, pp. 873–887, 2006.

[150] J. A. Brydson, "4 - Relation of Structure to Thermal and Mechanical Properties," *Plast. Mater. (Seventh Ed.*, pp. 59–75, 1999.

[151] T. G. Fox, P. J. Flory, T. G. Fox, and P. J. Flory, "Second-Order Transition Temperatures and Related Properties of Polystyrene . I . Influence of Molecular Weight Second-Order Transition Temperatures and Related Properties of Polystyrene . I . Influence of Molecular Weight *," *J. Appl. Phys.*, vol. 581, no. 21, pp. 581–591, 1950.

[152] K. Balani, V. Verma, A. Agarwal, and R. Narayan, *Biosurfaces: A Materials Science and Engineering Perspective*. 2015.

[153] ASTM International, "ASTM D6641 / D6641M-16e1, Standard Test Method for Compressive Properties of Polymer Matrix Composite Materials Using a Combined Loading Compression (CLC) Test Fixture." West Conshohocken, PA, 2016.

[154] S. Y. Hobbs, "Row Nucleation of Isotactic Polypropylene on Graphite Fibres," *Nat. Phys. Sci.*, vol. 234, no. 44, pp. 12–13, 1971.

[155] F. L. Matthews and R. D. Rawlings, *Composite materials: science and engineering*, 2nd ed. New York: Springer, 1999.

[156] B. Li, M. Zhao, and X. Wan, "The influence of void distribution on transverse mechanical properties of unidirectional composites," *8th Int. Conf. Mech. Aerosp. Eng.*, pp. 209–214, 2017.

[157] D. Hull, *An Introduction to Composite Materials*. 1983.

[158] C. Dong, “Effects of Process-Induced Voids on the Properties of Fibre Reinforced Composites,” *J. Mater. Sci. Technol.*, vol. 32, no. 7, pp. 597–604, 2016.

[159] SGL Group, “Unidirectional glass fiber tape with thermoplastic matrix datasheet.” 2017.

[160] J. J. Murray, E. J. Pappa, D. Mamalis, G. Breathnach, A. Doyle, T. Flanagan, S. Di Noi, and C. M. Ó Brádaigh, “Characterisation of carbon fibre reinforced powder epoxy composites for wind energy blades,” *Proceedings of 18th European Conference on Composite Materials*. Athens, 2018.

[161] Evonik Industrial, “VESTAPE Uni-directional tapes for structural lightweight design datasheet.”

[162] TenCate, “TenCate Cetex ® TC910 datasheet.” 2018.

[163] N. Dilsiz and J. P. Wightman, “Surface analysis of unsized and sized carbon fibers,” *Carbon N. Y.*, vol. 37, no. 7, pp. 1105–1114, 1999.

[164] T. G. Fox and S. Loshaek, “Influence of molecular weight and degree of crosslinking on the specific volume and glass temperature of polymers,” *J. Polym. Sci.*, vol. 15, no. 80, pp. 371–390, 1955.

[165] S. Samborski, A. Gliszczynski, J. Rzeczkowski, and N. Wiacek, “Mode I interlaminar fracture of glass/epoxy unidirectional laminates. Part I: Experimental studies,” *Materials (Basel).*, vol. 36, no. 8, pp. 1119–1127, 2019.

[166] “ASTM D5528-13: Standard test method for mode I interlaminar fracture toughness of unidirectional fiber-reinforced polymer matrix composites,” 2014.

[167] Spolano, “Caprolactam Material Data Sheet,” 2012.

[168] “Weather & Climate: Average Humidity in Edinburgh,” 2019. [Online]. Available: https://weather-and-climate.com/average-monthly-Humidity-perc,Edinburgh-uk,Scotland. [Accessed: 23-Oct-2019].

[169] “Weather & Climate: Average Humidity in Auckland,” 2019. [Online]. Available: https://weather-and-climate.com/average-monthly-Rainfall-Temperature-Sunshine,Auckland,New-Zealand. [Accessed: 23-Oct-2019].

[170] ClimaTemps, “Sunshine & Daylight Hours in Phoenix, Arizona, USA,” 2019. [Online]. Available: http://www.phoenix.climatemps.com/sunlight.php. [Accessed: 23-Oct-2019].

[171] V. Arikan and O. Sayman, “V. Arikan, O. Sayman, Comparative study on repeated impact response of E-glass fiber reinforced polypropylene & epoxy matrix composites,” *Compos. Part B Eng.*, vol. 83, pp. 1–6, 2015.

[172] K. Vallons, A. Behaeghe, S. V. Lomov, and I. Verpoest, “Impact and post-impact properties of a carbon fibre non-crimp fabric and a twill weave composite,” *Compos. Part A Appl. Sci. Manuf.*, vol. 41, no. 8, pp. 1019–1026, 2010.

[173] A. T. Nettles and L. Scharber, “The Influence of GI and GII on the compression after impact strength of carbon fiber/epoxy laminates,” *J. Compos. Mater.*, vol. 52, no. 8, pp. 991–1003, 2018.

[174] V. J. Morris, A. R. Kirby, and A. P. Gunning, *Atomic force microscopy for biologists*. 2009.

[175] R. S. McLean and B. B. Sauer, “Tapping-mode AFM studies using phase detection for resolution of nanophases in segmented polyurethanes and other block copolymers,” *Macromolecules*, vol. 30, no. 26, pp. 8314–8317, 1997.

[176] M. Kalloudis, E. Glynos, S. Pispas, J. Walker, and V. Koutsos, “Thin films of poly(isoprene-b-ethylene oxide) diblock copolymers on mica: An atomic force microscopy study,” *Langmuir*, vol. 29, no. 7, pp. 2339–2349, 2013.

[177] E. Lasseuguette, J. McClements, V. Koutsos, T. Schäfer, and M. C. Ferrari, “Ionic liquid mediated surface micropatterning of polymer blends,” *J. Appl. Polym. Sci.*, vol. 135, no. 14, p. 46109, 2018.

Appendices

A. Pressure drop in check valves

The cracking pressure can be varied between 0.21 bar and 3.5 bar. We have set the cracking pressure in the TP-RTM equipment to ~ 0.5 bar. Therefore, the added details in red should be followed. Curves from the Swagelok datasheet (Fig. A1) show valaues for pressure drops at 0.21 and 3.5 bar cracking pressures and the relationship between flow rate and pressure drop for each. This data is presented for water but due to the similar viscosity and denisty to caprolactam, it is assumed to be the same. An approximation for 0.5 bar is made based on values interpolated from Fig. A1. While the relationship for the 0.21 bar line isn't linear, it is assumed so to reduce complexity. Interpolation calculations for pressure at 0 L/min and 8 L/min are calculated as follows:

$$P_{0L/min} = 1 + \left(\frac{0.50 - 0.21}{3.50 - 0.21}\right)(4 - 1) = 1.26\ bar$$

$$P_{8L/min} = 2.5 + \left(\frac{0.50 - 0.21}{3.50 - 0.21}\right)(12 - 2.5) = 3.33\ bar$$

Now a line euquation relating flow rate and pressure drop can be prodcued for a cracking pressure setting of 0.50 as follows:

$$P = 0.26Q + 1.26$$

Or in SI units, the equation is:

$$P = 1.59 \times 10^9 Q + 126{,}000$$

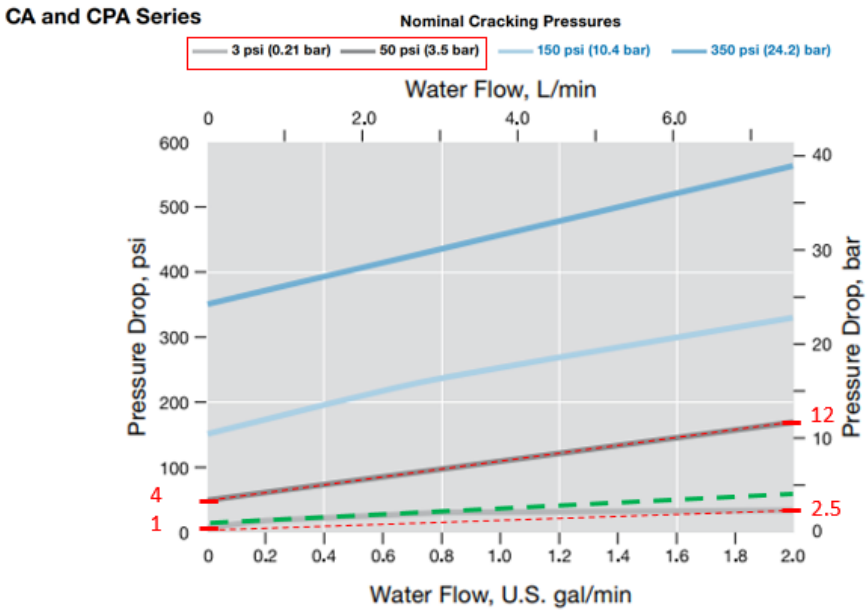

Fig. A1: Curves for check valve cracking pressures taken from Swagelok datasheet.

B. APA-6 Synthesis: Anionic ROP

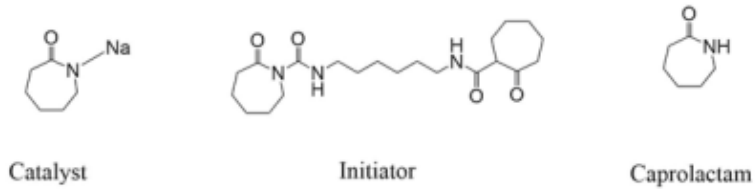

Catalyst Initiator Caprolactam

1. Dissociation of catalyst

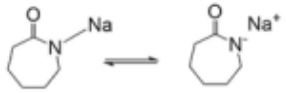

Catalyst

2. Formation of Acyllactam Group (at both ends)

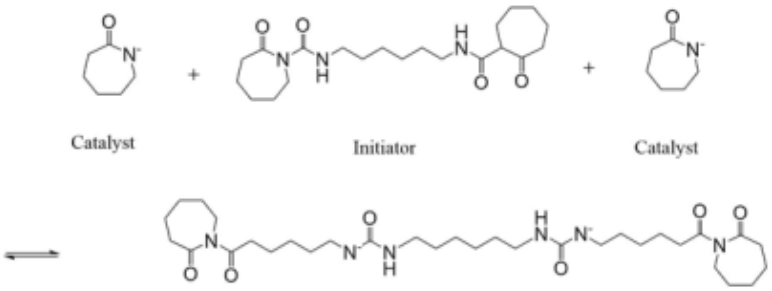

Catalyst Initiator Catalyst

Two-sided Acyllactam

3. Initiation (at both ends)

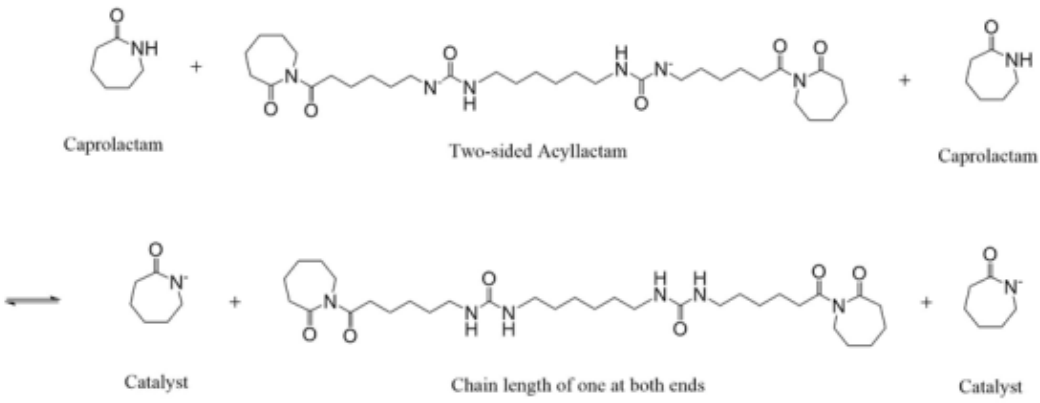

Caprolactam Two-sided Acyllactam Caprolactam

Catalyst Chain length of one at both ends Catalyst

4. Complex Formation (at both ends)

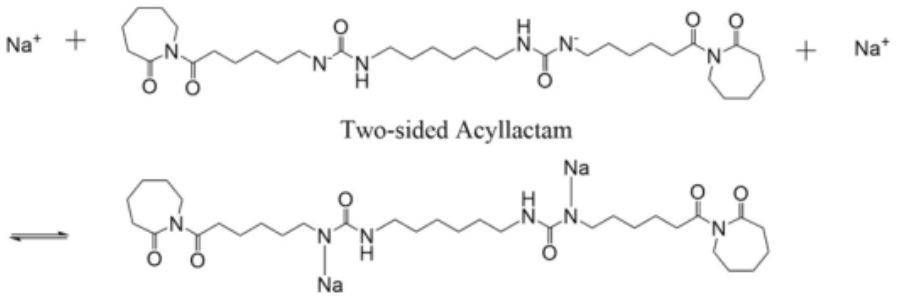

Two-sided Acyllactam

5. Propogation (chain growth from both ends)

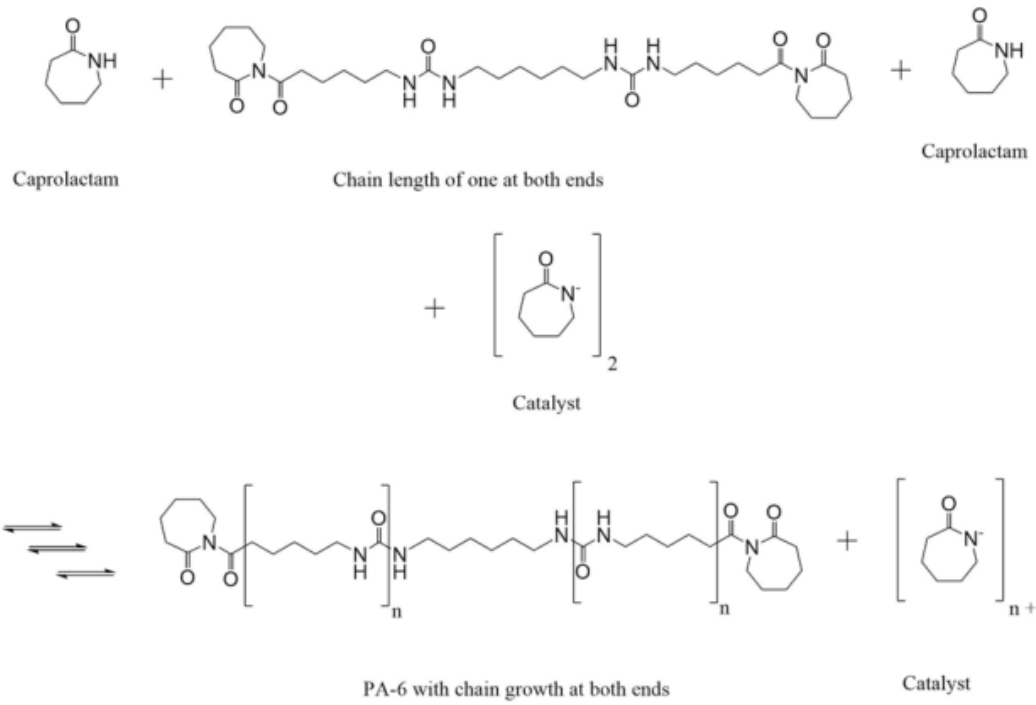

C. Quality Assurance Form

THE UNIVERSITY of EDINBURGH

Quality Assurance for fibre reinforced composite laminates

Composites Group, University of Edinburgh

Aim: Method of measuring **accuracy** and **consistency** of laminate properties

Basic metrics: thickness, density, fibre volume fraction

Other metrics: Void content (segmentation from CT/microscope images), degree of conversion, molecular weight

Laminate reference number:

General Comments:

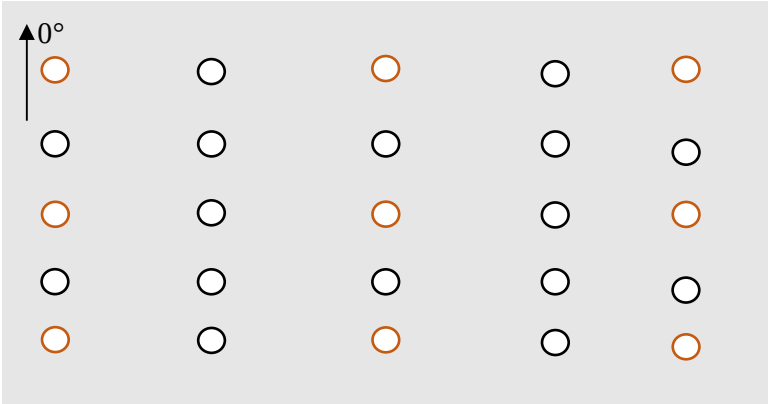

Thickness:

Thickness determined at 25 locations on laminate.

Average (mm)	
Standard deviation (mm)	

Density:

Density determined from 9 samples in each laminate using Archimedes' principle.

Average (g/cm^3)	
Standard deviation (g/cm^3)	

FVF:

Fibre volume fraction determined from 9 samples in each laminate using burn off in the furnace.

Average (%)	
Standard deviation (%)	

Voids:

Void content determined from 9 samples.

Average (%)	
Standard deviation (%)	

Tg (Molecular weight):

DMTA using 3 pt. bend configuration and the tan delta peak determined.

Average (°C)	
Standard deviation (°C)	

D. Sample preparation

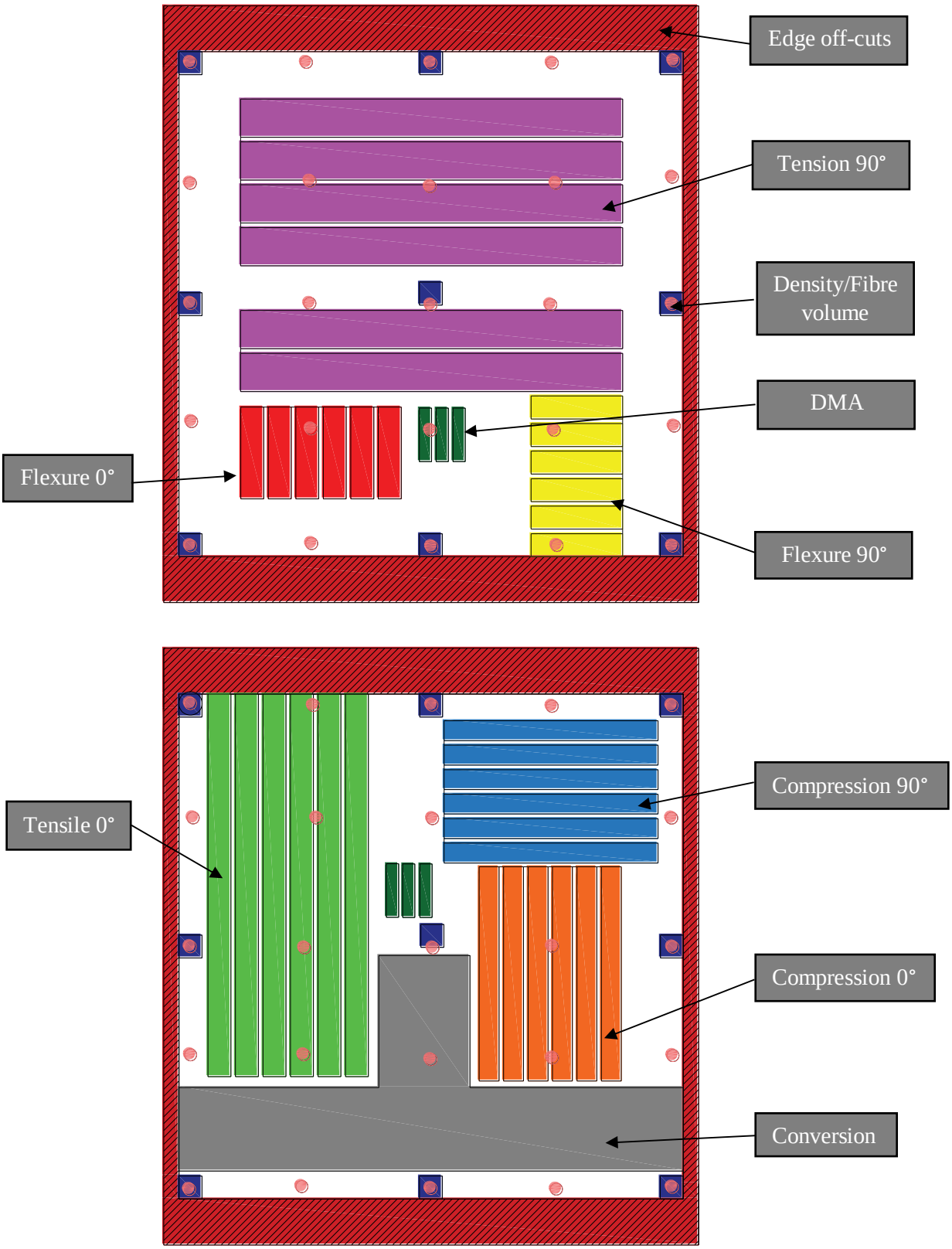

Fig. D1: Extraction positions of specimens from laminates. The pink spots represent the points from where thickness measurements were taken prior to specimen extraction.

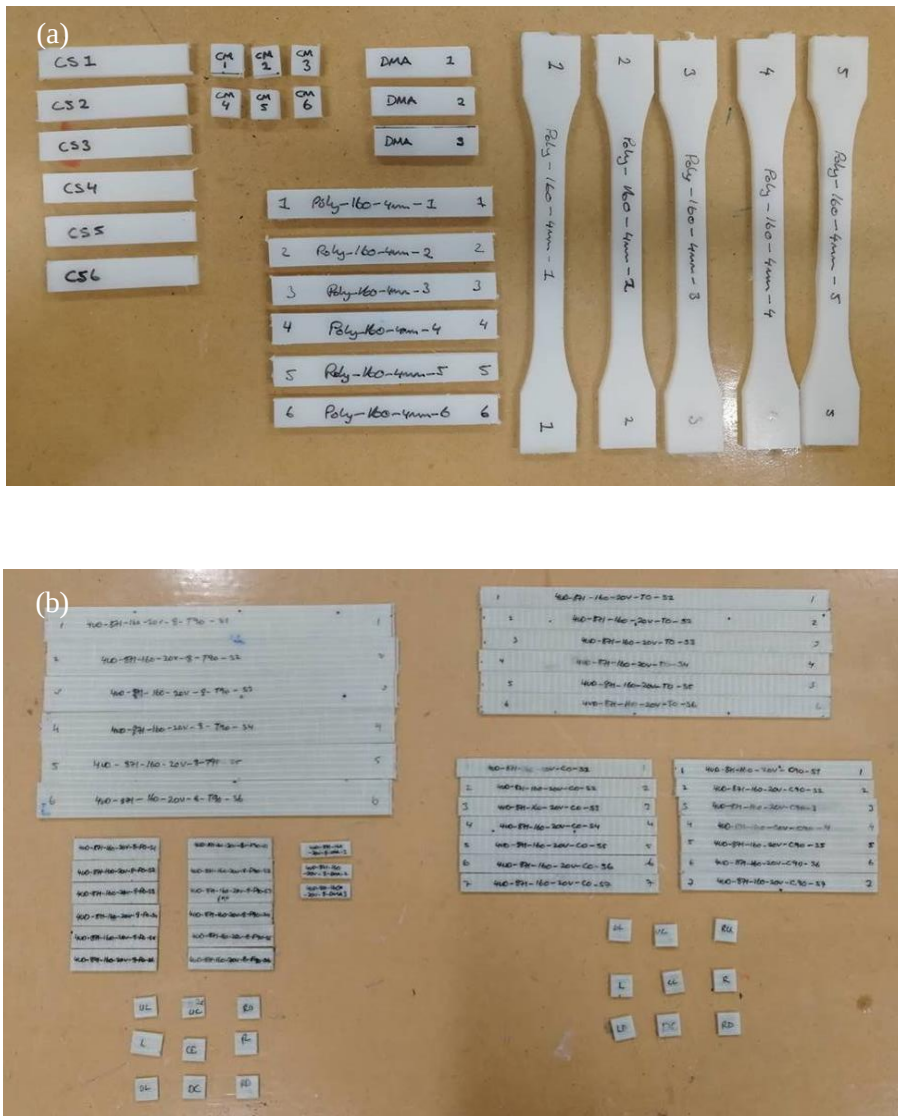

Fig. D2: (a) polymer samples and (b) composite samples.

E. AFM supplemetary information

Dendritic Structure of 871 Sizing

Fig. E1 presents AFM height images of the 871 fibres where the dendritic structure of the sizing on the fibre surface is clearly visible across a larger surface area (4 μm^2). Furthermore, the sizing pattern is consistent across images of different fibres (Fig. E1 (a) and (b)).

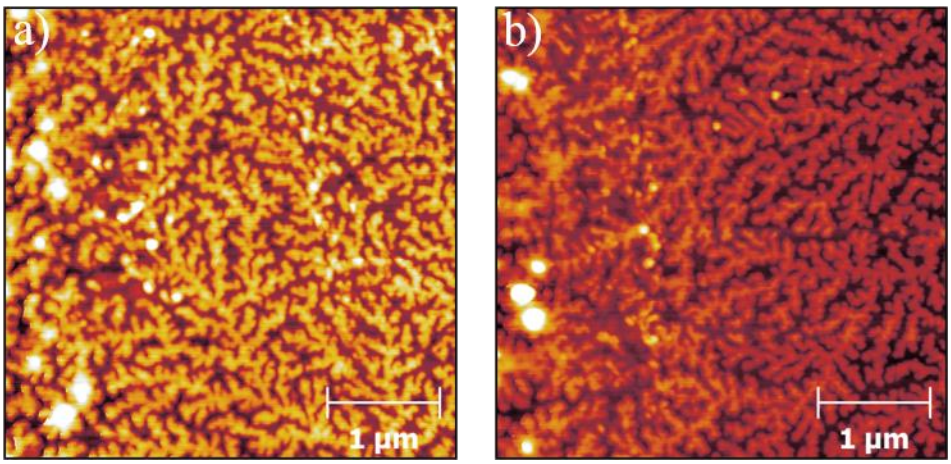

Fig. E1: 4 μm^2 AFM height images of the 871 fibres which clearly show the dendritic structure of the sizing over a larger length scale. a) 871 Fibre 1, b) 871 Fibre 2.

Phase AFM Images

Fig. E2 shows phase AFM images of each fibre type which correspond to the height images in Fig. 6.7. Phase images use colour contrast to display the phase angle shift between the driving signal and the output signal of the AFM cantilever during tapping mode. The phase angle shift is determined by the viscoelastic properties of the surface, and consequently, it can be used to identify different materials within an image. However, the surface topography can also influence the phase angle shift, and therefore the colour contrast in phase images [174]–[177]. In the present study, phase images were utilised to provide qualitative information regarding the composition of the sizing structures on each of the fibres surface. Fig. E2 (a) shows the typical phase image of the desized fibre where there is generally very little contrast across most of the surface which is expected as the sizing has been mostly removed. There is some contrast in the areas of the image where there are still remnants of the sizing, however this is likely influenced by the surface topography rather than any considerable differences in viscoelastic properties. Fig. E2 (b) shows the phase image for the 871 fibre where the dendritic structures of the sizing is clearly observed. There is not significant contrast between the sizing

and fibre surface which suggests that their viscoelastic properties are not drastically different at the nanoscale. Figure E2 (c) shows the phase image for the 886 fibre, where once again there is only minimal contrast across the image. Any areas of significant contrast corresponds to the larger aggregates of sizing, which suggests that the contrast is significantly influenced by surface topography. For both the 871 and 886 fibre, it appears that the viscoelastic properties are similar for the fibres and sizing and are generally consistent across both of the materials.

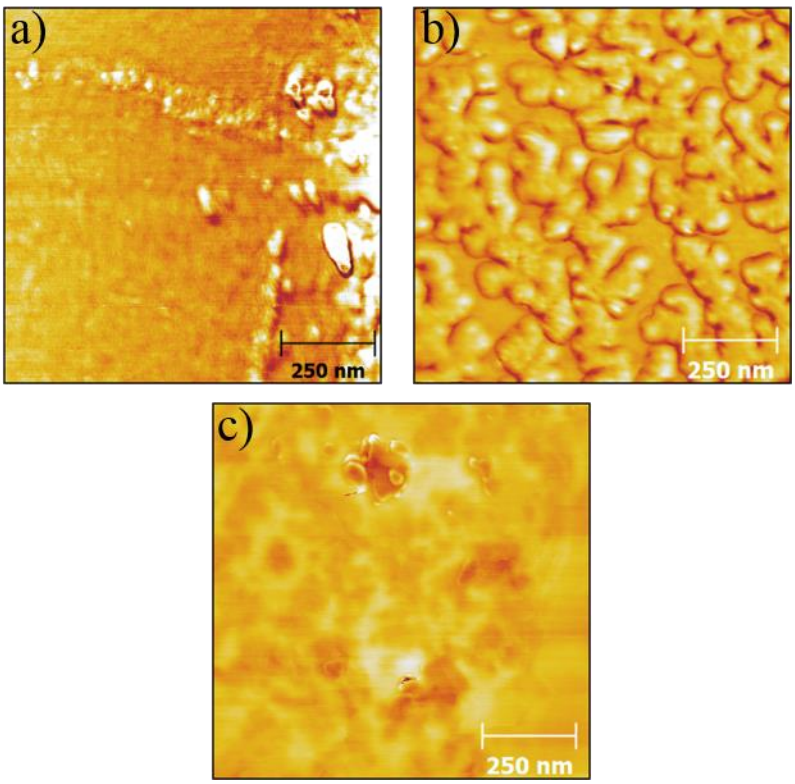

Fig. E2: AFM phase images of the three fibre types which correspond to the height images in Figure 1 of the manuscript. (a) desized fibre, (b) 871 fibre, (c) 886 fibre.

F. Additional mechanical test results

The results from the additional mechanical testing carried out on the 886 composite material are presented in Table F.1 below. The longitudinal (0°) strength and modulus values have been normalised to 50%. The laminates from which the samples were extracted had a measured fibre volume fraction of 53.3% and a degree of conversion of 96%.

Table F.1: Mechanical test results for 886 composite.

	Strength	Modulus	Strain at break
Compression (0°)	465.4 ± 41.7	42.0 ± 2.4	1.14 ± 0.06
Compression (90°)	96.48 ± 6.63	7.87 ± 0.35	3.2 ± 0.9
Flexural (0°)	742.6 ± 39.3	33.6 ± 1.3	2.3 ± 0.3
Flexural (90°)	73.0 ± 3.0	9.5 ± 0.5	1.14 ± 0.08

G. Additional mechanical test results

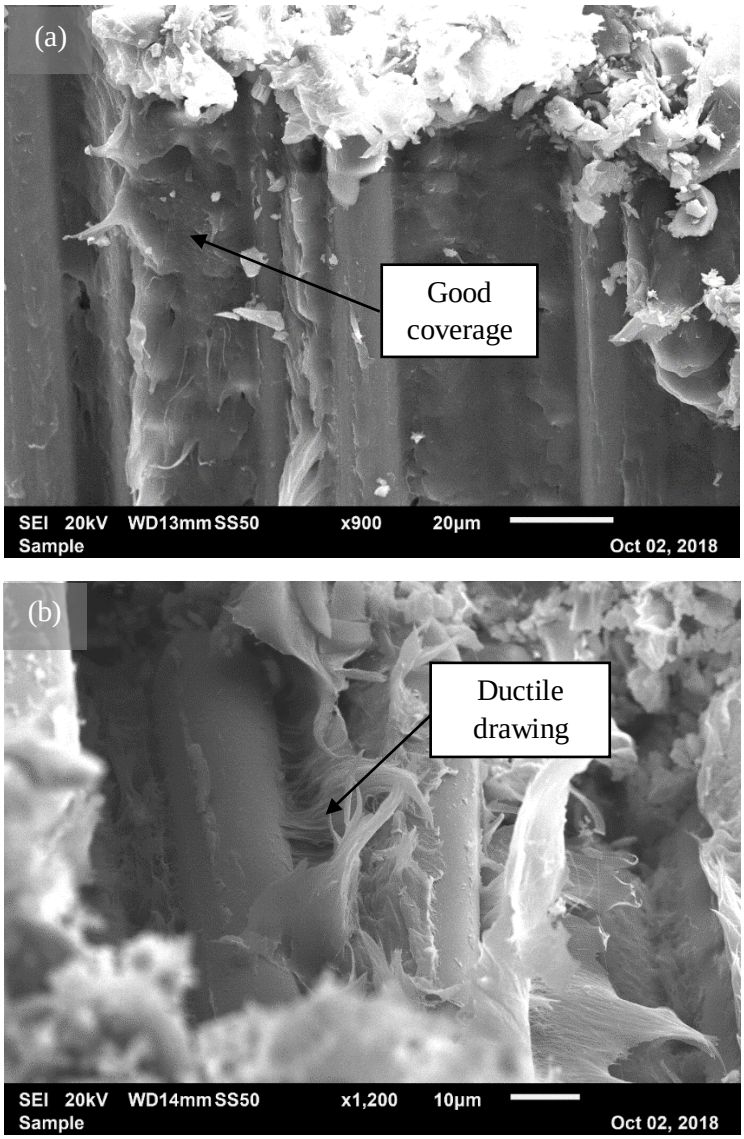

Fig. G.1: SEM images of failed 886 composite surface after longitudinal flexural testing.

H. Fibre testing

To determine the strength and modulus of the unsized, 871 and 886 fibres, tensile tests were carried out.

Preparation and testing:

Plain single ply card was cut into 5 mm by 60 mm strips. A diamond shape was cut into the centre of each strip and pencil marks drawn at 25 mm from either side of the centerline. A single glass fibre was laid onto the strip and Loctite super glue was dripped onto the fibre at the marked 25 mm lines and left to set. The specimens were secured into a 200 N screw driven Deben micro-tensile tester with a 5 N loadcell. The centre diamond cutouts were carefully split using a pair of wire snips to create a free region of 50 mm of fibre. A crosshead speed of 0.1 mm/min was applied to the fibre and the resultant force and extension were recorded to fibre failure. This was repeated five times for each test group. The test setup is shown in Fig. H.1.

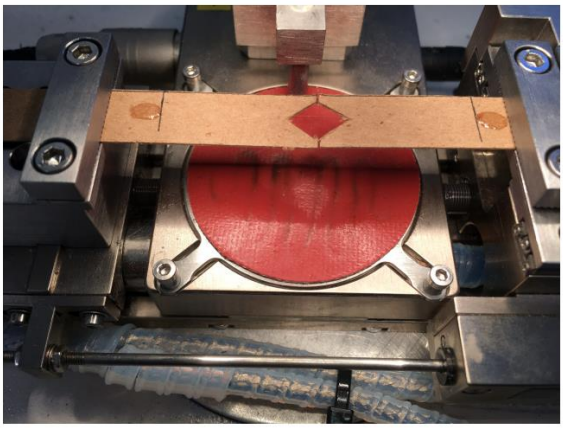

Fig. H.1: Test setup for fibre testing using Deben micro-tensile tester.

Results and discussion:

The results show that the 886 fibres had the highest strength and modulus. This was unsurprising based on SEM observations which showed that the diameter of the 886 fibres was higher than the other two as a result of the sizing. Due to the fact that the cross sectional area was based purely on the fibre area and not that with the sizing, it presented higher values.

Table H.1: Mechanical properties of unsized, 886 and 871 fibres.

	X_{50}^{T} (MPa)	E_{50}^{T} (GPa)	Percentage increase in ultimate tensile strength relative to unsized group
Unsized	581.2 ±159.7	95.9 ±31.6	-
886	2271.7 ±472.5	110.9 ±20.9	290.8%
871	1539.7 ±601.6	88.3 ±38.5	164.9%

I. Single Fibre Pull-out

To determine experimental values for the fibre-matrix interfacial shear strength (σ^{fm}), single fibre pull-out tests were carried out for the unsized, 886, 871 fibre cases. In order to prepare the samples, a mould was made. The mould consisted of 2 halves made from silicone rubber such that when combined, samples could be moulded inside.

Sample manufacture and testing:

The mould halves and fibres were dried in the oven at 105 °C for 30 minutes. The individual fibres were laid out across one of the mould halves, parallel to each other with separation of approximately 20 mm. The fibres were laid straight across the cavity as represented by the white dashed lines in Fig. I.1. The top half of the mould was placed on top, sealing the mould closed. The two halves were sandwiched together with high temperature tape applying a small amount of pressure to prevent leaking occurring . The assembled setup was laid out in the oven for drying with a thermocouple taped to the inside as shown in Fig. I.1. It was then heated to a steady-state temperature of 160 °C in an oven, at which point the APA-6 was cast in the cavity from the TP-RTM machine via a silicone rubber tube through the back of the oven. The machine parameters, mixing ratios and processes were otherwise identical to Chapter 4.

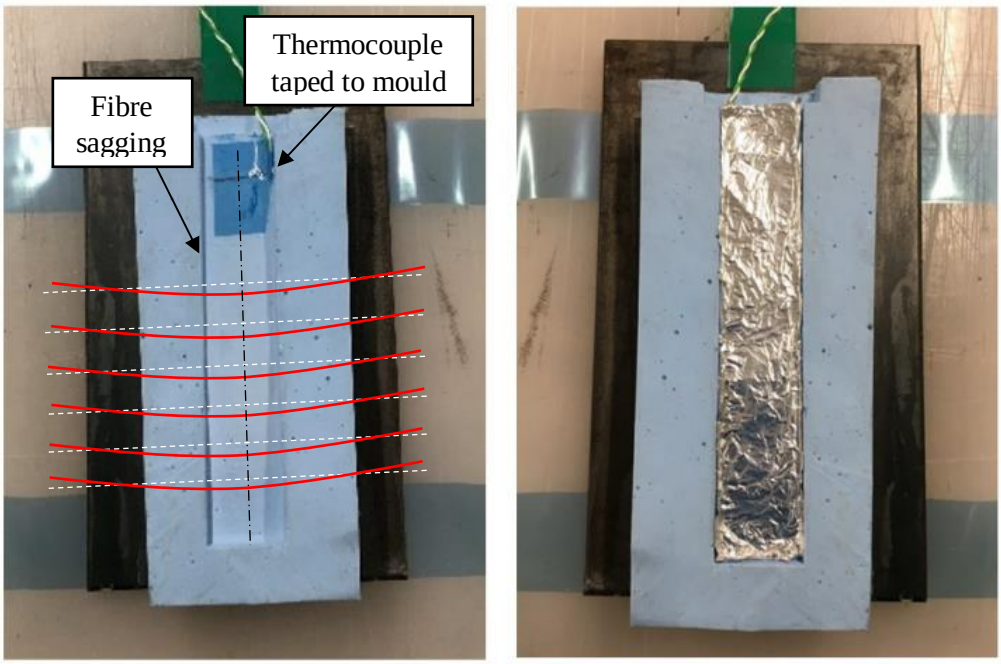

Fig. I.1: Mould halves used for single fibre pull-out tests. Due to their small size, the fibres cannot be seen. The dashed white lines represent the fibres as they were positioned in the mould before processing, the red lines represent the sagging of fibres which occurred during pouring and the dashed black line represents the cutting path after demoulding.

The polymerised blocks were demoulded with the fibres emebedded along the centreplane of their thickness. It was discovered that as a result of pouring, the fibres sagged slightly as shown by the red lines in Fig. H.1. The block was cut along the centreline shown in black in Fig. H.1 and between fibres to create 12 sample blocks. Rectangle shapes from card similarly to Appendix F were used, except this time, the diamond cut out was now made at between 30 and 35mm from one side of the card. This dimension was chosen as it allows the same cutting of card to create free fibre region, but also minimises the required fibre free length to the length of the custom-made cross-head grip for the Deben rig. The PA6 and fibre free end were secured to the card strip on either side of the diamond with super glue.

The specimens were loaded into the grips of the Deben rig which was fixed with a 5 N load cell. The centre diamond cutouts were carefully split using a pair of wire snips to create a region of 50 mm of fibre. A crosshead speed of 0.1 mm/min was used for testing. At least 5 tests were carried out for each of the three cases. An example fo a partially pulled out fibre is shown in Fig. H.2

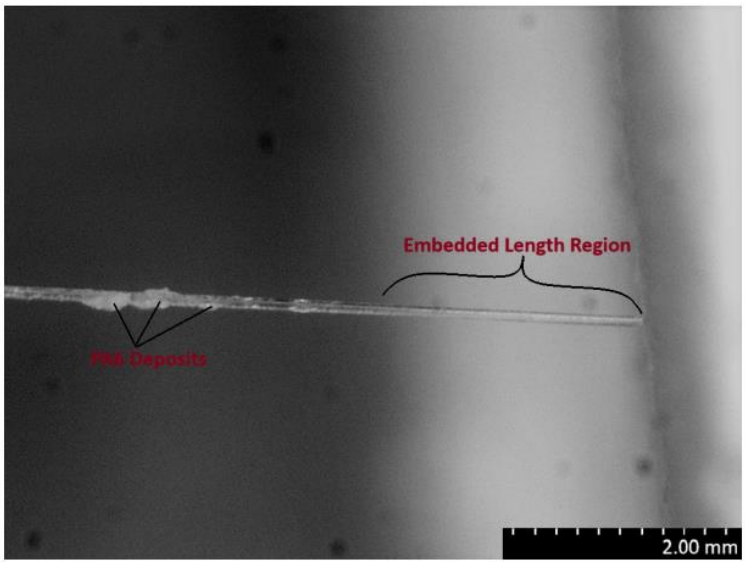

Fig. I.2: Image of parially pulled out fibre.

σ^{fm} was determined as the stress calculated at peak debonding force in the force-displacement curves for the single fibre pull-out tests. The formula used to calculate interfacial shear strength was that in equation I.1.

$$\sigma^{fm} = \frac{F_{max}}{\pi D_f L_e} \tag{I.1}$$

Results and discussion:

The results of singe fibre pull-out tests are shown in Table I.1. Full fibre pull-out was achieved for the 886 whereas only partial pull-out was achieved or failure before pull-out for the 871 and unsized cases. Some of the latter cases had longer embed lengths, meaning that a greater force was required to pull them out. Due to sagging during manufacturing, the free length of many of the fibres extruded from the polymer at an angle ($\emptyset$). As a result, during testing, the free length wasn't being pulled in line with the embedded part of the fibre. This meant that the effective pulling force was a component of the force read by the load cell, $F\cos\emptyset$. This meant a higher amount of force was required to pull the fibres out. The angle also added a large stress concentration. With these factors taken into account, combined with the higher strength of the 886 fibres (shown in Appendix H), this is not unsurprisng. To solve these problem, methods to keep the fibres aligned during processing would need to be considered and a shorter embed length.

Table I.1: Single fibre pull-out test results for the unsized, 886 and 871 cases.

	Indicative σ^{IFSS} (MPa)		
Specimen	Unsized	886	871
1	n.a.	3.43	0.966
2	n.a.	1.46	1.843
3	n.a.	2.50	n.a.
4	n.a.	2.77	n.a.
5	0.77	0.55	n.a.
6	n.a.	1.99	n.a.
Average	0.77	2.12 ±1.02	1.40 ±0.62